ПЯТЫЙ
МОСКОВСКИЙ
СИМПОЗИУМ
ПО СОЛНЕЧНОЙ СИСТЕМЕ

# THE FIFTH MOSCOW SOLAR SYSTEM SYMPOSIUM

program
abstracts

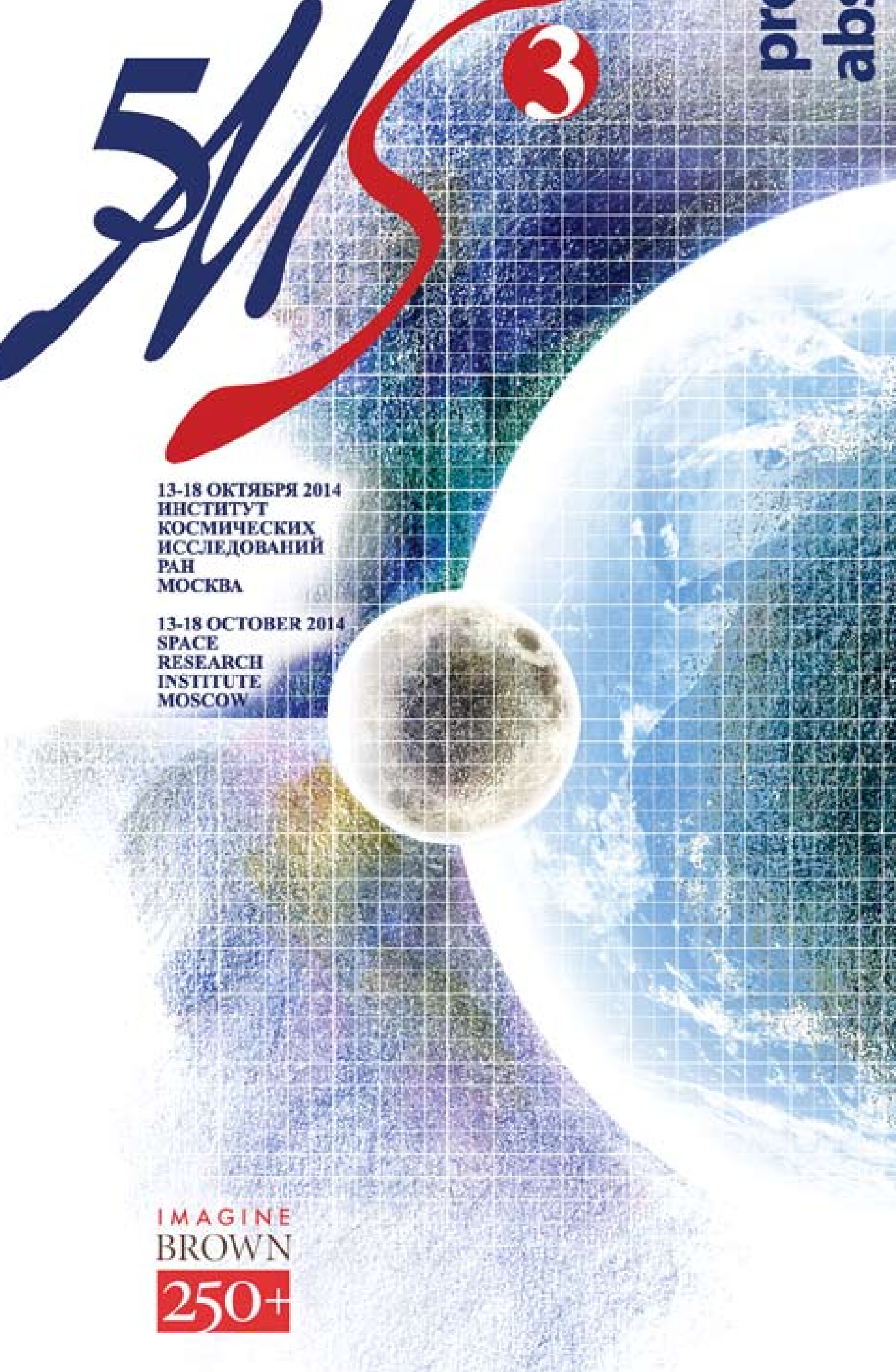

13-18 ОКТЯБРЯ 2014
ИНСТИТУТ
КОСМИЧЕСКИХ
ИССЛЕДОВАНИЙ
РАН
МОСКВА

13-18 OCTOBER 2014
SPACE
RESEARCH
INSTITUTE
MOSCOW

IMAGINE
BROWN
250+

# overview 5M-$S^3$ program

# THE FIFTH MOSCOW SOLAR SYSTEM SYMPOSIUM (5M-$S^3$)

## IKI RAS, 13-18 october 2014

| | 13 october | 14 october | 15 october | 16 october | 17 october |
|---|---|---|---|---|---|
| 10.00 | opening session. NEW HIGHLIGHTS RESULTS | session 2. MOON | session 3. DUST AND DUSTY PLASMA IN SPACE | session 5. NEW PROJECTS AND EXPERIMENTS | visit to space industry enterprise: GAGARIN RESEARCH&TEST COSMONAUT TRAINING CENTER |
| 10.20 | | | | | |
| 10.40 | | | | | |
| 11.00 | | | | | |
| 11.20 | | | | | |
| 11.40 | coffee | coffee | coffee | coffee | |
| 12.00 | session 1. MARS | | | | |
| 12.20 | | | | | |
| 12.40 | | | | | |
| 13.00 | lunch | lunch | session 4. VENUS / lunch | session 6. GIANT PLANETS AND THEIR MOONS / lunch | |
| 14.00 | | | | | |
| 14.20 | | | | | |
| 14.40 | | | | | |
| 15.00 | | | | | |
| 15.20 | | | | | |
| 15.40 | | | | | |
| 16.00 | coffee | coffee | coffee | BROWN -250th / coffee | |
| 16.20 | | | | | |
| 16.40 | | | | | |
| 17.00 | | | | | |
| 17.20 | | | | | |
| 17.40 | | | | | |
| 18.00 | **POSTER SESSION**. welcome party | | | concert | |
| 18.20 | | | **POSTER SESSION** | | |
| 18.40 | | | | | |
| 19.00 | | social events in MOSCOW | | 5M-S3 and BROWN- 250th reception | |
| 19.20 | | | social events in MOSCOW | | |
| 19.40 | | | | | |
| 20.00 | | | | | |

# 5M-S3 SCIENTIFIC PROGRAM

| | | | |
|---|---|---|---|
| | **13 october 2014** | | |
| | **opening session. NEW HIGHLIGHTS RESULTS** | | **10.00-11.40** |
| 5MS3-OS | **Lev ZELENYI** | Welcome | 10.00-10.10 |
| 5MS3-NHR-01 | **Peter WURZ** et al | Early Activity of comet Churyumov-Gerasimenko: ROSINA in situ Measurements of the Coma | 10.10-10.40 |
| 5MS3-NHR-02 | **James HEAD**, **III** | An Overview of the MESSENGER Mission to Mercury: New Perspectives on an Old Planet and its Environment | 10.40-11.10 |
| 5MS3-NHR-03 | **R.ELPHIC**, **T.STUBBS** and LADEE science PI team | Results from the Lunar Atmosphere and Dust Environment Explorer (LADEE) | 11.10-11.40 |
| | **coffee-break** | | 11.40-12.00 |
| | **session 1: MARS** | | **12.00-18.00** |
| | **convener: Oleg KORABLEV** | | |
| 5MS3-MS-01 | **Eduard DUBININ** et al | Large-amplitude coherent structures in plasma near Mars | 12.00-12.20 |
| 5MS3-MS-02 | **Oleg VAISBERG** | Atmospheric losses of Mars induced by solar wind | 12.20-12.40 |
| 5MS3-MS-03 | **Stas BARABASH** et al | Solar wind interaction with Phobos | 12.40-13.00 |
| | **lunch** | | 13.00-14.00 |
| 5MS3-MS-04 | **Valery SHEMATOVICH** | Non-thermal dissipation of the Martian upper atmosphere | 14.00-14.20 |
| 5MS3-MS-05 | **Vladimir KRASNOPOLSKY** | Observations of the CO dayglow at 4.7 μm on Mars: Variations of temperature and CO mixing ratio at 50 km | 14.20-14.40 |
| 5MS3-MS-06 | **Olivier WITASSE** et al | Comet C/2013 A1 (Siding Spring) flyby of Mars: Mars Express safety concerns and science plans | 14.40-15.00 |
| 5MS3-MS-07 | **James HEAD, III** et al | Late Noachian “Cold and Icy Highlands” Model: Geological Predictions for Equilibrium Environments and Non-equilibrium Melting Scenarios | 15.00-15.20 |
| 5MS3-MS-08 | **James CASSANELLI** and **James HEAD** | Volcano-ice Interactions in a Late Noachian “Icy Highlands” Mars: Implications for Groundwater Recharge and Outflow Channel Water Sources on the Tharsis Rise | 15.20-15.40 |
| 5MS3-MS-09 | **James DICKSON** et al | Multi-phase, punctuated gully erosion on Mars: Seasonal insolation effects on the melting and refreezing of surface ice in the McMurdo Dry Valleys | 15.40-16.00 |
| | **coffee-break** | | 16.00-16.20 |
| 5MS3-MS-10 | **Erica JAWIN** et al | Paraglacial Geomorphology on Mars: The Distribution of Post-Glacial Features across the Mid-Latitudes | 16.20-16.40 |
| 5MS3-MS-11 | **Jürgen OBERST** et al | Dynamic Shape and Down-Slope Directions on Phobos | 16.40-17.00 |

| | | | |
|---|---|---|---|
| 5MS$^3$-MS-12 | **Sergey RAEVSKIY** et al | Diagnostic properties of body waves for sounding the interiors of Mars | 17.00-17.20 |
| 5MS$^3$-MS-13 | **Yaroslaw ILYUSHIN** et al | Surface clutter in ground penetrating radar sounding: real MARSIS echoes computer simulations | 17.20-17.40 |
| 5MS$^3$-MS-14 | **Vladimir GUBENKO** et al | The internal waves and saturation degree in the Earth's atmosphere from radiosonde wind and temperature measurements and applications to RO waves in planetary atmospheres | 17.40-18.00 |
| | **POSTER SESSION (all sessions)** | | **18.00-19.00** |

| | 14 october 2014 | | |
|---|---|---|---|
| | **session 2: MOON**<br>**conveners: Igor MITROFANOV, Lev ZELENYI** | | **10.00-19.00** |
| | **session 2.1. LUNAR DATA ANALYSIS AND INTERPRETATION** | | **10.00-13.00** |
| 5MS$^3$-MN-01 | **Sergei IPATOV** | Formation of embryos of the Earth-Moon system as a result of a collision of two rarefied condensations | 10.00-10.20 |
| 5MS$^3$-MN-02 | **Yangxiaoyi LU** | Analysis of the iron content and morphology of CE-3 landing site | 10.20-10.40 |
| 5MS$^3$-MN-03 | **James HEAD** and L. **WILSON** | Lunar Regional Pyroclastic Deposits: Sources of Volatiles and the Role of Near-Surface Volatile Enhancement | 10.40-11.00 |
| 5MS$^3$-MN-04 | **Ekaterina KRONROD** et al | Possible temperature profiles of the lunar mantle | 11.00-11.20 |
| 5MS$^3$-MN-05 | **Alexey BEREZHNOY** et al | Search for Meteoroid Impacts on the Moon | 11.20-11.40 |
| | **coffee-break** | | 11.40-12.00 |
| 5MS$^3$-MN-06 | **Vladislav SHEVCHENKO** | Space Cornucopia on the Lunar Poles | 12.00-12.20 |
| 5MS$^3$-MN-07 | **Michael SHPEKIN** and **Ch.R.MUKHAMETSHIN** | Problem of joint photogrammetric processing images obtained by different cameras from different orbits | 12.20-12.40 |
| 5MS$^3$-MN-08 | **Anton SANIN, I.MITROFANOV, M.LITVAK, W.BOYNTON, K.HARSHMAN, R. STARR, L. EVANCE, R.SAGDEEV, E. CHIN, T. McCLANAHAN, T. LIVENGOOD** | Water distribution at lunar poles according to LEND neutron mapping | 12.40-13.00 |
| | **lunch** | | 13.00-14.00 |
| | **session 2.2. FUTURE LUNAR INVESTIGATIONS AND MISSIONS** | | **14.00-19.00** |
| 5MS$^3$-MN-09 | **Lev ZELENYI, I. MITROFANOV, A.PETRUKOVICH, V.KHARTOV, A.LUKYANCHIKOV** and **V.DOLGOPOLOV** | The sequence of missions “Luna-Glob”, “Luna-Resours” and “Luna-Grunt” | 14.00-14.20 |
| 5MS$^3$-MN-10 | **Lev ZELENYI, I. MITROFANOV** and **V.TRET’YAKOV** | Scientific investigations onboard “Luna-Glob” and “Luna-Resource” landers | 14.20-14.40 |
| 5MS$^3$-MN-11 | **Berengere HOUDOU** | European approach to lunar exploration in cooperation with Russia | 14.40-15.00 |
| 5MS$^3$-MN-12 | **James CARPENTER** | Accessing and assessing the lunar resources with PROSPECT | 15.00-15.20 |
| 5MS$^3$-MN-13 | **Alexander KOSOV** et al | Coherent Luna’s radio beacon and its scientific potential | 15.20-15.40 |
| 5MS$^3$-MN-14 | **Dmitri SKULACHEV** et al | Lunar Regolith Investigation Using Microwave Radiometer/ Scatterometer | 15.40-16.00 |
| | **coffee-break** | | 16.00-16.20 |

| | | | |
|---|---|---|---|
| 5MS$^3$-MN-15 | **Alexander GUSEV** et al | Fine effects of spin-orbit dynamics of the Moon, Lunar radio beacons and Lunar Navigation Almanac for ChangE-3/4, Luna-Glob-Resource, SELENE-2 missions | 16.20-16.40 |
| 5MS$^3$-MN-16 | **Alexander BASILEVSKY** et al | Survival times of meter-sized rock boulders on the surface of airless bodies | 16.40-17.00 |
| 5MS$^3$-MN-17 | **Oleg KOZLOV** et al | Mobile scientific platform: possibility of development and application outlook | 17.00-17.20 |
| 5MS$^3$-MN-18 | **Irina KARACHEVTSEVA** et al | Methods and instruments for the complex spatial analysis of the potential landing sites on the Lunar subpolar area | 17.20-17.40 |
| 5MS$^3$-MN-19 | **Mikhail IVANOV** et al | Landing site selection for Luna-Glob mission in crater Boguslawsky | 17.40-18.00 |
| 5MS$^3$-MN-20 | **Ryan CHAU** and **Austin MARDON** | Using the Moon as a Stepping Stone to Reach Other Planets | 18.00-18.20 |
| 5MS$^3$-MN-21 | **James HEAD** et al | Human Exploration of the Moon: A Science and Engineering Synergism roadmap for the Future | 18.20-18.40 |
| 5MS$^3$-MN-22 | **Lev ZELENYI** and **Igor MITROFANOV** | Integrated lunar program of Roscosmos: manned and robotic missions | 18.40-19.00 |

| | | | |
|---|---|---|---|
| | **15 october 2014** | | |
| | **session 3: DUST AND DUSTY PLASMA IN SPACE** | | **10.00-13.00** |
| | **conveners: Alexander ZAKHAROV, Mark KOEPKE** | | |
| 5MS$^3$-DP-01 | **Nikolay BORISOV** et al | The influence of frozen water under the surface on dust motion in the Lunar polar region (**invited)** | 10.00-10.20 |
| 5MS$^3$-DP-02 | **Mark KOEPKE** et al | The concept of separate charging and discharging energy-dependent work functions based on experimental and simulation circulating-loop analysis of granular materials properties and charge state (**invited**) | 10.20-10.40 |
| 5MS$^3$-DP-03 | **Sergey POPEL** et al | Fine-dispersed particles and dusty plasmas at the Moon (**invited**) | 10.40-11.00 |
| 5MS$^3$-DP-04 | **Tatiana BURINSKAYA** | Non-monotonic potentials above the day-side lunar surface exposed to the solar radiation (**invited)** | 11.00-11.20 |
| 5MS$^3$-DP-05 | **Evgeny ROSENFELD** et al | Relation between the charge/discharge processes of dust particles and the dynamics of dust clouds over the Moon surface (**invited**) | 11.20-11.40 |
| | **coffee-break** | | 11.40-12.00 |
| 5MS$^3$-DP-06 | **Tatiana SALNIKOVA** and **S.J.STEPANOV** | On the dust matter in the neighborhood of the Lagrange libration points | 12.00-12.20 |
| 5MS$^3$-DP-07 | **Barbara ATAMANIUK** and **H. ROTHKAEHL** | Polish Contribution to ESA Juice mission (RPWI). Dusty plasma and turbulent plasma investigations as a tools for diagnostic Space Weather conditions | 12.20-12.40 |
| 5MS$^3$-DP-08 | **Evgenij ZUBKO** et al | Reflectance of interplanetary dust particles inferred with the Umov effect | 12.40-13.00 |
| | **lunch** | | 13.00-14.00 |
| | **session 4: VENUS** | | **14:00-18:20** |
| | **convener: Ludmila ZASOVA** | | |
| 5MS$^3$- VN -01 | **Vladimir KRASNOPOLSKY** | Chemistry of Venus' Atmosphere | 14.00-14.20 |
| 5MS$^3$- VN -02 | **Imant VINOGRADOV** et al | Vertical profiling of sulphur dioxide and other gases contents and isotope ratios in the Venussian atmosphere by a diode laser spectrometer ISKRA-V on board of the Venera-D lander | 14.20-14.40 |
| 5MS$^3$- VN -03 | **Vladimir KRASNOPOLSKY** | Observations of the CO dayglow at 4.7 mu, CO mixing ratios, and temperatures at 74 and 105 km on Venus | 14.40-15.00 |
| 5MS$^3$- VN -04 | **Ludmila ZASOVA** et al | Oxygen night airglow in Venus atmosphere (VIRTIS/VEX) | 15.00-15.20 |

| | | | |
|---|---|---|---|
| 5MS$^3$- VN -05 | **Alexander RODIN** | Non-hydrostatic GCM simulations of subsolar-antisolar circulation in the Venus atmosphere | 15.20-15.40 |
| 5MS$^3$- VN -06 | **Nikolay IGNAIEV** et al | Haze above the clouds of Venus from VIRTIS / Venus Express limb night side observations | 15.40-16.00 |
| | **coffee-break** | | 16.00-16.20 |
| 5MS$^3$- VN -07 | **Denis BELYAEV** et al | Sulphur dioxide distribution in Venus' night-side mesosphere | 16.20-16.40 |
| 5MS$^3$- VN -08 | **Mikhael BONDARENKO** and **A. GAVRIK** | Venus - the Life cycle of 5-15km Gravity Waves: from the Upper Cloud to Extinction in the Thermosphere as Observed from Occultation Data | 16.40-17.00 |
| 5MS$^3$- VN -09 | **Mikhail IVANOV** and **James HEAD** | Embayed craters on Venus: Testing the catastrophic and equilibrium resurfacing models | 17.00-17.20 |
| 5MS$^3$- VN -10 | **Alexander BAZILEVSKIY** et al | Current volcanism on Venus: Evidence from the VEx VMC observations | 17.20-17.40 |
| 5MS$^3$- VN -11 | **Mikhail KRESLAVSKY** et al | New Constraints on Resurfacing History of Venus from Impact Craters | 17.40-18.00 |
| 5MS$^3$- VN -12 | **Alexander PAVELYEV** et al | Bistatic radar investigation of the North and South poles surface of Venus using reanalysis of Venera's 15 and 16 data | 18.00-18.20 |
| | **POSTER SESSION (all sessions)** | | **18.20-19.20** |

| | | | |
|---|---|---|---|
| | **16 october 2014** | | |
| | **cession 5: NEW PROJECTS AND EXPERIMENTS**<br>**convener: Oleg KORABLEV** | | **10.00-13.00** |
| 5MS³-NP-1 | **Leonid KSANFOMALITY** | Physics of planetans—oceanic planets | 10.00-10.20 |
| 5MS³-NP-2 | **Marina Diaz MICHELENA** | New Instruments for Planetary Mineralogy | 10.20-10.40 |
| 5MS³-NP-3 | **Hideo HANADA** et al | Development of a telescope for observation of the lunar rotation and experiments on the ground | 10.40-11.00 |
| 5MS³-NP-4 | **Igor ALEXEEV** | Mercury Magnetosphere | 11.00-11.20 |
| 5MS³-NP-5 | **Victor OSTROVSKII** and **E.A. KADYSHEVICH** | Life Origination Hydrate Theory (LOH-Theory): the reaction mechanism and set of necessary and sufficient conditions | 11.20-11.40 |
| | **coffee-break** | | 11.40-12.00 |
| 5MS³-NP-6 | **Olivier Witasse** et al | The ExoMars Programme | 12.00-12.20 |
| 5MS³-NP-7 | **Masaki FUJIMOTO** | Frequency matters: ISAS's strategy for small but edgy planetary explorations | 12.20-12.40 |
| 5MS³-NP-8 | **Andrey PATRAKEEV** et al | PHOBOS Sample Return: next approach | 12.40-13.00 |
| | **lunch** | | 13.00-14.00 |
| | **session 6: GIANT PLANETS AND THEIR MOONS**<br>**conveners: Oleg KORABLEV, Konstantin MARCHENKOV** | | **14.00-16.00** |
| 5MS³-GP-1 | **Ivan VASKO** et al | Standing shear Alfven waves driven by the Jupiter dipole wobbling | 14.00-14.20 |
| 5MS³-GP-2 | **Vladimir KRASNOPOLSKY** | Chemical composition of Titan's atmosphere: Observations and the photochemical model | 14.20-14.40 |
| 5MS³-GP-3 | SERGEY **BULAT** et al | Is there life in subsurface oceans of Jovian moons? The borehole frozen water of the subglacial Lake Vostok (East Antarctica) and its microbial content | 14.40-15.00 |
| 5MS³-GP-4 | **Anatoly ZUBAREV** et al | New methodology for study of the basic geodetic parameters and relief of outer planetary bodies: Galilean satellites and Enceladus | 15.00-15.20 |
| 5MS³-GP-5 | **Anatoly MANUKIN** et al | Gravity-inertial measurements on Europa - Jupiter's moon | 15.20-15.40 |
| 5MS³-GP-6 | **Alexander BATKHIN** | Quasi-capture in Hill problem | 15.40-16.00 |
| | **coffee-break** | | 16.00-16.30 |
| | **CELEBRATION OF THE 250th ANNIVERSARY OF THE FOUNDING OF BROWN UNIVERSITY AND 40 YEARS OF BROWN-VERNADSKY AND IKI COOPERATION** | | **16.30-18.00** |

# POSTER SESSION

13 october 18.00-19.00
15 october 18.20-19.20

| | | |
|---|---|---|
| | **MARS** | |
| 5MS$^3$-PS-01 | **Daria KUZNETSOVA** and **M. GRITSEVICH** | Classification of meteor events in the Martian atmosphere |
| 5MS$^3$-PS-02 | **Boris VORONIN** et al | Calculation of line broadening coefficients and temperature exponents for CO-CO2 colliding system |
| 5MS$^3$-PS-03 | **Svetlana GUSLYAKOVA** et al | Long-term nadir observations of the O2 dayglow by SPICAM IR |
| 5MS$^3$-PS-04 | **Nadegda CHUJKOVA** et al | Anomalous internal structure of the terrestrial planets from gravitational field and topography: first results of the exploration of Mars |
| 5MS$^3$-PS-05 | **Timothy GOUDGE** et al | An Assessment of Source to Sink Mineralogy for the Jezero Crater, Mars Paleolake System |
| 5MS$^3$-PS-06 | **James HEAD, III** and **K.R. RAMSLEY** | Impact ejecta from Mars to Phobos: Regolith bulk concentration and distribution, and the sufficiency of Mars ejecta to produce grooves as secondary impacts |
| 5MS$^3$-PS-07 | **Eliott ROSENBERG** and **James HEAD** | The Water Volume Required to Erode the Valley Networks on Mars: Implications for Late Noachian Climate |
| 5MS$^3$-PS-08 | **James DICKSON** et al | Stratigraphic relationships between gullies and the Latitude Dependent Mantle on Mars: Evidence for cyclical emplacement, burial, inversion and removal of young fluvial features in the mid-latitudes |
| 5MS$^3$-PS-09 | **Evgeniy LAZAREV** et al | New version of Mars Globe |
| 5MS$^3$-PS-10 | **Soile KUKKONEN** et al | Mapping and dating the resurfacing events on Martian outflow channels: A case study of Harmakhis Vallis in the eastern Hellas rim region |
| 5MS$^3$-PS-11 | **David WEISS** and **James HEAD** | Testing the Glacial Substrate Model for Double-Layered Ejecta Craters on Mars |
| 5MS$^3$-PS-12 | **Tamara GUDKOVA** et al | Free oscillations for interior structure models of Mars |
| 5MS$^3$-PS-13 | **Vladimir ZHARKOV** and **T.V. GUDKOVA** | On non-hydrostatic deviations in the core-mantle boundary of Mars |
| 5MS$^3$-PS-14 | **Luis VAZQUEZ** et al | New Approaches for the Analysis of Geomagnetic Data |
| 5MS$^3$-PS-15 | **Luis VAZQUEZ** et al | An approach to calculate solar radiation fluxes on the Martian surface |
| 5MS$^3$-PS-16 | **Pascal ROSENBLATT** and **B. PINIER** | Phobos' origin: Revisiting the capture scenario. Tidal evolution of the post-capture orbit |
| | **MOON** | |
| 5MS$^3$-PS-17 | **Yuri BARKIN** et al | The drift and steps of the center of mass of the Moon with respect to the crust and interpretation of unexplained secular changes of the lunar orbit |
| 5MS$^3$-PS-18 | **Yuri BARKIN** | The unified theory of natural processes of planets, satellites and the Sun |
| 5MS$^3$-PS-19 | **Vladimir BUSAREV** et al | New spectral features of some asteroids |
| 5MS$^3$-PS-20 | **Vladislav SHEVCHENKO** and **Yangxiaoyi LU** | Lunokhod 1 and Chang'e 3 Landing Sites: Comporative Characteristics |
| 5MS$^3$-PS-21 | **Gennady KOCHEMASOV** | KREEP-like terrains rising in wide subsided basalt filled hemospheric expanses of Earth, Mars, and Moon: a common reason |

| | | |
|---|---|---|
| 5MS$^3$-PS-22 | **Gennady KOCHEMASOV** | A new planetological thinking: orbits create structures |
| 5MS$^3$-PS-23 | **Jennifer WHITTEN** and **James W. HEAD** | Ancient volcanism on the Moon: The global distribution and composition of cryptomaria |
| 5MS$^3$-PS-24 | **Sergey VOROPAEV** | Figures of equilibrium of self-gravitating inhomogeneous mass |
| 5MS$^3$-PS-25 | **Lauren JOZWIAK** et al | Lunar floor-fractured craters: probes of shallow crustal magmatism on the Moon |
| 5MS$^3$-PS-26 | **Vladimir CHEPTCOV** et al | Low Pressure as Extraterrestrial Factor Influencing on the Viability of Microorganisms |
| 5MS$^3$-PS-27 | **Boris IVANOV** | Ceres as a target for the impact cratering |
| 5MS$^3$-PS-28 | **Ekaterina FEOKTISTOVA** | The nature of NSR N1 area in the crater Peary |
| 5MS$^3$-PS-29 | **Natalia KOZLOVA** et al | New techniques of lunar image processing and artificial modeling of surface |
| 5MS$^3$-PS-30 | **Ryan CHAU** and **Austin MARDON** | Lunar Caving and Lava Tubes |
| 5MS$^3$-PS-31 | **Alexander KOKHANOV** et al | Mapping and the morphometric measurements of small lunar craters |
| 5MS$^3$-PS-32 | **Koji MATSUMOTO** et al | Lunar internal structure modeling using Apollo seismic travel time data and the latest selenodetic data |
| 5MS$^3$-PS-33 | **Albert ABDRAKHIMOV** and **Alexander BASILEVSKY** | Comparison of local geology of Chang'e 3 landing site and in the middle of Lunokhod-1 traverse |
| 5MS$^3$-PS-34 | **Andrei SADOVSKI** and **Alexander SKALSKY** | Deflection of solar wind protons from the lunar magnetic anomalies |
| 5MS$^3$-PS-35 | **Vladimir SMIRNOV** et al | Radiolocation as an effective tool for remote sensing of the subsurface structure of the lunar soil |
| 5MS$^3$-PS-36 | **Sergey ASEEV** et al | The Gas-Analytical-Complex for analysis of volatiles in the Lunar polar regolith during the Luna-Resource mission (2019) |
| | **DUST AND DUSTY PLASMA IN SPACE** | |
| 5MS$^3$-PS-37 | **Evgeny LISIN** et al | Dusty plasma sheath near the lunar surface (numerical simulation) |
| 5MS$^3$-PS-38 | **Gennady DOLNIKOV** et al | Dust Particles investigation for future Russian lunar missions |
| 5MS$^3$-PS-39 | **Elena SERAN** and **Michel GODEFROY** | Electric charging of dust particles: Impact on the variations of electric field and electric resistivity of air |
| 5MS$^3$-PS-40 | **Andrei SHIRYAEV** et al | Photoluminescence of silicon-vacancy defects in meteoritic nanodiamonds |
| 5MS$^3$-PS-41 | **Oleg KHAVROSHKIN** and **Vladislav V. TSYPLAKOV** | The exolife: new factors |
| 5MS$^3$-PS-42 | **Tatiana MOROZOVA** et al | Nonlinear dust acoustic waves in a dusty plasma over the Moon |
| 5MS$^3$-PS-43 | **Vasily DMITRIEV** et al | A toolkit for meteor orbit determination using numerical integration of equations of motion |
| | **VENUS** | |
| 5MS$^3$-PS-44 | **Anna FEDOROVA** et al | Cloud top and water vapor variations in the Venus' mesosphere from the SPICAV observations |
| 5MS$^3$-PS-45 | **Evgeniya GUSEVA** | Morphometry of rift-assosiated volcanoes on Venus and Earth |
| 5MS$^3$-PS-46 | **Leonid KSANFOMALITY** | Viscoplastic medium on the surface of Venus |

| | | |
|---|---|---|
| 5MS$^3$-PS-47 | **Igor KHATUNTSEV** et al | Variations of the zonal flow at Venus cloud tops from VMC/VEX UV images in period from 2006 to 2014 |
| 5MS$^3$-PS-48 | **Marina PATSAEVA** et al | Correlation of the cloud top wind pattern with cloud morphology at the upper cloud level of Venus at 25°S-75°S from VMC/ Venus Express |
| | **NEW PROJECTS AND EXPERIMENTS** | |
| 5MS$^3$-PS-49 | **Mikhail GERASIMOV** et al | The Martian Gas-Analytic Package for the Landing Platform Experiments of the ExoMars 2018 |
| 5MS$^3$-PS-50 | **Imant VINOGRADOV** et al | Diode laser spectroscopy for the ExoMars-2018 mission stationery landing platform |
| 5MS$^3$-PS-51 | **Ilya KUZNETSOV** | Proposal of the Dust Complex onboard the ExoMars-2018 lander |
| 5MS$^3$-PS-52 | **Anatoly MANUKIN** | Seismic and gravity measurements on Mars within the “ExoMars” |
| 5MS$^3$-PS-53 | **Konstantin LUCHNIKOV** et al | Mass-spectrometric method for unveiling signs of life via analysis of the elemental composition of the supposed biomass extracted from regolith of Mars |
| 5MS$^3$-PS-54 | **Konstantin LUCHNIKOV** et al | Characterization of ion formation conditions in LA TOF MS by virtue of indirect MCP detector illumination |
| 5MS$^3$-PS-55 | **Sergey PAVLOV** et al | Correlated study of particles returned by the HAYABUSA space probe from the 25143 Itokawa asteroid by SRXTM, NG-MS, IR and Raman microscopy |
| 5MS$^3$-PS-56 | **Gennady KOCHEMASOV** | Self-destructing small cosmic bodies: Churyumov-Gerasimenko comet and some earlier examples |
| 5MS$^3$-PS-57 | **Oleksandr POTASHKO** | Comet Churyumov-Gerasimenko is not ice |
| 5MS$^3$-PS-58 | **Elena BELENKAYA** and **I.I. ALEXEEV** | FTEs in the Mercury magnetosphere: Dependence on IMF |
| 5MS$^3$-PS-59 | **Michael SHPEKIN** | Some principles of creating astrometric observatory on the Moon territory |
| 5MS$^3$-PS-60 | **Oleg KHAVROSHKIN** and **V.V. TSYPLAKOV** | Two gamma – ray radiation sources: elements synchronizing, solar periodicity |
| 5MS$^3$-PS-61 | **Ryan CHAU** and **Austin MARDON** | Mental Health Care Considerations for Long Term Space Missions |
| | **GIANT PLANETS AND THEIR MOONS** | |
| 5MS$^3$-PS-62 | **Yurii CHETVERIKOV** et al | The content of helium and molecular hydrogen in accretion ice of the subglacial Lake Vostok, East Antarctica |
| 5MS$^3$-PS-63 | **Anna DUNAEVA** et al | Ice/rock ratio in Ganymede and Titan in the context of their internal structure, origin and evolution |
| 5MS$^3$-PS-64 | **Maxim ZAITSEV** et al | Experimental study of the shock-evaporative transformation of meteoritic organics during hypervelocity impacts for the characterization of exogenous organic matter on the surfaces of icy satellites |
| 5MS$^3$-PS-65 | **Andrei MAKALKIN** and V.A. Kronrod | Gas drag and capture of planetesimals in accretion disks of Jupiter and Saturn with account of ablation and fragmentation |
| 5MS$^3$-PS-66 | **Pyotr LYSSENKO** et al | Some Recent Spectrophotometric Studies of Jupiter and Saturn |
| 5MS$^3$-PS-67 | **Vladislav SIDORENKO** | Dynamics of “jumping” Trojans |

# EARLY ACTIVITY OF COMET CHURYUMOV-GERASIMENKO: ROSINA IN SITU MEASUREMENTS OF THE COMA

**Peter Wurz[1], Kathrin Altwegg[1], Hans R Balsiger[1], Annette Jaeckel[1], Martin Rubin[1], Lena Le Roy[1], Sébastien Gasc[1], Ursina Calmonte[1], Chia-Yu Tzou[1], Urs A. Mall[2], Axel Korth[2], Bjoern Fiethe[3], Johan MSJ De Keyser[4], Jean-Jacques Berthelier[5], Henri Reme[6], Tamas I Gombosi[7], Stephen Fuselier[8] and ROSINA team,**
*[1]University of Bern, Bern, Switzerland,*
*[2]Max Planck Institute for Solar System Research, Katlenburg-Lindau, Germany,*
*[3]Technical University of Braunschweig, Braunschweig, Germany,*
*[4]Belgian Institute for Space Aeronomy, Brussels, Belgium,*
*[5]LATMOS Laboratoire Atmosphères, Milieux, Observations Spatiales, Paris Cedex 05, France,*
*[6]IRAP, Toulouse, France, [7]Univ of Michigan, Ann Arbor, MI, USA,*
*[8]SW Rsrch Inst-Space Sci & Engr, San Antonio, TX, USA.*
*Contact: peter.wurz@space.unibe.ch*

## Introduction:

The European Space Agency's Rosetta spacecraft (Glassmeier et al., 2007) is now close to the comet 67P/Churyumov-Gerasimenko (67P/C-G). On board is the Rosetta Orbiter Spectrometer for Ion and Neutral Analysis (ROSINA) instrument suite (Balsiger et al., 2007). ROSINA consists of two mass spectrometers, the Double Focusing Mass Spectrometer (DFMS) and the Reflectron-type Time-Of-Flight (RTOF), as well as the COmet Pressure Sensor (COPS). ROSINA is designed to detect and monitor the neutral gas and thermal plasma environment in the comet's coma by in situ investigation. The two mass spectrometers have high dynamic ranges and complement each other with high mass resolution (DFMS) and high time resolution and large mass range (RTOF). Especially the unprecedented sensitivity and mass resolution of DFMS together with the large mass range of RTOF allow determining precisely light species (e.g. isotopologues) as well as detecting heavy organic species. The pressure sensor COPS measures total gas densities, bulk velocities, and gas temperatures.

At present data for the composition of cometary comae at large heliocentric distances, from 3.5 AU and closer, are available from ROSINA. The Rosetta mission presents a unique opportunity to directly sample the parent species in the thin cometary atmosphere of a Kuiper-belt object at distances in excess of 2.5 AU from the Sun and relate it to ground-based observations. Distances that far from the Sun are of particular interest as the chemical composition of the comet's coma changes from the highly volatile species to a water dominated coma. We will report on the first measurements of the volatile inventory obtained from ROSINA observations as Rosetta is following comet 67P/C-G at close distance.

### References:

H. Balsiger, K. Altwegg, P. Bochsler, P. Eberhardt, J. Fischer, S. Graf, A. Jäckel, E. Kopp, U. Langer, M. Mildner, J. Müller, T. Riesen, M. Rubin, S. Scherer, P. Wurz, S. Wüthrich, E. Arijs, S. Delanoye, J. De Keyser, E. Neefs, D. Nevejans, H. Rème, C. Aoustin, C. Mazelle, J.-L. Médale, J.A. Sauvaud, J.-J. Berthelier, J.-L. Bertaux, L. Duvet, J.-M. Illiano, S.A. Fuselier, A.G. Ghielmetti, T. Magoncelli, E.G. Shelley, A. Korth, K. Heerlein, H. Lauche, S. Livi, A. Loose, U. Mall, B. Wilken, F. Gliem, B. Fiethe, T.I. Gombosi, B. Block, G.R. Carignan, L.A. Fisk, J.H. Waite, D.T. Young, and H. Wollnik, *ROSINA - Rosetta Orbiter Spectrometer for Ion and Neutral Analysis*, Space Science Review 128 (2007), 745-801.

K.-H Glassmeier, H. Boehnhardt, D. Koschny, E. Kührt, and I. Richter, *The Rosetta Mission: Flying Towards the Origin of the Solar System*, Space Science Reviews 128 (2007), 1–21.

# RESULTS FROM THE LUNAR ATMOSPHERE AND DUST ENVIRONMENT EXPLORER (LADEE)

**Richard Elphic[1], Timothy Stubbs[2], G. Delory[3], P. Mahay[3], M. Benna[3], M. Horanyi[3], A. Colaprete[3], J. Halekas[3], T. Stubbs[3], D. Hurley3, M. Sarantos[3], S. Kempf[3], S. Noble[3]**
*[1]NASA Ames Research Center, Mo_ett Field, California, United States,*
*[2]NASA Goddard Space Flight Center, Greenbelt, Maryland, United States*
*[3]LADEE Science PI Team*
*Contact: richard.c.elphic@nasa.gov, timothy.j.stubbs@nasa.gov*

On 6 September, 2013, a near-perfect launch of the _rst Minotaur V rocket successfully carried NASA's Lunar Atmosphere and Dust Environment Explorer (LADEE) into a high-eccentricity geocentric orbit. After 30 days of phasing, LADEE arrived at the Moon on 6 October, 2013.

LADEE's science objectives are twofold: (1) Determine the composition of the lunar atmosphere, investigate processes controlling its distribution and variability, including sources, sinks, and surface interactions; (2) Characterize the lunar exospheric dust environment, measure its spatial and temporal variability, and e_ects on the lunar atmosphere, if any. After a successful commissioning phase, the three science instruments have made systematic observations of the lunar dust and exospheric environment. These include initial observations of argon, neon and helium exospheres, and their diurnal variations; the lunar micrometeoroid impact ejecta cloud and its variations; spatial and temporal variations of the sodium and potassium exospheres; and the search for sunlight extinction caused by dust. LADEE also made observations of the e_ects of the Chang'e 3 landing on 14 December 2013, and the Geminid meteor shower.

# LARGE-AMPLITUDE COHERENT STRUCTURES IN PLASMA NEAR MARS

**E. Dubinin[1],M. Fraenz[1], C. Mazelle[2], S. Barabash**
*[1]Max-Planck-Institute for Solar System Research, 37077 Göttingen, Germany;*
*[2]Institut de RechercheenAstrophusique et Planetologie, Toulouse, France;*
*[3]Swedish Institute of Space Physics, Kiruna, Sweden.*
*Contact: dubinin@mps.mpg.de*

Mars has no a global magnetic field which could protect its atmosphere and ionosphere from solar wind. Moreover due to the extended hydrogen exosphere the interaction starts already at large distances from the planet that results in appearance of wave phenomena typical for comets. Closer to the planet oxygen ions of the ionospheric origin begin to dominate and multi-ion effects become important. Mars is also a unique object since the Larmour radius of pickup heavy planetary ions ($O^+$ and $O^+_2$) is much larger than the characteristic size of the obstacle. Besides that the magnetosheath width occurs comparable to the Larmour radius of solar wind protons based on the bulk speed implying the important role of kinetic effects. All these features strongly affect the wave environment at Mars. Here we present the observations of large-amplitude coherent waves at Mars and discuss their role in ion energization and escape.

# ATMOSPHERIC LOSSES OF MARS INDUCED BY SOLAR WIND

**O. Vaisberg,**
*Space Research Institute, Russia, Profsoyuznaya 84/32.*
*Contact: olegv@iki.rssi.ru*

Experiments on first Martian satellites Mars-2, -3, and -5 showed existence of planetary magnetic and plasma tail formed by interplanetary magnetic flux tubes mass-loaded by planetary ions. This tail provided the channel through which significant flux of atmospheric constituents escaped the Mars. The measured flux of these ions suggested that the solar wind induced atmospheric losses are important for evolution of Martian atmosphere.

Subsequent measurements on Phobos-2 and Mars Express provided more detailed picture of planetary ions escape including additional escaping ions populations and revealing solar cycle variations of the escaping flux. The main known populations of solar wind induced planetary ions include three ones resulting from pick-up process and one representing hydrodynamic acceleration process. There are some discrepancies between several plasma experiments both in measured flux densities and in calculated total loss rates. However, solar cycle variations and significant escape flux increases caused by the solar wind disturbances are well established.

Computer MHD and hybrid simulations provide important global framework of solar wind interaction with Mars and identification of observed plasma populations. There are some discrepancies between experimental and modeling results in importance of different loss components and in total loss values, simulations usually provide smaller total loss figures. The talk summarizes both experimental and simulation results, similarities and differences within and between two methods, and discusses open issues for future research and expectations for new results provided by two spacecrafts heading towards Mars.

# SOLAR WIND INTERACTION WITH PHOBOS

**Stas Barabash, Yoshifumi Futaana, Mats Holmström,**
*Swedish Institute of Space Physics, Box 812, 98128, Kiruna, Sweden.*
*Contact: stas@irf.se*

Study of the solar wind – Phobos interaction is important both for establishing the origin of Phobos and for understanding the space plasma interaction with bodies of a size between the electron and proton gyro radii.

We review the topic starting from the first observations on the Soviet Phobos-2 mission followed by negative (no interaction signatures) results of Martian Global Surveyor (MGS), and focus on the most recent measurements by Mars Express (MEX). The MEX polar orbit crosses the equatorial plane at the Phobos orbit and MEX regularly flies by Phobos on distance down to below 60 km from the moon center. From nine flybys at a distance of less than 200 km the plasma sensor ASPERA-3 (Analyzer of Space Plasmas and Energetic Atoms) only once detected plasma disturbances, which might be associated with Phobos. On July 23, 2008 backscattered protons were observed from a distance of ~500 km from Phobos during high speed high density solar wind. The backscattered efficiency was estimated to be 0.5-10% (*Futaana et al., 2010)* similar to the lunar regolith. However, no similar disturbance were observed later even at the closest-ever flyby on December 29, 2013, 07:09 UT at a distance of 58 km from the center of Phobos. The later may be due to low solar wind speed and Phobos being likely inside the induced magnetosphere.

It is very unlikely that Phobos outgasses any significant amount of material or is magnetized strongly enough to affect the solar wind plasma. Currently it is assumed that Phobos interacts with the solar wind in the manner similar to the Moon. Phobos' regolith absorbs the majority of the impinging solar wind ions and backscatters a small fraction (< 1%) of protons. The backscattered protons interacting with the solar wind would result in the generation of the cyclotron waves, a phenomena still to be observed. No detection of oxygen ions on a distances of 100 km from Phobos sets the upper limit for the Phobos outgassing $<10^{20}s^{-1}$. It is very unlikely that Phobos contains any volatiles. However, sputtering of the regolith by the solar wind particles or/and ions in the Martian environment (*Cipriani et al., 2011*) may release surface's atoms creating a neutral gas envelop around the moon.

# NON-THERMAL DISSIPATION OF THE MARTIAN UPPER ATMOSPHERE

**V. I. Shematovich**
*Institute of Astronomy RAS,48 Pyatnitskaya str., Moscow 119017, Russian Federation.*
*Contact: shematov@inasan.ru*

**Introduction:**

Solar forcing on the upper atmosphere of Mars via both absorption of the XUV (soft X-rays and extreme ultraviolet) radiation results in the formation of an extended neutral corona populated by the suprathermal (hot) H, C, N, and O atoms (see, e.g., Johnson et al., 2008). The hot corona, in turn, is altered by an inflow of the solar wind plasma and local pick-up ions onto the planetary exosphere. Such inflow results in the formation of the superthermal atoms (energetic neutral atoms - ENAs) due to the charge exchange with the high-energy precipitating ions and can affect the long-term evolution of the atmosphere due to the atmospheric escape.

The origin, kinetics and transport of the suprathermal H, C, and O atoms in the transition regions (from thermosphere to exosphere) of the Martian upper atmosphere are discussed. Reactions of dissociative recombination of the ionospheric ions $CO_2^+$, $CO^+$, and $O_2^+$ with thermal electrons are the main photochemical sources of hot atoms. The dissociation of atmospheric molecules by the solar XUV radiation and accompanying photoelectron fluxes and the induced exothermic photochemistry are also the important sources of the suprathermal atoms. Such kinetic systems with the non-thermal processes are usually investigated with the different (test particles, DSMC, and hybrid) versions of the kinetic Monte Carlo method.

Kinetic energy distribution functions of suprathermal and superthermal (ENA) atoms in the Martian upper atmosphere were calculated using the stochastic model of the hot planetary corona (Shematovich, 2004, 2010; Groeller et al., 2014), and the Monte Carlo model (Shematovich et al., 2011, 2013) of the high-energy proton and hydrogen atom precipitation into the atmosphere respectively. These functions allowed us to estimate the space distribution of suprathermals, and to obtain the rates of the non-thermal escape from the Martian upper atmosphere. It was found that at present time the Martian neutral atmosphere is lost with total rates of $2.3–2.9\times10^{25}$ $s^{-1}$ of suprathermal oxygen atoms for low and high solar activity conditions with dissociative recombination of $CO_2^+$ and $CO_2^+$ being the main sources. The total loss rates of carbon are found to be 0.8 and $3.2\times10^{24}$ $s^{-1}$ for low and high solar activity respectively, with photodissociation of CO being the main source.

Results of calculations were also compared with the observations of the UV emissions by the UV spectrometer of SPICAM instrument and ENA spectra measurements made by ASPERA-3 instrument onboard of the ESA Mars Express spacecraft.

This work is supported by the RFBR project No. 14-02-00838a and by the Basic Research Program of the Presidium of the Russian Academy of Sciences (Program 22).

**References**

Johnson et al., Sp. Sci. Rev., 2008, v. 139, 355.
Shematovich, Solar System Res., 2004, v.38, 28.
Shematovich, Solar System Res., 2013, v.47, 437.
Shematovich et al., J. Geophys. Res., 2011, v.116, A11320; 2013, v. 118, 1231.
Groeller et al., Planet. Space Sci., 2014, v.98 , 93.

# OBSERVATIONS OF THE CO DAYGLOW AT 4.7 μM ON MARS: VARIATIONS OF TEMPERATURE AND CO MIXING RATIO AT 50 KM

**Vladimir A. Krasnopolsky**[1,2],
[1]*Catholic University of America, Washington, DC 20064, USA;*
[2] *PhysTech, Moscow, Russia.*
*Contact: vlad.krasn@verizon.net*

The CO (2-1) and (1-0) dayglow at 4.7 μm was observed on Mars at the peak of northern summer ($L_S$ = 110°) using the CSHELL spectrograph at NASA IRTF. There are six (2-1) and two (1-0) emission lines in the observed spectra (Fig. 1). They are contaminated by the solar CO lines and some martian and telluric lines. Fitting by synthetic spectra results in intensities of the dayglow lines and reflectivities of Mars at 4.7 μm. Mean reflectivity at 109°W from 50°S to 50°N is 0.15, similar to that observed by Mariner 6 and 7 in four regions on Mars.

The CO (1-0) dayglow is excited by absorption of sunlight at 4.7 μm; the emission is optically thick with a non-LTE line distribution and peaks near 87 km. The (1-0) line intensities are converted to the (1-0) band intensity using the line distribution from Billebaud et al. (1991). Mean intensity of the CO (1-0) dayglow is 1.7 MR with a weak limb darkening to 1.3 MR. This dayglow is poorly accessible for diagnostics of the martian atmosphere. The CO (2-1) dayglow is excited by absorption of the sunlight by the CO (2-0) band at 2.35 μm with minor contributions from photolysis of $CO_2$ and the CO (3-0) band at 1.58 μm. The dayglow is quenched by $CO_2$ and peaks at 50 km. Intensities of the observed six (2-1) lines result in rotational temperatures that should be equal to ambient temperatures at 50 km. These temperatures are retrieved from 50°S to 90°N (Figure 2) and vary in the range of 140-170 K with a mean value of 153 K. The observed intensities of the CO (2-1) dayglow are corrected for airmass and the surface reflection and give vertical intensities that are equal to 2.1 MR at 20°N to 50°N decreasing to 1.5 MR at 90°N and 1 MR at 45°S. The dayglow intensities depend on CO mixing ratio at 50 km and solar zenith angle. Retrieved CO mixing ratios at 50 km (Figure 3) gradually increase from 1100 ppm at 40°S to 1600 ppm at 70°N. This behavior is very different from that observed in the lowest scale height at the same season with increase to southern polar regions because of condensation of $CO_2$ near the south pole (Krasnopolsky, 2003).

The difference reflects complicated dynamic processes in the atmosphere. This is the first observation of CO in the middle atmo-

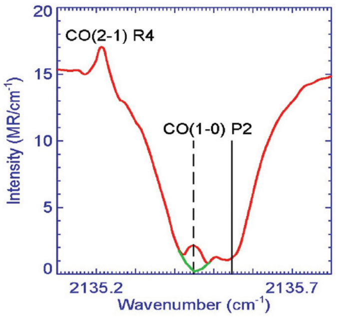


**Fig. 1.** Fine structure of the CO (1-0) P2 line: telluric and Doppler-shifted Martian absorption lines and Martian emission lines are seen.

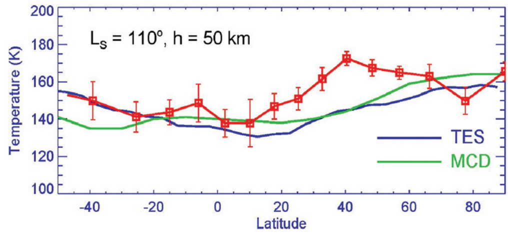


**Fig. 2.** Observed temperatures at 50 km are compared with TES limb data and those from Mars Climate Database.

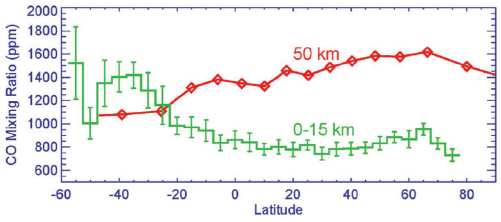


**Fig. 3.** Observed variations of the CO mixing ratio at 50 km are compared with those measured in the lowest scale height at the same season.

sphere of Mars, and the observed behavior of CO should be further studied in both observation and theory. The CO (2-1) dayglow is a tool for remote sensing of temperature and CO at 50 km on Mars using ground-based and spacecraft instruments. The observed CO and temperatures may be used to test photochemical GCMs for Mars.

# COMET C/2013 A1 (SIDING SPRING) FLYBY OF MARS: MARS EXPRESS SAFETY CONCERNS AND SCIENCE PLANS

**O. Witasse[1],M. Khan[2], M. Denis[2], A. Johnstone[2],T. Morley[2], M. Mueller[2], G. Drolshagen[1], A. Guilbert-Lepoutre[1], D. Koschny[1], H. Svedhem[1], P. Martin[3], A. Cardesin[3], P. Pardo Voss[3] andR. Lainé[4]**
*[1]ESA, ESTEC, PO Box 299, Noordwijk, the Netherlands;*
*[2]ESA, ESOC, Darmstadt, Germany;*
*[3]ESA, ESAC, Villanueva de la Cañada (Madrid), Spain;*
*[4]Sailcut;*
*Contact: Olivier.Witasse@esa.int*

Comet C/2013 A1 (**Siding Spring**) was discovered in early 2013, and its trajectory reconstruction indicates that it will flyby Mars at close distance on 19 October 2014 at about 18:33 UTC. The estimated closest approach is around 132,000 km, at a relative velocity of 56 km/s. This flyby is a unique opportunity, aswe have never seen a comet fly this close to a terrestrial planet.The Mars Express project has been preparing this encounter very carefully since mid-2013. There have been four main phases of preparation:

1) from mid-2013 to end 2013: the project was monitoring the evolution of the ephemerides of the comet, studied the geometry of the encounter, and evaluated the risks due to impacting dust particles. Available information on dust fluxes was assessed, ground-based observations with the VLT and other telescopes were analysed.At the end of this phase the decision was made to change the phasing of the spacecraft along its orbit at little fuel cost, such that it is hidden behind Mars for ~ 27 minutes around the time of the comet nucleus closest approach. The actual correction maneuver took place on 23 June 2014.
2) From January until end of June 2014: further assessments of the risks from potential particle impacts were conducted. A strategy regarding mission and science operations, including spacecraft and payload risk mitigation, was defined to reduce both the probability of a spacecraft impact and their criticality. . An update of the forecast of dust impacts indicated that the risk is much lower than anticipated. This allowed the start of the preparation of the science planning with the Principal Investigator teams.
3) July-August 2014: the science plan was prepared. Mars Express will be in the position to observe from close distance a comet originating from the Oort cloud, the reservoir of the most primitive comets. The planning includes imaging of the nucleus and characterisation of the coma. In addition, we will have the opportunity to study how the comet interacts with Mars' atmosphere, in other words, how the atmosphere responds to an impulsive phenomenon. Thirdly, there will be the possibility to study how the solar wind is disturbed by the comet.
4) September 2014 until the flyby: monitoring of the activity of the comet, in case safety measures have to be taken. If needed, the now envisagedscience plan can be replaced by a spacecraft protection plan, to be decided up to two weeks before execution.

This presentation will explain how the Mars Express project prepared this encounter, both from the engineering and science point of view. A truly interdisciplinary project!

# LATE NOACHIAN "COLD AND ICY HIGHLANDS" MODEL: GEOLOGICAL PREDICTIONS FOR EQUILIBRIUM ENVIRONMENTS AND NON-EQUILIBRIUM MELTING SCENARIOS

**J.W. Head[1], R. Wordsworth[2], F. Forget[3], J.-B. Madeleine[3], I. Halevy[4],**
*[1]Dept. of Earth, Environmental and Planetary Sciences, Brown University, Box 1846, Providence, Rhode Island, 02912, USA;*
*[2]Dept. of Geosciences, University of Chicago, Chicago, IL 60637, USA;*
*[3]Lab. De Météorolog Dynamique du CNRS, Université Paris 6, Paris, France;*
*[4]Weizmann Inst. Sci. Rehovot, Israel.*
*Contact: james_head@brown.edu*

**Introduction:**Forget et al. [1] and Wordsworth et al. [2,3] recently presented improved 3D global simulations of the early martian climate performed assuming a faint young Sun and denser $CO_2$atmosphere, including a self-consistent representation of the water cycle [2], with atmosphere–surface interactions, atmospheric transport, and the radiative effects of $CO_2$ and $H_2O$ gas and clouds taken into account. They found that for atmospheric pressures greater than a fraction of a bar, atmospheric-surface thermal coupling takes place and the adiabatic cooling effect (ACE) causes temperatures in the southern highlands to fall significantly below the global average. Long-term climate evolution simulations indicate that in these circumstances, water ice is transported to the highlands from low-lying regions for a wide range of orbital obliquities andthat an extended water ice cap forms on the southern pole (Fig. 1). Conditions are too cold to allow long-term surface liquid water. Punctuated events, such as meteorite impacts and volcanism, could potentially cause intense episodic melting under such conditions. Because ice migration to higher altitudes is a robust mechanism for recharging highland water sources after such events, Wordsworth et al. [2,3] suggested that this globally sub-zero, Late Noachian 'icy highlands' (LNIH)climate scenario may be sufficient to explain much of the fluvial geology without the need to invoke additional long-term warming mechanisms, or an early "warm and wet" Mars.Here we explore the predictions for geologic settings and processes in both equilibrium and non-equilibrium climate states [4-6] as first steps in the comprehensive testing of the "icy highlands" model.

**Geology of the "icy highlands" equilibrium environment:1)** ***Global permafrost***:With mean annual temperature (MAT) consistently well below 0°C [2], LNIH Mars is characterized by a global permafrost layer that forms a shallow perched aquifer [7,8] composed of a dry active layer whose thickness is defined by vapor diffusive equilibrium with the atmosphere. Permafrost thickness is determined by local and regional geothermal heat flux and mean surface temperatures, is thinner than today and varies with altitude and latitude, likely averaging several km thick [9,10]. **2)*****Surface hydrological cycle***: The LNIH climate is dominated by an expanded south polar cap, snow and ice accumulation in the highlands, and a global cryosphere; $H_2O$ at lower elevations will be mobilized and transported to the highland cold traps (Fig. 1). Altitude-dependent distribution of snow and ice is further modulated by both latitude dependence and atmospheric circulation patterns [2,3]. **3)*****Thickness and continuity of snow and ice***: To a first order, mean thickness will be determined by total water inventory and the percentage of the inventory available at and near the surface, neither value being well constrained for the Late Noachian [11]. We assume the current polar/near-surface water ice inventory (~5 M $km^3$; ~30 m Global Equivalent Layer (GEL)) and thus that available ice is *supply limited*[12]. Snow and ice will occur in several highlands environments: a) <u>Snow patches and continuous snow cover</u>: These will vary with seasonal and short term climate change, and locally with wind patterns and insolation shadowing as seen in Antarctica [13]. b) <u>Non-Flowing Ice Deposits</u>: Accumulations in excess of a few meters will occur as firn/ice deposits [14] but will not be thick enough to flow [15].c) <u>Flowing Glacial Ice Deposits</u>: Where ice thickness exceeds hundreds of meters and has an appropriate basal slope [15], it will flow, but still be cold-based unless it is thick enough (unlikely in the supply limited scenario) to raise the local melting geotherm into the base of the ice [16].**4)** ***LNIH global distribution of snow and ice***: Based on typical conditions simulated by the GCM [1,2] we assume a plausible Equilibrium Line Altitude (ELA) of +1 km;Fig. 2 portrays the LNIH. a) <u>*Poles*</u>: There is no north polar cap under nominal obliquity and the south polar cap is much larger [2,3], approximately the size of the Dorsa

Argentea Formation (DAF), interpreted to be an ice-sheet remnant [17]. On the basis of glacial flow modeling [18], the thickness of the DAF may have approached 3 km, and involve limited basal melting. b) _Hellas hemisphere_: Snow and ice are focused on the rim of Hellas, across the southern midlands, and in the Elysium rise; ice deposit margins are very closely coincident with the distribution of valley networks (VN), open-basin lakes (OBL) and closed-basin lakes [6]. c) _Tharsis hemisphere_: The LNIH Tharsis rise, a region thought to be characterized by an elevated geothermal gradient, is covered with snow and ice, a phenomenon that may help explain the charging of the Tharsis aquifer to source the outflow channels [19,20]. Classic VN (Warego Valles) are also near the margins of the ice accumulation [21].

**LNIH melting scenarios: 1) *Equilibrium top-down heating and melting*:** Under some climate equilibria, extreme orbital parameter-induced seasonal top-down melting might occur, producing daily or seasonal temperatures above 0°C [2]. This could produce transient melting conditions, as observed in the McMurdo Dry Valleys [7]. **2) *Punctuated top-down melting*:** a) _Impact_: Impacts [22] are predicted to produce arunaway greenhouseatmosphere, rain and short-term flooding. Local ejecta deposits and impact-generated widespread dust could change surface albedo and influence melting [23]. b)_Volcanism_: Gases ($SO_2$, $H_2S$, $CO_2$) released by punctuated volcanism [4,5]; such punctuated phases may be constantly recurring, but warming may only last for decades [5], and may be regional [24]. Local to regional dispersed volcanic ash [23,25] could alter melting patterns. c) _Direct ice melting_:Lava flows emplaced on or against ice deposits can induce melting and flooding [26]. **3) *Sustained top-down heating*:** Should top-down heating be maintained long enough ($10^1$-$10^2$ yrs), water in the upper permafrost would begin to melt at the top of the ice table. Longer sustained heating ($10^4$-$10^6$ yrs)could melt through the permafrost,first locally, then regionally. **4) *Bottom-up heating and melting***: Accumulation of ice to thicknesses exceeding hundreds of m [15] could raise the global mean melting geotherm to the base of ice but on a regional scale ice thickness may be supply-limited. In enhanced heat flow areas (e.g., Tharsis), basal melting may occur [19]. **5) *Combinations of factors*:** Any one (or more) of these can combine with orbital parameters already favoring melting. **6)*Timescales to penetrate cryosphere*:** Starting with a nominal LNIH climate scenario [2,3]and heat flux [18], we calculate that it would take of order $10^4$ to $10^6$ yrs for the nominal global cryosphere to be breached and for the hydrological cycle to change from horizontally stratified (with a perched aquifer) to influent and vertically integrated with the groundwater system. The difficulty in sustaining MAT above 0°C for sustained periods [2] makes this scenario unlikely globally; local regions of elevated heat flux (e.g., Tharsis, Elysium) will be exceptions [19]. **7) *The role of impacts in cryosphere penetration*:** Impacts of sufficient size (in excess of ~25 km) can penetrate the cryosphere and potentially form a short term connection to a groundwater reservoir [27]; effects depend on global groundwater budget and regional hydrostatic pressure.

**IV. Nominal Late Noachian Icy Highlands (LNIH) climate model and geological process predictions:** For most of the Late Noachian, an icy highlands caused by atmospheric-surface coupling and the adiabatic cooling effect appears to be the nominal equilibrium state (Fig. 1). Orbital parameter variations cause regional redistribution of ice, with limited melting only under extreme circumstances; any local meltwater rapidly freezes and returns to the highlands. Non-equilibrium conditions that could raise MAT above 0°C can be reached through punctuated events such as impact crater formation and high rates of volcanic outgassing, but the duration of the warming effects of individual events is very short geologically. This leads to some predictions for processes that can be used to test the LNIH model:**1) <u>Global cryosphere</u>:** For most top-down melting scenarios, the global cryosphere remains intact. **2) <u>Altitude dependence of melting</u>:** Melting should preferentially occur around the lower margins of ice deposits, where closest to melting point.**3) <u>Water reycling</u>:** During and following any melting events, water returns to the uplands, constantly recharging the source region.**4) <u>Relative constancy of source region locations</u>:** Because of the general constancy of LN topography, meltwater returns to the same place, providing automatic recharge of source areas.**5) <u>Character of ice source regions</u>:** Variations in topography, altitude, slope and insolation geometry will govern ice accumulation and melting particularly near ice margins. **6) Melting rates and recharge:** Raising MAT to >0°C will provide significant volumes of meltwater from top-down melting to form VN and create OBL. **7) Likelihood of multiple events:** Top-down melting scenarios favor multiple events; transition to equilibrium returns water to icy source regions. **8) LNIH hydrological cycle**

**model:** Long-term equilibrium icy highlands climate alternating with multiple episodic, but widely spaced short pulses of top-down melting; cycle favors immediate recharge of ice in same source regions. **9) Valley network formation:** Caused by multiple episodic melting events (number, duration and intensity currently unknown) of snow/ice in icy highlands; presence of shallow ice table during melting events influences infiltration and channel shape and enhances erosion rates [8]. Stream/network geometry controlled by cold-based ice patterns [8]. **10) Tharsis and Elysium:** Areas with elevated geotherms are favored for basal melting and aquifer recharge [19]. These predictions provide a basis for further analysis and testing of the LNIH model [2,8,14-16].


**References:**

1. F. Forget *et al*., *Icarus, 222,* 81 (2013); 2. R. Wordsworth *et al*., *Icarus, 222,* 1 (2013); 3. R. Wordsworth *et al*., *5th Mars Atmos.* (2014); 4. J. Head, L. Wilson, LPSC 42, #1214 (2011); 5. I. Halevy, J. Head, *3rd Conf. Early Mars*, #7043 (2012); *5th Mars Atmos.* (2014); 6. J. Head, *LPSC 44*, #1523 (2013); *5th Mars Atmospheres Workshop* (2014); 7. J. Head and D. Marchant, *Antarctic Science*, in review (2013); 8. J. Head et al., *LPSC 45* (2014); 9. S. Clifford, *JGR* 98, 10973 (1993); 10. M. Mellon et al., *JGR* 102, 19357 (1997); 11. M. Carr, J. Head, *LPSC 45* (2014); 12. J. Fastook, J. Head, *PSS*, in press (2013); 13. D. Marchant, J. Head, *Icarus* 192, 187 (2007); 14. J. Cassanelli, J. Head, *LPSC 45* (2014); 15. J. Fastook, J. Head, *LPSC 45* (2014); 16. M. Carr, J. Head, *GRL* 30, 2245 (2003); 17. J. Head, S. Pratt, *JGR* 106, 12275 (2001); 18. J. Fastook *et al*., *Icarus* 219, 25 (2012); 19. P. Russell, J. Head *PSS* 55*,* 315 (2007); 20. J. Cassanelli, J. Head, LPSC 45 (2014); 21. K. Scanlon *et al*., *GRL* 40, 4182 (2013); 22. T. Segura *et al., Icarus* 220, 144 (2012); 23. L. Wilson, J. Head, *JVGR*185*,* 290 (2009); 24. L. Kerber *et al., 5th Mars Atmos.* (2014); 25. L. Kerber *et al*., *Icarus* 219*,* 358 (2012); 26. J. Head, L. Wilson, Ann. Glaciol., 45, 1 (2007); 27. P. Russell, J. Head, *GRL*29, 1827 (2002).


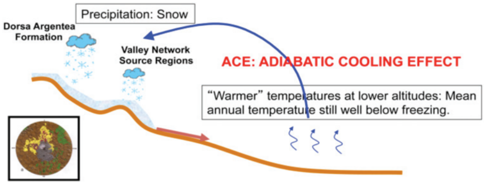


**Fig. 1.** Noachian icy highlands climate regime; snow at high elevations, a MAT well below 0°C, and a horizontally stratified hydrologic system.

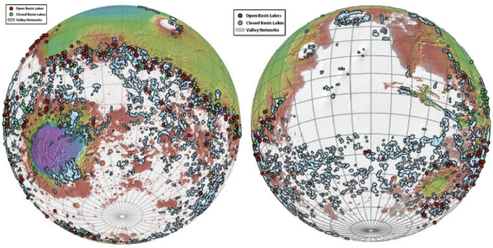


**Fig. 2.** Global view of the *Noachian icy highlands* (white areas above the surface ice stability line). Top) Hellas hemisphere: km-thick Dorsa Argentea Formation ice cap near bottom; 10-100s m thick ice cover (white) extends to the vicinity of the dichotomy boundary. Bottom) Tharsis hemisphere. Valley networks (blue), closed-basin lakes (green dots), and open-basin lakes (red dots) are well-correlated with margins of ice sheets.

# VOLCANO-ICE INTERACTIONS IN A LATE NOACHIAN "ICY HIGHLANDS" MARS: IMPLICATIONS FOR GROUNDWATER RECHARGE AND OUTFLOW CHANNEL WATER SOURCES ON THE THARSIS RISE

**J.P. Cassanelli[1],J.W. Head[1],**
*[1]Brown University Department of Earth, Environmental, and Planetary Sciences Providence, RI 02912, USA.*
*Contact: James_Cassanelli@Brown.edu*

**Introduction:**

The formation of the martian outflow channels during the Late Hesperian and Amazonian by catastrophic drainage of groundwater [1] is problematic for "cold and icy" early Mars climate scenarios. This is because undera "cold and icy" climate regime, a globally contiguous layer of impermeable, perennially frozen ground will extend into the subsurface of Mars [*e.g.* 2], preventing infiltration groundwater recharge.Recent global climate modeling effortspredict generally "cold and icy" conditions,where a Late Noachian (LN) water cycle, combined withslight increases in the atmospheric pressure, results in atmosphere-surface thermal coupling [3,4]. As a result, high-standing areas across Mars are adiabatically cooled, promoting transport of water ice to areas of high elevation where cold temperatures preserve deposited ice. This leads to the accumulation of regional ice sheets throughout the Tharsis region and the southern highlandsthat characterize the Late Noachian "icy highlands" (LNIH) Mars climate scenario [3,4].

We assume that the growth of the LNIH regional ice sheets is a supply-limited process (since there is no mechanism to return ice to the lowlands), constrained by a supply 5X the currently observed near-surface/polar water ice budget on Mars (current inventory ~30 m GEL) [5].Distribution of this water ice reservoir across Mars,above a predicted equilibrium line of +1 km [4], results in average ice sheet thicknesses of ~700 m and predominately cold-based glaciation [6]. Growth of the LNIH regional ice sheets across Tharsis Rise coincides with a period of increased volcanic activity [*7*], presumably resulting in elevated geothermal heat fluxes and widespread volcano-ice interactions.

A previous assessment has shown that regionally elevated geothermal heat fluxes throughout the Tharsis region (due to volcanic and magmatic activity during the LN) are not sufficient to cause widespread basal melting and groundwater recharge [8]. Extremely elevated geothermal heat flux values (which can be sustained near active volcanic features e.g. edifices and source vents) were shown to produce groundwater recharge through a "heat-pipe drain pipe" basal melting mechanism [8]. However, the recharge provided by this mechanism is not sufficient to explain outflow channel formation [8].Here,in the context of the LNIH model, we assess the implications of the supraglacial emplacement of constructional Tharsis lava flows atop the pre-existing LNIH ice sheets for meltwater generation and groundwater recharge.

**Short-term Thermal Interaction:**

Intuitively, the short-term thermal interaction between a supraglacial lava flow and the underlying ice is dominated by the transfer of heat from the cooling lava to the ice below and the atmosphere above. To determine the amount of heat that is transferred to the underlying ice we implement an analytical solution of the one-dimensional heat conduction equationfollowing[9].Under nominal LN climate conditions, lava flows that are emplaced across the top of the ice sheets will not encounter a surface comprised of solid ice, but rather snow and firn [10] resulting in more rapid melting during lava emplacement.Analysis of the heat transfer from lava flows of varying thickness indicates that thinner lava flows will contribute a much higher heat flux to the ice but over a much shorter period of time (Tab. 1).Despite the lower heat transfer rates the sustained duration of heat transfer from the thicker lava flows ultimately results in much more melting throughout the cooling period (Tab. 1).After the emplacement of the first flow, subsequent flows will contribute much less heat to the underlying ice sheet because of the intervening solidified lava.

With respect to meltwater generation and fate, the emplacement of supraglacial lava flows has several implications: (1)The water that is produced by melting of the surficial firn layer will begin to infiltrate down through the permeable firn layer of the ice sheet unless the meltwater production rate exceeds the infiltration capacity of the firn. If the infiltration capacity is able to accommodate the melt then infiltration will continue until melting stops or until the amount of meltwater produced exceeds the total storage capacity of the firn. (2)Supraglacial lava flows will be effective at eliminating the surficial firn layer of the ice sheet. Thus, as melting proceeds the firn layer will become diminished and the permeabilities and the storage capacity will decrease.Once the firn layer is removed, meltwater will then either escape to the lava flow margins, flow down into the ice through cracks, crevasses and moulins, or pool beneath the lava flow (potentially causing phreatomagmatic eruptions if enough steam is generated) (Fig. 1a). (3) Meltwater produced during the initial phase of lava emplacement and cooling is not likely to contribute significantly to groundwater recharge (since the ice sheets will be cold-based, the portion of meltwater that is able to penetrate down into the ice will refreeze at, or before, the ice sheet base).(4) Following the removal of the firn layer, continued melting of ice by supraglacial lava flows willresult in the channelization of meltwater along the ice sheet surface. These channels will drain to the glacial margins and may then erode fluvial channels into the martian surface.

**Long-term Thermal Interaction:**

The long-term thermal effects of supraglacial lava flow emplacement will be to construct a thermal blanket, insulating the ice sheet and increasing basal temperatures.As basal temperatures rise, the melting isotherm (which defines the extent of perennially frozen ground which comprises the cryosphere) will move up from depth, reducing the thickness of the cryosphere (which is ~1.2 km under the 700m LNIH ice sheets at the nominal surface temperature of 225 K [3,4], and background geothermal heat flux of 55 mW/m$^2$ [11]).Sufficient accumulation of lava flows will lift the melting isotherm to the ice sheet base, resulting in basal melting.The thickness of supraglacial lava flows required to raise the melting isotherm will be considerably reduced in the Tharsis region, where the regional geothermal heat flux is likely to have been elevated (~60-100 mW/m$^2$; 12) above the nominalLN heat flux due to widespread volcanic and magmatic activity [7] (Fig 1c).

Once the melting isotherm has been raised to the base of the LNIH ice sheets, the underlying cryosphere will have been removed. If the LN cryosphere was porous andsaturated in ice (possibly due to vapor diffusion from a deeper groundwater system [13], or from freezing of a prior aquifer system that existed under “warm and wet” conditions [14]), this would result in the melting and release of a significant amount of water to the groundwater system.Meltwater that is then produced from basal melting of theburied LNIH ice sheets(due to elevated melting isotherm) will either:(1) infiltrate down into the substrate (Figure 1c, 1d), or (2) become sequestered beneath the ice due to the presence of an impermeable underlying layer (*e.g.*competent bedrock).

Since the temperature gradient in the ice sheet beneath a thickness of accumulated lava flows will be effectively linear (because there will be no snow accumulation and little ice movement),the temperaturesat any depth and the thickness of supraglacial lava flows needed to cause melting can easily be estimated from the linear temperature gradient $dT / dz = G / \int_O^l K_T$ where: $z$ = Depth [m], $G$ = Geothermal heat flux [W/m$^2$], and $\int_O^l K_T$ = Integral of the thermal conductivity [W/ m K] from the top of the lava flows to any depth z.At a nominal LN mean annual surface temperature of 225 K and geothermal heat flux of 55 mW/m$^2$[11], the temperature at the base of the regional ice sheets will be on average ~240 K (using a conservative average thermal conductivity of 2.5 W/m k [10]).The underlying cryosphere will extend down ~1.2 km (assuming a column-averaged thermal conductivity of 2 W/m k [15]).

We find that, in order to bring the melting isotherm to the base of the 700 m LNIH ice sheets supraglacial lava flows, at an average thermal conductivity of ~0.8 W/m K [16], would have to accumulate to a depth of ~500 m above the ice. If the supraglacial lava flows accumulate to a thickness of ~700 mthe melting isotherm will reach the base of the lava flows, such that all 700 m of LNIH ice sheets and the underlying cryosphere will be thermally unstable and subject to melting.The melting rate of the ice (or of the cryosphere if ice saturated) will be dependent upon the amount of heat flow out of the ground minus the heat flow that goes towards melting[17]. Making the unreasonable assumption that the 700 m of lava were to be emplaced instantaneously,complete melting of an ice saturated LN cryosphere and the LNIH ice sheets would take ~0.5 Myr.Given the predicted average Tharsis eruption rates [18],vertical accumulation of lava flows will occur at ~2.5x10$^{-4}$ m/yr, accumulation of 700 m of lava flows would require nearly 3 Myr,melting of the LN cryosphere and LNIH ice sheets will be limited largely to the accumulation rate of Tharsis lava flows.

If the requisite 700 m of lava flows are able to accumulate over all of Tharsis region above the +1 km equilibrium line altitude (~2x10$^{7}$ km$^{2}$), then ~1.4x10$^{7}$ km$^{3}$ of meltwater will be generated by melting of the LNIH ice sheets, and ~4x10$^{6}$ km$^{3}$ of meltwater will be released from the cryosphere. The total recharge produced (~1.8x10$^{7}$ km$^{3}$)iscomparable to the volume of water required to carve the outflow channels (~3x10$^{6}$ to 2x10$^{10}$ km$^{3}$ [19]).Additionally,the hydrostatic head required for outflow channel formation will be provided due to the elevation of the Tharsis region recharge area [19].

**Conclusions:**

**(1)** Meltwater generated by the initial emplacement of supraglacial lava flows is limited, and is not likely to provide groundwater recharge. **(2)** Initial emplacement of supraglacial lava flows will effectively remove the surficial snow and firn layer and may lead to ice sheet surface channelization and meltwater runoff. **(3)** Ground water recharge from LNIH Tharsis volcano-ice interactions will come primarily from basal melting induced by the long-term raising of the melting isotherm as lava flows are built upon the ice sheets.**(4)** Meltwater generation will be limited by the vertical accumulation rate of the Tharsis lava flows. **(5)** The total volume of meltwater generated by accumulating ~700 m of lava flows across the Tharsis rise is comparable to the volume of water needed to form the outflow channels.

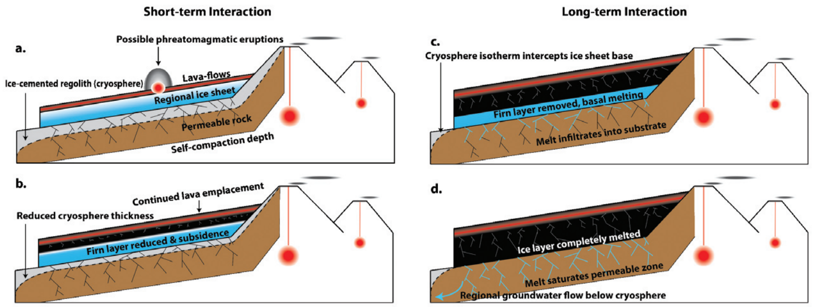


**Fig. 1.** Conceptual representation of the short-term (**a.&b.**) and long-term (**c.&d.**) volcano-ice interactions resulting from the emplacement of supraglacial lava flows.

| | | | | |
|---|---|---|---|---|
| 10 min | 17500 (60) | 4500 (15) | 2300 (7.5) | 1200 (4) |
| 1 hr | 14500 (45) | 4000 (13) | 2200 (7) | 1200 (4) |
| 24 hr | 7500 (25) | 2900 (9) | 1600 (5.25) | 1000 (3.25) |
| 7 day | 50 (0.25) | 2300 (7) | 1400 (4.5) | 800 (2.5) |
| 30 day | 0 | 1300 (4) | 1168 (3.75) | 700 (2.25) |
| 1 yr | 0 | 0 | 200 (0.5) | 400 (1.25) |
| Total Melt | ~3 m | ~15 m | ~30 m | ~60 m |

**Table 1.**Heat transfer rates (W/m$^{2}$) at the lava-ice interface for supraglacial lava flows from 1 to 20m thick with corresponding ice melting rates (μm/s), and the total amount of ice melted during the cooling period.

**References:**

[1] Head, J.W. et al. (2003) GRL, 30, 1577. [2] J. Head, D. Marchant (2014) Ant. Sci. [3] Forget et al. (2013) Icarus, 222, 81-99. [4] Wordsworth et al. (2013) Icarus, 222, 1-19. [5] M. Carr, J. Head (2014) LPSC 45, 1427.[6] J. Fastook, J. Head (2014) LPSC 45, 1115. [7] Phillips et al. (2001), Science, 291, 2587-2591. [8] J. Cas-sanelli et al. (2014) LPSC 45, 1501. [9] L. Wilson and J. Head (2007) Annals of Glaciology, 45, 83-86. [10] J. Cassanelli, J. Head (2014) in rev. [11] Solomon et al. (2005) Science, 307, 1214-1220. [12] Jellinek, A.M. et al. (2008) J.Geophys. Res. Planets, 113. [13] S. Clifford (1991) J.Geophys. Res. Lett. 18, 2055-2058. [14] R. Crad-dock, A. Howard (2002) J.Geophys. Res. Planets, 107, 5111. [15] Clifford, S.M. et al. (2010)J.Geophys. Res. Planet,s115. [16] E. Rob-ertson, D. Peck (1974) J.Geophys. Res., 79, 4875-4888. [17] P. Rus-sell, J. Head. (2007) PSS, 55, 315-332. [18] Wilson, L. et al. (2001)J. Geophys. Res., 106, 1423-1433. [19] K. Harrison, R. Grimm (2004) GRL. 31.

# MULTI-PHASE, PUNCTUATED GULLY EROSION ON MARS: SEASONAL INSOLATION EFFECTS ON THE MELTING AND REFREEZING OF SURFACE ICE IN THE McMURDO DRY VALLEYS

**J. L. Dickson[1], J. W. Head[1], J. S. Levy[2], G. A. Morgan[3],**
*[1]Brown Univ. Dept. Earth, Env. and Planet. Sci., Providence, RI 02906, [2]University of Texas Institute for Geophysics, Austin, TX 78758. [3]Center for Earth and Planetary Studies, Smithsonian Institution, Washington, D.C., 20013.*

## Introduction:

Gullies on Mars form in locations where $H_2O$ ice is most likely to accumulate: steep pole-facing slopes in the mid-latitudes (30°-45°) and all slope orientations at higher latitudes (45°-70°) [1-3]. Melting of ice at these locations is difficult to achieve under typical/average conditions on Mars in the last several million years [4-5]. A “wet” hypothesis, however, does explain the formation of gullies in the most Mars-like region on Earth, the McMurdo Dry Valleys (MDV) of Antarctica [6-12]. A detailed understanding of MDV gullies will provide testable hypotheses for their Martian counterparts.

Average conditions in the MDV do not favor the melting of surface ice, yet peak conditions allow small amounts of ice to melt during austral spring/summer [6–12]. Since November, 2006, we have instrumented a suite of gullies on the equator-facing wall of the South Fork of Upper Wright Valley (see [7]), at the limit of ephemeral fluvial activity within the MDV [12]. From these data, which include in-situ data loggers and time-lapse camera stations, we are able to describe the unusual conditions required to achieve net annual erosion of gully channels.

## Gully activity (typical season):

6 of the 7 seasons showed the following sequence of fluvial activity through spring and early summer (Fig. 1 a-b; 2):

1) *Late-November to Early-December*: Melting of seasonal in-channel snow and in-channel ice remaining from the previous summer.
2) *January*: Diurnal pulses of meltwater originating in the gully alcove extend toward the gully fan, advancing at an average rate of ~8 m/day (Fig. 1).
3) *February*: Flow ceases and yields an ice-reservoir trapped on channel floors (Fig. 3), which is buried by sediment during winter katabatic wind events.

For these seasons, summer erosion (< 15 cm) is balanced by winter eolian sedimentation, and no net erosion has been observed.

## Gully activity in 2010-2011:

Both gullies in South Fork experienced punctuated flood events in early- and mid-December, a month before the typical arrival of alcove-sourced meltwater (Fig. 1 c-d; 2). This activity included (1) intense diurnal pulses of meltwater with rapid channel switching, (2) erosion rates of ~1.6 cm/hr, including incision into an impermeable permafrost layer during flow events, totaling 81 cm of erosion over 7 days in a 5 m-wide channel, and (3) emplacement of ~10 cm of new fan material on the floor of the valley. Field observations from January, 2014 re-

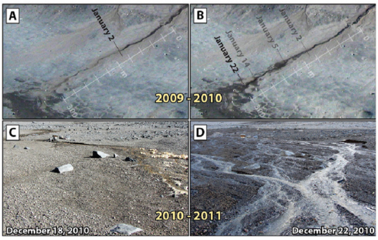


**Fig. 1.** (a/b) Average season: Diurnal pulses sourced by peak-season melting of alcove snowpacks. (c/d) Flood season: High-energy braided streams in early season.

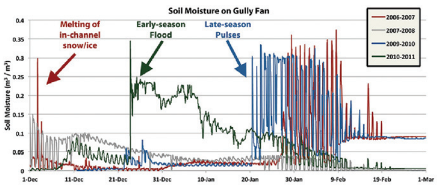


**Fig. 2.** Average season conditions do not see significant fluvial activity until late January, if at all. 2010-2011 saw early-season flooding with standing water/ice on the gully fan.

vealed that the channels carved by this event have persisted for > 3 years with only ~10 cm of eolian infilling.

Temperature records for December, 2010, when the flooding occurred, are comparable to previous seasons. Surface temperatures in November, 2010, however, show an exceptionally warm period along the valley wall, where temperatures reached 13°C. Of the 120 November days from 2007-2010, the 9 warmest were recorded in 2010, and 6 of those occurred early in the month. This warmth was not recorded at the gully fan, which was still under the mid-day shadow cast by the opposite valley wall.

**Thermal gradient inversion:** The cross-sectional profile of South Fork creates a geometry that yields warmer conditions along the wall than on the floor in spring and late summer (Fig. 4). This gradient is inverted when the valley floor is exposed to direct mid-day insolation over the northern valley wall (Fig. 4). Most often (as in 2009), this inversion occurs before melting conditions are achieved along the valley wall (Fig. 4a). In rare instances, this inversion happens after melting has occurred on the wall, as in November, 2010 (Fig. 4b).

In this latter scenario, conditions are such that intense early-season heating along the wall can produce meltwater that will freeze as it approaches the colder valley floor (Fig. 5). This creates a concentrated in-channel ice-reservoir in close proximity to gully fans. Once exposed to peak insolation in December, this reservoir melts again and produces net-erosion conditions in gully channels and net-accumulation conditions on gully fans (Fig. 5).

**Implications for Mars:** Insolation geometry is critical to gully formation on Mars, based upon orientation and latitude trends measured in both hemispheres [1–3]. From these observations in the MDV, the gully channel itself may be an important reservoir for surface/near-surface ice. This sequence of ice concentration and melting under peak conditions could explain how fluvial features can form on an otherwise hyper-arid and frozen Amazonian Mars.

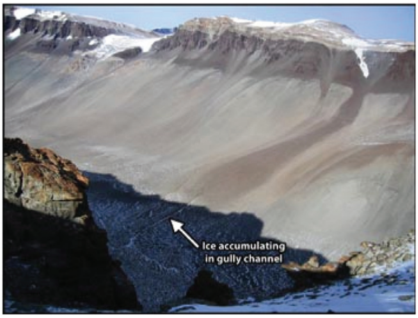


**Fig. 3.** Late-season insolation in South Fork. Image acquired March 2, 2010. Meltwater that forms along the valley wall freezes in-channel at lower elevations.

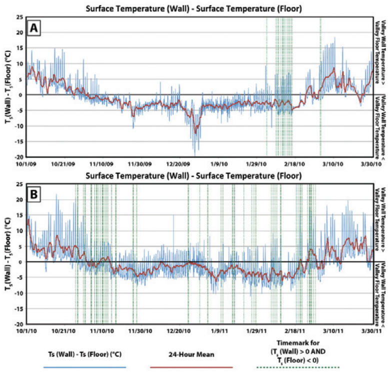


**Fig. 4.** Difference between valley wall surface temperature and valley floor surface temperature. Green lines indicate when the temperature on the wall was greater than 0° while the temperature on the floor was less than 0°C.

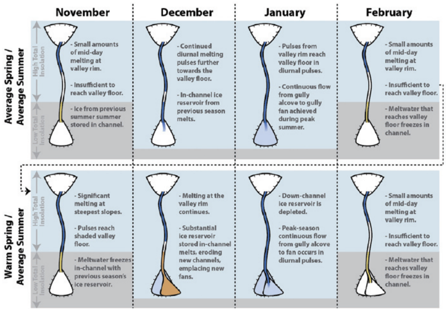


**Fig. 5.** Schematic for differential inso-lation-induced concentration of in-channel ice deposists. In a typical spring (i.e. 2009-2010), meltwater formed along the valley wall is insuffi-cient to reach the valley floor. In a warm spring (i.e. 2010-2011), this meltwater does reach the valley floor, which is still under low-insolation con-ditions due to the steep-wall geometery of South Fork. Thus, it freezes in-channel to create a hyper-concentrated ice reservoir. Once peak-insolation conditions occur on the valley floor in early-December, this reservoir is melted once again to generate exceptionally high-energy fluvial activity on the floor of the valley.

**References:**

[1] Malin and Edgett, 2000, *Science*, 288, 2330. [2] Heldmann and Mellon, 2004, *Icarus*, 168, 285. [3] Dickson and Head, 2009, *Icarus*, 204, 63. [4] Costard et al., 2002, *Science*, 295, 110.[5] Williams et al., 2009, *Icarus*, 200, 418.[6] Levy et al., 2007, *LPSC*, 28, 1728.[7] Morgan et al., 2007, *LPSC*, 38, 1656.[8] Morgan et al., 2009, *LPSC*, 41, 1043. [9] Morgan et al., 2010, *LPSC*, 41, 1043. [10] Dickson and Head, 2011, *LPSC*, 42, 1252. [11] Head et al., 2007, *ISAES*, 151. [12] Marchant and Head, 2007, *Icarus*, 192, 187.

# PARAGLACIAL GEOMORPHOLOGY ON MARS: THE DISTRIBUTION OF POST-GLACIAL FEATURES ACROSS THE MID-LATITUDES

**E. R. Jawin[1],J. W. Head[1],D. R. Marchant[2],**
*[1]Department of Earth, Environmental, and Planetary Science, Brown University, 324 Brook Street, Providence, RI 02908 USA; [2]Department of Earth & Environment, Boston University, Boston, MA 02215 USA. Contact:Erica_Jawin@brown.edu*

**Introduction:**In terrestrial environments affected by glaciation, a short period of modification has been identified immediately following a period of deglaciaion which represents the environmental response to ice loss. This *paraglacial period* is characterized by elevated sediment transport rates and relatively rapid modification, and the period ends once these rates return to non-glacial or equilibrium conditions (*1–3*). The paraglacial period should not be confused with *periglacial* processes and features, which occur in cold, nonglacial environments or at glacial margins.

The martian climate during the Amazonian is known to vary due to orbital forcing and obliquity variations (*4*, *5*). These variations are thought to have led to repeated ice migration from the poles to lower latitudes and back (*6*, *7*). In support of this theory, ice-related features have been documented in the mid- to low-latitudes in the form of concentric crater fill (CCF), lineated valley fill (LVF), lobate debris aprons (LDA), and tropical mountain glaciers (*8–10*). As much of Mars experienced periods of glaciation and deglaciation, it is expected that a martian paraglacial period also exists, representing the transition from a glacial to post-glacial climate.

To identify this martian paraglacial period, craters bearing CCF were analyzed across the mid-latitudes for evidence of ice loss and geomorphic features responding to this loss. A global survey was taken of craters based on the survey from (*11*) to identify the global distribution of paraglacial geomorphic features. Understanding the global distribution of these features, their associations, and variation in morphology will aid in determining the duration, location, and extent of the martian paraglacial period.

**The Paraglacial Period:**On Earth, a suite of "land systems" have been identified which comprise a range of features and processes typical of the paraglacial period: 1) rock slopes, 2) sediment-mantled slopes, 3) glacial forelands, and three additional land systems (alluvial, lacustrine, and coastal systems) which will not be addressed here due to their unlikely occurrence on Mars in the Amazonian(*2*). The combination of these separate landsystems describe the paraglacial period, as many features typical of the period can form in non-glacial environments; as such, the paraglacial period is viewed as a combination of features and processes representing the broad scale environmental response to deglaciation (Figure 1) (*1*, *2*, *12*, *13*).

The rock slope land system is characterized by stress redistribution throughout the environment, triggered by debuttressing due to glacial retreat; features typical of this land system include rock slope failure (RSF), rock slides, and uphill-facing scarps or *sackungen*(*2*, *14*, *15*). The sediment-mantled slope landsystem refers to the erosion and deformation of unconsolidated sediments exposed by glacial retreat. The downslope movement of these sediments often channelizes and forms gullies through sediment-gravity flow as well as water-assisted flow (*16*). Mass wasting off ice-cored lateral moraines is also typical of this landsystem, triggered through dry and wet activity (*17*). Finally, the glacial foreland land system is characterized by small-scale mass movement and freeze-thaw or thermal cycling. These processes create features including solifluction and gelifluction lobes and polygons (*2*). When these multiple land systems are viewed in a holistic sense, they describe various aspects of the environment which are all forming due to the initial instability caused by deglaciation, and a chronology of environmental response can be created (Figure 1).

**The Martian Paraglacial Period:** Evidence of glaciation in martian mid-latitude craters remains in the form of concentric crater fill. Remnant ice persists under a layer of till in the CCF, despite the current atmospheric pressure lying below the triple point of water. Evidence of deglaciation also exists in the form of spatulate depressions which are believed to form from the sublimation of near-pure glacial ice at the base of crater walls. A suite of stratigraphically younger geo-

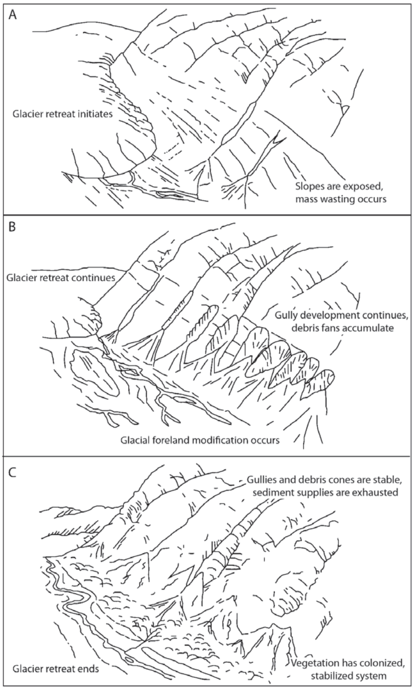


**Fig. 1.**.Broad chronology of the terrestrial paraglacial period. (A) Glacial retreat is followed by immediate sediment erosion and rock slope modification, triggering mass wasting and gully incision. (B) As glacial retreat continues, gullies continue to incise and glacial fore-lands are modified. (C) The paraglacial period ends when sediment transport rates return to non-glacial lev-els and gullies and debris cones are stable, often due to vegetation. This stage is not currently seen on Mars. Modified from (13).

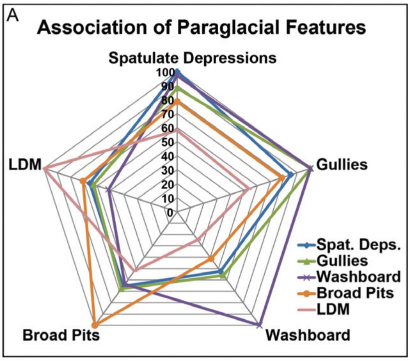


**Fig. 2.** Percentage association between paraglacial fea-tures in the mid-latitudes. For example, 41% of craters with broad pits also contain washboard terrain(orange line). Gullies occur in 100% of craters that contain wash-board terrain (purple line), while washboard terrain is only present in 25% of craters that contain latitude-dependent mantle (LDM) (pink line). Data collection is ongoing.

morphic units have been identified in association with these spatulate depressions which are postulated to represent paraglacial modification; these features include washboard terrain, gullies, crater wall polygons, and broad pits (*18*). The formation of these features appears to be consistent with an environmental response to ice loss. Gullies, for example, transport sediment from alcoves near the crater rim through channels, and are deposited in sediment fans. This sediment is transported through dry processes as well as with small quantities of liquid water, sourced from windblown snow trapped in the alcoves. Washboard terrain, characterized by parallel uphill-facing scarps, is located in association with gully sediment fans, and is believed to form through the extensional slumping and sliding of unconsolidated sediment on top of a subsurface ice layer. This movement may also be aided by small amounts of meltwater, sourced from the melting of the basal ice and/or infiltrated meltwater from the gully (*19*). Crater wall polygons and broad pits are expected to form in relation to the sublimation of near surface ice through a sediment layer.

**Global analysis of Paraglacial Features:**Identifying the variation in the distribution of these features is vital to better understanding key aspects of the martian paraglacial period. To that end, a global analysis is underway which documents the distribution of paraglacial features across the mid-latitudes. Included in this survey are the following features: spatulate depressions, gullies, washboard terrain, crater wall polygons, broad pits, rim crest pits, raked terrain, dunes, and latitude-dependent mantle (LDM) (see (*19*) for a discussion of each feature). The location of each feature is noted, so that global distributions, as well as associations between separate features, can be observed. While data collection is currently ongoing, certain trends are currently visible in the associations between features (Figure 2). For example, washboard terrain is only found in craters which also bear gullies. Additionally, washboard terrain is often not found in craters that contain evidence of LDM (~40% of LDM-bearing craters contain washboard terrain). Additionally, most craters which contain spatulate depressions also contain gullies. These associations suggest interdependences on formation mechanisms, such as between washboard terrain and gullies, while dissociations suggest factors which may inhibit formation, such as washboard terrain in LDM. The further documentation of paraglacial features across the mid-latitudes will help to describe these relationships more accurately.

**Conclusions:** The paraglacial period on Mars is similar to that occurring on Earth, in that it represents an environmental response to large-scale deglaciation and ice loss. The martian paraglacial period in the late Amazonian is characterized by a suite of geomorphic units occurring in glaciated mid-latitude craters including spatulate depressions, gullies, washboard terrain, crater wall polygons, and broad pits. These features appear to be widespread across the mid-latitudes and occur in varying associations. Certain features may be dependent on others to form (e.g. washboard terrain and gullies), while certain other environmental factors may inhibit the formation of certain paraglacial features (e.g. LDM and washboard terrain). The presence of a global analysis of paraglacial features on Mars will help to identify formation rates, ages, and locations of features, and will also help to constrain the timing and duration of the martian paraglacial period.

**References:**

**1. Church, Ryder,** *Geol. Soc. Am. Bull.***83, 3059–72 (1972).2. Ballantyne,** *Quat. Sci. Rev.***21, 1935–2017 (2002).3. Ballantyne,** *The Holocene***. 12, 371–76 (2002).4. Laskar** *et al.***,** *Icarus***. 170, 343–64 (2004).5. Madeleine** *et al.***,** *Icarus***. 203, 390–405 (2009).6. Forget,** *et al.,Science***. 311, 368–71 (2006).7.Head***et al.,Nature***. 426, 797–802 (2003).8. Squyres,** *J. Geophys. Res. Solid Earth***. 84, 8087–96 (1979).9. Baker***et al.,Icarus***. 207, 186–209 (2010).10. Head, Marchant,** *Geology***. 31, 641–44 (2003).11. Dickson***et al.,Icarus***. 219, 723–32 (2012).12. Eyles, Kocsis,** *Sediment. Geol.***65, 197–8 (1989).13. Ballantyne, Benn,** *Advances in Hillslope Processes***, vol. 2, pp. 1173–95 (1996).14. Gutiérrez-Santolalla***et al., Geomorphology***. 69, 298–314 (2005).15. Bovis,** *Geol. Soc. Am. Bull.***93, 804–12 (1982).16. Ballantyne, Benn,** *Arct. Alp. Res.***26, 255–69 (1994).17. Curry***et al.,J. Quat. Sci.***21, 211–25 (2006).18. Jawin***et al.,LPSC, 45th***(2014), Abs. 2218.19. Jawin***et al.,in prep.*

# DYNAMIC SHAPE AND DOWN-SLOPE DIRECTIONS ON PHOBOS

**J. Oberst, X. Shi, S. Elgner, K. Willner, all at**
*German Aerospace Center (DLR), Institute of Planetary Research, Berlin, Germany*
*Contact: Juergen.Oberst@dlr.de*

**Introduction:**

Phobos is moving deep in the gravity field of Mars. Being locked in its orbit, the small satellite is exposed to strong centrifugal and tidal forces, which vary over the surface and may be directed against its self-gravitational forces. Therefore, actual magnitudes and directions of forces acting on the surface of Phobos, in particular, down-slope directions are often not obvious and require careful studies of the shape and applicable force vectors, to derive what we briefly term, "Dynamic Shape" or "Dynamic Topography". Previous detailed studies of Phobos' surface were hindered by the limited resolution and coverage of spacecraft images as well as topographic data. Here we report on our investigations using a new Phobos shape model and high-resolution images obtained by the Mars Express spacecraft.

**Data and Methods:**

The large volume of images acquired by the High Resolution Stereo Camera (HRSC) and its Super Resolution Channel (SRC) onboard the Mars Express spacecraft during its regular flybys of Phobos reveals many details of the surface for the first time [Witasse et al., 2013; Wählisch et al., 2013]. Based on these images, a 100 m-resolution Digital Terrain Model (DTM) has been developed [Willner et al., 2013], which enables modeling of the dynamical environment at the surface on small scale. The dynamic shape of Phobos is modeled by using a polyhedron with vertices and faces derived from the DTM (Fig. 1, left). Surface self-gravitation is calculated under the assumption of uniform density [Shi et al., 2012]. In addition, we consider averaged tidal effects from a point-mass Mars and centrifugal effects from a uniform synchronous rotation. To demonstrate the tidal influence, we adopt the concept of "dynamic height", which indicates the relative highs and lows of the surface potential [Thomas, 1993].

**Results:**

Thus, we obtain a "Dynamic Shape" model, which may be visualized by appropriate techniques (Fig. 1, right).The model reveals distinct (dynamic) topographic highs as well as pronounced sinks that are not obvious in the geometric shape. On the basis ofdynamic slopes, we plan to study surface processes and regolith displacementonPhobos. Correlations found between dynamic shape and surface features might provide new constraints on the geophysical history of Phobos. Results can also help understand dynamics of granular material in a highly perturbed microgravityenvironment. Insights into regolith mobility on Phobos are also useful for future mission planning and landing site selection. We will show full details of our model and present appropriate discussions at the conference.

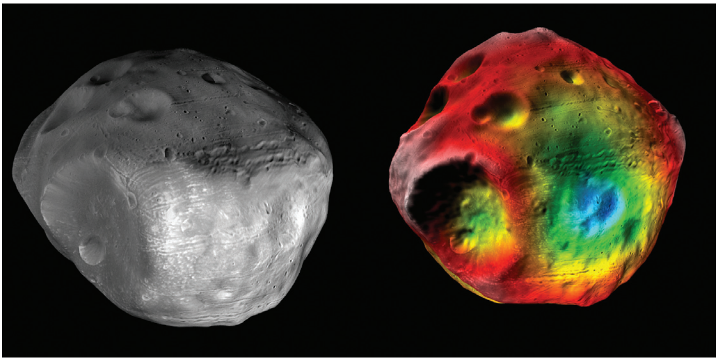

Fig.1: Left: HRSC image mosaic draped over the Phobos geometric shape model (Leading and Mars facing hemisphere). Right: Dynamic shape visualized for this same hemisphere. Red and blue colors indicate high and low levels of dynamic heights. Regolith will tend to be displaced from red to blue areas.

**References:**

Shi, X., Willner, K., Oberst, J., Ping, J., and Ye, S., 2012. Working models for the gravitational field of Phobos. Science China, Physics, Mechanics & Astronomy 55 (2), 358–364.Thomas, P. C., 1993. Gravity, Tides, and Topography on Small Satellites and Asteroids: Application to Surface Features of the Martian Satellites. Icarus 105, 326-344. Willner, K., Shi, X., Oberst, J., 2013. Phobos Shape and Topography Models.http://dx.doi.org/10.1016/j.pss.2013.12.006.Witasse O. et al., 2013. Mars Express investigations of Phobos and Deimos. http://dx.doi.org/10.1016/j.pss.2013.08.002i.Wählisch, M., Stooke, P. J., Karachevtseva, I. P., Kirk, R., Oberst, J., Willner, K., Nadejdina, I. A., Zubarev, A. E., Konopikhin, A. A., and Shingareva, K. B., 2013.Phobos and Deimos Cartography. http://dx.doi.org/10.1016/j.pss.2013.05.012.

**Acknowledgements:**

X. Shi was supported by a grant from the German Academic Exchange Service(DAAD).
J. Oberst greatly acknowledges being hosted by MIIGAiK and supported by Russian Science Foundation, project #14-22-00197

# DIAGNOSTIC PROPERTIES OF BODY WAVES FOR SOUNDING THE INTERIORS OF MARS

**S. Raevskiy, T. Gudkova, V.N.Zharkov**
*Schmidt Institute of Physics of the Earth, B.Gruzinskaya 10, Moscow 123995, Russia*
*Contact: rs1989@rambler.ru*

**Introduction:** At the moment Martian interior structure models are constrained by the satellite observational data (the mass, the moment of inertia factor, the Love number k2) [1] and high pressure experimental data [2]. Seismological observations could provide unparalleled capability for studying Martian interiors. Two future missions include seismic experiments on Mars - project “InSight” of NASA [3] and project “MISS” (Mars Interior Structure by Seismology) [4] in the frame of ExoMars of RSA and ESA. The main instrument for “InSight” is a very broadband seismometer.

**Software product:** To estimate travel times for direct P, S, core reflected PcP, ScS and core refracted PKP body waves as a function of epicentral distance and hypocentral depth, as well as their amplitudes at the surface for a given marsquake, software product was developed in Matab, as it encompasses many plotting routines that plot resulting travel times and ray paths. The computational results have been compared with the program TTBox [5]. The code computes seismic ray paths and travel times for one-dimentional spherical interior model (density and seismic velocities are functions of a radius only). The theory is given in [6].

**Travel-times**: Calculations of travel times tables for direct P, S, core reflected PcP, ScS and core refracted PKP waves and their amplitudes are carried out for a trial seismic model of Mars M14_3 from [7] ( the core radius is 1800 km, the thickness of the crust is 50 km) and model A from [8]. The parameters of the models are shown in Fig. 1. The travel times of P, S, PcP, Scs and PKP waves, computed for a focus at 200 km depth for the seismic models M7_4 from [7] and A from [8] are plotted as a function of epicentral distance in Fig.2. Direct and core reflected P and S waves are recorded to a maximum epicentral distance equal to about 100°, and PKP arrivals can be detected for epicental distances larger than 150°. The shadow zone in the model M14_3 is wider in comparison with the model A, as the liquid core radius of the seismic model under consideration is larger. The problem if it is possible to reveal differences between the models with and without water content in mantle minerals is considered.

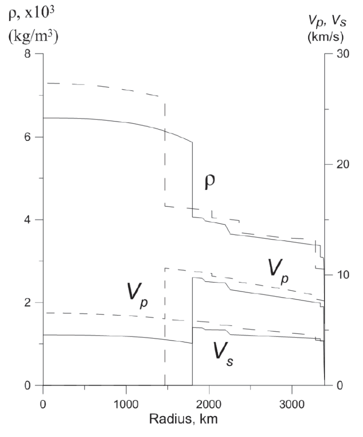


**Fig. 1.** Density and sesmic velocity profiles along the radius for the interior structure model M14_3 from [7] (solid line) and model A from [8] (dashed line).

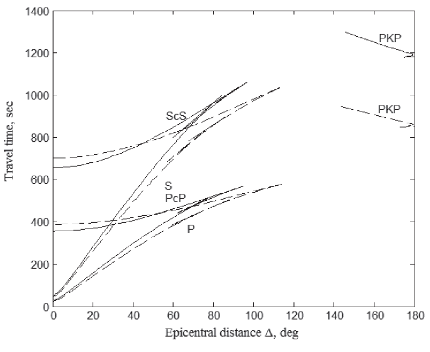


**Fig. 2.** Travel-times of direct (P and S), core reflected (PcP and ScS) and core refracted (PKP) body waves arrivals as a function of epicentral distance for a source at 200 km depth, using models M14_3 from [7] (solid lines) and A from [8] (dashed lines).

In the frequency domain, the amplitude of ground acceleration recorded in the far-field at a frequency $\omega$, either on the vertical (P wave) or horizontal (SH-wave) component, can be written as [9]

$$\left|a_j(r,r_\eta,\omega)\right| \approx \frac{\omega^2}{4\pi\sqrt{\rho c_j}} \frac{M_j(\omega)}{\sqrt{\rho_\eta c_{\eta j}^5}} \frac{F_j(r,r_0)}{R_j(r,r_0)} A_j(r,r_\eta,\omega),$$

$$M_j(\omega) = \frac{M(0)}{\left[1+(\omega/\omega_0)\right]^2},$$

where ρ is the density, c is either the P- or S-wave velocity. The subscript *j* refers to the wave type under consideration (P or S), and subscript η indicates that the value is evaluated at the source.

The factors M, R and A are the frequency dependent scalar seismic moment, the geometric spreading and the correction due to attenuation, respectively.

The corner frequencies $\omega_0$ are empirically defined following the scaling laws in [10]. Based on the estimates of Martian seismicity [11] seismic moment *M* (0) was assumed to be $10^{13}$ – $10^{15}$ Nm. Geometrical spreading is

$$R_j = \frac{1}{r_0}\left|\frac{\rho_\eta V_{j\eta}}{\rho_0 V_{j0}} \frac{\sin i_\eta}{\sin\Delta\cos i_0} \frac{di_\eta}{d\Delta}\right|^{\frac{1}{2}}$$

where *i* - is takeoff angle, Δ – epicentral distance. η indicates that the value is evaluated at the source, subscript 0 - the value is evaluated at receiver point. Calculated amplitude spectral densities for the model M14_3 from [7] plotted in the Fig. 3. Figure 4 represents maximum peak-to-peak amplitudes in two frequency ranges (0.1 – 1 Hz) and (0.5 – 2.5 Hz) for the model M14_3 from [7].

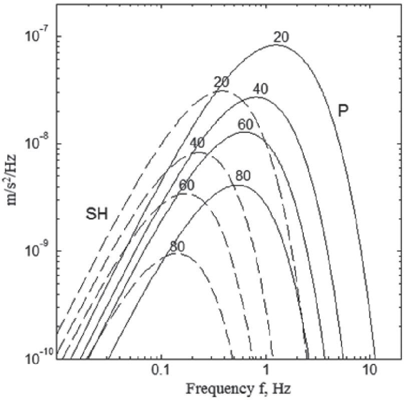


**Fig. 3.** Amplitude spectral densities of the P (solid lines) and SH (dashed lines) wave packets, recorded on the vertical and horizontal component, respectively, using the model M14_3 from [7], for $Q_s$ = 250 as a function of frequency for different epicentral distances (in degrees). Seismic source is at the depth of 200km, seismic moment $M_0$ is $10^{14}$ N m.

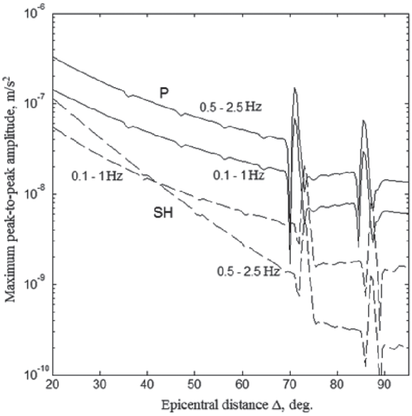


**Fig. 4.** Maximum peak-to-peak amplitudes in two frequency ranges (0.1 – 1 Hz) and (0.5 – 2.5 Hz) for the model M14_3 from [7] $Q_s$ = 250, plotted as function of epicentral distance. Seismic source is at the depth of 200km, seismic moment $M_0$ is $10^{14}$ N m. Solid lines, P-waves; dashed lines, S-waves.

**Acknowledgements:**

This work was supported by Grant No. 12-02-00378 from the Russian Fund for Fundamental Research.

**References:**

[1] Konopliv, A.S. et al. (2011) Icarus, 211, 401-428. [2] Bertka, C. and Fei, Y. (1997) J. Geophys. Res. 102, 5251-5264. [3] Lognonné, P., et al. (2012) Abstract, 3MS3-1-7. [4] Gudkova, T.V. et al., (2013) Sol. Syst. Res, 47, 1. [5] Knapmeyer, M. (2004) Seismological Research Letters. 75, 6,. 726-733. [6] Bullen, K.E. and Bolt, B.A. (1985) An introduction to the theory of seismology, Cambridge Univ. Press. [7] Zharkov, V.N. et al. (2009) Phys.Earth Planet.Int, 172, 324-334. [8]F. Sohl, T. Spohn (1997), J. Geophys. Res., E102., 1613–1635. [9] Aki,K., Richards, P. G. (1980) Quantitative seismology. [10] Sato, T., Hirasawa, T. (1973) J. Phys. Earth. 21, 415-431. [11] M. Knapmeyer et al. (2006) J. Geophys. Res. 111.

# SURFACE CLUTTER IN GROUND PENETRATING RADAR SOUNDING: REAL MARSIS ECHOES COMPUTER SIMULATIONS

**Ya.A. Ilyushin[1,2], R. Orosei[3], O. Witasse[4], B. Sanchez - Cano[5],**
*[1]Moscow State University, Physical Faculty Leninskie gory, ulitza Lebedeva 119992 GSP-2 Moscow Russia*
*Contact: ilyushin@physics.msu.ru,*
*[2]Kotel'nikov Institute of Radio Engineering and Electronics, Russian Academy of Sciences Mokhovaya st., 11-7, Moscow, 125009, Russia*
*[3] Istituto di Radioastronomia, Istituto Nazionale di Astrofisica, Via Piero Gobetti 101, 40129, Bologna, Italy*
*Contact: roberto.orosei@inaf.it*
*[4]European Space Agency Keplerlaan 2200 AG Noordwijk The Netherlands*
*Contact: owitasse@cosmos.esa.int ;*
*[5]Radio and Space Plasma Physics Group, Department of Physics and Astronomy, University of Leicester, University Road, Leicester LE1 7RH, United Kingdom*

**Abstract:** Synthetic aperture radar echoes coming from planetary surface are evaluated numerically for realistic surface topography. Simulation results are validated against true MARSIS radargrams. Applications to ionopheric studies are discussed.

**Introduction:** Space-borne radar sounding is now effectively applied for surface and subsurface probing of planetary bodies.

In subsurface sounding with ground penetrating radar (GPR), only nadir echoes from the diurnal surface and buried interfaces are useful. Side echoes coming from rough surface of the planet mask these nadir signals. The first experiment on deep radar probing of Moon, carried from the manned space mission Apollo, showed the ultimate need in the a priori information about the surface (high-resolution images, topography data etc.). This information should be incorporated in the data processing scheme in real experiments. Being started from manual sorting of echoes and visual identification of signatures produces by elements of the surface terrain, now this approach uses computer simulation of the radar wave echoes based on realistic topographic data. These data are now available for Earth, some planets and their satellites.

**Numerical algorithms.** In the real GPR experiment, aperture synthesis and some other processing techniques are typically applied for partial suppression of the off-nadir echoes. All these procedures should be adequately represented in the numerical simulation. For this reason, the simulation algorithm may be quite complicated and resource consuming. This is probably why only a few such radar echo simulators are known, and those few algorithms still exploit great simplifications, which reduce their physical adequacy and limit the numerical accuracy.

In the algorithm created by Nouvel et al. [1] the arbitrary rough surface is approximated by a mosaic of tilted square facets. The individual reflections from these facets are evaluated within the Kirchoff approximation and then coherently summed. It is well known that square tile mosaic (rather than triangular) cannot make continuous 3D surface. These artificial discontinuities unavoidably produce unphysical echoes, which are the artifact of this particular model. In addition, no aperture synthesis simulation technique applied in that model is reported in [1], although it might be implemented there. Both continuous approximation of the surface shape and aperture synthesis have been applied in [2], but for the very specific case of the so-called Martian polar valleys (surface features typical for the North Polar Cap of Mars). Here we present the echo simulation algorithm for arbitrary shape of the surface, also based on Kirchoff approximation, but using continuous surface shape approximation on the triangular grid and performing the aperture synthesis correctly. The idea is now to compare, for the same orbit, the new simulation results with results of the facet algorithm [1].

**Ionospheric studies with GPR.** Frequency dispersion of the ionospheric plasma corrupts phase relations among the spectral components of the signal and therefore destroys matched filtering, normally applied for the radar signal processing. At the same time, ionospheric distortions of the signal carry useful information about height distribution of the ionospheric plasma density. Dispersion curve of the ionospheric plasma, retrieved by adaptive scheme of distortion compensation, can then be used for assessment of basic ionospheric parameters (TEC, critical frequency etc.) For correct separation of the regular ionopheric phase shift from other systematic and stochastic distortions, everything in the radar experiment should be simulated as thoroughly as possible. Therefore, surface clutter modeling is a necessary part of GPR experiment, both for ionospheric and subsurface research. Within the Kirchoff approximation, ionospheric and surface clutter are independent multiplicative contributions to the signal, so that for both of them necessary numerical techniques can be individually developed, tested and optimized. The progress in surface clutter numerical models recently made gives us hope to improve ionospheric correction of real GPR signals, and to improve ionospheric parameter retrievals from these GPR data.

**Conclusion and remarks.** Adequate computer simulation of Martian GPR experiment with the application to the real MARSIS radar sounder data is the principal goal of the work presented here. Synthetic radargrams, obtained with numerical algorithms developed by the authors, are shown. Simulation procedure includes preliminary processing of the MOLA topography data available for every part of the Martian surface, simulation of the rough surface reflection within Kirchoff approximation and unfocused aperture synthesis, exactly as it is applied in real MARSIS signal processing. Comparative analysis with real radargrams obtained from MARSIS instrument during the MEX 9466 orbit is also presented.

**Acknowledgements.** This study has been partially supported by the European Space Agency (ESA) and Russian Fundamental Research Fund with the grant 13-02-12065 ofi-m “Fundamental problems of the microwave remote sensing of the Earth from space”. One of the authors thanks the administration of the Scientific Research Computing Center of the Moscow State University for granting the access to the computational resources of the parallel computing system SKIF-GRID “Tchshebyshev”.

**References.**

1. Nouvel, J.-F., A. Herique, W. Kofman, and A. Safaeinili (2004), Radar signal simulation: Surface modeling with the Facet Method, Radio Sci., 39, RS1013, doi:10.1029/2003RS002903.
2. Ilyushin Ya.A. Martian northern polar cap: Layering and possible implications for radar sounding Planetary and Space Science 52 (2004) 1195–1207.

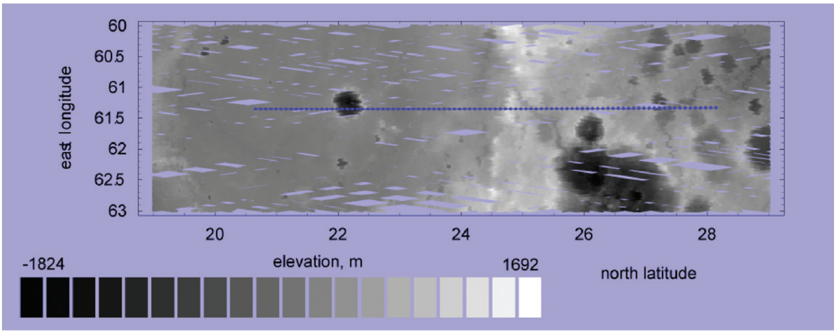


**Fig. 1.** MARSIS ground track (MEX orbit 9466, the southmost part) and surrounding MOLA topography.

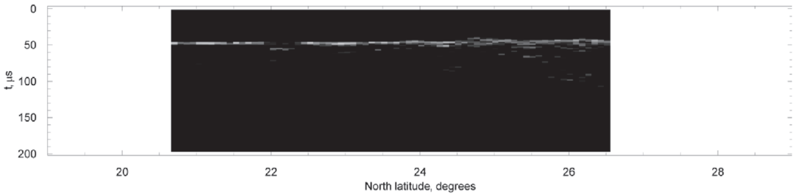


**Fig. 2.** Simulated MARSIS radargram (MARSIS Band IV 5 MHZ, Doppler filter 0)

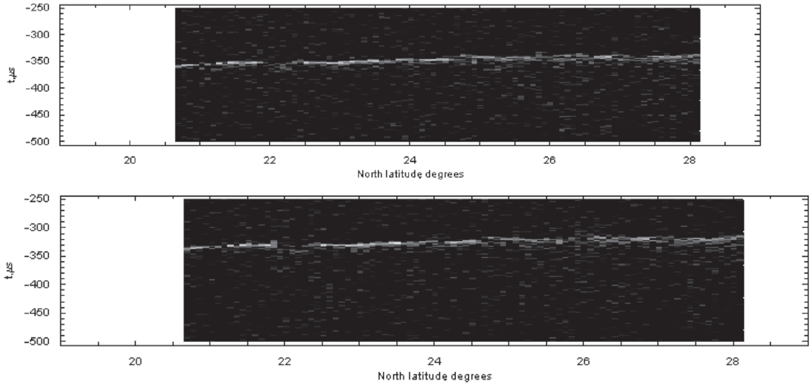


**Fig. 3.** True MARSIS radargrams (both MARSIS band IV, 5 MHz)

# THE INTERNAL WAVES AND SATURATION DEGREE IN THE EARTH'S ATMOSPHERE FROM RADIOSONDE WIND AND TEMPERATURE MEASUREMENTS AND APPLICATIONS TO RO WAVES IN PLANETARY ATMOSPHERES

**V.N. Gubenko, I.A. Kirillovich, A.G. Pavelyev,**
*Kotelnikov Institute of Radio Engineering and Electronics RAS, Vvedenskogo sq. 1, 141190 Fryazino, Moscow region, Russia.*
*Contact: vngubenko@gmail.com*

**Introduction:**

Internal gravity waves (IGWs) affect the structure and circulation of the Earth's atmosphere by transporting energy and momentum upward from lower atmosphere. Observations of the temperature and wind velocity fluctuations in the middle atmosphere have shown that wave amplitudes grow with increasing altitude, however, no quickly enough in order to correspond to amplitude growth due to exponential decrease of density in the absence of energy dissipation. The theory of saturated IGWs explains such rate of the wave amplitude growth in the following way: any wave amplitude in excess of the threshold value will lead to instability and the production of turbulence that acts to prevent further growth of the wave amplitude. The mechanisms that contribute most to the dissipation and saturation of the dominant IGW motions in the atmosphere are thought to be the dynamical (shear) and convective instability. For high-frequency waves, the threshold amplitude required to achieve shear instability is virtually identical to that required for convective instability. But for low-frequency IGWs, the shear instability threshold falls well below that necessary for convective instability. The knowledge of actual and threshold wave amplitudes is important when the effect of IGWs on the background atmosphere is to be assessed. The internal wave saturation assumption plays the key role for radio occultation (RO) investigations of IGWs in planetary atmospheres [Gubenko et al., 2008, 2011, 2012], therefore a radiosonde study of wave saturation processes in the Earth's atmosphere is actual task. The results of determination of the actual and threshold amplitudes, saturation degree and other characteristics for identified IGWs in the Earth's atmosphere found from high-resolution radiosonde measurements SPARC (http://www.sparc.sunysb.edu/) of horizontal wind and temperature are presented. The usefulness of these observations in conjunction with RO studies of IGWs in the planetary (Earth, Mars, Venus) atmospheres is discussed. The work was carried out under partial support of the RFBR grant 13-02-00526-a and Program 22 of the RAS Presidium.

**References**

Gubenko V.N., Pavelyev A.G., Andreev V.E. Determination of the intrinsic frequency and other wave parameters from a single vertical temperature or density profile measurement // J. Geophys. Res. 2008. V. 113. No.D08109, doi:10.1029/2007JD008920.
Gubenko V.N., Pavelyev A.G., Salimzyanov R.R., Pavelyev A.A. Reconstruction of internal gravity wave parameters from radio occultation retrievals of vertical temperature profiles in the Earth's atmosphere // Atmos. Meas. Tech. 2011. V. 4. No.10. P. 2153–2162, doi:10.5194/amt-4-2153–2011.
Gubenko V.N., Pavelyev A.G., Salimzyanov R.R., Andreev V.E. A method for determination of internal gravity wave parameters from a vertical temperature or density profile measurement in the Earth's atmosphere // Cosmic Res. 2012. V. 50. No.1. P. 21–31, doi: 10.1134/S0010952512010029.

# FORMATION OF EMBRYOS OF THE EARTH-MOON SYSTEM AS A RESULT OF A COLLISION OF TWO RAREFIED CONDENSATIONS

**S. I. Ipatov[1,2],**
[1]*Vernadsky Institute of Geochemistry and Analytical Chemistry of Russian Academy of Sciences, Kosygina 19, 119991, Moscow, Russia;*
[2]*Space Research Institute of Russian Academy of Sciences, Profsoyuznaya st. 84/32, Moscow, Russia.*
*Contact: siipatov@hotmail.com*

**Main Points of the Abstract:**The angular momentum of the present Earth-Moon system could be acquired at the collision of two identical rarefied condensations with sizes of Hill spheres which total mass was about 0.1 of the mass of the Earth. Solid embryos of the Earth and the Moon could be originated as a result of contraction of the condensation formed at the collision. Depending on eccentricities of planetesimals that collided with solid embryos of the Earth and the Moon, the Moon could acquire 0.04-0.3 of its mass at the stage of accumulation of solid bodies while the mass of the growing Earth increased by a factor of ten.

Introduction: Many authors (e.g., [1-3]) suppose that the Earth-Moon system formed as a result of collision of the solid Earth with a Mars-sized object.Galimov and Krivtsov [4] presented arguments that the giant impact concept has several weaknesses. It is considered that one of the weaknesses of the impact theory is that the Moon would consist almost exclusively of material from the impactor, but the rocks from the Moon and the Earth are similar. Ipatov[5]simulated the evolution of a disk of planetesimals initially divided into groups according to their distances from the Sun. He showed that the composition of large enough embryos in the terrestrial feeding zone could be similar due to mixing of planetesimalsduring planet formation.So in principle, it could be possible that composition of some impactors collided with the embryo of the Earth could not differ much from that of the embryo.Lyra et al. [8] showed that in the vortices launched by the Rossby wave instability in the borders of the dead zone, the solids quickly achieve critical densities and undergo gravitational collapse into protoplanetary embryos in the mass range $0.1M_E$-$0.6M_E$ (where $M_E$ is the mass of the Earth).

Ipatov [6] and Nesvorny et al. [9] supposed that transneptuniansatellite systems were formed from rarefied condensations. According to [6], the angular momenta acquired at collisions of condensations moved in circular heliocentric orbits could have the same values as the angular momenta of discovered transneptunian and asteroid binaries. Ipatov [7] obtained that the angular momenta used in [9] as initial data in calculations of the contraction of condensations leading to formation of transneptunian binaries could be acquired at collisions of two condensationsmoved in circular heliocentric orbits. Ipatov supposed that the number of collisions of condensations at which the formed condensation with mass equal to that of a solid body with diameter $d$>100 km got the angular momentum needed for formation of a satellite system can be about the number of small bodies with$d$>100 km having satellites, i.e., the fraction of condensations formed at collisions leading to formation of satellite systems among all condensations can be about 0.3 for solid primaries with $d$>100 km formed in the transneptunian belt. The model of collisions of condensations explains negative angular momenta of some observed binaries (e.g., 2000 CF105, 2001 QW322, 2000 QL251), as about 20 percent of collisions of condensations moving in circular heliocentric orbits lead to retrograde rotation.

The Angular Momentum at a Collision of Two Condensations:Using the formulas presented in [6], we obtained that the angular momentum $K_{EM}$ of the Earth-Moon system equals to the angular momentum $K_{s2}$at a typical collision of two identical condensations with size of Hill spheres, which total mass equals$0.13M_E$. For circular heliocentric orbits, the maximum value of $K_{s2}$is greater by a factor of $0.6^{-1}$than the above typical value [6]. In this case, the above total mass is $0.096M_E$. Therefore, the angular momentum of the Earth-Moon system could be acquired at a collision of two condensations with a total mass not smaller than $0.1M_E$. We suppose that solid proto-Earth and proto-Moon couldformby contraction of a condensation (e.g., according to the models of contraction of a condensation presented in [4,9]). Not all material of collided preplanetesimals could be left in the condensation formed at the collision. So the total mass of collided preplanetesimals could exceed $0.1M_E$.

Angular Velocities of CondensationsNeeded for Formation of Satellite Systems: In calculations of contraction of condensations (of mass *m* and radius *r* equal to 0.6 of the Hillradius$r_H$) presented in [9], trans-Neptunian objects with satellites were formed at initial angular velocities $\omega_o$ from the range $0.5\Omega_o$–$0.75\Omega_0$, where $\Omega_0=(Gm/r^3)^{1/2}$ (*G* is the gravitational constant). In3-D calculations of gravitational collapse of a condensation presented in [4], binaries were formed at $\omega_o/\Omega_0$ from the range of 1-1.46. Forsmaller$\omega_o/\Omega_0$, satelliteswerenotformed, and a considerable fraction of angular momentum could be in particles that left the formed condensation. Thedifferenceinresultspresentedin [4] and [9] canbecaused, inparticular, bydifferentchaoticvelocitiesofparticles/bodiesconstitutingcondensationsand by different sizes of condensations. The sizes of condensations in calculations presented in [4] were smaller than Hill spheres. Forexample, inoneoftheircalculations (page 108 in [4]) the radius of the condensation exceeded the radius of the corresponding solid planet by a factor of 5.5, whilethe Earth radius is smaller by a factor more than 200 than the Hill radius.

At a collision of two identical condensations, the angular velocity can be as high as $\omega=1.575\Omega$, with a mean value of about $\omega\approx0.945\Omega$, where $\Omega=(G\cdot M_S)^{1/2}a^{-3/2}$ is the angular velocity of a condensation around the Sun[6].As $\Omega_o/\Omega\approx1.73(r_H/r)^{3/2}$, then $\Omega_o\approx1.73\Omega$ at $r=r_H$. In this case $\omega$ can be as high as $0.9\Omega_o$, but it is smaller for smaller *r*.

Collided condensations could have non-zero angularmomentabefore the collision. So in principle the resulting angular velocity of the formed condensation can exceed $0.9\Omega_o$.According to Safronov [10], the initial angular velocity $\omega_o$ of a rarefied condensation is $0.2\Omega$ for a sperical condensation and $0.25\Omega$ for a flat circle. The initial angular velocity is positive and is not enough for formation of satellites.If two identical uniform spherical condensations with $\omega_o$collided without additional angular momentum, then the angular velocity of the spherical condensation formed at the collision is $\omega_2=2^{-2/3}\omega_o$; e.g., $\omega_2=0.126\Omega$ at $\omega_o=0.2\Omega$. The ratio of $\omega/\omega_2=0.945/0.126=7.5$ shows that in the case of a collision of equal mass condensations the increment to the angular velocity due to a typical collision is greater by a factor of several than the angular velocity which is due to initial rotation of condensations.The angular velocity of a condensation of radius $r_c$ formed as a result of compression ofthe condensation, with the Hill radius $r_H$ and the angular velocity $\omega_H$, equals $\omega_{rc}=\omega_H(r_H/r_c)^2$[6].Thereforeanyinitialangularvelocitiesconsidered in [4,9] can be reached after contraction of the condensation formed at a collision of condensations not greater than Hill spheres.

**The Growth of Solid Embryos of the Earth and the Moon:**GalimovandKrivtsov [4]studied the growth of the rotating planet-satellite system in the accumulation of the matter of the dust cloud. Inparticular, theyobtainedthatthepresentmassesofthe Earth-Moonsystemcanbegotattheinitialtotalmassofthesystemequalto 0.047 ofthepresentvalue and at the initial ratio of the embryos equal to 4.07 (for the growth of masses of the Earth and the Moon by a factor of 26.2 and 1.31, respectively). These studies were made for the model when velocities of incoming dust were zero at the edges of a cylinder around the Earth-Moon system. In the case of eccentrical heliocentric orbits of particles, this model is not true. In simulations presented in [5],mean eccentricities of planetesimalsin the terrestrial zone exceeded 0.2 (and later 0.3) at some stages of evolution.

Let us consider the model of the growth of solid embryos of the Earth and the Moon to the present masses of the Earth and the Moon ($M_E$and $0.0123M_E$, respectively) by accumulation of smaller planetesimals for the case when the effective radii of proto-Earth and proto-Moon are proportional to *r* (where *r* is the radius of a considered embryo). Such proportionality can be considered for large enough eccentricities of planetesimals. In this case, based on $dm_M/m_M=k\cdot(m_M/m_E)^{2/3}dm_E/m_E$ we can obtain $r_{Mo}=m_{Mo}/M_E=[(0.0123^{-2/3}-k+k\cdot(m_{Eo}//M_E)^{-2/3})]^{-3/2}$, where$k=k_d^{-2/3}$, $k_d$is the ratio of the density of the growing Moon of mass $m_M$to that of the growing Earth of mass$m_E$($k_d$=0.6 for the present Earth and Moon), $m_{Mo}$ and $m_{Eo}$are initial valuesof$m_M$ and $m_E$.For $r_{Eo}=m_{Eo}/M_E=0.1$, we have $r_{Mo}=0.0094$ at $k$=1 and $r_{Mo}=0.0086$ at$k=0.6^{-2/3}$. At these values of $r_{Mo}$, the ratio $f_m=(0.0123-r_{Mo})/0.0123$of the total mass of planetesimals that were accreted by the Moon at the stage of the solid body accumulation to the present mass of the Moon is 0.24 and 0.30, respectively. In this case for the growth of the mass of the Earth embryo by a factor of ten, the mass of the Moon embryo increased by a factor of 1.31 and 1.43, respectively.

If we consider that effective radii of the embryos are proportional to $r^2$ (the case of small relative velocities of planetesimals), then integrating $dm_M/m_M=k_2\cdot(m_M/m_E)^{4/3}dm_E/m_E$, we can get $r_{Mo2}=m_{Mo}/M_E=[(0.0123^{-4/3}-k_2+k_2\cdot(m_{Eo}/M_E)^{-4/3})]^{-3/4}$, where $k_2=k_d^{-1/3}$. In the case of $r_{Eo}=m_{Eo}/M_E=0.1$, we have $r_{Mo}=0.01178$ at $k_2=1$ and $r_{Mo}=0.01170$ at $k_2=0.6^{-1/3}$, and $f_m$ equals 0.042 and 0.049, respectively. In this case for the growth of the Earth embryo mass by 10 times, the Moon embryo mass increased by the factor of 1.044 and 1.051 at $k_2=1$ and $k_2=0.6^{-1/3}$, respectively. In the above model, depending on eccentricities of planetesimals, the Moon could acquire 0.04-0.3 (the lower estimate is for almost circular heliocentric orbits) of its mass at the stage of accumulation of solid bodies during the time when the mass of the growing Earth increased by a factor of ten. Probably the initial mass of a solid proto-Earth could exceed $0.1M_E$, and so the growth of the Moon embryo could be smaller than the estimate obtained for the growth of the mass of the Earth embryo by a factor of ten.

We suppose that the condensations that contracted and formed the embryos of other (not the Earth) terrestrial planets did not collide with massive condensations, and therefore the condensations formed at collisions did not get large enough angular momentum needed to form massive satellites.

This study was supported by Program no. 22 of the Presidium of the Russian Academy of Sciences. References:

[1] Canup R.M., Barr A.C., Crawford D.A.: Icarus, Vol. 222, pp. 200-219, 2013.
[2]Clery D.: Science, Vol. 342, pp. 183-185, 2013.
[3] Cuk M., Stewart S.T.: Science, Vol. 338, pp. 1047-1052, 2012.
[4] Galimov E.M., Krivtsov A.M.: Origin of the Moon. New concept. / De Gruyter. Berlin. 168 p., 2012.
[5] Ipatov S.I.: Solar System Research (translated from Astron.Vestnik), v. 21, N 3, pp. 129-135, 1987.
[6] Ipatov S.I.: Mon. Not. R. Astron. Soc., Vol. 403, pp. 405-414, 2010.
[7] Ipatov S.I.: In Proc. IAU Symp. No. 293 “Formation, detection, and characterization of extrasolar habitable planets”, Cambridge University Press, pp. 285-288, 2014.
[8] Lyra W., et al.: Astron. Astrophys., Vol. 491, pp. L41-L44. 2008.
[9] Nesvorny D., Youdin A.N., Richardson D.C.: Astron. J., Vol. 140, pp. 785-793, 2010.
[10] Safronov V.S.: Evolution of the protoplanetary cloud and formationof the Earth and the planets,Moscow. Nauka.1969. English translation: NASATTF-677, 1972.

# ANALYSIS OF THE IRON CONTENT AND MORPHOLOGY OF CE-3 LANDING SITE

**Yangxiaoyi Lu,**
*Beijing Planetarium, No. 138 Xizhimenwai Main Street, Beijing 100044, China; Contact: luyangxiaoyi@gmail.com*

**Introduction:**

The landing site of CE-3 is 340.49 °E, 44.12 °N, located in the northern part of Mare Imbrium and about 140 km east to Sinus Iridum. In particular, more accurately able to determine the content of iron (Fe) in the frozen lava of volcanic melts. Their concentration was different for different parts of the surface morphology.After processing the spacecraft «Lunar Prospector», received a general map of the distribution of iron (Fig 1). The content of iron on the left side map is much larger than on right parts of the map.

**Discussion:**

the «Mare» - the result of immense outpourings of lava from the bowels of the Moon, caused by small asteroids' impacts on the surface.The content of iron in the regolith can be cosmogonic indicator of the evolution of the Moon, as shown above. On the surface of the landing site of CE-3, the rocks with a predominance of iron are concentrated in the lunar maria(Fig 2). Age of rocks is inversely proportional to the iron content.Surface morphology of the area is relatively flat. Two basalt units high-iron and less-iron are mapped. The part which have high iron contents is younger the other part (Y.Lu, 2009).

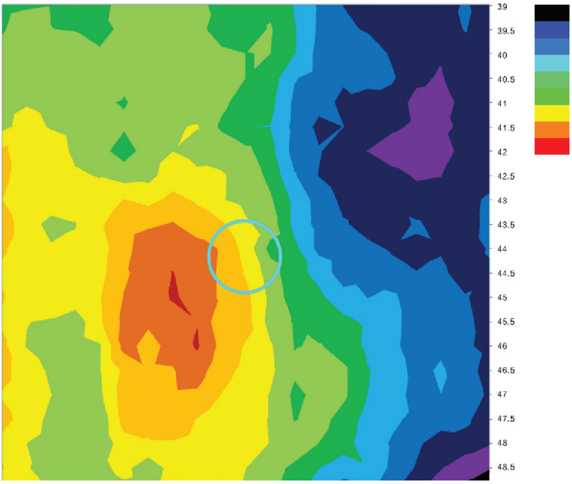


**Fig. 1.** FeO content map of mare basalts at Chang'E-3 landing site. (by LP data. Y. Lu 2014.)

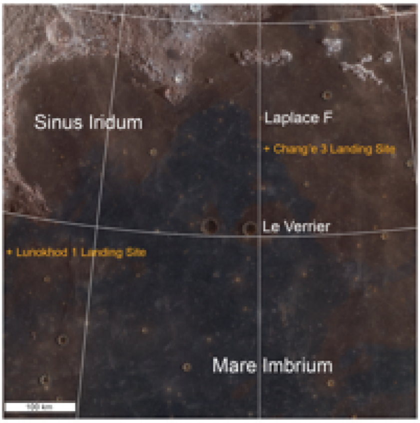


**Fig. 2.** LROC Color image (by LROC WAC)

# LUNAR REGIONAL PYROCLASTIC DEPOSITS: SOURCES OF VOLATILES AND THE ROLE OF NEAR-SURFACE VOLATILE ENHANCEMENT

**J.W. Head, III[1], L. Wilson[2],**
*[1]Department of Earth, Environmental and Planetary Sciences, Brown University, Box 1846, Providence, Rhode Island, 02912, USA;*
*[2]Lancaster Environment Centre, Lancaster University, Lancaster LA1 4YQ, UK.*
*Contact: james_head@brown.edu;*

## Introduction:

Lunar pyroclastic deposits can be subdivided into several modes of occurrence [1], suggesting different modes of emplacement. Some smaller pyroclastic deposits are interpreted to have erupted during strombolian/hawaiian activity [2], while others are linked to vulcanian activity related to dike and sill emplacement below crater floors [3,4]. The largest pyroclastic deposits (Orientale dark ring, Aristarchus Plateau, Sinus Aestuum, Rima Bode, Mare Vaporum, Sulpicius Gallus, and Taurus Littrow) cover regions >1000 km$^2$ [1], and their mode of emplacement has been less clear than that of the smaller, more isolated deposits. In the case of the Aristarchus Plateau, very high effusion rate eruptions leading to sinuous rilles [5] and associated pyroclastic emplacement have been implicated. The location of specific vents, and thus eruption styles, has been less clear for the remainder of the large deposits, partly due to burial and obscuration by post-pyroclastic deposit effusive volcanism [6]. Important evidence related to candidate modes of emplacement come from analysis of the Orientale dark ring, a 154 km diameter pyroclastic deposit that was shown to emanate from a linear depression interpreted to be the remains of an elongated vent at the top of a dike [7]. In this interpretation, a wide dike stalled just below the surface, and the low-pressure environment led to gas buildup along the top of the dike, ultimately leading to the eruption of an Io-like pyroclastic plume to produce the dark pyroclastic ring. The central elongate depression thus represents evidence of this shallow dike emplacement-related activity. Additional evidence for the association of pyroclastics with dike-emplacement activity comes from analysis of the ascent and eruption of magma [8], where it was shown that the low-pressure environment associated with the dike tip propagation could enhance formation of volatiles *during* dike ascent so that the dike could arrive at the surface with the top of the dike already saturated with magmatic foam, and not requiring secondary buildup as in the vulcanian [3] or the Orientale dark halo [7] cases. Could this mechanism, arrival of volatile magmatic foam-laden dikes to the shallow subsurface [8], perhaps combined with further shallow crustal gas formation [8] subsequent to stalling, lead to the penetration of foams to the surface and eruption of magmatic foams to produce regional pyroclastic deposits?

Distribution and Characteristics of Linear Features: The association of linear rilles (interpreted to be the surface manifestation of stress fields associated with shallow dike emplacement [9]) with some of these deposits (e.g., Rima Bode, Sinus Aestuum [10]) motivated us to use these data to assess whether eruptions of magmatic foam-laden dikes [8] from such candidate vents could help to explain the nature and distribution of regional pyroclastic deposits. Here we analyze the dispersal and emplacement of regional pyroclastics from shallowly intruded dikes and magmatic foams in general.

Dispersal of pyroclasts: The observed spatial relationships between linear rilles and dark mantle deposits suggest that pyroclast ranges are commonly up to 100 km. The maximum range, $R$, that can be reached by a clast ejected at speed $v$ when the acceleration due to gravity is $g$ is $R=v^2/g$ (1) which implies that $v$ is up to $[(100\times10^3\times1.622)^{1/2} =]$ 403ms$^{-1}$. The corresponding time of flight is ~350 s, a value consistent with the cooling rates and cooling times estimated by Saal et al. [11] for lunar volcanic glass beads: 2-3 K s$^{-1}$ over intervals of 2-5 minutes, i.e. 120-300 s. If we assume a larger range (200 km) then $v$ = 570ms$^{-1}$ and the time of flight is 497 s.

Volatile issues: A reasonable way of linking the released magmatic volatile mass fraction, $n$, to the final gas speed at the end of complete gas expansion, $v$, is to assume that the gas expands adiabatically and that the pyroclasts acquire all of the gas speed. In that case $v = \{[2\, nQT\mathrm{g}] / [m\, (\mathrm{g} - 1)]\}^{1/2}$ (2) where $\Theta$ is the universal gas constant, 8314 J K$^{-1}$ kmol$^{-1}$, $T$ is the magmatic temperature,

$\gamma$ is the ratio of the specific heats of the gas at constant pressure and constant temperature, and $m$ is the molecular mass of the gas. In practice some heat is transferred from pyroclasts to gas early in the expansion, maintaining the gas temperature near-magmatic for a while and thus increasing the gas speed and hence the pyroclast range. However, pyroclasts must eventually decouple from the gas when the gas expansion becomes so large that the system enters the Knudsen regime, and this reduces the potential range. Using eq. (2) as a compromise between the over- and under-estimates, and rearranging: $n = [v^2 m (\gamma - 1) / [2\ QT\gamma]$ (3). Measurements of the volatile chemistry of erupted lunar basalts allow the amounts of volatiles released during explosive eruptions to be estimated. An oxidation-reduction reaction between graphite and various metal oxides at pressures less than ~40 MPa commonly produced up to 2000 ppm CO [12,13]. Saal et al. [11] estimated estimated that in addition up to700 ppm $H_2O$, 325 ppm S, 15 ppm F and 0.5 ppm Cl could be released by exsolution. The amount of energy per unit mass available from the expansion of volatiles is inversely proportional to their molecular mass. As CO, with molecular mass $m$ = 28 kg kmol$^{-1}$, is the dominant volatile, it is appropriate to scale the amounts of other volatiles to CO, so that their equivalent amounts become [(28/18) × 700 =] 1089 ppm $H_2O$, [(28/64) × (325/2) =] 71 ppm $S_2$, [(28/19) × (15/2) =] 11 ppm $F_2$ and [(28/35.45) × 0.5/2) =] 0.2 ppm $Cl_2$. The total is ~3170 ppm of equivalent $m$ = 28 kg kmol$^{-1}$. At magmatic temperatures, say $T$ = 1600 K, the value of $\gamma$ for CO is very close to 1.3; the value for $H_2O$ is ~1.25 and since the other species are present in small amounts it suffices to use a weighted average of $\gamma$ = 1.28. Equation (2) then implies that the maximum speed at which pyroclasts are likely to be ejected on the Moon in purely magmatic explosive activity is $\{[2 \times 3170 \times 10^{-6} \times 8314 \times 1600 \times 1.28] / /[28 \times 0.28]\}^{1/2}$ = 117 m s$^{-1}$, corresponding to a range of 8.5 km.

This range is very much less than the observed value of ~100 km, implying greater ejection speeds and hence greater gas mass fractions in the eruption products. Equation (3) shows that if $v$ is the 403 m s$^{-1}$ needed to reach 100 km, $n$ must be at least $\{[403^2 \times 28 \times 0.28] /[2 \times 8314 \times 1600 \times 1.28] =\}$ 0.037, i.e., 3.7 mass % or 37000 ppm. Thus the amount of released gas needed to eject pyroclasts to a range of 100 km is ~10 times greater than the total available from a typical lunar magma, ~ 3000 ppm. If the range is 200 km, so that $v$ = 566 m s$^{-1}$, then the value of $n$ that is needed is ~74000 ppm, ~25 times more than is available.

Volatile concentration: The low pressure always present in the propagating tip of a dike means that as dikes approach the surface their upper tips will consist of a cavity containing gas underlain by a region where gas bubbles concentrate into a foam [8]. If the dike fails to break through to the surface, gas bubbles migrate up through the foam to increase the size of, and pressure in, the gas cavity. Additional foam is generated beneath the gas cavity if the dike is wide enough to allow convection to occur because this brings magma from depth to shallow enough levels for additional pressure-dependent gas release. Head et al. [7] showed that these processes acting in a ~500 m wide dike produced an ~25-fold gas concentration leading to an explosive eruption emplacing a ~150 km diameter circular pyroclastic deposit in Mare Orientale. Wilson et al. [14] found that a 4-fold gas concentration led to the ~30 km radius pyroclastic deposits around Hyginus crater as gas migrated to the active vent system from the outer margins of the dike whose injection induced the associated Rima Hyginusgraben; additional local gas venting caused multiple collapse craters along the graben.

A generic example of this process based on Head et al. [7] and Wilson et al. [14] would involve a 100 km long linear rillegraben induced by a 300 m wide dike making the horizontal cross-sectional area of the dike $3 \times 10^7$ m$^2$. Magmatic foam would occupy the upper ~ 8 km of the dike where the pressure was less than 40 MPa. If the foam evolved to 80% gas volume fraction, close to the upper limit for foam stability [15] then at an average pressure of 20 MPa and a magmatic temperature of 1750 K the average density of the $m$ = 28 kg kmol$^{-1}$ gas would be 40 kg m$^{-3}$ and this would contribute a partial density of [(40 × 0.8) =] 32 kg m$^{-3}$. If the remaining 20% of the foam consisted of magma with density 3000 kg m$^{-3}$ this would contribute a partial density of [(3000 × 0.2) =] 600 kg m$^{-3}$. The gas would then represent a mass fraction of [32/(600 + 32) =] 0.0506, i.e., ~5 mass % or ~50000 ppm. Using eq. (2), release of this foam would produce an eruption speed of 487 m s$^{-1}$ ejecting pyroclasts to ~147 km. The mass of magma in the foam would be its partial density, 600 kg m$^{-3}$, multiplied by the volume of foam, [($3 \times 10^7$ m$^2$ area × 8000 m depth) =] $2.4 \times 10^{11}$ m$^3$, i.e. $1.44 \times 10^{14}$ kg. If this magma were deposited as pyroclasts over an area of 100 km (the rille length) × 147 km (the maximum range) with a bulk density on landing of 2000 kg $m^{-3}$, the resulting deposit thickness would be 4.9 m. We infer that essentially all of the observed dark mantle regional pyroclastic deposits on the Moon can be explained by minor variations on this scenario.

**References:**

1. L. Gaddis *et al., Icarus* 161, 262, 2003.2. C. Weitz*et al., JGR* 103, 22725, 1998.3. J. Head, L. Wilson, *PLSC* 10, 2861,19794. L. Jozwiak*et al*., *LPSC 45*, 2014.5. L. Wilson, J. Head, *JGR* 86, 2971, 1981. 6. J. Head, *PLSC* 5, 207, 1974.7. J. Head *et al*., *JGR* 107, 5001, 2002. 8. L. Wilson, J. Head, *GRL* 30, 1605, 2003. 9. J. Head, L. Wilson, *PSS* 41, 719, 1993. 10. L. Wilson et al., *LPSC 45*, 1223, 2014. 11. A. Saal*et al*., *Nature* 454, 192, 2008. 12. M. Nicholis, M. Rutherford, *LPSC 37*, 2601, 2006.13. M. Rutherford, P. Papale, *Geology* 37, 219, 2009.14. L. Wilson *et al.,Icarus* 215, 584, 2011. 15. C. Jaupart, S. Vergniolle, *JFM* 203, 347, 1989.

# POSSIBLE TEMPERATURE PROFILES OF THE LUNAR MANTLE

**E. V. Kronrod[1], O. L. Kuskov[1], V. A. Kronrod[1],**
*[1]Vernadsky Institute of Geochemistry and Analytical Chemistry, 19, Kosygin Str. Moscow, Russia 119991*
*Contact: kendr_ka@bk.ru*

In this work we have considered possible lunar thermal conditions, surface heat flow values and bulk concentrations of radioactive elements in the Moon. We have estimated the range of possible temperature profiles of the lunar mantle and determined possible uranium content in the Moon and surface heat flows.

For calculation of the temperature profiles and the radioactive source intensity one-dimensional stationary model of thermal conductivity has been used [Kronrod E.V. et al., 2013]. We propose the following model of the Moon. It consists of the crust, the upper mantle with a heat source $Q_{up}$, the lower mantle with a heat source $Q_{low}$ and the core. The depth of the crust varies from 34 km to 43 km and the density is 2580 kg/m$^{-3}$ [Wieczorek M.A. et al., 2012]. The depth of the lower boundary of the upper mantle is 750 km, the radius of the core is 350 km. The temperature at the crust-mantle boundary (350-550 $^o$C) have been estimated from temperature gradient and upper mantle temperature [Kuskov O.L. et al., 2009]. The maximal temperature at the depth of 1250 km (1650 $^o$C) is close to the solidus temperature at the same depth.

Based on the assumption that Th/U=3.7, K/U=2000 [Hagermann A. et al., 2006], heat conductivity coefficient k=4 W m$^{-1}$K$^{-1}$, we have estimated uranium concentration in the upper ($C_{Uup}$) and lower mantle ($C_{Ulow}$, $C_{Ulow}$= $C_{Ubulk}$), surface heat flow ($J_s$) and the corresponding temperature distributions in the lunar mantle. As a result, we have estimated that for the whole range of temperatures at the depth of crust-mantle boundary we can obtain the temperature 1600-1650$^o$C (close to the solidus value) at the depth of 1250 km. Bulk uranium concentration in the Moon $U_{bulk}$ =16-23 ppb. The minimal values correspond to U concentration of 80ppb, maximal - 240ppb. Surface heat flow – (7.8*10$^{-3}$ – 10 *10$^{-3}$ )W/m$^2$ . The temperature at the depth of 1000 km is 1440-1460 $^o$C. Temperature gradient in the upper mantle is within 1.2-1.4 $^o$C/km and in the lower mantle at the depth of 1000-1200 km the gradient is 0.5- 0.7 $^o$C/km.

**Acknowledgements**

This research was supported by Russian Academy of Sciences under Programs 22 and 28, and by RFBR grant 12-05-00178 and 12-05-00033.

**References**

Kronrod E.V., Kuskov O.L. (2013) Temperature profile of the lunar mantle: agreement with seismic and thermal models.
Wieczorek, M.A., Neumann, G.A., Nimmo, F. et al. (2012). The Crust of the Moon as Seen by GRAIL, Sciencexpress /http://www.sciencemag.org/content/early/recent/5 December 2012 / Page 1/ 10.1126/science.1231530.
Kuskov, O.L., Kronrod, V.A. (2009). Geochemical constraints on the model of the composition and thermal conditions of the Moon according to seismic data, Izv. Phys. Solid Earth., Vol. 45, pp. 753–768
Hagermann, A., Tanaka, S. (2006). Ejecta deposit thickness, heat flow, and a critical ambiguity on the Moon, Geophys. Res. Lett. 33, L19203, doi:10.029/2006GL027030.

# SEARCH FOR METEOROID IMPACTS ON THE MOON

**A. A. Berezhnoy[1], Yu. V. Pakhomov[2], K. I. Churyumov[3], R. Lena[4], V. Mangano[5], M. Iten[6], S. Velichko[7, 8], S. Sposetti[9], Yu. I. Velikodsky[8]**
*[1] Sternberg Astronomical Institute, Moscow State University, Universitetskij pr., 13, Moscow, 19991 Russia; [2] Institute of Astronomy, Russian Academy of Sciences, Pyatnitskaya Street 48, Moscow, 119017 Russia; [3] Astronomical Observatory, Shevchenko National University, Observatorna Street 3, Kiev, 04053 Ukraine; [4] Geologic Lunar Research (GLR) Group, Via Cartesio 144, sc. D, 00137 Rome, Italy; [5] INAF-IAPS, Institute of Astrophysics and Planetology from Space, via del Fosso del Cavaliere 100, 00133 Rome, Italy; [6] Garden Observatory via Terriciole 15, CH-6596 Gordola, Switzerland; [7] Terskol branch, Russian Academy of Sciences, Pyatnitskaya Street 48, Moscow, 119017 Russia; [8]Institute of Astronomy, Kharkiv National University, 35 Sumskaya Street, Kharkiv, Ukraine; [9] In Fun I Vign 7, CH-6525 Gnosca, Switzerland. Contact: ber@sai.msu.ru*

**Introduction:**

Quick increase of brightness of Na D1 and D2 lines during maximum of Perseid 2009 meteor shower on August 13, 2009, 0-1 UT was detected and explained by impacts of Perseid meteoroids [1]. Theoretical studies show that alkali metals are released to the lunar exosphere mainly in the form of atoms during collisions between meteoroids and the Moon [2]. For further study of the properties of the lunar exosphere, additional observations were performed in February and March 2014 during the quiet period, when the activity of meteor showers was minimal.

**Spectral Observations and Data Analysis:**

The spectroscopic observations of NaI D1 (5896 Å), NaI D2 (5890 Å), and KI (7699 Å) resonance lines in the lunar exosphere were performed on February 3, 5, and 6, and March 9, 2014 with echelle spectrographs MMCS (Multi Mode Cassegrain Spectrometer) and MAESTRO (MAtrix Echelle SpecTROgraph) at the 2-m Zeiss telescope (Terskol branch of Institute of Astronomy of Russian Academy of Sciences, Kabardino-Balkaria, Russia). At MMCS the slit of the spectrograph has height of 10″ and width of 2″, and at MAESTRO 4″ and 2″, respectively. One, five, and six spectra were obtained at the distance of 100″ (180 km) from the lunar limb above the north pole on February 3 (16:39-16:59 UT), 5 (16:10-18:23 UT), and 6 (16:43-19:21 UT), respectively. Nine spectra were obtained at the distance of 100″ (180 km) from the lunar limb above the north pole on March 9, 2014 between 17:24 and 21:22 UT. The exposure time of each spectrum was equal to 1 200 s.

We used the CCD with size of 1245x1152. At MMCS 32 spectral orders in the range from 3738 to 7738 Å were registered. The resolution was R = 13 500; the signal to noise ratio in the spectra was about 100 at the position of NaI D1 line. At MAESTRO these values are 45 000 and 100, respectively, and the wavelength range is from 3559 to 10283 Å.

The intensity of Na D2 line on February 3, 5, and 6, 2014 was estimated about 10 R, this value is significantly lower than that during the Perseid 2009 meteor shower, about 150 R [1]. Significant short-term variability of the intensity of Na D2 line was not detected during beginning of February 2014.

**Search for impact-produced optical flashes at the Moon:**

During the survey carried out in 2014 year two probable meteoroid impacts on the lunar surface, during post-new Moon periods, were detected. These flashes were independently and simultaneously recorded by two telescopes (125 mm refractor and 280 mm reflector) equipped with videocams (Watec 902H2Ult) placed in Switzerland at a distance of 10.0 km.

The first event was detected on January 7, 2014 at 18:19:31 UT (at selenographic coordinates of 15.5°W and 19.5°N) lasting 2 video fields (0.04 s), but due to lacking comparison stars the peak brightness of the flash was not measured.

The second event, recorded by two Swiss observatories, occurred on March 6, 2014 at 18:56:10 UT (see Fig. 1), during attempt of the simultaneous spectral observations of the lunar exosphere. The third observatory in Rome (equipped with a 130 mm refractor) was not operated due to clouds. The coordinates of the flash was determined to 20.0°W and 8.5°S. The faint flash reached a peak brightness of 9.0 ± 0.3 V mag (airmass 1.46). The whole duration of the flash corresponds to about 0.04 s lasting 2 video fields (1 field = 20 ms). According to the International Meteor Organization [3] at the beginning of March 2014 the Gamma Normids (GNO) meteor shower ($V_\infty$ = 56 km $s^{-1}$) was active. However, the impact could also be attributable to a sporadic meteoroid ($V_\infty$ = 16.9 km $s^{-1}$). Based on a nominal model with conversion efficiency from kinetic to optical energy of $2x10^{-3}$, the mass of the impactor is estimated to be about 0.08 kg or 0.9 kg assuming a GNO shower or a sporadic origin, respectively. It should be noted, however, that these values are “nominal”, since the results includes uncertainties in the projectile density, meteoroid mass, and luminous efficiency. Based on a modeling analysis (Gault’s scaling law assuming the density of both meteoroid and lunar material to be 3000 kg $m^{-3}$), the meteoroid likely produced a crater of about 3-6 m in diameter [4].

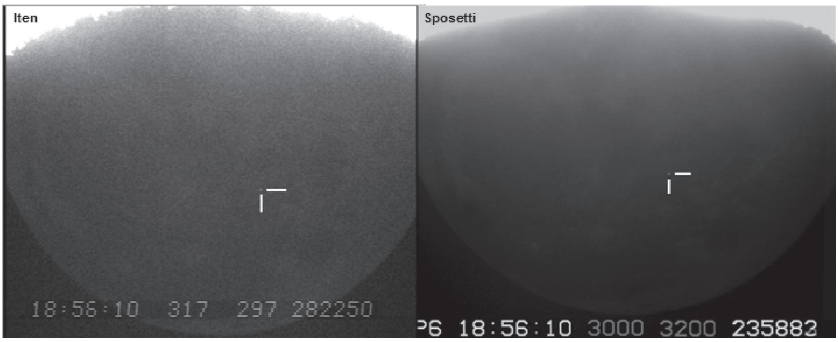


**Fig. 1.** Detected impact of meteoroid on the Moon on March 6, 2014, 18:56:10 UT.

Due to bad weather spectral observations of the lunar exosphere were not performed on March 6, 2014. However, sensitivity of used technique is not high enough for detection of increase in Na and K line intensities after faint flashes similar to that occurred on March 6, 2014. We can easy detect significant changes in the properties of the sodium lunar exosphere only after 20 kg high-speed impact [1].

## Conclusions:

Used technique for search for optical flashes on the Moon is suitable for detection of even faint flashes caused by 0.1 kg high-speed meteoroids. The intensity of Na D2 line during quiet period on February 3-6, 2014 was significantly lower than that during maximum of the Perseid 2009 meteor shower. This observed fact can be interpreted that during activity of main meteor showers meteoroid bombardment is the main source of exospheric Na atoms at the poles of the Moon.

Additional simultaneous spectral observations of the lunar exosphere and search for optical flashes are required during activity of main meteor showers such as Geminids, Quadrantids, and Perseids.

**Acknowledgements:**

Authors would like to thank the staff of Terskol Observatory for performing of the observations.

**References:**

[1] Berezhnoy, A.A., Churyumov, K.I., Kleshchenok, V.V. et al. Properties of the lunar exosphere during the Perseid 2009 meteor shower, Planetary and Space Science, Vol. 96, pp. 90-98, 2014

[2] Berezhnoy, A.A. Meteoroid bombardment as a source of the lunar exosphere, Advances in Space Research, Vol. 45, pp. 70-76, 2010.

[3] IMO site, 2014 http://www.imo.net/node/1540

[4] Melosh, H. J., 1989. Impact Cratering: A Geologic Process. Oxford Univ. Press, New York

# SPACE CORNUCOPIA ON THE LUNAR POLES

**V.V. Shevchenko,**
*Sternberg State Astronomical Institute, Moscow University, 119991 Moscow, Universitetsky pros. 13, Russian Federation;*
*Contact: : vladislav_shevch@mail.ru*

**Introduction:**

In recent times, you can hear the debate on the use of resources concentrated in the near-Earth asteroids. According to recent data 90% of the total number of asteroids are of stone and only a few per cent is made of metal (iron-nickel). But even in a small (diameter about 1 km and a mass of 2 billion tons) stone asteroid the metal fraction is about 200 million tons. Bulk of this fraction accounts for iron. Small components are nickel - 30 million tons, cobalt - 1.5 million tons, and platinum group metals (silver, gold, platinum) - 7500 t. Market value of just this very small part of the asteroid could reach more than $ 150 billion. Particular attention should be paid to the cobalt content. On Earth, this metal is mainly used for special alloys with qualities such as high heat resistance, superhardness, resistance against corrosion, etc. Industrial cobalt content in the ore is from fractions of a percent up to 4%. World reserves of cobalt today are estimated to be about 3 million tons. Consequently, only one small stone asteroid contains half of all terrestrial strategic resources of this metal.

**Rare metals on the surface of the Moon:**

In fact, all the gold, cobalt, iron, manganese, molybdenum, nickel, osmium, palladium, platinum, rhenium, rhodium and ruthenium, which are now extracted from the upper layers of the Earth are often remnants of the asteroid that fell to Earth during the early bombardment, when after cooling crust on the planet hit a huge number of asteroid material. Natural to assume that a similar saturation of the surface rocks and rare-earth metals occur on the Moon, which is close to the Earth also underwent enhanced bombardment of asteroid and comet percussionists type. Previously it was thought that a body falling to the Moon, almost evaporates in the moment of impact, leaving no trace on the lunar surface. New computer simulations have shown that if the velocity of the asteroid does not exceed 12 km /s, the remnants of the impactor does not evaporate, and stored on the floor of the crater in the form of crushed material. Researchers have tried to estimate the number of such deposits on the Moon, by calculating the rate of asteroid that fell to Earth satellite in the past, the depth and size of craters formed at the same time. The number of possible asteroid “treasures” was surprisingly large - about a quarter of the existing lunar craters may contain fragments of the fallen bodies. Thus, by the number of possible lunar resources rightly include nickel, cobalt and platinum asteroid origin. Figure 1 shows map of heights of the impact crater Shackleton, located near the South pole of the Moon. The measurements were performed with a laser radar from Lunar Reconnaissance Orbiter (NASA/GSFC/Arizona State University). It is possible that small elevations on the crater floor are the remains of a fallen asteroid.

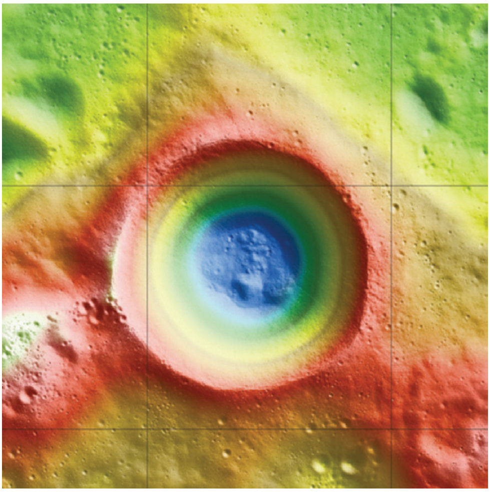

**Fig. 1.**

Absence of pronounced emission in the outer shaft of the crater Shackleton indicates a relatively low rate of fall impactor, perhaps less than 12 km\s (Figure 2, NASA/GSFC/Arizona State University).

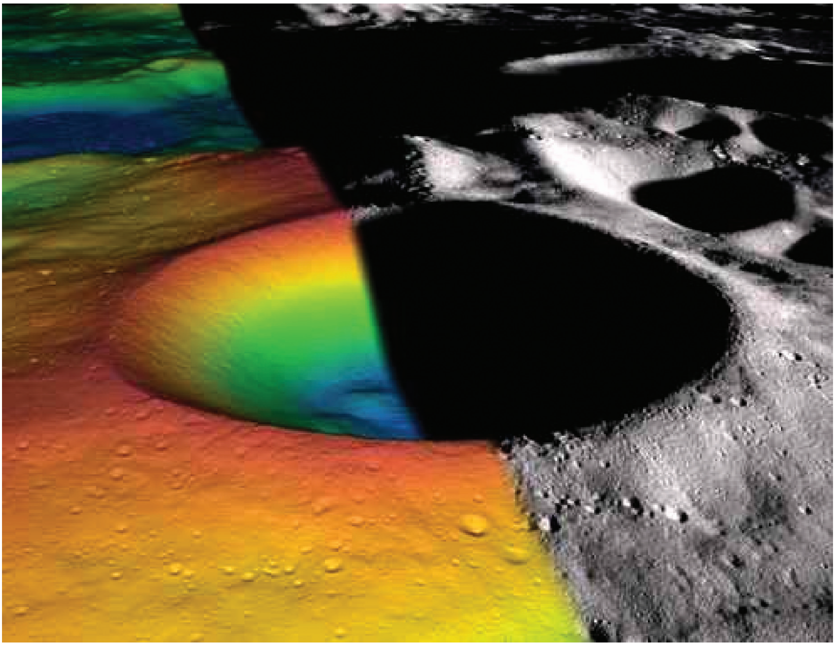

**Fig. 2.**

Lunar geologists have believed that minerals such as magnesium-rich spinel and olivine observed in the central peaks of lunar craters may be due to the excavation of layers of the lunar surface given the observation that oblique (slanting) high-speed lunar impacts in which some asteroid material survive are scattered away from the impact site. So, a new study has found that the Moon's impact craters may contain remnants of asteroids that created them, suggesting that further studies need be done to determine the composition of the lunar surface due to contamination by material from asteroids.

**The economic aspect:**

The largest known metal asteroid (16) Psyche contains $1.7\times10^{19}$ kg of iron-nickel ore (which is 100,000 times greater than the reserves of the ore in the earth's crust). This amount would be enough to meet the needs of the world's population within a few million years, even assuming a further increase in demand. A small portion of the extracted material may also contain precious metals. Of course, on the surface of the moon falling asteroids smaller. But in this case, the implementation of lunar resources can be cost-effective. For example, in 1997 prices relatively small metallic asteroid with a diameter of 1.5 km contained a variety of metals, including precious, in the amount of 20 trillion dollars. If as a result of the fall of the asteroid on the lunar surface (inside impact crater) is preserved only 1% of the material falling body, and even then it may be cost-effective implementation. It should be noted that in terms of technology will only need to collect and load into a transport device is already finely divided material lying on the surface.

# PROBLEM OF JOINT PHOTOGRAMMETRIC PROCESSING IMAGES OBTAINED BY DIFFERENT CAMERAS FROM DIFFERENT ORBITS

**M.I. Shpekin,Ch.R.Mukhametshin**
*Kazan Federal University, Russia, Kazan, Kremlevskaya str. 18,*
*Contact: MichaelS1@yandex.ru*

**Introduction.** The task of building a high-precision system of lunar coordinates that would cover throughout its territory  remains relevant. One way to solve it is a joint photogrammetric processing of orbital surveys carried out in different countries. Analysis of existing images received and delivered to Earth from lunar orbits shows that this solution leads to the need for joint photogrammetry images taken by different cameras from different orbits at different epochs.

The authors examine the possible algorithms to solve this problem. On the example of the orbital  survey of Sovietand American spacecrafts “Zond” and “Apollo” the results of a joint photogrammetric processing images of the missions are shown.

Images used by the authors refer to the equatorial zone of the far side of the Moon. They cover an area near the meridian 180 degrees in the vicinity of the crater Aitken. Images of “Zond-8” have been digitized by the authors in Moscow using a photogrammetric scanner of State University Of Land Use Planning(MIIZ) supported by the Russian Foundation for Basic Research. Digitized images of “Apollo-17” were manufactured in the United States and we have borrowed them from the website of the University of Arizona. It is important to note that the original orbital images of these missions were carried out on the film, in contrast to all later and modern ones. Another important feature is that the film was delivered to Earth. “Zond-8” delivered the film in automatic mode, and  “Apollo-17” films were brought to Earth by the crew of the spacecraft.

**Statement of the problem**. Joint processing of images taken by different cameras from different orbits is understood in this report as a photogrammetric method for determining the three-dimensional selenocentric coordinates of points on the filmed territory that are depicted at least on two images. So far, the simplest version of the decision is examined. It refers to the case when the reference catalog points can be identified on the both images. Then the scheme for solving the problem consists of two stages. In the first stage the exterior orientation elements are calculated,the second - to solve the direct photogrammetric resection simultaneously for two images. As a result of this decision three-dimensional positions of the measured points are obtained .The decision is performed separately for each measured point. All the measured coordinates of the points as the reference, and determined before processingare corrected by introducing them to the corrections for lens distortion and deformation of the film. For a camera with a focal-plane shutter the amendments are taken into account according to the dynamical photogrammetry formulas.

Authors are going to describe the algorithm for solving in a separate publication. Here we will mention only the main differences between our algorithm and the classical scheme of construction of the stereopairs.The main difference is that in our version restrictions on the uniformity of the images are removed. Images of one route can be called  provisionally  homogeneous when they’re done with one camera with small angles of mutual inclinations. Our equations take pictures from any angle and magnitude of the slopes, as well as pictures taken by different cameras. The speech is about cameras with different focal lengths. Due to remove of these limitations cameras may be at any point of space and, in particular, at different orbits.

This method brings its disadvantages. For example, in this case there is no adjustment of the measurement. If the survey was taken from different orbits, there is no chance to adjust the positions of the projection centers by photogrammetric orbit.

**The main results.** Fig. 1 and 2 show the geometrical conditions under which the used images were obtained. The differences between the coordinates of the control points of the processing of the two stereopairs, and catalog coordinates of these points are shown on Fig.3.  The differences for all three coordinates on the same graph with different colors are given.The abscissas - the control points index numbers in the catalog CNIIGAiK, and the ordinate - the difference in km. Below the abscissa the same difference in digital form in km is shown. The first stereopair (top) includes 29 control points, the second (lower graph) -18.

Analysis of Figure 3 shows that the difference in the coordinates for the control points lies within an average of 2 km.Three points of 29 oneshave gone beyond 2 km for the first stereopair. We believe that the most likely reason - the measurement error. Noteworthy differences in the behavior of the axis X. They are superior to the average values obtained for the axes Y and Z. This effect is in full accordance with the geometry of the survey, as projecting rays are directed precisely along the axis X. Overall, the difference is for the main part of the for control points within 0.5-1.0 km.

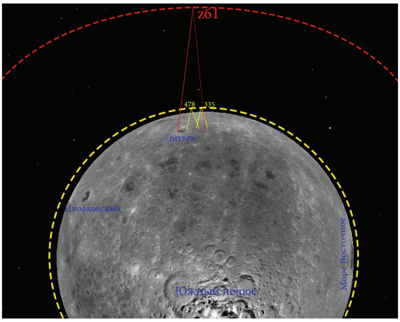


**Fig. 1**

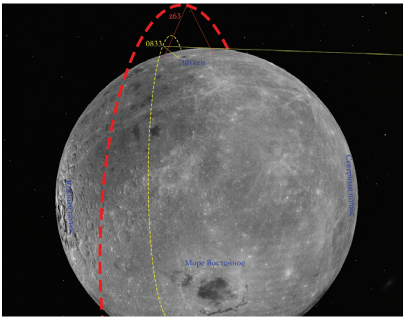


**Fig. 2**

“Zond-8” (red dotted line) and “Apollo 17” (yellow dotted line) orbits are shown in two perspectives: in Figure 1 - view from the south pole, in Figure 2 - view from the western hemisphere. The index numbers of images also are written, respectively red and yellow.

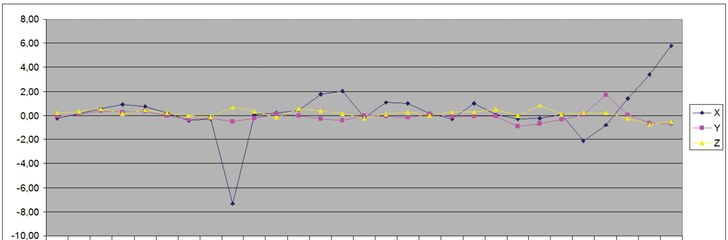


| | 56 | 57 | 58 | 59 | 60 | 61 | 85 | 86 | 88 | 89 | 90 | 92 | 94 | 95 |
|---|---|---|---|---|---|---|---|---|---|---|---|---|---|---|
| X | -0,2 | 0,16 | 0,55 | 0,90 | 0,73 | 0,21 | -0,4 | -0,2 | -7,3 | 0,03 | 0,20 | 0,44 | 1,74 | 2,06 |
| Y | -0,0 | 0,03 | 0,38 | 0,26 | 0,34 | -0,0 | -0,3 | -0,2 | -0,5 | -0,2 | 0,10 | -0,0 | -0,2 | -0,3 |
| Z | 0,23 | 0,34 | 0,56 | 0,16 | 0,43 | 0,24 | -0,0 | -0,1 | 0,65 | 0,35 | -0,1 | 0,56 | 0,38 | 0,15 |

| | 96 | 97 | 98 | 99 | 101 | 102 | 103 | 106 | 130 | 139 | 141 | 142 | 143 | 144 | 145 |
|---|---|---|---|---|---|---|---|---|---|---|---|---|---|---|---|
| X | -0,1 | 1,06 | 0,99 | 0,14 | -0,2 | 1,02 | 0,05 | -0,2 | -0,2 | 0,05 | -2,1 | -0,8 | 1,41 | 3,40 | 5,76 |
| Y | -0,0 | -0,0 | -0,1 | 0,11 | -0,1 | -0,0 | -0,0 | -0,9 | -0,7 | -0,3 | 0,07 | 1,70 | 0,03 | -0,6 | -0,7 |
| Z | -0,2 | 0,09 | 0,26 | 0,00 | 0,30 | 0,27 | 0,49 | -0,0 | 0,86 | 0,12 | 0,22 | 0,21 | -0,2 | -0,7 | -0,5 |

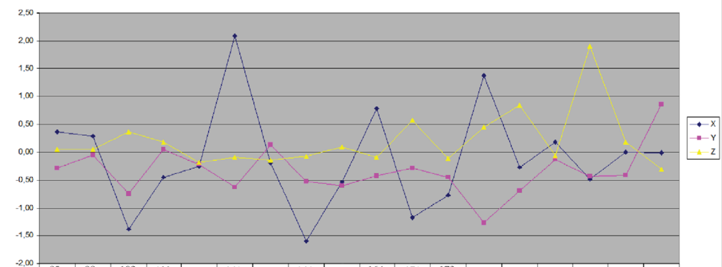


| | 95 | 98 | 102 | 103 | 139 | 141 | 143 | 144 | 145 | 164 | 171 | 173 | 175 | 176 | 181 | 182 | 186 | 189 |
|---|---|---|---|---|---|---|---|---|---|---|---|---|---|---|---|---|---|---|
| X | 0,36 | 0,29 | -1,38 | -0,45 | -0,25 | 2,09 | -0,19 | -1,60 | -0,54 | 0,78 | -1,17 | -0,77 | 1,37 | -0,27 | 0,19 | -0,49 | 0,01 | -0,01 |
| Y | -0,28 | -0,05 | -0,74 | 0,06 | -0,22 | -0,63 | 0,13 | -0,53 | -0,60 | -0,42 | -0,28 | -0,45 | -1,26 | -0,70 | -0,13 | -0,44 | -0,41 | 0,86 |
| Z | 0,05 | 0,06 | 0,37 | 0,19 | -0,18 | -0,08 | -0,14 | -0,07 | 0,10 | -0,09 | 0,57 | -0,11 | 0,45 | 0,84 | -0,06 | 1,90 | 0,18 | -0,30 |

**Fig.3.** Difference of selenocentric coordinates for control points for the two stereopairs.

**Conclusion.**Despite the venerable age of these surveys, the task of processing the Soviet and American images and today remains relevant as a full-fledged joint photogrammetric analysis of these materials, unfortunately, was not carried out.

Meanwhile, such an analysis would create a unified system of lunar coordinates covering the entire moon’s equator. Unified system for lunar coordinates, built by rigorous methods of analytical photogrammetry, could provide better solutions to the problems of navigation near the Moon, as well as problems selenodesy and lunar cartography.

# EUROPEAN APPROACH TO LUNAR EXPLORATION IN COOPERATION WITH RUSSIA

**B. Houdou[1], R. Fisackerly[1], J. Carpenter[1], D. De Rosa[1], J. Schiemann[1], B. Patti[1],**
[1]*European Space Agency, Keplerlaan 1, 2201 AG, Noordwijk, Netherlands. Contact: Berengere.Houdou@esa.int*

**Introduction:** In ESA the Moon is considered as a stepping stone for the development of cooperative robotic and human exploration capabilities beyond Low Earth Orbit, beginning with robotic precursor missions. The Moon also plays a major role in the exploration plans of ESA's international partners, in particular Russia. In the context of broader cooperation between ESA and Russia in exploration of the Solar System, agencies, industries and institutes from both sides are actively engaged in setting up a cooperation on the Russian-led Luna-Resource Lander mission (Luna-27), with a view to a Lunar Polar Sample Return (LPSR) mission (Luna-28). This paper outlines the main European objectives and approach regarding this cooperation.

**Product-based Approach:** Europe's objectives in accessing the lunar surface are to further develop key technologies and generate knowledge that will enable future human and robotic exploration of the Solar System. ESA acknowledges that cooperation with international partners will be key to making this happen. ESA is now focused on developing core exploration products which can be provided to the missions of partners for flight before the end of the decade, based on many years of technology development and lunar landing mission studies.

PILOT (Precise and Intelligent Landing using On board Technology) enables global access to locations of interest on the surface, precisely and safely. Its new functions enhance the landing capability of platforms and are fundamental to the surface exploration of challenging sites. It consists of an autonomous Visual Navigation and Hazard Detection and Avoidance (VN&HDA) system with a camera and a LIDAR. PILOT also includes a suite of ground-based tools for characterisation of the landing sites.

PROSPECT (Package for Resource Observation and in-Situ Prospecting for Exploration, Commercial Exploitation and Transportation) enables investigation of potential resources at any given location on the Moon, including the polar regions. This surface package provides the end-to-end sampling chain, from access to subsurface samples and extraction, to identification and analysis, while ensuring preservation of volatiles at low temperature where they are present. It consists of a subsurface acquisition system, which interfaces with a miniaturised sample processing and analysis laboratory.

SPECTRUM (Space Exploration Communications Technology for Robustness and Usability between Missions) enables communications between multiple lunar exploration assets, in-flight, on-surface and on-ground. Through this core function SPECTRUM enables the return of scientific and engineering flight data for operations, as well as for post-flight exploitation. It consists of a UHF communications system that provides a link between a lander on a planetary surface and an orbiting platform. SPECTRUM also includes ground segment services to support direct communications between spacecraft and the Earth for operations.

ESA is planning to contribute to the Luna missions of Roscosmos with the exploration products above and activities are ongoing in European institutes and industry to develop them for the precise needs and constraints of those missions. In parallel the approach aims to generate research opportunities which will address the scientific challenges of exploration whilst providing opportunities for fundamental scientific research.

**Conclusion:** A European-Russian cooperation on near- and medium term lunar exploration missions, with a focus on Lunar-Resource Lander and looking forward to Lunar Polar Sample Return, offers an opportunity for Europe to realise its own exploration objectives. Based on the significant European experience across a range of areas, and on the principle of mutual benefit, ESA and its partners in Russia are building a lunar exploration programme which offers immediate benefits and which paves the way for future cooperation in human exploration.

# ACCESSING AND ASSESSING THE LUNAR RESOURCES WITH PROSPECT

**J. D. Carpenter[1], S. Barber[2], P. Cerroni[3], D. De Rosa[1], R. Fisackerly[1], A. Fumagalli[4], B. Houdou[1], C. Howe[5], P.G. Magnani[4] A. Morse[2], E. Monchieri[6], B. Patti[1], P. Reiss[7], L. Richter[8], F. Rizzi[4], S. Sheridan[2], L. Waugh[6], I.P. Wright[2],**
*[1]ESA ESTEC, Keplerlaan 1, 2201AZ, Noordwijk, The Netherlands,*
*[2]The Open University, UK,*
*[3]INAF, Italy,*
*[4]Selex-ES, Italy,*
*[5]RAL Space, UK,*
*[6]Airbus SD, UK,*
*[7]Technische Universitaet Muenchen, Germany,*
*[8]Kayser-Threde, Germany.*
*Contact: james.carpenter@esa.int*

**Introduction:**
A Package for Resource Observation and in-Situ Prospecting for Exploration, Commercial exploitation and Transportation (PROSPECT) is in development by ESA for application at the lunar surface as part of the Russian Luna-27 mission. PROSPECT builds on extensive flight heritage and technology developments over several decades. Establishing the utilization potential of resources found in-situ on the Moon may be key to enabling sustainable exploration in the future. The purpose of PROSPECT is to support the identification of potential resources, to assess their utilization potential, whilst providing data with important implications for fundamental scientific investigations.

**System Functions:**
*Drilling and sampling:* PROSPECT will drill that to depths of up to 2m, from where samples shall be extracted be extracted and then handled, whilst minimizing alteration of the samples and losses of ice and other volatiles. The drill is derived from heritage on EXOMARS [1] and Rosetta [2], currently in-situ at comet 67P/Churyumov-Gerasimenko. *Assessment of sample mineralogy and volatile content:* infrared spectra are recorded [3] in order to assess mineralogy and water content. *Sample heating and chemical extraction:* samples are sealed in ovens, derived from EXOMARS [4], Rosetta and technology programmes. Heating in vacuum extracts ices and solar wind implanted volatiles and pyrolyses some volatiles from minerals. Reacting gasses (e.g. $O_2$, $H_2$, $CH_4$, $H_2$) may also be introduced to the ovens [5, 6, 7]. *Gas compositional analysis:* evolved gasses can be analyzed using an ion trap mass spectrometer [5] to give a qualitative measure of composition. *Gas chemical processing:* refinement or conversion to other chemicals [5] can then be performed to prepare gasses for isotopic analysis. *Gas isotopic analysis*: isotopes of the elements of interest are measured using a magnetic sector mass spectrometer, along with measurements of standards [5] to ensure high accuracy.

**Conclusions:** PROSPECT is a package for the investigation of lunar volatiles and other potential resources on the Moon, with additional benefits for fundamental science. The package builds on extensive flight heritage and a unique set of capabilities, developed over decades by a number of groups across Europe.

**Acknowlegement:**
We would like to acknowledge the important contributions of our colleague Colin Pilinger, who sadly died earlier this year.

**References:**
[1] Magnani P. et al. (2010) *Proceeding of i-SAIRAS*. [2] Marchesi M. et al. (2001), *Proceedings of the 9th European Space Mechanisms and Tribology Symposium*, 91 - 96. [3] Coradini A. et al. (2011) EPSC-DPS EPSC-DPS Joint Meeting 2011 abstract. [4] Schulte W. et al. (2010), *Proceeding of i-SAIRAS*. [5] Wright I.P. et al. (2012) *Planetary and space science*, 74, 1, 254-263. [6] Sebolt W. et al, (1993) in Resources of Near Earth Space, The University of Arizona Press, 129. [7] Schwandt et al., (2012) *Planetary and space science*, 74, 1, 49-56.

# COHERENT LUNA'S RADIO BEACON AND ITS SCIENTIFIC POTENTIAL

**A.S. Kosov, V.V. Korogod, U.A. Nemliher, D.P. Sculachev,**
*IKI RAS, 84/32Profsouznaya, Moscow, Russia.*
*Contact: akosov@iki.rssi.ru*

**Introduction:**

It is planned to upgrade radio beacon instrument, included into future Russian Luna-Resource mission. Thenew radio beacon will have possibility to operate in coherent mode. The coherent mode means synchronization of the beacon's transmitters by reference signal sending from the Earth. Future Luna's missions(ESA, China, Japan, NASA) worldwide are planning radio science experiments with coherent radio beacons on Luna's landers. Currently coherent radio beacon is successfully working on Chinese lander Chang'E-3. Coherent mode of operation is realized by *X*band(7.2 GHz) reference signal sending from Earth. The Luna's radio beacon should receive the signal, convert the signal to transmitter's frequencies (8.4 GHz and 32 GHz) and send the transmitted signals back to Earth. Due to the coherency of reference and transmitted back signals it is possible to measure the relative velocity with accuracy about 0.01 mm/sec and shifts with accuracy about 0.1 mm.

**Radio Beacon structure:**

The structure of coherent radio beacon is shown on figure 1.

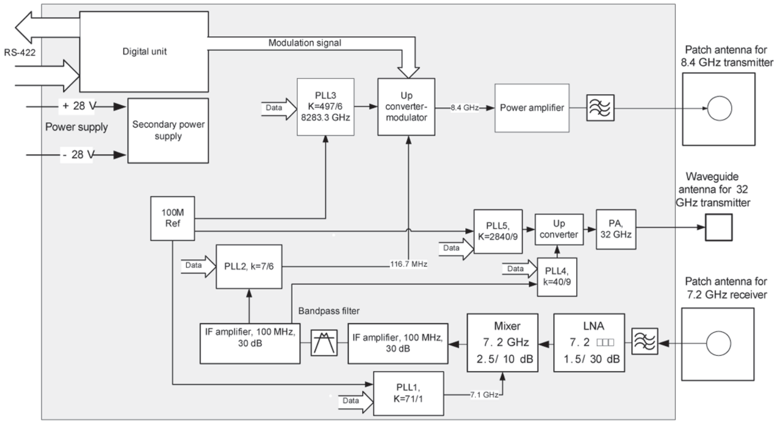


**Fig. 1.** Structure of the coherent radio beacon.

The instrument coherent radio beacon is a single box with mass about 2 kg and volume bout 2 liters. There are three antennas: patch receiver antenna at frequency 7.2 GHz (X band), patch transmitter antenna at frequency 8.4 GHz (X band) and waveguide transmitter antenna at frequency 32 GHz (Ka band). Main beams of X band antennas are directed to the Earth, main beam of Ka band antenna is directed to zenith. The received reference signal at 7.2 GHz is converted to transmitted signals at 8.4 GHz and 32 GHz without loss of coherency. Such type of conversion is possible by means of fore PLL circuits with special ratios of frequency translation. As a result frequency fluctuations of internal reference source will not affect to the frequency of transmitted signals. The instrument is capable to irradiate up to 0.5 W in each channel. The antennas gain is 5-7 dB. Polarization is circular right.

The instrument can operate in autonomic mode without reference signal from Earth. In the mode the receiver is turned off, and the PLL3 and PLL5 are tuned to frequencies 8.4 and 32 GHz respectively. The frequency stability in autonomic mode is determined by internal reference oscillator.

**Scientific Experiments:**

Due to unprecedented accuracy of velocity and shifts measurements where is a possibility to arrange a lot of valuable radio science experiments. There are three types of possible radio science experiments. The first one is the measurements of Doppler shift and relative velocity with accuracy 0.01 mm/sec, the second one is the measurements of position and shifts of radio beacon with accuracy about 10 mm using VLBI network on Earth, and the three one is the SBI (Same Beam Interferometer) experiments. SBI experiment chart is shown on figure 2. For SBI experiments several radio beacons on Moon surface should work simultaneously and be synchronizedfrom a single Earth's reference source. SBI experiments allow to measure 3D displacements with accuracy about 0.1 mm. The sources and values of estimated accuracy errors (phase errors and equivalent distance shift errors) are shown in table 1 [1].

**Table 1.**Sources and values on SBI measurement errors.

| Error sources | Error on SBI measurement |
|---|---|
| Noise atEarthstation | <0.028 mm <1.0º |
| Noise at KaT receiver | <0.006 mm <0.2º |
| Residual errorsafterKaTcalibration | <0.014 mm <0.5º |
| Phase instability | <0.056 mm<2.0º |
| Residual troposphericdifferentialdelayaftercalibration | <0.050 mm <1.8º |
| Ionospheric differentialdelay | <0.005 mm <0.2º |
| **TOTAL** | **<0.09 mm<3.0º** |

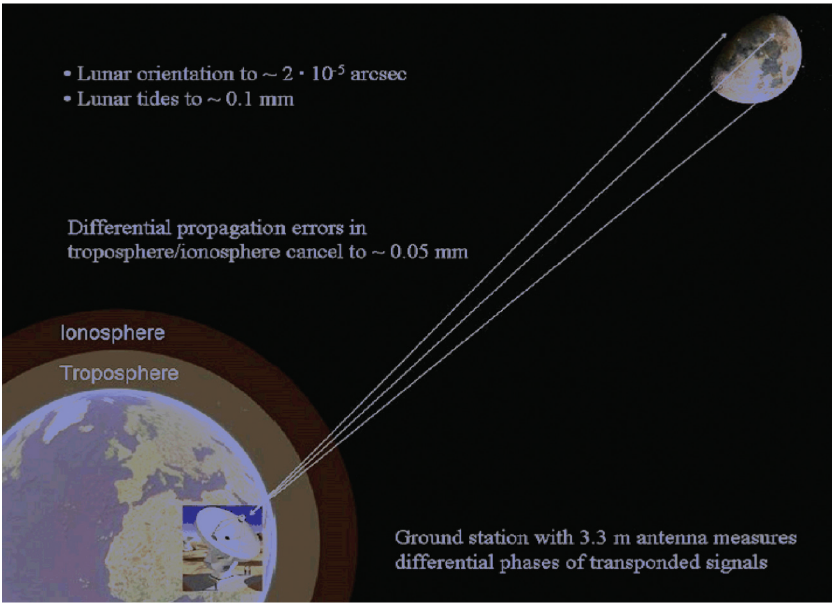


**Fig. 2.**SBI experiment chart.

### Scientific experiments objectives [2]:

- improvement of the reference frames for the Earth;
- better understanding of the Moon's interior, and in particular, through the determination of the moments of inertia of the whole Moon and of its core (inner core and outer core), the core oblateness, the free and forced librations, and the tides and their dissipation, obtain a better determination of the core radius and of the possible presence of an inner core, of the mantle mineralogies, and of the core composition, and therewith better constrain the Moon's evolution;
- better determination of the parameters of General Relativity, through the values of the PPN parameters and even tests for the violations of general relativity in the context of other metric theories of gravity;
- better lunar rotation dynamics, lunar orbit, and lunar ephemeris, incorporating the numerous Newtonian perturbations as well as the much more subtle relativistic phenomena, which are all use for spacecraft missions.

**References:**

[1] M. Gregnanin at al, Same beam interferometry as a tool for the investigation of the lunar interior, Planetary and Space Science 74 (2012) 194–201.
[2] V. Dehant at al, Geodesy instrument package on the Moon for improving our knowledge of the Moon and the realization of reference frames, Planetary and Space Science 68 (2012) 94–104.

# LUNAR REGOLITH INVESTIGATION USING MICROWAVE RADIOMETER/SCATTEROMETER

**D. P. Skulachev, V. V. Korogod, A. S. Kosov, Y. A. Nemliher,**
*Space Research Institute (IKI), Russia, 117997, Moscow, 84/32 Profsoyuznaya Str.*
*Contact: dskulach@mx.iki.rssi.ru*

Planned Russian space mission "Luna-Resource" involves research on a wide range of tasks. The search for traces of water and volatile components in the lunar regolith is one of such tasks. We do not discuss in this paper the ways of getting or nature of occurrence of ice patches in the regolith. We offer to evaluate the presence of such inclusions by examining the regolith thermal properties.

It is known that the density of the solar radiation incident on the lunar surface depends mainly on selenological latitude and current height of the Sun above lunar horizon. Diurnal fluctuations of the solar radiation cause periodic temperature changes of the regolith — so called heat waves. Heat waves extend deep into the regolith, fading with increasing depth. At a depth of about half a meter the amplitude of thermal waves become insignificant, and the temperature of the regolith remains constant, without any diurnal fluctuations.

The landing of the "Luna-Resource" module is planned in the polar region, where the steady temperature in the depth of the regolith is below 100 K. In these conditions, water ice and frozen gases can exist in the structure of the regolith for extremely long time.

We assume that the presence of even small amounts of ice leads to a freezing of regolith grains and, consequently, to a significant change its thermal properties. In particular, it should significantly increase the regolith thermal conductivity and thermal diffusivity. That, in turn, will increase the depth of penetration of the diurnal heat waves. We expect to determine heat waves parameters by measuring the lunar regolith temperatures at different depths and in different times of the lunar day.

Temperature measurement of the lunar regolith is a rather difficult experimental task. A contact method is the most simple and accurate. It uses thermal sensors buried in the regolith on a different depth. Unfortunately the sensors deployed in the regolith severely violates existing thermal field, and the time to reach thermal equilibrium reaches hundreds and thousands of hours. This is because the thermal diffusivity of the regolith is very small.

We plan to estimate the temperature of a remote method, by measuring the natural thermal radiation of the regolith. A microwave radiometer is installed on a lunar landing module for this purpose. The radiometer operates at three different frequencies. The frequency is selected so as to receive heat radiation coming from the regions of the regolith located at different depths - from close to the surface to fields at a depth of about half a meter.

Microwave modulation radiometer "RAT" applied for measurement. The radiometer has two inputs; it records the temperature difference of the objects connected to the inputs. The first input is connected with nadir antenna directed to the moon surface. The second input is connected with zenith antenna directed on open sky. The Moon has no atmosphere, so the radio brightness temperature which registers the zenith antenna is close to the temperature of the microwave background radiation (2.75 K). The zenith antenna beam width is about 45 angular degrees, so the influence of cosmic radio sources can be neglected.

Thus microwave radiometer "RAT" registers the difference between the regolith temperature and the background radiation temperature. The radiometer calibration is performed in the mode, when the first input of the radiometer is connected to (instead of the nadir antenna) a match load with a known temperature (about 300 K). The sensitivity of the radiometer "RAT" is about 0.25 K.

After measurements are made at different frequencies at different times one can compare experimental data with estimated values, defined on the basis of the current position of the Sun and known dielectric and thermal properties of the lunar regolith. The magnitude of the differences between the experimental and calculated data will allow us to estimate ice amount in the lunar regolith. This assessment will to some extent depend on used models of the lunar regolith.

The nadir antenna can catch thermal emission not only from the regolith but also from large stones in the regolith depth. A microwave subsurface radar may detect such stones. Dielectric properties of rocks and the regolith differ. Electromagnetic power transmitted by the radar reflects from the boundary of rocks and regolith and the radar receiver registers reflected signal. The intensity of the reflected signal allows estimating the value of the stone, and the delay between the transmitted and the reflected signal allows determining the distance to the obstacle. Microwave radiometer is not sensitive to the distance to the radiating object, and radar does not feel the temperature. Thus radar and microwave radiometer to a certain degree are complementary to one another.

We plan to use radar with linear frequency modulation operating in the lower part of the radiometer “RAT” frequency band. The radiometer “PAT” nadir antenna is used as the radar antenna. It allows us to avoid measurement errors associated with fields of view distinction of the radiometer and the radar.

# FINE EFFECTS OF SPIN-ORBIT DYNAMICS OF THE MOON, LUNAR RADIO BEACONS AND LUNAR NAVIGATION ALMANAC FOR CHANGE-3/4, LUNA-GLOB-RESOURCE, SELENE-2 MISSIONS

**A. Gusev[1,2], J. Ping[2], N. Petrova[1], H. Hanada[3].**
*[1]Kazan federal university, 18, Kremlevskaya str., Kazan, 420008, Russia.*
*[2]Lunar and Deep Space Exploration Center, NAOC CAS, 20A, Datun Road, Chaoyang Distric, Beijing, 100012,China; [3]RISE project, Mizusawa VLBI observatory, NAOJ, 2-12,Hoshigaoka, Mizusawa, Oshu, Iwate, 023-0861, Japan.*
*Contact: Alexander.Gusev@mail.ru ;*

Our current knowledge of the internal structure of the Moon reviewed and it will be shown that new data from the international lunar missions can improve them. The emphasis will put on the evidences of lunar core existence and on the necessity to take this fact into account in the lunar librations theory.

Our goal is to show how the millisecond precision observations of lunar physical librations in the project ChangE-3/4, Luna-Glob-Resource, ILOM: the optical telescopes or radio beacons on the Moon, or the long-term observations of the lunar satellite with high-precision camera and laser altimetry by Differential, Inverse and Same Beam Interference (SBI) VLBI may be used for determining the parameters of Lunar liquid/solid core.

We discuss geophysical parameters, geometrical and dynamic ellipticity of liquid core and viscose-elastic mantle of the multi-layer Moon. The given characteristics are important for the evaluation of free librations of the Moon’s layers – Chandler Wobble (CW), Free Core Nutation (FCN), Inner Core Wobble (ICW), Free Inner Core Nutation (FICN).

It is shown, that the analytical theory physical libration the Moon can be used as the convenient tool for carrying out of modeling of the future supervision from a lunar surface, for understanding of distinctions in lunar systems of coordinates and carrying out of the approached estimations of influence of changes in Moon dynamic characteristics on navigating problems. The considered questions pawn a basis of formation of a lunar navigation almanac.

Conception of the Lunar Navigation Almanac (LNA) for ChangE-3/4, Luna-Glob-Resource, SELENE-2 missions will be discussed. New phase of exploration of the Moon require detailed measurements of position and velocity of instruments on Lunar surface, selenographic coordinates system, cartography, surface and near-surface navigation, correlation and data reduction of scientific experiments, such as radio beacons, laser CCR, lunar seismology, geological sampling, etc.

The LNA should contain precise and detailed information about position of stars, Sun, planets in selenographic coordinates system, transition from the lunar time to the universal time and inversely. The lunar navigation for observations from a lunar surface requires the high-accurate theory of the lunar motion and rotation. The LNA should include a system of the formulae and constants for reduction of ICRF-coordinates of a star onto a visible place, which is bound with instantaneous Lunar equator (axis of Lunar rotation).

# SURVIVAL TIMES OF METER-SIZED ROCK BOULDERS ON THE SURFACE OF AIRLESS BODIES

**A.T. Basilevsky[1,2], J.W. Head[2], F. Horz[3], K. Ramsley[2],**
*[1]Vernadsky Institute, RAS, Moscow 119991 Russia, atbas@geokhi.ru,*
*[2]Brown University, Providence, RI, 02912 USA, [3]LZ Technology Inc., Houston, TX 77058, USA.*

**Introduction.** This study considers the survival times of meter-sized rock boulders seen on the surfaces of airless bodies. As the starting point, we employ estimates of the survival times of such boulders on the surface of the Moon by Basilevsky et al. (2013), then discuss the role of destruction due to day-night temperature cycling, and finally consider the meteorite bombardment environment on Phobos, Deimos and the asteroid Itokawa in terms of projectile flux and velocities. We then estimate the survival times of meter-sized boulders on these bodies.

**Survival times of meter-sized rocks on lunar surface.** The survival times of hand specimen-sized rocks exposed to the lunar surface environment were estimated based on experiments modeling the destruction of rocks by meteorite impacts, combined with measurements of the lunar surface meteorite flux, (e.g., Horz et al., 1975). For estimations of the survival times of meter-sized lunar boulders Basilevsky et al. (2013) suggested a different approach based on analysis of spatial density of the boulders on the rims of small lunar craters of known absolute age. It was found that for a few million years, only a small fraction of the boulders ejected by cratering process are destroyed, for several tens of million years ~50% are destroyed, and for 200-300 Ma, ~90 to 99% of the original boulder population are destroyed. Following Horz et al. (1975) and other works, Basilevsky et al. (2013) considered that the rocks are mostly destroyed by meteorite impacts although stresses due to diurnal temperature cycling may also contribute to the destruction.

**Destruction of rocks by thermal-stress.** High diurnal temperature variations on the surface of the Moon and other airless bodies imply that thermal stresses may be a cause of the surface rockdestruction. Delbo et al. (2014) interpreted the observed presence of fine debris on the surface of small asteroids as due to thermal surface cycling. They stated that because of the very low gravity on the surface of these bodies, ejecta from meteorite impacts should leave the body, so formation there of fine debris has to be due to thermal cycling. Based on experiments on heating-cooling of cm-scale pieces of ordinary and carbonaceous chondrites and theoretical modeling of expansion of the cracks formed they concluded that thermal fragmentation breaks up rocks larger than a few centimeters more quickly than do micrometeoroid impacts. According to them at 1 AU distance from the Sun the lifetime of 10 cm rock fragments on asteroids with a period of rotation from 2.2 to 6 hours should be only ~$10^3$ to $10^4$ years with the following trend: the larger the rock the faster it gets destroyed.

But although Delbo et al. are obviously correct stating that the impact ejecta should leave small asteroids, the low-velocity part of escaping ejecta will mostly stay in orbits close to the orbit of this given asteroid and part of the ejecta will eventually return to it. Moreover, directly beneath the impact point the target rock should be fractured and crushed but may not leave the body (Figure 1).These two points question the Delbo et al. conclusions.

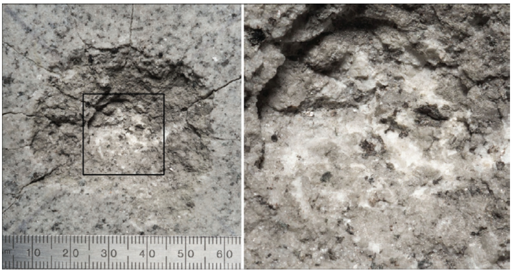

**Fig. 1.** Experimental impact crater ~5 cm in diameter formed in the 10x10x10 cm granodiorite cube by impact of a 3.2 mm diameter stainless steel sphere at 5.47 km/s. Whitish coloration of the central part of the crater floor is due to the presence of finely crushed target material. Divisions on the ruler are in millimeters.

**Observations of lunar rocks of known age of surface exposure.** We check the validity of the Delbo et al. estimates for the 1 AU asteroidsthrough observations of rock fragments on the Moon which is also at 1 AU from the Sun and thermal cycling on its surface is strong. The thermal cycling period on the Moon is 708 hours, longer than the 2.2 to 6 hours assumed by Delbo et al. for asteroids. So for our comparisons we measure time not in years, but in number of thermal cycles. Then, the estimates by Delbo et al.of the survival times of several-centimeter-sized rocks on asteroids, are ~$3.5 \times 10^6$ to $1.5 \times 10^7$ thermal cycles correspondingly.

We discuss two types of rock fragments: 1) Rocks ~20 cm across that are close to the sizes considered by Delbo et al.;so if the survival time estimates of these authors are correct, one should expect that, when these values are reached, the rocks have to be destroyed. 2) Rock boulders of 3 to 5 m across; for these one shouldexpect that when the survival time for the several-centimeter-size rock is reached, the several-centimeter-thick surface layer of these blocks has to be destroyed and form a fillet at the boulder base. Figure 2 shows three examples of the rocks of the first type and Figure 3 — three examples of the second type.

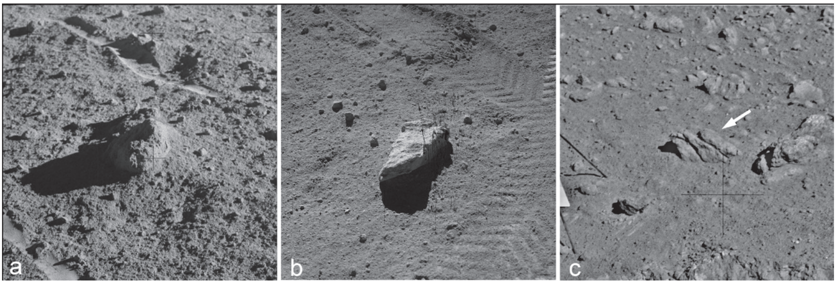

**Fig. 2.** Rocks on the rims of dated lunar craters: a) the 20-cm rock Big Berthaon the rim of 26 Ma old Cone Crater, Apollo 14; b) the 20-cm rock on the rim of 50 Ma-old North Ray Crater, Apollo 16; c) the ~20-cm rock on the rim of 30 Ma-old Shorty Crater, Apollo 17.

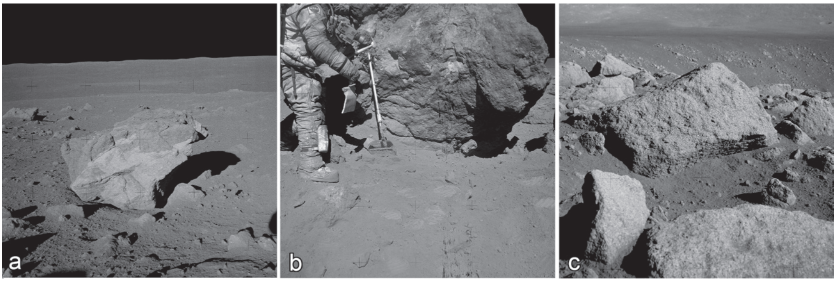

**Fig. 3.** Meter-sized rocks; a) the 2 m wide Contact Rock on the rim of 26 Ma-old Cone crater, Apollo 14; b) part of the 5 m wide Outhouse Rock on the rim of 50 Ma-old North Ray crater, Apollo 16; c) meter-sized rocks on the rim of 90 Ma-old Camelot crater, Apollo 17.

It is seen in Figures 2 and 3 that the 20 cm-rocks show no or minor fine fracturing and the meter-sized rocks show no filets at their bases. The exposure ages of these rocks are from 26 to 90 Ma, that is ~3 to $7.5 \times 10^8$ thermal cycles — by 1.5-2 orders magnitude larger than the Delbo et al. estimates of the lifetime of the decimeter-sized rocks. So if theirestimates were applicable to the lunar rocks, we should not see the 20-cm rocks considered– they should be destroyed many times over, and the observed meter-sized rocks should besurrounded by very prominent filets, which we do not see.So, on the basis of these observations, we conclude that the role of meteorite impacts in rock destruction is dominant while that of thermal cycling is secondary.

**Calculations of meteorite flux, impact velocities and rock survival times on different airless bodies.** Based on numerical modeling of orbital parameters taken from the complete catalog of 393,347 Main Belt, Trojans, and inner minor planets (as of June, 2014)considered as a proxy for the distribution of potential impactors, it was possible to estimate the meteorite flux and impact velocities for a number of airless bodies, including Phobos, Deimos andasteroidsItokawa, Vesta, Ceres,and an average of thefirst 150 discovered Trojans. From these calculations, we deduced the survival times of meter-sized rock boulders on the surface of these bodies:

| Body | Meteorite flux | | | Impact velocity, m/s | | | Survival time | | |
|---|---|---|---|---|---|---|---|---|---|
| | LH. | TH | Ave-rage | LH | TH | Ave-rage | LH | TH | Ave-rage |
| the Moon | | | 1 | 15414 | 13458 | 14469 | | | **1** |
| Phobos | 3.79 | 3.60 | | 11651 | 7528 | | ~0.4 | ~1 | **~0.8** |
| Deimos | 3.59 | 3.49 | | 10890 | 8283 | | ~0.5 | ~0.9 | **~0.7** |
| Itokawa | | | 3.3 | | | 6800 | | | **~1.4** |
| Vesta | | | 319 | | | 4659 | | | **~0.03** |
| Ceres | | | 320 | | | 4912 | | | **~0.03** |
| Trojans | | | 1.29 | | | 3602 | | | **~12.5** |

LH = Leading hemisphere, TH = Trailing hemisphere.

**Conclusion.** The results given in the Table show that the survival times of meter-sized boulders on Phobos, Deimos and asteroids Itokawa, Vesta, Ceres and the Trojansshow a big diversity: for Phobos, Deimos and Itokawathey are close to those for lunar boulders, for Vesta and Ceres they are by about two orders of magnitude smaller and for Trojans they are by an order of magnitude larger. This should also have implications to the issues of regolith maturity on these bodies and taken into account in analysis of the Dawn mission results.

**References:**

1) Basilevsky et al. (2013) Planet. Space Sci. 89 118–126. 2) Delbo et al. (2014) Nature 508, 233-236. 3) Horz et al. (1975) The Moon 13, 235–238.

# MOBILE SCIENTIFIC PLATFORM: POSSIBILITY OF DEVELOPMENT AND APPLICATION OUTLOOK

**Kozlova T.O., Kozlov O.E., Kiselev A.B., Sytenko I.N.**
*Space research institute of the Russian Academy of science, Moscow*

An automatic interplanetary station “Luna-Resource-1” is designed to explore the South Pole area of the Moon. The mission’s scientific objective is to study the local exosphere, the composition of the lunar regolith and also search for water and volatiles in the lunar subsurface.

The mobile scientific platform (MSP) is a small, autonomous and innovative moon rover of about 20kg. Use the MSP together with the Lander makes it possible to raise the contact planetary research to a new qualitative level - to switch from point study to areal surface research. It allows to accumulate statistical data as well as detailed study of the most interesting formations.

MSP allows to substantially increase the scientific data volume because of possibility to study regolith at the 100m distance from the Lander at the area of about 50 000 $m^2$, to image the objects which are not seen from the Lander, to search for water traces at the 20-30m distance from the Lander. Study of the stones which are ejected from impact craters allows to receive data of the structure of the abyssal rock. MSP will enable access to the most interesting samples and deliver them to the scientific instruments on the Lander for studying chemical and mineral composition.

MSP development follows past experience in rovers and robots design. The MSP concept has a four-wheel chassis configuration with possibility of operating autonomously or with assistance from Earth.

Cooperation with Germany and Czech specialists increases the technical level of MSP development and decreases the financial needs of every party.

# METHODS AND INSTRUMENTS FOR THE COMPLEX SPATIAL ANALYSIS OF THE POTENTIAL LANDING SITES ON THE LUNAR SUBPOLAR AREA

**A. Kokhanov[1], I. Karachevtseva[1],A. Zubarev[1], I. Nadezhdina[1], V. Patratiy[1],N. Kozlova[1], E. Matveev[1],A. Garov[1] and J.Oberst[1,2,3]**
*[1]Moscow State University of Geodesy and Cartography (MIIGAiK), MIIGAiK ExtraterrestrialLaboratory (MExLab), Gorokhovskiy per., 4, 105064, Moscow, Russia;*
*[2]German Aerospace Center (DLR);*
*[3]Technical University of Berlin,Berlin, Germany*
*Contact: i_karachevtseva@miigaik.ru*

**Introduction:**

The lunar south polar area – is the region of interests for the Russian space program, which includes several landing missions. For lunar landing site characterization concerning accuracy and safety of landing we are developing photogrammetry and geo-spatial methods.

**Developed technology and software:**

We have developed photogrammetry image processing of LRO NAC to derive high resolution DEM and orthoimages on base of PHOTOMOD software [1]. For simulating and analyzing illumination conditions for the sub-polar area we are developing the special software based on global and local DEMs and software for automatic search and preliminary estimation LRO NAC images concerning availability of stereo-pairs using its metadata.

**Used data and GIS-processing results:**

Besides various DEMs and orthomosaics at different level of detail derived from LRO cameras [2] and Kaguya TC [3], for the south sub-polar areawe have collected another data – LEND hydrogen map [4], DIVINER temperature maps [5], Mini-RF data [6], map of permanently shadowed areas [7]. We have combined all data and processed them with different spatial techniques for analyzing andto choose area on the scientific criteria and safety.

Surface roughness is a critical indicator for safety and suitability of the landing sites [8], so we have made:

- Calculation and analysis of surface roughness at various scales using DEMs [9].
- Studying of small lunar craters [10] and mapping boulders distribution [11] to determine roughness hazard.
- Mapping of slopes distribution at different bases [12].

To storage results of the studies we are developing a Planetary data server (http://cartsrv.mexlab.ru/geoportal/) with free access to data via Geo-portal [13], which now contains the results of image processing and archive lunar data for small part of Moon surface for Lunokhod-1,2 area [14]. To integrate various types of lunar mapping products we are developing spatial data model, which can provide easy and flexible access to the information system. Our lunar geodatabase can be used for support of future missions. The developing technological solutions are open-source, which makes it possible to increase the functionality.

**Acknowledgements:**

A. Kokhanov was supported by grant from the Ministry of Education and Science of the Russian Federation andthe German Academic Exchange Service (DAAD) –"Cartography support for Russian lunar missions"(№ 11.9177.2014).

**References:**

[1] Zubarev A. E. et al. (2012), [EPSC2012-477]. [2] Robinson et al., (2010) Space Sci. Rev. 150, 81-124. [3] Haruyama, J et al. (2008), Earth, Planets, and Space. № 60, pp. 243-255.[4] Sanin et al., (2012), J. Geophys. Res., 117 E00H26 [5] Greenhagen B. T. (2013), LEAG 2013, #7028. [6] Patterson and Bussey (2013) LEAG 2013, #7046 [7] McGovern et al, (2013) Icarus 223, pp. 566-581 [8] De Rosa D. (2012), PSS. 74, pp. 224-246 [9] Kokhanov et al., 2013 Mod. probl. remotesens. of the Earth from Space №10. pp. 136-153 (in Russian). [10] Basilevsky et al., (2014) PSS, 92. pp. 77-87. [11] Kokhanov et al., (2012) [3MS3-PS-09]. [12] Kokhanov et al., (2013) ICC-26 abs. #1148.[13] Karachevtsevaet al., (2014), PSS, special issue "Phobos book"http://dx.doi.org/10.1016/j.pss.2013.12.015[14] Kozlova et al., (2014) ISPRS Archives MTSTC4-2014-103, Volume XL-4, 2014, pp. 121-126.

# LANDING SITE SELECTION FOR LUNA-GLOB MISSION IN CRATER BOGUSLAWSKY

**M.A. Ivanov[1], H. Hiesinger[2], A.M. Abdrahimov[1], A.T. Basilevsky[1], J.W. Head[3], J-H. Pasckert[2], K. Bauch[2], C. van der Bogert[2]**
*[1]Vernadsky Institute RAS, Kosygin St., 19, Moscow, Russia,*
*[2]Muenster University, Muenster, Germany, [3]Brown University, Providence, RI USA, Contact: Mikhail_Ivanov@brown.edu*

## Introduction:

Crater Boguslawsky (73°S, 43°E, about 100 km in diameter) is the target of the Russian, lander-oriented, Luna-Glob mission to the Moon. The lander-oriented mission Luna-Glob is aimed to study physical conditions and composition of regolith in a region near the South Pole of the Moon (http://www.lg.cosmos.ru) and to test new generation of technologies for soft landing. The Luna-Glob lander should carry a suite of instruments to study the surface chemistry and mineralogy, including signatures of volatiles: neutron and gamma spectrometer, mass-spectrometer and IR spectrometer added by several TV cameras (http://www.lr.cosmos.ru/devices).

## Primary landing site characteristics:

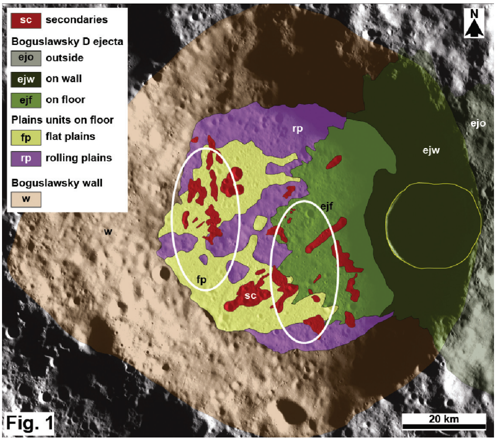


Two ellipses, 30 by 15 km each, were selected on the floor of the crater as the primary landing areas: the western ellipse is centered at 72.9°S, 41.3°E and the eastern ellipse is centered at 73.9°S, 43.9°E (Fig. 1).

The crater is located within elevated and heavily cratered terrain, which likely represents a portion of the southern rim of the SPA basin [Wilhelms et al., 1979]. Neither Boguslawsky itself nor its close surroundings show evidence for the suppression of the neutron flux from the surface [Mitrofanov et al., 2012]. This means that in this region the possible accumulation of hydrogen-bearing phases in regolith (i.e., ice, water-bearing minerals, etc.) are below the background level of hydrogen concentration [Feldman et al., 2000]. Thus, the other types of materials that can be sampled at the landing point should be considered as the main goal of the mission. Specifically, these are materials that form the SPA rim and likely represent some of the oldest rocks on the Moon, which existed prior to the SPA impact event.

## Materials on the floor of Boguslawsky:

The low depth/diameter ratio of Boguslawsky suggests that the crater has been partly filled after its formation. The nature of the filling materials is very important for the selection of a specific landing point on the floor of Boguslawsky. Although volcanic flooding of the crater is plausible, the more likely process of filling of Boguslawsky is the emplacement of ejecta from remote large craters/basins. Three morphologically distinctive units are the most abundant within the selected landing ellipses: rolling plains (rp), flat plains (fp), and ejecta from crater Boguslawsky-D (ejf), which is on the eastern wall of Boguslawsky.

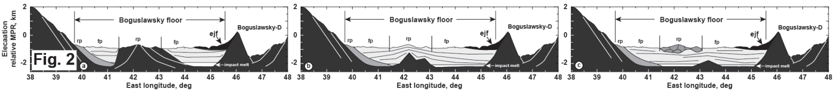


In Figures a-c, the interior of Boguslawsky is filled either by remote ejecta (more likely), or volcanic materials (less likely), or both. In any case, ejecta from Boguslawsky-D (ejf) represent local materials that are the most desirable for sampling.

The possible structure of the crater interiors (Fig. 2) suggests that smooth plains and rolling plains in the center of the floor are related to ejecta from remote and unknown sources. Such a possible nature of these units makes them to be less desirable targets for landing because analyses of these materials may cause large uncertainties in interpretation of the results. In contrast, ejecta from

Boguslawsky-D represent local materials re-distributed by the Boguslawsky-D impact from the wall onto the floor of Boguslawsky. Thus, this unit, which makes about 50% of the eastern landing ellipse, represents a target of higher scientific priority.

**Safety of landing:**

Analysis of the frequency distribution of the surface slopes at the 30-m baseline shows that the Boguslawsky-D ejecta have about the same percentage of slopes smaller than 7° (94%) as flat plains in both landing ellipses (97-98%). The 7° slopes are considered as the upper safety limit for landing. Thus, the Boguslawsky-D ejecta represent almost as safe target as the most horizontal unit of flat plains and satisfy the safety constraints of the mission.

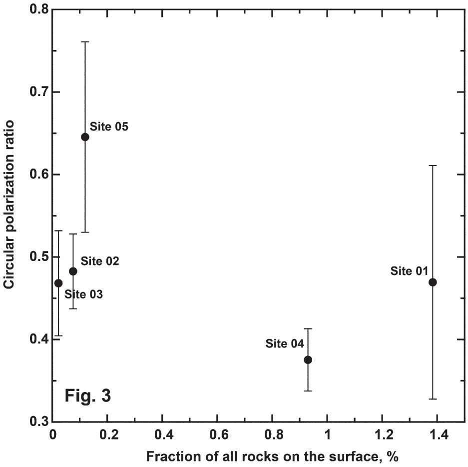


**Fig. 3.** The values of the circular polarization ratio do not correlate with the rock abundance on the surface

Large boulders (larger than ~0.5 m) exposed on the surface are very serious threats to landers. The values of circular polarization ratio characterizing the Boguslawsky-D ejecta are the largest and, thus, this unit is among the rockiest ones within the landing ellipses. In our investigation, however, we have found no correlation between the CPR values and density of rocks on the surface. (Fig. 3).

Inspection of high-resolution NAC images demonstrated that the surface of the Boguslawsky-D ejecta is essentially rock-free and the main contribution to the CPR signal is from rocks that are below the surface. The higher concentration of rocks from the Boguslawsky wall in the subsurface of the Boguslawsky-D ejecta makes this unit an even more desirable target because local materials, which likely represent rocks of the SPA rim, could be accessed and analyzed relatively easily in this area.

**Conclusion:**

Interpretation of the possible nature of units within the landing ellipses and the results of the analysis of the spatial and size-frequency distribution of the surface slopes and boulders indicate that the ejecta from Boguslawsky-D crater represent a target of high scientific importance that is completely within the safety restrictions of the Luna-Glob mission.

**References:**

Wilhelms et al., Geologic map of the South Side of the Moon. US Geological Survey Map I-1192, 1979.
Mitrofanov et al., 2012, GJR, 117, E00H27, doi:10.1029/2011JE003956, 2012.
Feldman et al., GJR, 105, 4175-4195, 2000

# USING THE MOON AS A STEPPING STONE TO REACH OTHER PLANETS

**R. R. Chau, A. A. Mardon,**
*[1]The Antarctic Institute of Canada, 11919-82 Street NW, Edmonton, Alberta, Canada;*
*[2]The Antarctic Institute of Canada, 11919-82 Street NW, Edmonton, Alberta, Canada.*
*Contact: aamardon@yahoo.ca*

**Introduction:**

The moon would provide a much more economic rocket launching surface than the earth because of the difference in gravity and atmosphere. It is well know that the moon has a reduced gravity because of its mass, density and volume relative to the earth considering the moon has a gravity field only 16.6% of the earth's gravity field [1]. However, most values given only provided an average gravity rating as if the moon was a perfectly round sphere with no inconsistencies. New mapping provided by the GRAIL satellites give new maps of free-air and Bouguer gravity anomalies on the surface of the moon [2]. This new data can be used accordingly to find appropriate sites to launch spacecraft and other satellites from the surface of the moon.

**References:**

[1] Earth's Moon:  Facts & Figures.
(n.d.). In Earth's Moon: Facts and Figures. Retrieved July 22, 2013
[2] Maria T. Zuber et al. (2013) Gravity Field of the Moon from the Gravity Recovery and Interior Laboratory (GRAIL) Mission. Science, Vol. 339 no. 6120, pp. 668-671.

# HUMAN EXPLORATION OF THE MOON: A SCIENCE AND ENGINEERING SYNERGISM ROADMAP FOR THE FUTURE

**J.W. Head, III[1],D.R. Scott (Apollo 15 Commander)[1], J.A. Hoffman (STS Astronaut; STS-35, 46, 51-D, 61, 75)[2],**

*[1]Dept. of Earth, Environmental and Planetary Sciences, Brown University, Box 1846, Providence, Rhode Island, 02912, USA;*

*[2]Dept. of Aeronautics and Astronautics, Massachusetts Institute of Technology, Cambridge, MA 02139 USA*

*Contact: james_head@brown.edu*

**Introduction:** New data from the Renaissance period in lunar exploration, combined with a firm foundation of results from human and robotic Apollo and Luna mission, have provided a wealth of experience in science and engineering synergism and paved the way for new scientific destinations and engineering challenges and capabilities. High spatial and spectral resolution information together with high-resolution altimetry and gravity have revealed new minerals and rock types, as well as helping to define the locations of concentrations of these types of key deposits that can help in unraveling crustal history and the nature of the geologic processes (impact cratering, volcanism, tectonism, volatile migration and sequestration) that have influenced lunar evolution.

**Science Requirements and Legacy:** These findings have permitted scientists to define basic science-engineering requirements for future lunar exploration systems: these include full lunar access, longer stay times, extended surface mobility, enhanced down-mass and up-mass, robotic network development, communications and exploration infrastructure (communication and GPS spacecraft), orbital assets, and a mix of optimized human and robotic exploration. Furthermore, these results have clarified the focus and legacy of lunar exploration: The long-term goal is two-fold: 1) to understand the origin, evolution and future of the planetary bodies in our Solar System, including our Home Planet Earth, and 2) to derive an understanding of how to live and survive, and where to go, in the habitable zone of our own Solar System. In the words of Apollo 16 Commander John Young: “Single-planet species don’t survive.” On the basis of lunar exploration to date, we now know *where* to go and *what* to do to accomplish these objectives, starting with the Earth’s Moon. Examples include:

1) *In-Depth Exploration*: Target more extensive exploration around existing exploration sites (e.g., the Apollo 15 Hadley-Apennine Landing Site) (Fig. 1) to address the new questions raised by analysis of initial data collected on Apollo 15. What is the history of the lunar magnetic field recorded in the rille wall basalt layers? What is the source of the water-rich green pyroclastic glasses? What is the diversity of deep crustal rock types, as revealed by the 15415 anorthosite? What is the nature of the layering revealed in the Apennine Mountains Silver Spur? What is the distribution and variety of Imbrium basin ejecta as seen in the ancient 15455 shocked norite? What is the diversity of ages and compositions of the mare basalts exposed in the rille walls?

2) *New Exploration Destinations*: Target new sites such as the polar regions, and the floor and central peaks of Theophilus and Copernicus and ask new questions: What is the origin and distribution of water in the polar and non-polar regions? What is the distribution and nature of shocked and unshocked rocks in central peaks? What is the distribution and origin of olivine-rich rocks in central peaks and did they come from the lunar mantle? What is the mode of occurrence and origin of newly discovered spinel-rich lithologies? What are the relationships and relative abundances of shocked and unshocked anorthosite in central peaks? What does the chilled boundary layer of a melt sheet look like and how different is it from more slowly cooling melt below? How diverse are impact melt compositions and how much vertical segregation (differentiation?) is observed? Has the lunar mantle been sampled and what is its depth and composition? What are the implications for the early Earth and the formation, evolution, and future of other planetary bodies?

**Science and Engineering Synergism: Design Reference Missions:** Definition of engineering requirements is insufficient in itself for success; scientists must work hard to engage engineers in understanding their needs (and vice versa) and developing Science and Engineering Synergism (SES) where mutual bottom-up interactions and education lead to optimized plans and exploration results. A very productive way to develop SES is in the combination of scientific goals and engineering reality in Science Design Reference Missions (DRM). In order to address these questions we have been engaged in interactions between students and faculty at Brown University (Planetary Geoscience Group of the Department of Geological Sciences and School of Engineering) and the Massachusetts Institute of Technology (MIT) Department of Aeronautics and Astronautics as part of our NASA Solar System Exploration Research Virtual Institute (SSERVI) activity. Through meetings, seminars and “project/program reviews”, planetary scientists have helped define their dreams while engineers have come up with innovative approaches to realizing these dreams. The shoulder-to-shoulder interactions build on the success of Apollo and have produced DRMs that are innovative and considerably under the costs of recent human exploration defined by the Space Exploration Initiative, for example.

An example of such an approach is the study “Human Architecture for Lunar Operations (HALO): Orbits &Architecture for Global Access” (Nicholas et al., 2013) (Fig. 2). This Human Architecture for Lunar Operations proposes a new set of space vehicles and orbital maneuvers which support human missions to the lunar surface. Using the Apollo lunar orbit rendezvous architecture as a baseline, HALO incorporates many advancements in space technology since the 1960’s to increase the capabilities and scientific return. In a novel improvement, they propose using a highly elliptical polar lunar orbit (EPLO) before and after the surface phase to drastically reduce the required propellant for plane changes and nearly eliminate the sensitivity of the propellant mass to the landing site location. This allows for global access using a single, efficient system. In this scenario, this orbit would be entered directly from the trans-lunar orbit and the vehicle that remains in lunar orbit would reside there while the landing vehicle conducts the surface operations. As part of this study, Nicholas et al (2013) provide a full description of the architecture, its restructured vehicle set, and its advantages, as well as an analysis of EPLO stability to verify feasibility. Such bottom-up student-led initiatives are the breeding ground for a successful return of humans to the Moon with innovative solutions to address compelling scientific problems.

**Conclusions:** These types of scientific questions and Science Design Reference Missions can take advantage of 40 years of technology and operations development since the very successful Soviet and United States exploration missions to formulate new and enhanced exploration concepts. These new developments permit Lunar Human Exploration DRMs that produce longer stay times, more diverse mobility options, increased mobility and exploration radius, significantly more down-mass and up-mass, improved robotics to free up astronaut time for human exploration optimization, and full lunar access. These DRMs underline this new generation of lunar exploration capabilities, and show how a program of integrated human and robotic exploration using our combined experience, can lead to fundamental new insights into living, exploring and surviving in the habitable zone for the upcoming millennia.

# THE INFLUENCE OF FROZEN WATER UNDER THE SURFACE ON DUST MOTION IN THE LUNAR POLAR REGIONS

**N.D.Borisov[1], A.V.Zakharov[2]**
*[1]IZMIRAN, [2]IKI RAN*

It is argued that frozen water is present under the surface in the lunar polar regions. Possibly in the permanently shadowed craters ice exists even very close to the surface while for partly illuminated regions ice can be found at some depth. Almost everywhere the lunar regolith has extremely small electric conductivity. But the conductivity of the regions where ice is present is many orders of magnitude higher. This factor should be taken into account while discussing the motion of dust. Usually it is accepted that dust grains move above the surface of the Moon under the action of electric forces. To overcome the gravity electric fields should be very strong. Due to this electric current in the regolith in general case has to be taken into account because it contributes to the continuity of the total current. Such effect could be especially significant in the vicinity of permanently shadowed craters with frozen water due to high electric conductivity of the regolith. In relation with the forthcoming Russian lunar missions we discuss in what cases the frozen water under the surface restricts significantly the magnitude of the electric field. As a consequence the motion of dust grains above such regions should be suppressed. This effect can be used as an indication of the presence of frozen water under the surface.

# THE CONCEPT OF SEPARATE CHARGING AND DISCHARGING ENERGY-DEPENDENT WORK FUNCTIONS BASED ON EXPERIMENTAL AND SIMULATION CIRCULATING-LOOP ANALYSIS OF GRANULAR MATERIALS PROPERTIES AND CHARGE STATE

**Mark Koepke[1], Jonathan Tucker[1,2],Sofiane Benyahia[2], Lawrence Shadle[2], Alan Bristow[1]**
*[1]West Virginia University, Morgantown, WV, USA;*
*[2]National Energy Technology Laboratory, Morgantown, WV, USA;*
*Contact: mkoepke@wvu.edu*

Electrostatic charging in gas-solid multiphase fluid systems is a long standing problem thatremains poorly understood despite its potential to create safety hazards such as electrostatic discharges and explosions. A new laboratory facility is being developed for electrostatics and hydrodynamics research related to particle science and technology and to dusty lunar/martian regolith, surface, and atmosphere. The goal is to develop multi-scale models connecting micro- and nano-scale phenomena and properties with process-level variables. In anticipation of the future facility, a fundamental-level investigation of electrostatic charging behavior was carried out to improve our interpretation of observationsand identify the important variables.The results of the investigation provide better insight into the magnitude and directionality of the charging and discharging processes, which appear to be dependent upon separate charging and discharging energy-dependent work functions.  Discrete-element modeling that monitors collisional interaction energy reinforces this insight. We focus on the effects of the materials properties and operating conditions on the particle charging. Speculations on functional expressions of the work functions that are presumed to govern charge magnitude are presented from the data collected. A secondary focus of this study is evaluating methods to reduce or utilize the charges generated by the system. Other outcomes include (a) establishing a consistent foundation for materials characterization across projects, (b) reducing the characterization to five man-hours from start to finish, (c) including over 75 materials in the database, (d) achieving reproducibility and repeatability and further additional uncertainty reduction by internal cross-checking, and (e) granting public access to the processed and raw data.Support for author MK from the DOE grant DE-SC0001939 Plasma Science Center on Predictive Control of Plasma Kinetics: Multi-Phase and Bounded Systems and NSF grant PHYS-0613238 is gratefully acknowledged. Author JT gratefully acknowledges useful discussions with Kenneth Showalter.

# FINE-DISPERSED PARTICLES AND DUSTY PLASMAS AT THE MOON

**S. I. Popel, A. P. Golub, G. G. Dolnikov, A. Yu. Dubinskii, Yu. N. Izvekova, S. I. Kopnin, A. V. Zakharov, L. M. Zelenyi,**
*Space Research Institute RAS, 84/32 Profsoyuznaya Str., Moscow 117997, Russia. Contact: popel@iki.rssi.ru*

Here, we review the results on dusty plasmas over the Moon and formulate problems concerning the dusty plasma over the lunar surface. We discuss the lunar exosphere which is an important example of a dusty plasma system in nature. A powdery dust that levitates over the Moon is a constituent of the lunar exosphere. The discovery of the lunar dust was made in post-sunset Surveyor lunar lander TV camera images of the lunar horizon. These Surveyor images revealed the presence of a near-surface (*e.g.*, scale height of ~10-30 cm) glow. This effect was related to sunlight scattering at the terminators giving rise to "horizon glow" and "streamers" above the lunar surface. Subsequent investigations have shown that the sunlight was most likely scattered by electrostatically charged dust grains originating from the surface. During the Apollo missions 0.1 μm-scale dust was observed up to about 100 km altitude. A renaissance is currently being observed in investigations of the Moon, which are planned in the People's Republic of China, United States, Russia, India, and European Union. The Luna-25, Luna-26, Luna-27, Luna Sample Return, etc. missions are under preparation in Russia. The landing modules of the Luna-25 and Luna-27 spacecrafts are planned to be equipped with instruments for studying the properties of the dusty plasma over the surface of the Moon. The dusty plasma is studied by means of observations from the orbit of the US LADEE (Lunar Atmosphere and Dust Environment Explorer) launched in 2013. Fig. 1 presents schematically the main elements characterizing the dusty environment over the Moon [1 – 5].

The lunar surface is charged under the influence of the solar electromagnetic radiation, the solar wind plasma, and the plasma of the terrestrial magnetosphere tail. Upon interacting with the solar radiation, the lunar surface emits photoelectrons due to the photoelectric effect. This leads to the emergence of a layer of photoelectrons above the surface. Additional photoelectrons are emitted by the dust particles levitating above the lunar surface when these particles interact with the solar electromagnetic radiation. The dust particles located on the lunar surface or in the near-surface layer absorb photoelectrons, photons of the solar radiation, electrons and ions of the solar wind, and (if the Moon is

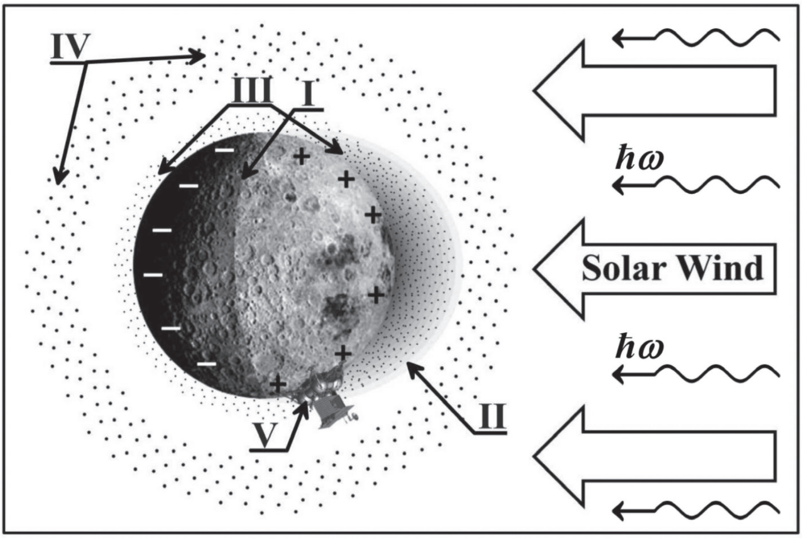


**Fig. 1.** The main elements characterizing the dusty plasma system over the Moon (the terminator (I), the photoelectrons (II), the near-surface dust particles (III), dust particles at high altitudes (IV), photons of solar radiation ħω, and the solar wind) as well as the lunar lander at a high lunar latitude in the South Hemisphere (V).

located in the terrestrial magnetosphere tail) electrons and ions of the magnetosphere plasma. All these processes promote charging of the dust particles, their interaction with the charged lunar surface, and the dust levitation and motion.

To explain the presence of submicron grains at altitudes of about 100 km the so-called dynamic fountain model for lunar dust has been proposed by [6]. Within this model it is possible to predict that a lunar orbiting spacecraft with a charged dust detector would observe very small (10 nm) positively charged grains and larger (10 to 100 nm) negatively charged those around the terminator region. However it appears that submicron dust grains could contaminate astronomical observations of infra-red, visible and UV light over the majority of the lunar surface, and not just at the terminator. Thus the dynamic fountain model for lunar dust is one of many ways in which dust could interfere with science and exploration activities on the Moon. Furthermore, the dynamic fountain model can predict only the maximum heights reached by dust grains. It does not give the values of a number for the dust particles above the Moon. To obtain the corresponding number one has to consider physical processes which are not taken into account in the dynamic fountain model.

Another phenomenon which can be responsible for an appearance of dust particles at high altitudes (of the order of 100 km) is related to impacts of meteoroids or man-made projectiles with the surface of the Moon [7]. The evolution of the impact plume can lead to the formation of charged particles. One type of the particles (small droplets) is created as a result of the process of condensation which takes place during the expansion of the vapor plume. The period of the formation of the centers of condensation is very short and all droplets have approximately the same size. The droplets move together with the substance of the plume. Their speed exceeds often the first astronautical velocity for the Moon, 1.68 km/s, and the droplets will not fall down the surface of the Moon. Moreover, the droplets with the speeds between the first and second astronautical velocities, *i.e.*, between 1.68 and 2.38 km/s, perform finite movement around the Moon. One can expect [3] an appearance of $\sim 3.6 \cdot 10^9$ particles (with the sizes of about 100 nm) per second from the lunar surface, the particles rising rather high altitudes (*e.g.*, about 100 km) over the lunar surface. This shows that the effect of condensation of micrometeoriod substance after impact can be important from the viewpoint of explanation of dust particle rise to high altitudes. The implicit confirmation of this effect is given by the observations performed by the US LADEE [8] where it was shown that the velocities of dusts at the altitudes of 30 to 110 km over the lunar surface are of about the first astronautical velocity for the Moon.

There are unsolved problems concerning dusty plasma parameters over the Moon and dusty plasma manifestations. Here we outline some of the problems which can be important for detailed study of the dusty plasma over the lunar surface.

**The quantum photoemission yield and work function of lunar regolith.** Unfortunately, the quantum yields are insufficiently justified [5]. This indicates the necessity of the determination of the quantum yield (and the work function) for lunar regolith directly on the Moon. This possibility can be provided within the future Luna-27 mission.

**Influence of implanted hydrogen on photoemission properties of lunar regolith.** Recent data from the Lunar Reconnaissance Orbiter [9] show the existence of hydrogen-enriched regions in the surface layer of the Moon at lunar latitudes exceeding 70$^{o}$ in the Southern Hemisphere. The sensitivity of the hydrogen-enriched regions of the surface of the Moon to photoemission can be much higher than that of surrounding regions [2]; this finally affects the charging of dust particles, their dynamics, and properties of the dusty plasma system over the lunar surface.

**Release of dust particles from the lunar surface.** Significant uncertainty exists as to the physical mechanism through which dust particles are released from the surface of the Moon. Adhesion has been identified as a significant force in the dust particle launching process which should be considered in future attempts to understand particle launching methods. The mechanisms of dust particle release from the lunar surface require further investigations.

This work was carried out as part of the Russian Academy of Sciences Presidium program no. 22 “Fundamental problems of Research and Exploration of the Solar System” and was supported by the Russian Foundation for Basic Research, project no. 12-02-00270-a. S.I. Kopnin acknowledges the financial support of the RF President Grant Council for support of young scientists and leading scientific schools (grant no. MK-3764.2013.2).

# NON-MONOTONIC POTENTIALS ABOVE THE DAY-SIDE LUNAR SURFACE EXPOSED TO THE SOLAR RADIATION

**T.M. Burinskaya**
*Space Research Institute RAN*

Basic equations describing stable non-monotonic altitude profiles of the electric potential arising near the Moon's surface due to the joint action of solar ultraviolet radiation and interactions with the plasma environment are obtained for two cases: the surface is in the solar wind and the surface is exposed to the terrestrial plasma sheet. The influence of the solar wind on the non-monotonic potential is investigated in a wide range of drift velocities for different values of the photoelectron density. It is found that for any photoelectron density the surface potential reaches its minimum value for a slow solar wind. This effect is most pronounced for the lunar regolith regions not enriched with hydrogen. When the Moon is exposed to both solar radiation and the terrestrial plasma sheet, the surface potential and the potential minimum are calculated as functions of the ion and electron temperatures for different values of the photoelectron density. It is shown that both potentials depend strongly on the temperature of plasma sheet populations, particularly in the range where the ratio of the ion temperature to the electron temperature is less than three. The obtained results can be used to study the dynamics of lunar dust grains under the condition that the total charge density of all dust grains is lower than the charge density of the ambient plasma.

# RELATION BETWEEN THE CHARGE/DISCHARGE PROCESSES OF DUST PARTICLES AND THE DYNAMICS OF DUST CLOUDS OVER THE MOON SURFACE

**E.V. Rosenfeld[1], A.V. Zakharov[2]**
*[1]Institute of Metal Physics, Ural Branch of the Russian Academy of Sciences, Ekaterinburg, Russia rosenfeld@imp.uran.ru*
*[2]Space Research Institute, the Russian Academy of Sciences, Moscow, Russia*

The formation of a double layer of photoelectrons (DLP) over the surface of atmosphereless bodies is discussed. It is shown that using the usual value of the photocurrent density $j_{ph} \approx 5\ \mu Am^{-2}$ for the Moon, the "charging time" for a solitary dust particle of radius $r$ (i.e. the time until formation of the DLP over its surface) varies from ten seconds for $r \approx 1$nm to tens of minutes for $r \approx 10$nm.On the other hand, the formation time of DLP over a flat surface is no more than a few microseconds. This difference arises from the sharp distinction between the charge density on the surface of equipotential spheres of different grain radii. As a result, the amount of charge of a solitary dust particle $q_{alone}=4\pi\varepsilon_0 rV$ ($|e|V$ is the energy of the ejected photoelectron) is by many orders of magnitude greater than the charge of the same dust particle lying on a flat surface $q_{surf} = 2\pi r_d^2 \sqrt{\varepsilon_0 j_{ph}} \left( \frac{m_e}{2|e|} \right)^{\frac{1}{4}} V^{\frac{1}{4}}$. At the same time, the charge $q_{surf}$ is too small in order that the electric field of the DLP appearing above the surface could raise the dust particle.

To acquire the charge of the order of $q_{alone}$, sufficient for levitate a dust particle should initially soar someway to such a height that the required number of photoelectrons would be ejected during the flight. Initially this might occur, for example, when a meteorite hitting the surface. However, in order to raise above the surface each time at dawn, the dust must maintain the positive charge accumulated during the day throughout the lunar night. If the fountain mechanism actually operates on the moon, it is the prerequisite. Therefore there is a need to ascertain how could persist the positive charges on the surface bombarded by a stream of solar wind electrons at night. In this regard, some problems of electric field shielding by fast-moving stream of collisionless plasma are discussed in the report as well.

# ON THE DUST MATTER IN THE NEIGHBORHOOD OF THE LAGRANGE LIBRATION POINTS

**T.V.Salnikova[1], S.J.Stepanov[2],**
*[1]Lomonosov Moscow State University, GSP-1, Leninskie Gory, 19991, Moscow, Russia,*
*[2]Dorodnitsyn Computing Center, Vavilov str., 40, 119333, Moscow, Russia.*
*Contact: tatiana.salnikova@gmail.com; stepsj@yandex.ru*

According to the criterion of the stability, the triangular libration points of the Earth-Moon system are stable in Lyapunov sense. There were indications on the existence of the clouds of interplanetary dust in the neighborhood of these libration points, discovered by polish astronomer K.Kordylevski. [1,2]. More then 50 years after the first observation even the existence of the elusive clouds is stil disputed. In view of the unavoidable perturbations — such that the influence of the Sun, the existence of the dissipative forces, destroying the gyroscopic stability, and many others, the triangular libration points must be unstable.

Let's consider an ensemble of N particles of the same mass, represented by their position in the neighborhood of the Lagrange libration points. If all particles have the same probability distribution, are independent and do not interact pair-wise, but only globally, one can reduce the dimension of the phase space: the system is statistically equivalent to a test particle of a mass M at position (x,y), with velocity (u,v), described at any time (t) by a distribution function f(x,y,u,v,t), satisfying to the Liouville equation.

We study the four body problem: Earth, Moon, Sun and a test particle. Only planar problem is under consideration, because the influence of the Sun on the test particle beyond the plane of the circle motion of the Earth and the Moon around their centre of mass is sufficiently small. Centre of mass is considered to move along the circular orbit around the Sun.

Analytical investigations of the periodic solutions close to the Lagrange libration points were made in [3,4] and others (see review in [5]). We prove a theorem about the existence of a periodic solution, using a method suggested by Hölder and later developed by Lewis [6] and others. The main attention is paid to the selection ofthe generic solution of the unperturbed problem. Then the boundary problem for the perturbed system has been investigated.

The periodic solution has been found numerically, using the monodromy matrix. According to Routh-Hurwitz criterion, this motion is stable in Lyapunov sense in linear approximation. The numerical experiment also shows the stability for the non-linear case. For small perturbations of the initial conditions, we get a one-parametric family of the invariant tori, capturing the periodic solution. These tori possibly represent the dust cloud, moving around the Lagrange libration point. The best conditions to observe this cloud are in the second quarter of the Moon phase, when the cloud is closer to the Earth and well illuminated by the Sun in the region, rather shifted from the libration point.

**References.**

[1] K.Kordylewski, Photographische Untersuchungen des Librationspunktes im System Erde-Mond. ACTA ASTRONOMICA Vol.11. (1961) n.3.
[2] J.Wesley Simpson, Dustcloud moons of the earth. Physics Today 20(2), 39 (1967).
[3] Kamel A.A., Perturbation theory based on Lie transforms and its applications to the stability of motion near Sun-perturbed Earth-Moon triangular libration points. Nasa, CR 1622, 1970.
[4] Schlechter H.B., Three-dimensional nonlinear stability analysis of the Sun-perturbed Earth-Moon equilateral points. - AIAA Journal, 1968, vol. 6, n. 7.
[5] Markeev A.P., Libration points in celestial mechanics and cosmodynamics. M. Nauka, 1978, 312 pp.
[6] D.C.Lewis, On the role of the first integrals in the perturbation of periodic solutions. Annals of Mathematics. Vol. 63, n. 3, 1956.

# POLISH CONTRIBUTION TO ESA JUICE MISSION (RPWI). DUSTY PLASMA AND TURBULENT PLASMA INVESTIGATIONS AS A TOOLS FOR DIAGNOSTIC SPACE WEATHER CONDITIONS

**B. Atamaniuk[1] , H. Rothkaehl [1], R Schreiber [1] , A.S. Volokitin[2,3]**
[1]*Space Research Centre PAS, Bartycka 18A, 00-716 Warsaw, Poland*
[2]*Inst. of Terrestrial Magnetism, Ionosphere and Radio Wave Propagation,RAS, Troitsk, Moscow, Region, 142190, Russia,*
[3]*Space Research Institute RAS, 84/32 Profsoyuznaya Str, Moscow, Russia.*
*Contact: batama@cbk.waw.pl*

The JUICE mission was selected by ESA in May 2012, as a first large mission within the Cosmic Vision Program 2015–2025.

The Radio & Plasma Waves Investigation (RPWI) consists of a highly integrated instrument package that will carry out measurements that allow for comprehensive science investigations of the space environments around Jupiter primarily near Ganymede, Europa and Callisto, as well as monitoring radio wave emissions in the Jupiter system.

I present the overview of our knowledge about the dust and dusty plasma in the Jovian system and the main concept of JUICE (JUpiter ICy moon Explorer) mission.

Then I concentrate on  the Radio & Plasma Waves Investigation ( RPWI) selected for implementation on the JUICE mission. RPWI consists of a highly integrated instrument package that provides a whole set of plasma and fields measurements.

The RPWI would be able to study:  wave polarization; electric fields of structures and waves responsible for accelerating charged particles; dust distribution (above about 1 μm size); Signatures of dust plasma interactions.

# REFLECTANCE OF INTERPLANETARY DUST PARTICLES INFERRED WITH THE UMOV EFFECT

**E. Zubko[1], G. Videen[2], Yu. Shkuratov[1],**
*[1]Institute of Astronomy, V.N. Karazin Kharkov National University, 35 Sumskaya St., Kharkov, 61022, Ukraine;*
*[2]Space Science Institute, 4750 Walnut Street, Boulder Suite 205, CO 80301, USA.*
*Contact: evgenij.s.zubko@gmail.com*

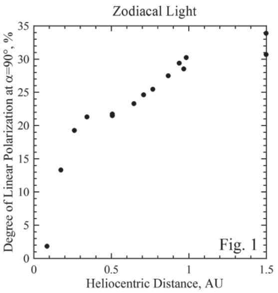


**Introduction:**

Ground-based observations of Zodiacal light reveal a strong dependence of the polarimetric response from interplanetary dust particles (IDPs) on their heliocentric distance *R*. For instance, Fig. 1 demonstrates the degree of linear polarization *P* measured in IDPs at a phase angle $\alpha$ = 90° (data are adapted from [1]). One can see, an increase of the distance to the Sun results in an increase of the linear polarization by an order of magnitude, from $P \approx 2\%$ at $R$ = 0.1 AU to $P > 30\%$ at $R > 1$ AU. This unambiguously suggests different physical and/or chemical properties of IDPs at various distances to the Sun.

Note, the degree of linear polarization in IDPs also varies with phase angle $\alpha$, whereas in the range $\alpha \sim 90°$, the polarization attains a maximum value $P_{max}$ [1]. Therefore, the observations presented in Fig. 1 can be attributed to the maximum of polarization $P_{max}$. However, $P_{max}$ inversely correlates with the geometric albedo *A* that is equal to the ratio of the intensity of light backscattered from a target particle to what is scattered from a white Lambertian disk having an equivalent geometrical cross section [2 and references therein]. This interrelation is an extension of *the Umov effect,* which is a long-known property in the optics of regoliths, for the case of single-scattering micron-sized particles. Here, we apply the extended Umov effect for analysis of polarimetric observations of IDPs and a quantitative retrieval of their reflectance.

**Technique for Numerical Simulation of Light Scattering from IDPs:**

In modeling of light scattering from IDPs, we exploit the so-called *agglomerated debris particles*. These model particles were developed to simulate cometary dust particles and, as was found in [3] and references therein, they can satisfactorily reproduce the photometric and polarimetric observations of comets. We also refer to [3] for a detailed description of the generation algorithm of agglomerated debris particles. Six example particles are shown on the top in Fig. 2. The model particles have an agglomerate and highly irregular morphology with packing density of constituent material being about 24%. In an assumption of organics, carbonaceous, or silicate composition, the bulk material density of the agglomerated debris particles spans the range from 0.35 to 0.83 g/cm$^3$. This is consistent with the findings in a laboratory study of IDPs that revealed an abundance of particles with the density ~0.7 g/cm$^3$ [4]. The application of agglomerated debris particles to IDPs also is validated from the predominantly cometary origin of IDPs [5].

We compute light scatteringing from agglomerated debris particles with the *discrete dipole approximation* (DDA). This is a flexible technique that places minimum limitations on target particle shape (see e.g., [6] and references therein). The light-scattering response in micron-sized particles is dependent on two parameters: the complex refractive index *m* and the size parameter *x*. The complex refractive index *m* relates the chemical and mineral composition of the particle material and its ability to scatter and absorb light. We consider 17 different refractive indices (see legend in Fig. 2) that can be relevant to comets (see discussion in [3]) and, therefore, IDPs. The size parameter quantifies the ratio of the particle size to wavelength $\lambda$: $x = 2\pi r/\lambda$, where *r* is the radius of the circumscribing sphere about the agglomerated debris particle. For each refractive index, we compute a wide range of the size parameter from $x$ = 1 to 32 (50 at $m = 1.2 + 0i$, $1.2 + 0.015i$, and 1.313 +0i; 26 at $m = 1.7 + 0i$). At $\lambda$ = 0.5 $\mu$m, the range of *x* corresponds to radius of agglomerated debris particles from $r$ = 0.08 $\mu$m to 2.55 $\mu$m (3.98 $\mu$m and 2.07 $\mu$m). Light-scattering properties are averaged over a minimum 500 particle shapes, and we also average light-scattering properties over particle size using the power-law size distribution $r^{-a}$, and consider index $a$ to range from 2 to 4.

**Results and Discussion:**

The results are presented in Fig. 2. Here the logarithm of the polarization maximum $P_{max}$ is plotted versus the logarithm of the geometric albedo $A$. This form of result presentation is reasoned in [2]. The results are grouped into three panels according to the material absorption. From left to right the imaginary part of refractive index Im($m$) increases from 0 to 0.05. Each curve represents the variation of the index $a$ in the power-law size distribution from 2 (the down end of curve) to 4 (the up end of curve). For convenience, we also demonstrate three levels of the degree of linear polarization $P$ = 10%, 20%, and 30% with dashed lines.

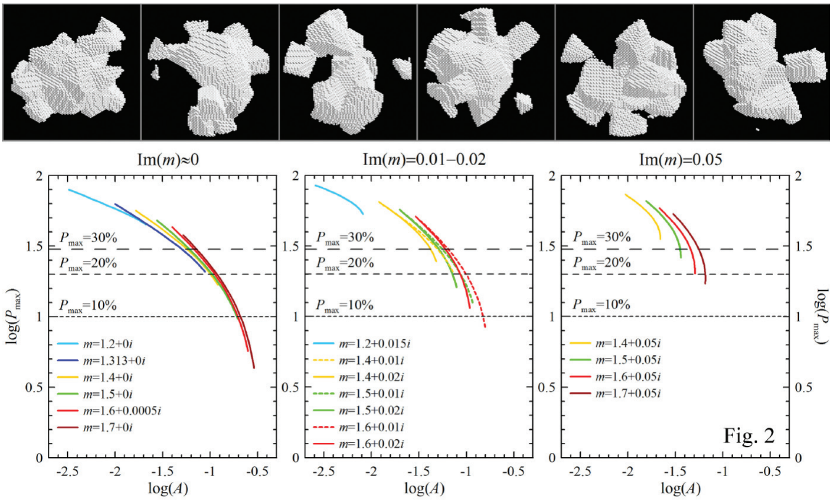


As one can see in Fig. 2, the spatial variations of the polarization in IDPs can be formally attributed to different values either in the power index $a$ or in the material absorption Im($m$). However, within the former scenario, the observations can be reproduced only at weak material absorption Im($m$) ≤ 0.01 and, simultaneously, a relatively high real part of refractive index Re($m$) ≥ 1.6. It is important to stress that these constraints do not agree with a relatively high content of carbon in IDPs sampled in the Earth stratosphere, ~13% by weight or ~50% by volume [7]. Thus, the spatial variations of the polarization unambiguously indicate large-scale chemical heterogeneity in the cloud of interplanetary dust. In the vicinity of the Sun (< 0.2 AU), IDPs lack carbonaceous materials; whereas, an increase of the heliocentric distance is accompanied with a growth of content of carbonaceous materials. This can be explained by evaporation of carbonaceous materials at small heliocentric distances. However, it also can be explained by different impact of radiation pressure on weakly and highly absorbing particles. Discrimination between these two explanations is a subject for future research.

Furthermore, Fig. 2 makes possible a quantitative retrieval of the geometric albedo $A$ in IDPs. For instance, in IDPs with $P_{max}$ = 10%, we obtain $A$ = 0.176 ± 0.027; whereas, at $P_{max}$ = 30%, $A$ = 0.055 ± 0.019. Therefore, the backscattering reflectance in particles located at $R$ = 0.2 AU is some three times greater than those at $R$ = 1 AU. This difference should be taken into account in analyses of the photometric observations of Zodiacal light.

**References:** [1] Levasseur-Regourd, A.-C., et al. 2001. Optical and thermal properties of interplanetary dust. In: Grün, E., et al. (Eds.), *Interplanetary dust*. Springer, Berlin, pp. 57–94, 804 p.. [2] Zubko, E., et al., 2011. The Umov effect for single irregularly shaped particles with sizes comparable with wavelength. *Icarus* 212, 403–415. [3] Zubko, E., et al., 2014. Dust in Comet C/1975 V1 (West). *MNRAS* 440, 2928–2943. [4] Flynn, G.J., Sutton, S.R., 1991. Cosmic dust particle densities – Evidence for two populations of stony micrometeorites. *Lunar Planet. Sci. Conf.* 21, 541–547. [5] Nesvorný, D., et al., 2010. Cometary origin of the Zodiacal cloud and carbonaceous micrometeorites. Implications for hot debris disks. *ApJ* 713, 816–836. [6] Zubko, E., et al. 2010. Validity criteria of the discrete dipole approximation. *Appl. Opt.* 49, 1267–1279. [7] Keller, L.P., et al. 1994. Carbon in primitive interplanetary dust particles. In: Zolensky, M.E., et al. (Eds.), *Analysis of interplanetary dust: NASA/LPI workshop*. American Institute of Physics, New York, pp. 159–164, 357 p..

# CHEMISTRY OF VENUS' ATMOSPHERE

**Vladimir A. Krasnopolsky**[1,2],
[1]*Catholic University of America, Washington, DC 20064, USA;*
[2]*PhysTech, Moscow, Russia.*
*Contact: vlad.krasn@verizon.net*

Chemistry of Venus' atmosphere involves seven elements (O, C, S, H, Cl, N, F) and the very dense and hot lower atmosphere. Formation of the sulfuric acid clouds is the main feature of photochemistry in the middle atmosphere. This process greatly reduces the abundances of $H_2O$ and $SO_2$ above 70 km that become very sensitive to small variations of eddy diffusion and the $H_2O/SO_2$ ratio in the cloud layer. The observed an order of magnitude variations are therefore readily explained and do not require exotic sources like volcanoes. Chlorine chemistry controls abundances of CO and $O_2$ via the ClCO cycle and related reactions. Sulfur chemistry involves the observable $SO_2$, OCS, $H_2SO_4$, SO, sulfur aerosol and a few intermediate species. Our photochemical model for the Venus atmosphere at 47-112 km includes 153 reactions of 44 species. Results for sulfur species are shown in Fig. 1.

VEX observations of the visible $O_2$ nightglow confirmed the results of Veneras 9 and 10 that the nightglow is very different from that on Earth. Vertical profiles of the nightglow on both planets were combined with the laboratory studies and predictions by theory to get a scheme of excitation, energy transfer, and quenching of the $O_2$ nightglow on Venus, Earth, and Mars.

A model for nighttime chemistry at 80-130 km was developed to reproduce the VEX observations of the $O_2$, NO, and OH nightglow and nighttime ozone (Fig. 2). The nighttime chemistry is initiated by fluxes of O, N, H, and Cl from the dayside atmosphere. The model established quantitative relationships between the observed nightglow intensities and fluxes of the proper species.

A model of coupled diffusion of $H_2O$ and $H_2SO_4$ in the cloud layer reproduces variations of mixing ratios of both species, concentration of sulfuric acid, and the observed structure of the cloud layer.

Chemical kinetic model for the lower atmosphere up to the cloud bottom simulates very slow chemistry that is driven by fluxes of $H_2SO_4$ and CO from the middle atmosphere, thermal chemistry in the lowest 10 km, photolyses of $S_3$ and $S_4$, and vertical transport of disequilibrium products.

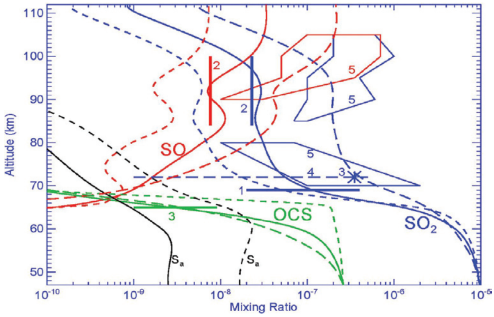


**Fig. 1.** Sulfur species and their variations in observa-tions and model by Krasnopolsky (2012)

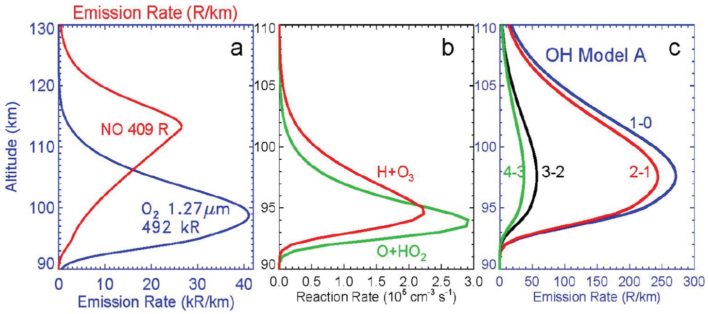


**Fig. 2.** Calculated vertical profiles of the UV NO, IR O2, and four bands of OH nightglow on Venus (Krasnopolsky 2013a)

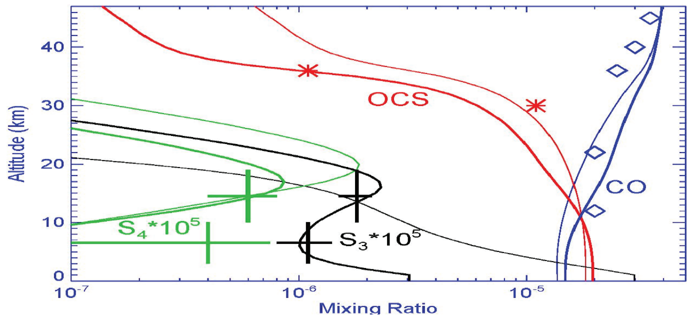


**Fig. 3.** Observed species in the model by Krasnopolsky (2013b)

**References**


Krasnopolsky, V.A., 2012. Icarus 218, 230-246.
Krasnopolsky, V.A., 2013a. Planet. Space Sci. 85, 78-88.
Krasnopolsky, V.A., 2013b. Icarus 225, 570-580.

# VERTICAL PROFILING OF SULPHUR DIOXIDE AND OTHER GASES CONTENTS AND ISOTOPE RATIOS IN THE VENUSSIAN ATMOSPHERE BY A DIODE LASER SPECTROMETER ISKRA-V ON BOARD OF THE VENERA-D LANDER

**I. Vinogradov[1,2], O. Korablev[1], V. Barke[1], A. Fedorova[1], M. Gerasimov[1], N. Ignatiev[1], Yu. Lebedev[1], A. Sapgir[1], A. Stepanov[1], A. Venkstern[1], M. Zaitsev[1], O. Benderov[2], D. Churbanov[2], I. Filatov[2], A. Klimchuk[2], A. Rodin[2,1], A. Nadezhdinskii[3], Ya. Ponurovskiy[3], M. Spiridonov[3], O. Grigoryan[4], A. Kalyuzhnyi[4], A. Titov[4], G. Durry[5], L. Joly[5], J. Cousin[5], N. Amarouche[6],**

*[1]Space Research Institute (IKI), 117997, 84/32 Profsoyuznaya Str., Moscow, Russia;*
*[2]Moscow Institute of Physics and Technology (MIPT), Institutsky Dr. 9, Dolgoprudny, Moscow Region, Russia;*
*[3]Prokhorov General Physics Institute, 119991, Vavilov Str., 38, Moscow, Russia;*
*[4]Special Design Bureau of Space Device Engineering of the Space Research Institute, 249100, Tarusa, Kaluga Region, Russia;*
*[5]GSMA, UMR CNRS 7331, Université de Reims, BP 1039, 51687 Reims, Cedex 2, France;*
*[6]Division Technique de l’Institut National des Sciences de l’Univers, CNRS, 92195 Meudon Cédex, France.*
*Contacts: imant@iki.rssi.ru, korab@iki.rssi.ru*

An experiment ISKRA-V (Investigation of Sulphurous Komponents of Rarefied Atmosphere of Venus) have been proposed for retrieving vertical profiles of the Venusian atmosphere composition, sulphurous and minor gases, and isotopic ratios from the Venera-D Lander board at its descent trajectory. Active work phase of the ISKRA-V instrument will be started at the moment of the Lander heat protection heat-shield removal near the altitude of 65 km and will be continued down to the surface level. Measurements will be continued at the descent point of the Lander. A multi-channel diode laser spectrometer is the core of the ISKRA-V instrument. Sequential operation of distributed feedback tunable diode lasers and quantum cascade lasers will provide for comprehensive studies of the ambient atmosphere dedicated composition. Laser beams will be coupled into an analytical composite multi-pass optical cell, filled in by a sampled interchangeable portion of the atmosphere, rarefied down to 50 mbar work pressure. Preliminary target molecules and isotope ratios are:

- sulfur dioxide SO2, carbon monoxide CO, carbon dioxide CO2, carbonyl sulphide OCS, water H2O;
- isotope ratios 13C/12C for CO and CO2, 16O/17O/18O for CO2, D/H and 16O/17O/18O for H2O, 34S/33S/32S for OCS.

The ISKRA-V experiment basics, instrument realization issues, forthcoming work team activity planning, and other moments of the mission are discussed in the report.

# OBSERVATIONS OF THE CO DAYGLOW AT 4.7 MU, CO MIXING RATIOS, AND TEMPERATURES AT 74 AND 105 KM ON VENUS

**Vladimir A. Krasnopolsky[1,2],**
[1]*Catholic University of America, Washington, DC 20064, USA;*
[2]*PhysTech, Moscow, Russia*
*Contact: vlad.krasn@verizon.net*

The CO dayglow at 4.7 μm on Venus was observed using a long-slit high-resolution spectrograph CSHELL at NASA IRTF with resolving power of $4\times10^4$. The observations covered a latitude range of ±60° at local time of 07:50 at low latitudes. Solar lines in the spectra are used to measure Venus reflectivity of 0.077 at 4.7 μm. Intensity ratio of the P2, P1, and R1 lines of the CO dayglow at the fundamental band (1-0) differs from that calculated by Crovisier et al. (2006) and is closer to that expected at local thermodynamic equilibrium.

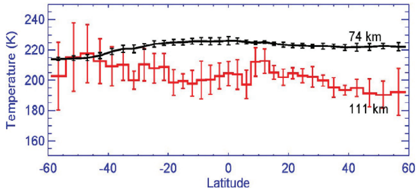


**Fig. 1.** Observed variations of temperature at 74 and 111 km.

The CO (1-0) dayglow is optically thick, its intensity weakly depends on the CO abundance, and it is poorly accessible for diagnostics of the Venus atmosphere. Six observed lines of the CO dayglow at the hot (2-1) band show a significant limb brightening typical of an optically thin airglow. Vertical intensities of the CO (2-1) band corrected for viewing angle and the Venus reflection are constant at 3.3 MR in the latitude range of ±50° at solar zenith angle of 64°. Rotational temperatures of the CO (2-1) dayglow should be equal to ambient temperature near 111 km. Latitudinal distribution of temperature has been derived (Figure 1), with a mean values of 203 K. A model of the CO (2-1) dayglow has been improved. The CO (v = 2) molecules are excited by absorption of the sunlight at the CO (2-0) and (3-0) bands at 2.35 and 1.58 μm and photolysis of $CO_2$ by the solar Lyman-alpha emission. The dayglow is quenched by $CO_2$, and the calculated mean dayside dayglow is 3.1 MR.

A weighted-mean dayglow altitude is 104 km. Variations of the dayglow with CO abundance and solar zenith angle are calculated and presented. The model results are used to convert the observed dayglow intensities into CO abundances at 104 km (Figure 2). The retrieved CO mixing ratios are constant from 50°S to 50°N with a mean value of 560 ± 100 ppm. The observed values of CO and temperatures are compared and discussed with those in other observations and models. Numerous CO and $CO_2$ absorption lines in the observed spectra are used to retrieve CO abundances and temperatures at 74 km on Venus. The measured CO mixing ratio is constant at 40 ppm from 50°S to 30°N with a weak increase to the higher latitudes (Figure 2). Temperature at 74 km is almost constant at 222.6 ± 3.4 K (Figure 1), in perfect agreement with VIRA.

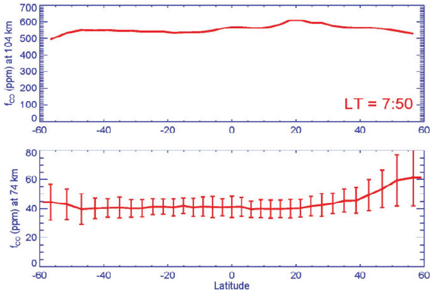


**Fig. 2.** Observed latitudinal variations of the CO mixing ratio at 74 and 104 km (bottom and top panels, respectively). Uncertainties of CO at 104 km are mostly from the model and evaluated at ~100 ppm.

# OXYGEN NIGHT AIRGLOW IN VENUS ATMOSPHERE (VIRTIS/VEX)

**L. Zasova, A. Shakun , I. Khatuntsev, N.Ignatiev, D. Gorinov.**
*Space Research Institute RAS, Moscow Russia,*
*Contact: zasova@iki.rssi.ru*

**Introduction:**

Mapping spectrometer VIRTIS-M on board Venus Express [1] made observations of the $O_2$ 1.27 μm airglow intensity distribution on the night side of Venus in nadir and limb modes in Southern and Northern hemispheres respectively. Horizontal distribution of the oxygen nightglow in the Venus atmosphere is an effective tracer of circulation in upper atmosphere and lower thermosphere (in the vicinity of the mesopause level (90-100 km). This is a transition region between two major circulation modes. In thermosphere the subsolar-to-antisolar (SS-AS) circulation prevails, while in mesosphere a zonal retrograde superrotation (ZRS) dominates [2]. Besides, the thermal tides are observed in mesosphere with diurnal and semi-diurnal amplitudes of exceeding 5 K at 90-100 km height [3]. Gravity waves are also present there, revealing itself in the vertical distribution of the O2 emission [4]. The layer of the $O_2$ emission is centered at 97 ± 3 km, with half width of the emitting layer 8 ± 3 km (VIRTIS-M, limb measurements [5]).

**Southern hemisphere observations:**

Nadir measurements are related to Southern hemisphere. Night glow and its intensity is strongly variable, distribution inhomogeneous, maximal observed emission rate exceeds 6 MR. To avoid high noisy data we use for analysis only those, obtained with exposure > 3 s. Maps of airglow were obtained in the coordinates "local time – latitude" for individual data cubes as well as the global map averaged over 718 orbits. Individual maps of the airglow show highly variable character of the O2 nightglow distribution. Maximum emission in low latitude region may be observed in the local time interval LT= 20 h ÷ 4 h. More detailed averaged map was obtained. It was found also evidence of the SS-AS circulation, Global map for southern hemisphere (from nadir data) has good statistics at $\varphi$ > 10-20°S and pretty poor at lower latitudes. Averaged over 718 orbits map shows maximum emission shifted from midnight by 1 – 2 hours to the evening (22-23h) and deep minimum of emission is found at LT=2-4 h at $\varphi$ > 20°S. This asymmetry is extended up to equatorial region, however statistic is poor there. No evident indication for existence of the Retrograde Zonal Superrotation (RZS) is found: maximum emission in this case, which is resulting from downwards flow, should be shifted to the morning terminator. Horizontal wind, measured independently from the same set of data show that at 22-23 h the horizontal wind changes its direction, indicating to downwelling; maximal wind speed coincides with minimum emission rate near morning terminator.

**Northern hemisphere:**

VIRTIS limb observations cover the low northern latitudes and they are more sparse at higher latitudes. Intensity of airglow at $\varphi$ = 0 - 20° N shows wide maximum, which is shifted by 1- 2 h from midnight to morning terminator. This obviously indicates that observed O2 night glow distribution in low North latitudes is explained by a superposition of SS-AS flow and RZS circulation at 90-100 km. This behavior is similar to the NO intensity distribution, obtained by SPICAV. Temporal variation was found at low latitudes of the Northern hemisphere: during 820 days observations three maxima were observed separated by 150 - 200 days approximately.

**Summary:**

Distribution of the $O_2$ night glow in both hemispheres indicates to more complex circulation in the transition region than SS-AS flow. In equatorial region and low latitudes of the Northern hemisphere the superposition of SS-AS and RZS reveals itself in the shift of the maximum of the O2 emission to the morning (2h), similar to that of the NO night glow, observed by SPICAV. No evidence of influence of the ZRS in Southern hemisphere from nadir data was found.

**Acknowledgements**: We acknowledge the Program 22 of Presidium RAS and Russian Foundation of Basic Research, grant 12-02-01280 for financial support of this work

**References**:[1] Piccioni, G., et al. 2009, ESA SP-1295.[2] Schubert,G., et al. 2007, Geophys.Monogr. Ser., 176. [3] Zasova, L., et al. 2007, PSS., 55, 1712 [4] Piccioni, G., al. 2009, JGR114. [5] Shakun, A, et al. 201), Cos. Res., 48, 3.[6] Gérard, J. e tal. 2008, GRL, 35, L02207

# NON-HYDROSTATIC SIMULATIONS OF THE SUBSOLAR-ANTISOLAR CIRCULATION IN THE VENUS ATMOSPHERE

**A. V. Rodin[1,2], I. V. Mingalev[3], K. G. Orlov[3]**
*[1]Moscow Institute of Physics and Technology, Dolgoprudny, Russia;*
*[2]Space Research Institute, Moscow, Russia; [3]Polar Geophysical Institute, Moscow, Russia.*
*Contact: alexander.rodin@phystech.edu*

**Introduction:**

General circulation of the Venus atmosphere is well known to consist of two major components: zonal retraograde superrotation (RZS), dominating in the lower and middle atmosphere below 90-95 km, and subsolar-antisolar circulation (SS-AS) that emerges in the upper mesosphere and thermosphere. In spite of the significant progress achieved in the general circulation models during recent decade, only one of these two regimes, depending on selected altitude range, was reproduced by the same GCM to date. The first simultaneous simulation of both RZS and SS-AS circulation modes has been recently done by means of the model with non-hydrostatic dynamical core based on full set of the gas dynamics equations [1]. In this work we analyze the SS-AS circulation pattern obtained by the model in more detail.

**Simulations:**

The model has resolution of 250 m in the vertical, and 0.7º in latitude and longitude.  Model setup includes prescribed thermal forcing in relaxation form, with some additional heating of the polar regions above the cloud layer [1]. Indeed, according to the cyclostrophic balance hypothesis, poleward meridional thermal gradient should results in decreasing zonal velocity with altitude, which, in turn, allows the development of a SS-AS circulation in the upper part of the model domain. Simulations start from developed superrotation state to minimize spinup time. After stabilization within ~8000 hours, wind field remains unchanged and ready for analysis. The model includes topography with the same spatial resolution as gas dynamics.

The only external parameterization used in simulations is thermal forcing determined by relaxation temperature, dependent on location, altitude and local time, and relaxation time which has meaning of the airmass thermal inertia. Selected distribution of these parameters provides realistic circulation pattern, as described in [1]. In the upper part of the model domain, relaxation time is small compared to dynamical spinup time, so thermal balance is expected to reach steady state.

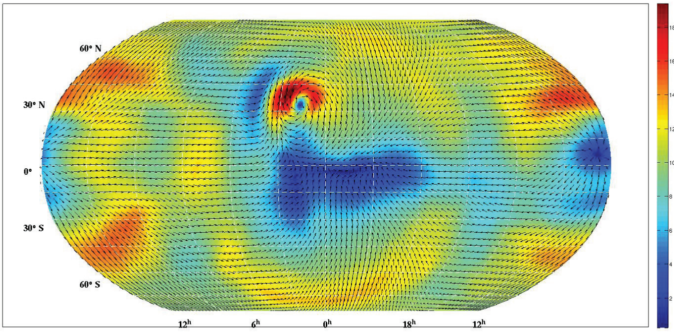


**Fig. 1.** Wind velocity distribution (m/s) vs. latitude and local time at 110 km above the surface according to non-hydrostatic GCM.

**Results:**

The model demonstrates developed SS-AS circulation above 100 km, with major upwelling well on the dayside and its downwelling counterpart on the nightside of Venus. However, the structure of these wells may not be trivial, as shown in Figure 1. Mesoscale vortices may occur along their periphery, whereas they cores are usually prolate along the equator and contain irregular caustics. Horizontal velocity maximizes in the symmetric circles between the far periphery of these wells terminator, and falls to zero inside the caustics. This pattern is consistent with ground-based Doppler measurements provided by high resolution heterodyne infrared spectroscopy on the Venus dayside [2] that shows no signature of superrotation at this altitude. In the intermediate altitude range, between 90 and 100 km, simulations show a complex superposition of tidal waves, mesoscale vortices and jet streams. Comparison of model results with observed distribution of $O_2$ and NO emissions, along with ground-based Doppler measurements, may help to understand interactions between two main regimes of the Venus atmospheric circulation.

**References:**

1. Rodin, A.V., I.V. Mingalev, K.G. Orlov. Gas dynamics simulations of the general circulation of Venus atmosphere. Submitted to Icarus, 2014

2. Sornig, M., G. Sonnabend, D. Stupar, P. Kroetz, H. Nakagawa, I. Mueller-Wodarg. Venus' upper atmospheric dynamical structure from ground-based observations shortly before and after Venus' inferior conjunction 2009. Icarus, Volume 225, Issue 1, p. 828-839, 2013.

# HAZE ABOVE THE CLOUDS OF VENUS FROM VIRTIS / VENUS EXPRESS LIMB NIGHT SIDE OBSERVATIONS

**N. I. Ignatiev[1,2], L. Zasova[1,2], D. Gorinov[1,2], G. Piccioni[3], P. Drossart[4],**
*[1]Space Research Institute of Russian Academy of Sciences, Profsoyuznaya 84/32, 117997 Moscow, Russia;*
*[2] Moscow Institute of Physics and Technology, Institutskiy per. 9, 141700 Dolgoprudny, Russia;*
*[3]Istituto di Astrofisica e Planetologia Spaziali, INAF, Rome, Italy;*
*[4]LESIA, Observatoire de Paris, Paris, France.*
*Contact: ignatiev@iki.rssi.ru*

## Introduction:

VIRTIS-M is a mapping spectrometer on Venus Express [1]. It worked on orbit around Venus from 2006 to 2009 years. Night side limb observations of Venus made by VIRTIS mapping spectrometer onboard Venus Express revealed a thermal emission scattered at the right angle by the upper haze above the cloud tops. This emission comes from the cloud tops in the spectral range of 4-5 microns and from the hot deep subcloud atmosphere and the surface in several spectral transparency windows between 1 and 2.5 microns. De Kok et al. [2] first demonstrated that the spectra of this emission can be used to retrieve the density of the upper haze and estimate its particle size. In particular they obtained vertical profiles of the density of the haze composed from ~1 micron size particles from the spectra of the thermal emission from the cloud tops in the interval of 4-5 microns for 4 orbits and two narrow latitudinal bands of 20-30N and 47-50. We extended this study to other spectral windows and analyzed a wide set of measurements obtained in 2006-2009.

## Observations:

Polar orbit of Venus Express with pericenter at 75N latitude allows carrying out limb measurements in the northern hemisphere. From the distance of 15 000 km the haze vertical profile is obtained with vertical resolution of 2.5 km. We analyzed almost all available limb measurements obtained in 89 measurement sessions from 44 orbits. The data were averaged in 5 degree latitude and 1 km altitude bins.

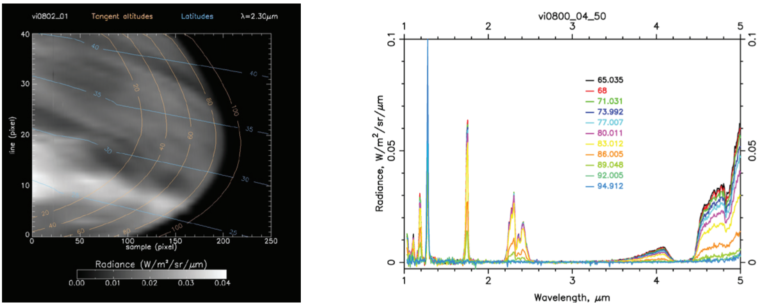


**Fig. 1.** Observations. Left: Venus night side limb image at 2.3 μm. Right: spectra corresponding to a number of tangent point altitudes.

## Modeling of limb spectra and inverse problem:

Our radiative transfer model takes into account multiple scattering in a pseudo-spherical geometry: the source function is calculated for a plane parallel atmosphere with a discrete ordinate method and then integrated along the optical path. Gaseous absorption is calculated with a line-by-line code with a number of recent improvements for the continuum absorption [3, 4]. The spectrum of the thermal radiation scattered by the clouds and observed at the night side limb depends on a number of factors: cloud particle density, particle size distribution and optical properties at all altitudes, temperature and pressure profiles and gaseous absorption, and, at shortest wavelengths, on the surface altitude. In principle, haze extinction and particle sizes can be retrieved by inverting the vertical limb intensity profiles at all wavelengths simultaneously by means of standard inverse methods for atmospheric sounding [e.g., 5]. However, such a straightforward approach meets considerable difficulties. First, the retrieval appears to be very time consuming due to the necessary direct numerical evaluation of the kernels of the inverse problem. Second, since the spectrum in different windows depends on a number of parameters simultaneously, especially on the cloud model below the cloud tops and gaseous continuum absorption, it appeared to be difficult to achieve convergence in the whole spectrum range without artificial absorption correction. Model spectrum in windows of 2.3 and 1.7 µm often agree well, but a simultaneous agreement with 1.18 µm window is often difficult to achieve. To simplify the task we retrieve separately for each spectral window the haze extinction profiles from the limb radiance vertical profiles, using a priori assumptions about particle sizes, namely the haze composed of “mode 1” (submicron) or “mode 2” (micron) particles. The haze extinction can be retrieved with confidence in the interval between 80 and 90 km. De Kok et al. [2] came to unexpected conclusion that the haze particles belong to “mode 2”. Our haze extinction profiles retrieved from 1.7 and 2.3 µm windows appeared to have no sensitivity to particle sizes (Fig. 2a).

**Results:**

About half of the available data volume has been successfully processed: 220 vertical profiles from 65 measurement sessions from 35 orbits (Fig 2b). As a rule, the haze extinction vertical profiles between 80 and 90 km obtained from different spectral windows and a priori mode 1 and 2 particle size distributions agree well between each other. The scale height of the haze density appeared to be about 3 km, which agrees with de Kok et al. [2], but smaller than 5 km obtained from solar and stellar occultation observations on SPICAV/SOIR. At low and middle latitudes limb unit optical depth may be as high as 89 km, while at high latitudes is never exceed 83 km. On the morning side the haze is lower than that on the evening side by about 2 km, which has an evident explanation of the haze is created during the day from the photochemical production of the sulfuric acid.

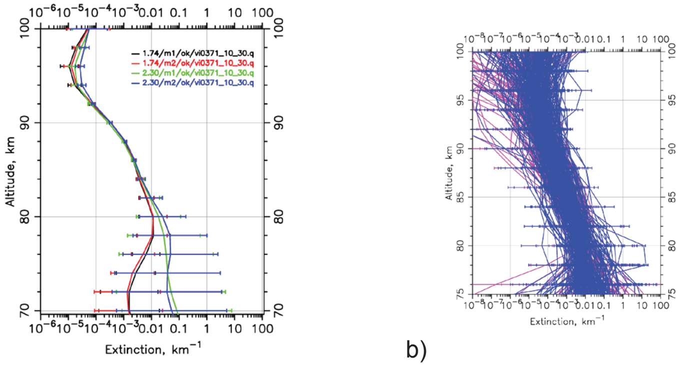


**Fig. 2.** Left: Haze extinction vertical profiles retrieved from 1.7 and 2.3 µm windows for a priori “mode 1” (submicron) and “mode 2” (1 micron) particles at 30 latitude on orbit 371. Right: all haze extinction vertical profiles obtained 1.7 and 2.3 µm windows for “mode 2” particles.

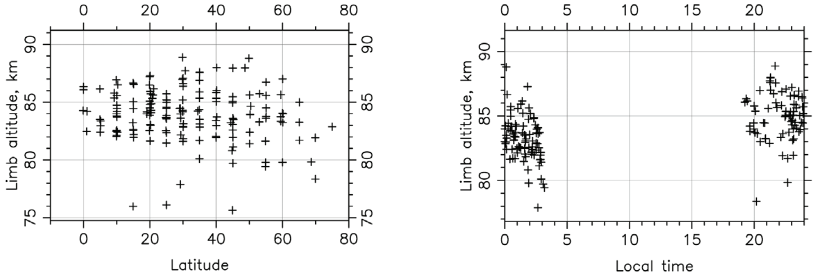


**Fig. 3.** Level of the limb unit optical depth as a function of latitude and local time.

**Acknowledgements:**

The Venus Express is a mission of the European Space Agency. We thank the Agenzia Spaziale Italiana (ASI) and the Centre National d’Études Spatiales (CNES) for the support and funding of the VIRTIS experiment. We thank all members of the Venus Express project and of the VIRTIS technical team. This work is supported by the Ministry of Education and Science of Russian Federation grant 11.G34.31.0074, the Russian Foundation of Basic Research grant 12-02-01280, and the Presidium RAS Program 22.

**References:**

[1] P. Drossart et al. (2007), Scientific goals for the observation of Venus by VIRTIS on ESA/Venus Express mission, Planet. Space Sci., Vol. 55, pp. 1653-1672. [2] R. de Kok et al. (2011), Scattering particles in nightside limb observations of Venus' upper atmosphere by Venus Express VIRTIS, Icarus, Vol. 211, pp. 51-57. [3] B. Bézard et al. (2011), The 1.10- and 1.18-μm nightside windows of Venus observed by SPICAV-IR aboard Venus Express, Icarus, Vol. 216, pp. 173-183. [4] R. Haus et al. (2013), Self-consistent retrieval of temperature profiles and cloud structure in the northern hemisphere of Venus using VIRTIS/VEX and PMV/VENERA-15 radiation measurements, Planet. Space Sci. 89, p. 77-101, 2013. [5] C. D. Rodgers (2000), Inverse Methods for Atmospheric Sounding - Theory and Practice: World Scientific Publishing.

# SULPHUR DIOXIDE DISTRIBUTION IN VENUS' NIGHT-SIDE MESOSPHERE

**D. A. Belyaev[1,2], D. G. Evdokimova[1], F. Montmessin[3], A. Piccialli[3], E. Marcq[3], J.-L. Bertaux[3],**
*[1]Space Research Institute (IKI), 84/32 Profsoyuznaya, 117810 Moscow, Russia;*
*[2]MIPT, 9 Institutskiy per., 141700 Dolgoprudny, Russia;*
*[3] LATMOS - UVSQ/CNRS/IPSL, 11 bddAlembert, 78280 Guyancourt, France.*
*Contact: bdenya.iki@gmail.com*

## Introduction:

Sulphur dioxide ($SO_2$) is a key component of Venus' atmosphere since the planet is totally covered by $H_2SO_4$ droplets clouds at altitudes 50–70 km. Any significant change in the $SO_x$ oxides above and within the clouds affects the photochemistry in the mesosphere (70-120 km). Recent continuous observations from the Venus Express orbiter (Belyaev et al., 2012; Marcq et al., 2013) and ground-based telescopes (Sandor et al., 2010; Krasnopolsky, 2010; Encrenaz et al., 2012) showed high variability of $SO_2$ abundance with years, diurnal time and latitude on the day-side and terminators (commonly from 20 to 500 ppbv above the clouds). In the night-side mesosphere $SO_2$ is not photo dissociative but, so far, its behaviour has never been explored in details.

**Results:**In this paper we present new results from sulfur dioxide observations made by SPICAV UV spectrometer onboard Venus Express orbiter (Bertaux et al., 2007) in regimes of stellar and solar occultation. In the mode of stellar occultation the instrument observes night-side mesosphere while at solar occultation it sounds evening/morning twilights. SPICAV UV can register $SO_2$ absorption bands in 190-220 nm and $CO_2$ bands in 120-200 nm at altitudes from 85 to 110 km (spectral resolution is 1-2 nm). As a result, vertical distribution of $SO_2$ and $CO_2$ concentrations has been retrieved in observation period from June 2006 to April 2014, at latitude range 80S-80N and Venus local time 18:00-06:00 (i.e. from evening time to morning). Thus, we may analyse sulphur chemistry between the twilight mesosphere and the night one. Moreover, annual variations have been compared with nadir dayside observations of $SO_2$ reported by Marcq et al. in 2013.On the average, mixing ratio of sulphur dioxide fluctuates around ~100 ppbv along altitude range 90-100 km.

**Acknowledgements:**

We acknowledge the grant 11.G34.31.0074 from the Russian government and the program №22 from the RAS.

**References:**

Belyaev D. et al., 2012. Vertical profiling of $SO_2$ and SO above Venus' clouds by SPICAV/SOIR solar occultations.Icarus 217, 740–751.
Bertaux et al., 2007. SPICAV on Venus Express: three spectrometers to study the global structure and composition of Venus atmosphere. Planet. Space Sci. 55, 1673–1700.
Encrenaz T. et al., 2012. HDO and $SO_2$ thermal mapping on Venus: evidence for strong $SO_2$ variability. A&A 543, A153.
Krasnopolsky V.A., 2010. Spatially-resolved high-resolution spectroscopy of Venus. 2. Variations of HDO, OCS, and $SO_2$ at the cloud tops. Icarus 209, 314-322.
Marcq E. et al., 2013. Variations of sulphur dioxide at the cloud top of Venus's dynamic atmosphere.Nature Geoscience, vol. 6, 25-28. DOI: 10.1038/NGEO1650.
Sandor B.J. et al., 2010.Sulfur chemistry in the Venus mesosphere from $SO_2$ and SO microwave spectra. Icarus 208, 49–60.

# VENUS - THE LIFE CYCLE OF 5-15KM GRAVITY WAVES: FROM THE UPPER CLOUD TO EXTINCTION IN THE THERMOSPHERE AS OBSERVED FROM OCCULTATION DATA

**M.Bondarenko[1], A. Gavrik[2],**
*[1]IRE RAS, Moscow, Russian Federation;*
*[2]IRE RAS, Moscow, Russian Federation.*
*Contact: linuxoid2013@mail.ru*

In 1983 and 1984 Soviet VENERA-15 and VENERA-16 missions conducted a large number of occultation experiments. The experimental data comprised vertical records of differential Doppler frequency and S-band (32cm) signal power which extended from 68-70km to 500 km and higher altitudes. Signals derived from these data reveal patterns identified as Gravity Waves (GWs) with wavelengths in the 5-15km range. In one “textbook” case we observed a spectacular portrait of a Gravity Wave with amplitude growth up to its breaking level just below the lower Chapman layer, resulting in perturbations comparable to the size of the second (lower) Chapman layer on the signal of power variations,with a 5.6km vertical wavelength and a typical saturated (1/x^3) spectrum.

Confirmation of this interpretation and possible source of GWs of this type were sought in data from other missions to Venus and found in the 2008-2014 VEX VIRTIS instrument data (from the current joint EU Venus Express mission), which provided a horizontal view of GWs with similar parameters on UV and NI images at 61 and 66 km levels [1]. This data matches VENERA-15,16 vertical GW recordings in the vertical wavelength (5-15km) and geographicaly by the latitude bin, pointing at the possible location of the source at the upper cloud layer. More GWs with similar parameters were obtained by the VEX teams from the VIRTIS M CO2 measurements at 110-140km altitude [2]. The conflation of these three pieces of evidence forms a fuller picture and leads to a realization that occultation data, if of sufficiently high quality, may contain recordings of the whole life cycle of Gravity Waves, from generation in or near the top levels of the cloud layers to extinction in the thermosphere, i.e. at altitudes where so far the dearth of GW data has been felt.

This suggests a new application of the upper ionospheric part of the occultation signal, currently routinely used only for obtaining electron density profiles in Venus studies.

Next the GW data in occultation measurements were analyzed to reveal patterns of the full GW life cycle, including the (possibly multistage) process of breaking in the thermosphere, by means of time-frequency transformations. The recorded GW traces were compared to theoretical predictions (Labas, Frits 2004) [3], and good agreement was noted of the observed dissipation altitude with theory for high-frequency GWs in atmosphere with slowly changing parameters, which accounts for the effects of viscous dissipation and thermal dumping.

This match was obtained with the aid of temperature and pressure profiles from SOIR data (based on spectroscopic measurements at the morning and evening terminator at altitudes between 60 and 170km) [4], which also allowed us to estimate approximate parameters of the vertically recorded GWs, such as intrinsic frequency and horizontal wavelength, confirming that VENERA-15,16 GWs and those observed horizontally by the VIRTIS instrument in the later VEX mission are of the same type, and considering the 22-30-year span between the missions, are therefore a permanent feature of the Venus atmosphere.

This approach suggests that occultations could serve as another remote sensing technique for the study of GWs at levels up to their breaking at the turbopause altitudes, with time-frequency transforms acting “as an analogue of the Wilson chamber” (or cloud chamber) of the early particle physics, to reveal traces of the GW growth and dissipation. This application should be relevant to environments other than Venus atmosphere, if occultation signals of sufficiently high quality are available.

Relevance of the proposed method to the uncovering of similar information from the VEX VeRa occultation data was also discussed.

This work was partially supported by Program No 22 of the Presidium of the Russian Academy of Science.

**References:**

[1] J. Peralta, R. Hueso, A. Sanchez-Lavega, G. Piccioni, O. Lanciano, and P. Drossart "Characterization of mesoscale gravity waves in the upper and lower clouds of Venus from VEX-VIRTIS images"

[2] R. F. Garcia, P. Drossart, G. Piccioni, M. Lopez-Valverde, and G. Occhipinti "Gravity waves in the upper atmosphere of Venus revealed by CO2 nonlocal thermodynamic equilibrium emissions"

[3] Sharon L. Vadas1 and David C. Fritts "Thermospheric Responses to Gravity Waves: Influences of Increasing Viscosity and Thermal Diffusivity"

[4] A. Mahieux, A. C. Vandaele, S. Robert, V. Wilquet, R. Drummond, F. Montmessin,and J. L. Bertaux "Densities and temperatures in the Venus mesosphere and lower thermosphere retrieved from SOIR on board Venus Express: Carbon dioxide measurements at the Venus terminator"

# EMBAYED CRATERS ON VENUS: TESTING THE CATASTROPHIC AND EQUILIBRIUM RESURFACING MODELS

**M. A. Ivanov[1,2], J. W. Head[2],**
*[1]Vernadsky Institute RAS, Kosygin St., 19, Moscow, Russia,*
*[2]Brown University, Providence, RI USA,*
*Contact: Mikhail_Ivanov@brown.edu*

**Introduction:**

The style of resurfacing on Venus is among the key problems in the geologic history of this planet [1-6]. There are two apparently alternative models of this process, catastrophic [1] and equilibrium [2] resurfacing. Both models are based on the fundamental properties of the crater population on Venus: (1) the spatial distribution of craters may be indistinguishable from complete spatial randomness and (2) only a small proportion of craters are modified by volcanic flows and/or tectonic structures. The spatial randomness of the distribution of craters has been tested in different ways and by different groups of researchers [2-4] with essentially the same result. We test the key prediction of the equilibrium model about the quantitative relationships of the size of the volcanic resurfacing events and the proportion of volcanically embayed craters. We assess these relationships in regard to two types of volcanic plains on Venus that characterize different epochs of the visible geologic history of the planet.

**Limits of the equilibrium model:** The model predicts that the craters remain randomly distributed if the diameter of the resurfacing areas is either smaller than about 4$^{o}$ (~420 km) or larger than about 74$^{o}$ (~7700 km). If the characteristic size of the resurfacing areas falls between these limits the interaction of resurfacing events with the crater population leads to the non-randomly distributed craters.

**Major volcanic units, their age relationships, and proportion of embayed craters:** There are two major types of volcanic plains on Venus: regional plains, rp, and lobate plains, pl. Together they cover ~52% of the surface of Venus [7]. Regional plains are significantly more abundant (~43% of the surface) and their homogenous radar backscatter suggests that they formed by vast lava flooding. Lobate plains (~9% of the surface) are characterized by a variable pattern of radar backscatter that consists of radar dark and bright lava flows.

The age relationships between regional plains and lobate plains are consistently the same over the entire surface of Venus [7]. In any specific place where these units are in contact, lobate plains embay regional plains and, because of this, are locally to regionally younger. The strikingly different morphologic characteristics of regional and lobate plains and their distinctly different ages [8-10] imply that these lava units correspond to different geological epochs with apparently different styles of volcanism [7]. The main characteristic of regional plains is that the majority of their area (slightly over 80%) is concentrated only in three largest occurrences of this unit. The sizes of occurrences of lobate plains are much more evenly distributed within the observable range of areas.

The total number of craters that occur either within or on the boundaries of the areas of regional plains is 582. Out of these, 563 craters appear to be superposed on the plains and the plains embay 19 of the craters. This gives the proportion of craters embayed by regional plains as ~3%. A similar (3 to 6%), and independent, estimate of the proportion of craters embayed by regional plains was reported by [11]. The total number of craters on lobate plains is 54 and the plains embay 27 of them, which gives the proportion of the embayed craters in the case of lobate plains as 50%.

**Testing the applicability of the equilibrium model:** Figure 1 shows how the actual proportions of the embayed craters correspond to the predicted characteristic sizes of volcanic fields (the resurfacing events) in the framework of the equilibrium model. The proportion of all embayed craters (regardless of the specific volcanic units that embays them) is ~7%. This value corresponds to the characteristic diameter of a volcanic resurfacing event ~1100 km or 10$^{o}$. According to the equilibrium model, events of these dimensions should lead to a noticeable deviation from spatially randomly distributed craters (Fig. 1). The likely proportion of craters embayed by regional plains is even smaller, ~3%. For such a proportion, the equilibrium model predicts the characteristic diameter of the resurfacing events to be ~2700 km or ~25$^{o}$. The resurfacing areas of this size are inconsistent with the constraint of the random/quasi-random spatial distribution of the craters (Fig. 1). In the case of lobate plains, however, the minimal proportion of embayed craters is 50%, which corresponds to the characteristic diameter of the resurfacing events less than ~90 km or 0.8$^{o}$ (Fig. 1). In the framework of the equilibrium model, events of these sizes would not disturb the randomness of the spatial distribution of craters.

**Conclusions:** One of the most important conclusions of our study is that both the equilibrium and catastrophic models fail to adequately describe the process of volcanic resurfacing during the entire visible portion of the geologic history of Venus [12]. According to the well-established stratigraphic relationships between regional and lobate plains [e.g., 13-18], strongly supported by the data on crater density [19], these distinctly different plains units represent two epochs of volcanic activity on Venus. The characteristic features (the size-frequency distribution of occurrences and the proportion of embayed craters) of the older regional plains are inconsistent with the predictions of the model of equilibrium resurfacing (Fig. 1). The fairly homogenous radar albedo of the surface of regional plains, the lack of flow fronts, the morphologically smooth surface, and the existence of a few huge fields that make up the majority of regional plains suggest emplacement of this unit by broad volcanic flooding. This style of emplacement may be attributable to a “catastrophic” volcanic resurfacing.

In contrast, the size-frequency distribution of fields of lobate plains and the proportion of the craters embayed by them are consistent with the predictions of the model of equilibrium resurfacing. A more gradual style of emplacement of lobate plains is also suggested by the large number of individual lava flows [20-22] that make up the surface of this unit. The independent observations of interaction of lobate plains with the craters possessing dark haloes also suggest that lobate plains form in a more balanced way with the flux of crater-forming meteoroids.

Thus, the style of volcanic resurfacing on Venus appears to have changed significantly during the observable portion of the geologic history of this planet [7]. Earlier in the preserved geological history, during formation of regional plains, volcanism acted in large regions and clearly at higher rates than the rate of formation of impact craters [11]. This leads to a very small proportion of the embayed craters (~3%). Later, during emplacement of lobate plains, volcanic sources were localized at distinctive centers and the net volcanic rate came to be comparable to the rate of crater formation, which caused a large percentage (50%) of craters to be embayed by lobate plains.

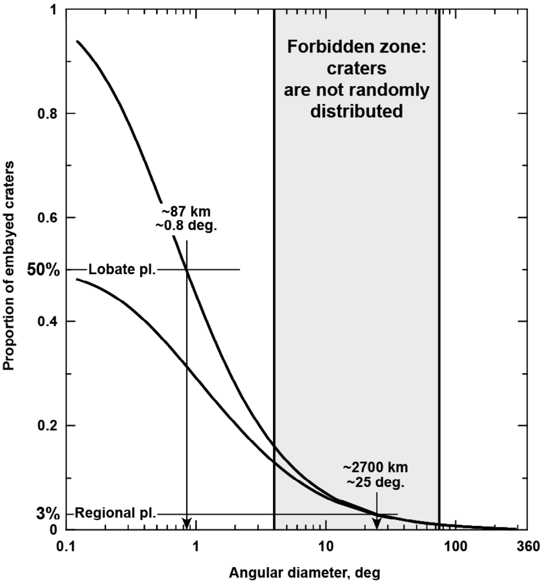


**Fig. 1.** Relationships between the proportion of modified craters and the size of resurfacing event that are predicted by the equilibrium model (Phillips et al., 1992). The upper curve bounds the proportion under the assumption that craters are never completely erased by resurfacing events. The lower curve bounds the proportion under the assumption that two successive resurfacing events completely erase craters. The actual proportion of craters embayed by regional plains requires large resurfacing events, the dimensions of which are inconsistent with random spatial distribution of craters on Venus.

**References:** 1) Schaber et al., JGR, 97, 13257,1992, 2)Phillips et al., JGR, 97, 15923, 1992, 3) Strom et al., JGR, 99, 10899, 1994, 4) Hauck et al., JGR, 103, 13635, 1998, 5) Romeo and Turcotte, PSS, 58, 1374, 2010, 6) Romeo, PSS, 87, 157, 2013, 7) Ivanov and Head, PSS, 84, 66, 2013, 8) Namiki and Solomon, Science, 265, 929, 1994, 9) Price et al., JGR, 101, 4657, 1996, 10) Guest and Stofan, Icarus, 139, 56, 1999, 11) Collins et al., JGR, 104, 24121, 1999, 12) Ivanov and Head, PSS, 59, 1559, 2011, 13) Basilevsky and Head, JGR, 103, 8531, 1998, 14) Basilevsky and Head, JGR, 105, 24583, 2000a, 15) Basilevsky and Head, PSS, 48, 75, 2000b, 16) Basilevsky and Head, JGR, 107, 2002a, 17) Basilevsky and Head, JGR, 103, 8531, 2002b, 18) Ivanov, LPSC-39, #1017, 2008, 19) Kreslavsky et al., LPSC-40, #1096, 2009, 20) Head et al., JGR, 97, 13153, 1992, 21) Roberts et al., JGR, 97, 15991, 1992, 22) Keddie and Head, JGR, 100, 11729, 1995.

# CURRENT VOLCANISM ON VENUS: EVIDENCE FROM THE VExVMC OBSERVATIONS

**E.V. Shalygin[1], W.J. Markiewicz[1], D. A.T. Basilevsky[1,2,5], D.V. Titov[3], N.I. Ignatiev[4], J.W. Head[5],**
*[1]Max-Planck-InstitutfurSonnensystemforschung, 37077 Göttingen, Germany;*
*[2]Vernadsky Institute, 119991 Moscow, Russia;*
*[3]ESA-ESTEC, SRE-SM, NoordwijkZH, The Netherlands;*
*[4]Space Research Institute, Moscow, Russia; [5]Brown University, Providence, RI, USA.*
*Contact: atbas@geokhi.ru*

**Introduction:**Venus is known to have been volcanically resurfaced in the last billionyears of Solar System history, and to have undergone a significant decrease in volcanic activity a few hundred million years ago [1,2]. The fundamental question is: Is Venus still volcanically active today, and if so, where and in what geological environment? Two works have been published recently onpossible present-day volcanism on Venus [3,4], but both propose geologically recent volcanism, not necessarily present day activity. Here we show evidence from the Venus Express (VEx) Venus Monitoring Camera (VMC) for transient bright spots that are consistent with the extrusion of lava flows.

**The VMC camera and data analysis approach:**The Venus Monitoring Camera onboard the European Space Agency Venus Express spacecraft provides the opportunity to observe changes in thermal emission of the surface of Venus that might be associated with current ongoing volcanic eruptions.VMC obtains images in four spectral channels; one of these, centered at 1.01 μm, registers the thermal emission from the surface of Venusinside an atmosphere transparency window [5]. At this wavelength, and with a mean temperature of the surface of ~740 K, the radiation flux from the surface strongly depends on the surface temperature, providing the opportunity to detect higher surface temperatures associated with a volcanic eruption. The appearance and disappearance of such thermal anomalies ("bright spots") in the VMC data would be strong evidence for transient volcanic events.

To isolate valid bright spots and identify transient events one has to account for brightness variations caused by changes in the surface temperature as a function of altitude (−8.1 K/km) and by light scattering in the atmosphere. Altitude-related effects can be accounted for using topographic data obtained by the Magellan Mission (MGN), and atmospheric effects can be modeled using radiative transfer methods and data on the atmospheric structure obtained from numerous *in situ* measurements by descent probes and by remote sensing methods. VMC is able to image the surface only on the night side when VEx is in the shadow of the planet. Observationsare performed at, or very close to, nadir geometry at latitudes from ~30°N to ~20°S.

**The VMC observations:** Here we discuss VMC observations of ~1.44 x $10^6$ $km^2$ area of northern AtlaRegio(5°N – 25°N, 180°E – 200°E), in a region of geologically recent volcanoes and rift zones in the western part of the geologically young Beta-Atla-Themis region (Fig. 1).

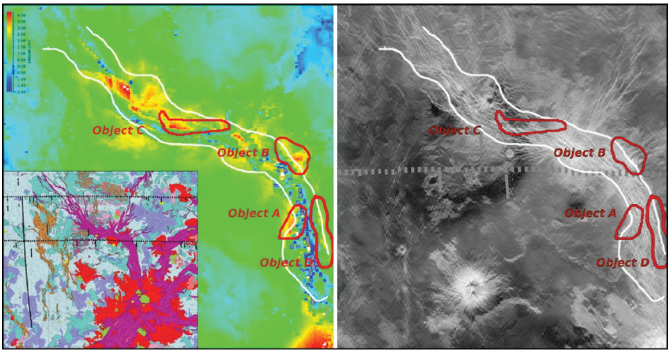


**Fig. 1.**GanikiChasma rift zone (white outlines) with four areas of bright spots (red outlines) on the background of the Magellan topographic map (left) and SAR image (right). In the inlet in the left part of the figure is shown a fragment of geologic map of this region by Ivanov and Head [1]. Rift zones are shown in violet, young volcanics - in red.

VMC performed 36 observational sessions in this area. From these data we constructed orbital mosaics and compiled maps of relative surface brightness. During the systematic analysis of these maps we found four bright features that are present at the same locations in several subsequent orbits, but that disappear afterwards (Fig. 1 and 2). These bright spots are detectable in the original VMC images and mosaics, but the contrast in the relative surface brightness maps (Fig. 2) is higher because altitude-related effects have been removed making the bright spots even more visible.

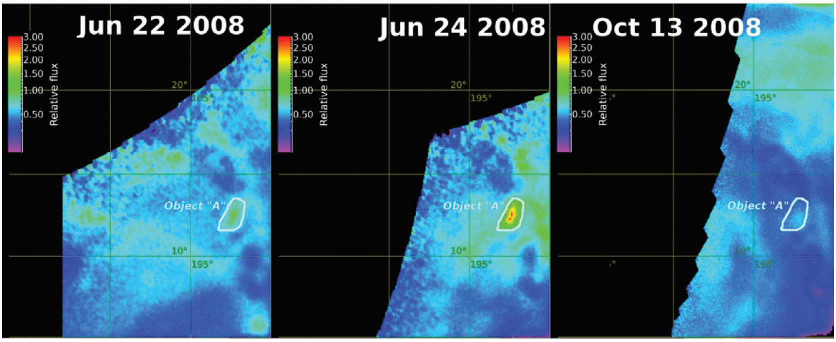


**Fig. 2.** The surface brightness maps for object A for 3 observation sessions: June 22 2008 – the hot spot is slightly visible, June 22 2008 – the hot spot is prominent, June 22 2008 – the hot spot is not visible.

The bright spots are located at the edges of the stratigraphically recent tectonic rift zone, GanikiChasma [e.g., 1,6]. The most prominent feature ("A") is seen in mosaics from VEx orbits 793 and 795. The next observation here was obtained from orbit 903, 108 days afterwards, and showed no anomalous brightness. Two additional bright spots ("B" and "C") behave in a similar way: they are bright in images obtained from two or three subsequent orbits and are not visible in orbits prior to or after these detections. Object "D" was imaged under conditions that do not permit the certain identification of change.

We considered the possibility that the bright spots might represent explosive eruptions but favor effusion because 1) the very high atmospheric pressure significantly inhibits explosive activity, 2) explosive eruptions are favored from edifices, rather than rifts, 3) candidate examples of explosive volcanic deposits are very rare in the geologic record, and 4) the linear alignment with the rift is more consistent with lava flows.

We modeled the abundance and geometry of surface thermal anomalies (hot spots) of extrusive volcanic origin that might be causing the bright anomalies and found that a few hot spots with an area of ~1 km$^2$ each and temperatures up to ~1100 K can explain brightening in VEx orbits 793 and 795 (object "A"). Small spots with temperatures up to ~950 K and larger areas up to 200 km$^2$ at 800 K can explain features observed in orbits 1147 and 1148 (objects "B" and "D"). These dimensions are similar to a wide variety of common active eruption phenomena (lava flows, lava channels, ponded parts of lava flows, and lava lakes)[7] and thus can readily explain the bright spot magnitudes above the ambient surface background. Similar configurations are well known in areas of active volcanism on Earth, and are observed elsewhere on Venus in older deposits [2].

We also considered potential artificial causes of the observed bright spots: (1) Bright spots caused by the camera – bad pixels. Butthe spots are present in several VMC images ineach considered orbit. The spacecraft rotates/moves during the imaging, so inevery other image a given point at the surface is registered in differentpixels. (2) Incorrect pointing information in the region with large altitude gradients. Butin this case,every artificially bright spot should be coupled with an artificial dark"ghost", whilethis is not observed. (3) "Holes" in the clouds. In the super-rotating atmosphere of Venus it is unlikely that a holewould not move for several tens of hours, but just change shape andtransparency.

**Summary:** The characteristics and behavior of the bright spots consideredsuggest that they represent the volcanic eruption of lava onto the surface of Venus, causing transient thermal anomalies.The detection of current volcanic eruptions in Venus Express VMC images indicates that the AtlaRegio rise area is presently geologically and geodynamically active and that historically observed variations in atmospheric chemistry [8] could be due to active volcanic eruptions. AtlaRegio should receive priority in terms of future Venus exploration and change detection experiments.

**References:**

[1] Ivanov & Head. Planet. Space Sci. 59, 1559–1600 (2011). [2]. Ivanov& Head. Planet. Space Sci. 84, 66-92 (2013). [3]Smrekar et al. Science 328, 605–608 (2010).[4]Bondarenko et al. Geophys. Res. Lett. 37, L23202 (2010). [5] Markiewicz et al. Planet. Space Sci. 55, 1701–1711 (2007). [6]Basilevsky.Geophys. Res. Lett. 20, 883–886 (1993). [7]Pyle, D. M., Sizes of volcanic eruptions, in *Encyclopedia of Volcanoes* (H. Sigurdsson, ed. in chief), 263-269, Academic Press (2000).[8] Esposito.Science 223, 1072-1074 (1984).

# NEW CONSTRAINTS ON RESURFACING HISTORY OF VENUS FROM IMPACT CRATERS

**M. A. Kreslavsky[1,2], M. A. Ivanov[3,4], J. W. Head[3],**
*[1]University of California - Santa Cruz, Santa Cruz, CA, USA,*
*[2]MIIGAiK, Moscow, Russia,*
*[3]Brown University, Providence, RI,USA,*
*[4]Vernadsky Institute, Moscow, Russia.*
*Contact: mkreslav@ucsc.edu*

**Introduction:**

Because of atmospheric shielding and endogenic resurfacing, the population of impact craters on Venus is small (about a thousand) and consists of large craters. This population has been used in numerous studies with the goal of deciphering the geologic and geodynamic history of Venus. The global spatial distribution of craters is statistically indistinguishable from a uniformly random distribution on a sphere. This means that the mapping of crater density alone cannot be used as a tool in geological analysis: any observed variations in local crater density may be attributed to random fluctuations due to the stochastic nature of crater emplacement. However, with addition of other information, crater statistics can still be useful for deciphering resurfacing history. In a number of works, the authors have modeled resurfacing on Venus as a time-varying random sequence of schematized volcanic and/or tectonic events that obliterate and/or modify impact craters concurrently with their emplacement. Another approach, which is consistently used in the present work, treats the resurfacing history as determined (although unknown) and only cratering is random. In comparison to a similar work by Price et al. (1996) the present work is more robust in the following ways: (1) we take advantage of the much more detailed geological map of Venus; (2) we distinguish geological units that predate and postdate each individual crater; (3) we rigorously account for the large size of craters.

**Methodology:**

*Geological information.* We used 1:15M scale global geological map of Venus (Ivanov and Head, 2011). This map contains the following geomorphological units listed in general stratigraphic order from the oldest to the youngest (see more detailed description in Ivanov and Head, 2011): t, tessera; pdl, densely lineated plains dissected by numerous subparallel narrow and short lineaments; pr, ridged plains comprising elongated belts of ridges; mt, mountain belts around Lakshmi Planum; gb, groove belts, plain material contemporaneous or predating regional plains and deformed by groove belts; psh, shield plains having numerous small volcanic edifices and locally predating regional plains; $rp_1$, regional plains, lower unit, mostly uniformly radar-dark, deformed by wrinkle ridges; $rp_2$, regional plains, upper unit, radar-bright plains superposed on $rp_1$ and deformed by wrinkle ridges; sc, shield clusters, morphologically similar to psh but occurring as small patches that postdate regional plains; ps, smooth plains of uniformly low radar brightness occurring near impact craters and at distinct volcanoes; pl, lobate plains, fields of lava flows that typically are not deformed by tectonic structures; rz, rift zones. Areas of these units are shown in **Fig. 1** with black columns; note log scale on the area axis in Fig. 1.

For each crater on Venus, one of us, M.A.I., registered unit(s) superposed by the crater and its continuous ejecta (that is units that predate the crater) and unit(s) that embay the crater (postdate it). This is done with the Magellan radar mosaics very uniformly and with complete consistency in unit definitions with the geological map. Of the 965 craters on Venus, 948 have sufficient Magellan image coverage and are used in this contribution; for these craters, a total of 1439 superposition relationships and 67 embayment relationships are registered. This information is used for the statistical analysis in the present contribution.

*Statistical inference.* We perform a statistical analysis of this set of observations with a buffered crater density approach, which rigorously and consistently takes into account the large size of craters and the fact that craters are known to predate and/or postdate more than one unit. For each unit there is a target area ("buffer"), where a projectile should hit to make age relationship between the unit and the crater distinguishable. This area is a function of crater size. Being convolved with the crater size-frequency distribution6 this function gives an effective area for each unit. These areas are shown with gray columns in

**Fig. 1** and are used for age inferences. Details and justification of this approach will be published elsewhere (Kreslavsky et al., 2014). The analysis yields formal confidence intervals for the mean ages of geological units. Craters superposed over one unit and embayed by another unit are treated in an analogous way: target areas for boundaries between pairs of units are used to derive effective areas and confidence intervals for the local mean age differences between unit pairs.

**Primary results:**

*Size-frequency distributiuons.* If we take the dependence of the target area on crater size into account, as outlined above, the size-frequency distributions of craters superposed on each unit turn out remarkably consistent with each other with a single exception. The exception is unit $rp_2$, which has a statistically significant excess of large superposed craters. We suggest that large craters and identification of $rp_2$ are not independent: in the broad vicinity of some large superposed craters, the $rp_2$ cannot be identified as such and is mapped as $rp_1$ instead. This leads to an apparent deficiency of large craters on $rp_2$. A possible mechanism of this is the following: A large impact event ejects a significant volume of fine-grained material forming extensive deposits known (for the youngest craters) as radar-dark parabolas and haloes. With time the radar-dark signature of the haloes and parabolas fades away by some mechanism(s), while the deposit itself remains in place and obscures pre-impact radar signatures. This prevents identification of $rp_2$ in some areas where $rp_2$ would be visible if the crater-related deposits were absent. For age inferences units $rp_2$ and $rp_1$ were merged into a single regional plain unit rp.

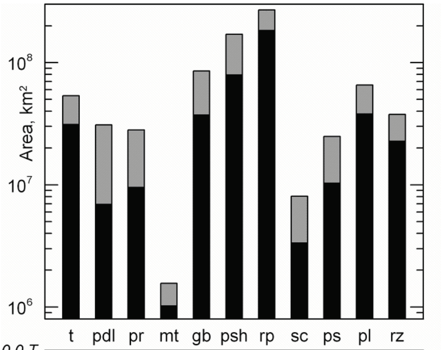


**Fig. 1**

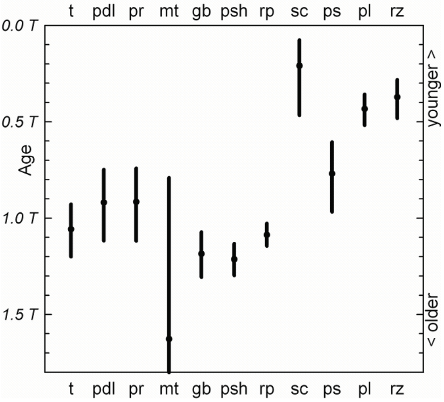


**Fig. 2**

*Mean crater retention ages.* **Fig. 2** shows 90% confidence intervals for the mean crater retention ages of all units. Ages are given in terms of *T*, the mean crater retention age of the entire observed population. *T* is poorly constrained and bracketed between 0.2 and 1 Ga (McKinnoin et al., 1997). It is seen in Fig. 2 that that there is a group of older units (t, pdl, pr, mt, gb, psh, rp) and a group of significantly younger units (sc, pl, rz), with ps occupying an intermediate position. The observed mean crater retention ages, taking the 90% confidence intervals into account, do not contradict the documented stratigraphic relationships between the units (Basilevsky and Head, 1998, Ivanov and Head, 2011). The difference between the mean age of any younger unit and any older unit is statistically significant and consistent with the observed stratigraphic relationships. This difference is also consistent with previously reported young crater retention ages of lobate plains (Price et al. 1996). Within each of the two unit groups the age differences are not statistically significant and thus do not con tradict the observed stratigraphic relationships.

*Mean age intervals.* Craters superposed on one unit and embayed by material of another unit provide constraints on the mean interval between local emplacement of the units. With a single exception, all such mean intervals are consistent with the difference in the mean ages from Fig. 2, taking the wide confidence intervals into consideration. The only exception is again related to the $rp_2$ unit: there are no craters superposed on $rp_1$ and embayed by $rp_2$. This observation is consistent with our explanation for the anomalous size-frequency distribution of craters superposed over $rp_2$ (see above).

Combining several units allows obtaining tighter age constraints. The mean interval between combined pre-rp units (t, pdl, pr, mt, gb, psh) and rp is bracketed between 0.08*T* and 0.15*T* (90% confidence), while mean interval between rp and combined younger volcanic units (ps, sc, pl) is bracketed between 0.46*T* and 0.75*T*.

**Interpretation:**

*Resurfacing history*. Our analysis reveals three robust facts about the relationships between craters and morphological units: (1) all size-frequency distributions are consistent with each other; (2) all units stratigraphically older than regional plains have a mean age close to that of regional plains; (3) all units stratigraphically younger than regional plains have a mean crater retention age significantly younger than the regional plains. These three facts are naturally and consistently explained in the framework of the directional geological evolution of Venus a.k.a. global resurfacing scenario (e.g., Basilevsky et al. 1997): (1) After ~*T* ago the overall resurfacing was minor, the total number of obliterated craters was minor, therefore preferential removal of small craters was negligible, and all size-frequency distributions are consistent with the production distribution. (2). Intensive tectonic and volcanic resurfacing before ~*T* ago is responsible for similar mean ages of the regional plains rp and all pre-rp units. (3) Formation of the post-rp units occurred slowly through the whole geological history after ~*T* ago, which produces ages close to ~0.5*T*, which is actually observed. The constraints on local time intervals between old units are not consistent with the catastrophic version of the global resurfacing (Schaber et al. 1992).

Crater densities alone give no constraints on synchronicity of the change in resurfacing style over the planet. However, analysis show that our primary results are very difficult to reconcile with the non-directional geological history (Guest and Stofan, 1999), a.k.a. equilibrium resurfacing.

*Surficial deposits*. Evidence for extensive surficial deposits associated with large old craters comes from the anomalous size-frequency distribution of craters superposed over regional plain subunit $rp_2$ and lack of craters embayed by it.

*Constraints on climate change*. The observed consistency of the crater size-frequency distributions of younger pl and older rp indicates that the atmospheric pressure was about constant during ~*T*.

**References:**

Basilevsky, A.T., Head, J.W. (1998) J. Geophys. Res. 103, 8531-8544.
Basilevsky, A.T. et al. (1997) In: Venus II, 1047.
Guest, J.E., Stofan, E.R. 1999. Icarus 139, 55-66.
Ivanov, M. A. and Head, J.W. (2011) Planetary Space Sci. 59, 1559-1600.
Kreslavsky, M. A. et al. (2014) Icarus, submitted manuscript.
McKinnon, W.B.,et al. (1997) In: Venus II, 969-1014.
Price, M.H. et al. (1996) J. Geophys. Res. 101, 4657-4672.
Schaber, G.G., et al. (1992) J. Geophys.Res. 97, 13257.

# BISTATIC RADAR INVESTIGATION OF THE NORTH AND SOUTH POLES SURFACE OF VENUS USING REANALYSIS OF VENERA'S 15 AND 16 DATA

**A.G.Pavelyev, R.R. Salimzjanov**
*Kotel'nikov Institute of Radio Engineering and Electronic of Russian Academy of Sciences, Fryazino Branch, Russia;*
*Contact: y.o.v@mail.ru*

1983, 1984 Venera 15 and 16 SAR observations were accompanied with bistatic radar experiments. Bistatic radar was aimed to test at wavelength 32 cm the refractive properties of the lower atmosphere and main electromagnetic and structural surface features of the North and Sourth polar areas of Venus at near grazing scattering angles in the 9°–11° interval. Results obtained near the North pole have been published earlier in 1990. Here we present reanalysis of unpublished bistatic radar data obtained in the South polar regions in the 73°–77°*S* latitude interval. These data are compared with the Magellan mapper images. Bistatic radar enabled us to infer the surface rms slopes and reflectivity. It is well known that, in general, the Venus' surface is more smother than the surfaces of Mars or Moon. Some locations in the North pole area were found to have the rms slope as low as 0.1°. The mean surface rms slopes inherent to the observed South pole areas vary in the 0.4°–0.7° interval on the horizontal scale 10-5000m. Reflectivity in these regions changes in the 0.2…0.4 interval, sometimes reaching the large values 0.5…0.55. High values of reflectivity seem to be consistent with focusing effect of large-scale relief.

**Acknowledgements.**

This study has been partially supported by the Program 22 of the Presidium of RAS "Fundamental Problems of research and exploration of the Solar System."

# PHYSICS OF PLANETANS — OCEANIC PLANETS

**L. Ksanfomality**

The development of principles, systems, and instruments enables the detection of exoplanets with 6–8 Earth masses or less. In terms of their masses, planetans (oceanic planets) should be placed between Earth-like rock planets and gas-and-liquid ice giants, like “hot neptunes” exoplanets. Physical properties of planetans can be predicted theoretically under definite specified conditions. For example, the depth of the ocean bounded by its adiabatic gradient can be predicted using the mass and thermodynamic characteristics of the planet; a model of outer spheres of an oceanic planet can be constructed based on the comparison between experimental data and theoretical studies. Major characteristics of planetans should be as follows. Their masses should be lower than 6–9 $M_E$ (Earth masses). Planetans are not able to retain $H_2$–He atmospheres, in which they differ dramatically from hot neptunes.

# NEW INSTRUMENTS FOR PLANETARY MINERALOGY

**M. Díaz-Michelena,**
*INTA, Ctra. Torrejón – Ajalvir km 4, Spain.*
*Contact: diazma@inta.es*

**Introduction:**
Mars and the Moon are magnetic. Crustal and surface rocks of Mars and the Moon show distinct magnetic signatures. This reflects local variations of the magnetic carriers which have been formed during its earliest formation period. During the geological history these magnetic signatures have been modified by impact, hydrothermal and volcanic processes. Thus, an improved magnetic mapping and understanding of its magnetic signatures may provide substantial information on its geological history.

There are several instruments that provide mineralogical information about the soil. Miniaturized magnetometers have been proven to be useful candidates for the measurement of crustal magnetic anomalies on terrestrial analogues (M. Díaz-Michelena & R. Kilian). For an improved understanding of the complex planetary magnetic signatures it is important to analyse Koningsberger ratios: relation between remanent and induced magnetization, and the magnetization structure of the rocks.

Magnetic instrumentation is generally avoided on board landers and rovers because in order to discern between the soil or rocks and the rover magnetic signatures, strong requirements are imposed to the mission.

In this presentation we will discuss about a magnetic solution to the problem: an instrument with an envelope of 1 kg and 3.5 W, relaxed magnetic cleanliness requirements and the capability to perform measurements of:

1) The magnetic susceptibility of the rocks
2) Their Natural Remanent Magnetization (NRM)
3) Magnetization of the progressively demagnetized states
4) Anisotropic Remanent Magnetization (ARM)

with the ultimate goal to give a number of the Koningsberger ratio and to derive features of the ancient magnetizing field.

Based on INTA experience on magnetometers, we propose a new generation of instruments capable to make a considerable progress in the field of planetary magnetometry.

# DEVELOPMENT OF A TELESCOPE FOR OBSERVATION OF THE LUNAR ROTATION AND EXPERIMENTS ON THE GROUND

**H.Hanada[1,2],S. Tsuruta[1], K. Asari[1], H. Araki[1,2], H. Noda[1,2], S. Kashima[1], K. Funazaki[3], A. Satoh[3], H. Taniguchi[3], H. Kato[3], M. Kikuchi[3], R. Yokokawa[3], S. Shinke[3], N. Petrova[4,5], A. Gusev[4]**
*[1]RISE Project, National Astronomical Observatory, Oshu, Iwate 023-0861, Japan;*
*[2]Department of Astronomical Science, The Graduate University for Advanced Studies (SOKENDAI), Mitaka, Tokyo 181-8588,Japan;*
*[3]Faculty of Engineering, Iwate University, Morioka 020-8550, Iwate, Japan;*
*[4]Kazan Federal University, Kazan 420008, Russia;[5]Kazan State Power Engineering University, Kazan 420066, Russia*
*Contact:hideo.hanada@nao.ac.jp*

**Introduction:**

Geodetic observation of the Moon, such as the lunar rotation, the gravitational fields and tidal deformation, is one of the essential and basic observations for investigating the interior of the Moon.We are developing also a small telescope like Photographic Zenith Tube (PZT) for observations of the lunar rotation through positioning of stars on the Moon with a target accuracy of 1 milliarcsecond (mas) as an ILOM project.

**Development of a Telescope for ILOM**

We have alreadydeveloped a bread board model (BBM) of a PZT type telescope for basic experiments of ILOM. Technical development for improvement of the accuracy, environmental test of key elements were made by using the BBM.We improved the BBM for aiming at observations on the ground. A new tripod makes it possible to set the telescope on the slope of less than 30 degrees. PZT has a potential to observe deflection of the vertical (DOV) with an accuracy better than 0.1 arcseconds. It will be possible to reduce the effect of atmospheric turbulence to be smaller than 0.1” by statistical procedure of observed data. It seems to be also possible to reduce the effect of the ground vibrations to be less than 0.1 arcsecondsif we correct for the variation of the centroid by using vibration data.The relation between the centroid variation and the ground vibrations, however, can be different according to the condition on the ground. The optimum method for the correction is adevelopment issue.

We will perform observations on the ground in order to check the total system of the telescope and the software. It is also important to evaluate the effect of the ground vibrations and temperature change upon the stellar position on CCD. The goal of the observations on the ground is to attain the accuracy of better than 0.1 arcseconds. Verification of 1 mas on the Moon will be possible in a laboratory equipped with a special space chamber providing the environment on the Moonin the future.

# MERCURY MAGNETOSPHERE

**I. Alexeev**
*Scobeltsyn Institute of Nuclear Physics, Lomonosov Moscow State University*

Till now the MESSENGER spacecraft completed more than 3400 orbits of the Mercury and we have more than $10^7$ points inside the Mercury magnetosphere where MESSENGER magnetometer measured the magnetic field vector. Based on these data the global magnetospheric current systems can be determined. Reconnection effects between IMF and magnetospheric field in the case of the Mercury have been studied. Deficit of the measured by MESSENGER magnetic field relative the model field give estimation of the plasma pressure in the cusp regions and in the tail plasma sheet. By extracted the inner magnetic field can be used to test a planetary dynamo model. The time series of the measurement during the 8 Mercurian years (or 3 Earth years) give possibility to estimate the secular planetary magnetic field variations. The proposed model determined not just inner magnetospheric field but also can be used to compare with measured magnetosheath magnetic field to understand the IMF compression and draping in the course of the solar wind flowing past the Mercury magnetosphere.

# LIFE ORIGINATION HYDRATE THEORY (LOH-THEORY): THE REACTION MECHANISM AND SET OF NECESSARY AND SUFFICIENT CONDITIONS

**V. E. Ostrovskii[1], E. A. Kadyshevich[2],**
*[1]Karpov Institute of Physical Chemistry, Vorontsovo Pole 10, Moscow, 105064 Russia;*
*[2]Obukhov Institute of Atmospheric Physics, Pyzhevsky 3, Moscow, 119017 Russia.*
*Contact: vostrov@cc.nifhi.ac.r;ostrovskii.victor@mail.ru*

**Introduction:**

The Life Origination Hydrate Theory (the LOH-Theory) [1–14] is the original one and has no common features with any other theory that considers mysterious origination of this phenomenon. This theory was presented at different steps of its development at about 30 international physical, chemical, thermodynamic, biological, geological, and specialized conferences in the form of lectures or oral presentations. The LOH-Theory gives the life origination mechanism realizable at any celestial body where appropriate conditions exist.

**The content of the LOH-Theory**

The LOH-Theory considers the life origination process as a sequence of thermodynamically caused regular and inevitable chemical transformations regulated by universal physical and chemical laws. The LOH-Theory bears on a number of experimental, thermodynamic, observation, and simulation researches. N-bases, riboses, nucleosides, and nucleotides and DNAs and RNAs formed repeatedly within structural cavities of localizations of underground and underseabed honeycomb $CH_4$-hydrate deposits from $CH_4$ and nitrate- and phosphate-ions that diffused into the hydrate structures; proto-cells and their agglomerates originated from these DNAs and from the same minerals in the semi-liquid soup after liquation of the hydrate structures. Each localization gave rise to a multitude of different DNAs and living organisms. The species diversity is caused by the spatial and temporal repeatability of the processes of living matter origination under similar but not identical conditions, multiplicity of the DNA forms in each living matter origination event, variations in the parameters of the native medium, intraspecific variations, and interspecific variations. The contribution of the last in the species diversity is, likely, significant for prokaryotes and those eukaryotes that are only at low steps of their biological organization; however, in the light of the LOH-Theory, of available long-term paleontological investigations, and of studies of reproduction of proliferous organisms, we conclude that, in toto, the contribution of interspecific variations in the species diversity was earlier overestimated by some researchers. The reason of this overestimation is that origination of scores of «spores» of different organisms in any one event and multiple reproductions of such events in time and Earth's space were not taken into consideration. The thermodynamic grounds and the reaction mechanisms that lie in the ground of the LOH-Theory are detailed.

The principal scheme of the living matter origination process according to the LOH-Theory is as follows.

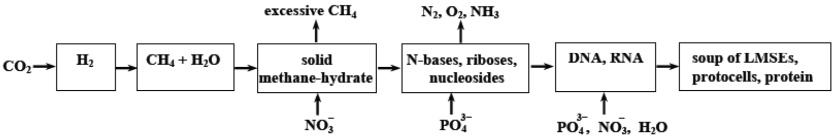


**Acknowledgements**

The work is supported by the Russian Foundation for Basic Research, project no. 12-05-01082-a.

**References**

1. Ostrovskii V.E., Kadyshevich E.A., Use of data on the polyacrylamide–water system in analyzing the equilibrium DNA–water structure, Russ. J. Phys. Chem., 74 (2000) 1114-1124.
2. Ostrovskii V.E., Kadyshevich E.A., Hydrate model of the equilibrium DNA—water systems, Int. J. Nanosci., 1 (2002) 101-121.
3. Ostrovskii V.E., Kadyshevich E.A., Thermodynamics of formation of nitrogen bases and D-ribose from mineral substances, Thermochim. Acta, 441 (2006) 69-78.

# THE EXOMARS PROGRAMME

**O. Witasse1, J.L. Vago, and D. Rodionov,**
*Research and Scientific Support Department of ESA, ESTEC, PO Box 299, 2200 AG Noordwijk, the Netherlands*
*Contact: Olivier.Witasse@esa.int*

The ExoMars Programme is an ESA-ROSCOSMOS cooperation with some NASA contributions. ExoMars consists of two missions, one in 2016 and one in 2018. The 2016 mission includes two elements: the Trace Gas Orbiter, an orbiting satellite devoted to the study of atmospheric trace gases, with the goal to acquire information on possible on-going geological or biological processes; and a European Entry, Descent, and landing Demonstrator Module named Schiaparelli, to achieve a successful soft landing on Mars. The orbiter will also provide data communication services for all surface missions landing on Mars until end 2022. The mission will be launched in January 2016, using a Proton rocket, and will arrive to Mars in October 2016. The 2018 mission will deliver a 300-kg-class rover and a landed platform to the surface of Mars using a landing system developed by Roscosmos. The mission will pursue one of the outstanding questions of our time by attempting to establish whether life ever existed, or is still present on Mars today. The rover will explore the landing site's geological environment and conduct a search for signs of past and present life, collecting and analysing samples with the Pasteur payload suite from within rocky outcrops and from the subsurface, down to a depth of 2m, using a drill. The platform will carry scientific measurements at the landing site. This presentation will describe the present status of the ExoMars project, the missions' profile, and the various elements' payload. ExoMars can be considered as a preparatory step for the future realisation of an international Mars Sample Return (MSR) campaign.

# FREQUENCY MATTERS: ISAS'S STRATEGY FOR SMALL BUT EDGY PLANETARY EXPLORATIONS

**M. Fujimoto[1],**
[1]*Institute of Space and Astronautical Science, Japan Aerospace Exploration Agency, 3-1-1 Yoshinodai, Chuo-ku, Sagamihara 252-5210, Japan*
*Contact: fujimoto.masaki@jaxa.jp*

What is clearly stated in the roadmap issued by ISAS, JAXA in 2013 is that operation of frequent small-scale planetary exploration program will be one of the pillar activities of the institute in the next 10~20 years. ISAS has categorized its spacecraft missions in to three categories: H-2A/H3 class missions to be launched by the biggest Japanese launcher, Epsilon class missions to be launched by the recently developed launcher of Epsilon and its future enhanced models, and the Mission of Opportunity category that assumes participation in foreign missions at the level of providing a (part of) science payload. Epsilon-class missions are considered to bread-and-butter for the institute and planned to be launched every two year. Epsilon launcher, when the future enhancement program is completed, will become able to bring ~500kg orbiters to Venus/Mars and a spacecraft of a similar size for rendezvous exploration of a near-Earth asteroid. That is, frequent small-scale planetary explorations will become doable by Epsilon, and they will certainly be worth of it if their objectives are edgy in terms of planetary sciences and if the mission shapes are edgy in terms of space technology. Indeed it has been the style of ISAS that the engineering and the science divisions work together to realize an exploration mission that would never happen without the closely combined effort. When this highest level statement is given, the question to ask is: What do the Epsilon class planetary exploration missions look like? In this talk, I will review the results of the study that has been performed to see the right-size-capability that should be requested to the Epsilon enhancement program and what new technology should be developed and be utilized on the spacecraft building side.

# PHOBOS SAMPLE RETURN: NEXT APPROACH

**L. Zelenyi[1], A. Zakharov[1], O. Korablev[1], A. Patrakeev[1], M. Martynov[2], A. Ivanov[2],**
*[1]Space Research Institute of RAS, Moscow, Russia,*
*[2]Lavochkin Association, Federal Space Agency, Khimki, Russia*

The Martian moons still remain a mystery after numerous studies by Mars orbiting spacecraft.

Their study cover three major topics related to (1) Solar system in general (formation and evolution, origin of planetary satellites, origin and evolution of life); (2) small bodies (captured asteroid, or remnants of Mars formation, or reaccreted Mars ejecta); (3) Mars (formation and evolution of Mars; Mars ejecta at the satellites). As reviewed by Galimov [2010] most of the above questions require the sample return from the Martian moon, while some (e.g. the characterization of the organic matter) could be also answered by in situ experiments. There is the possibility to obtain the sample of Mars material by sampling Phobos: following to Chappaz et al. [2012] a 200-g sample could contain 10-7 g of Mars surface material launched during the past 1 mln years, or 5*10-5 g of Mars material launched during the past 10 mln years, or 5*1010 individual particles from Mars, quantities suitable for accurate laboratory analyses.

The studies of Phobos have been of high priority in the Russian program on planetary research for many years. Phobos-88 mission consisted of two spacecraft (Phobos-1, Phobos-2) and aimed the approach to Phobos at 50 m and remote studies, and also the release of small landers (long-living stations DAS). This mission implemented the program incompletely. It was returned information about the Martian environment and atmosphere. The next profect Phobos Sample Return (Phobos-Grunt) initially planned in early 2000 has been delayed several times owing to budget di_culties; the spacecraft failed to leave NEO in 2011. The recovery of the science goals of this mission and the delivery of the samples of Phobos to Earth remain of highest priority for Russian scienti_c community. The next Phobos SR mission named Boomerang.

# STANDING SHEAR ALFVEN WAVES DRIVEN BY THE JUPITER DIPOLE WOBBLING

**I. Y. Vasko[1], A. V. Artemyev[1], L.M. Zelenyi[1], S. Kasahara[2]**
*[1]Space Research Institute (IKI), 84/32 Profsoyuznaya Str, Moscow, Russia;*
*[2]Institute of Space and Astronautical Science JAXA,Japan.*
*Contact: vaskoiy@yandex.ru*

**Introduction:**

We present Galileo observations of 10 h periodic variations of azimuthal and radial magnetic fields in the Jovian magnetotail (at X<-40 RJ, where the Jupiter Solar Equatorial (JSE) system is used). The radial magnetic field variations correspond to the magnetotail flapping motion generated by the diurnal Jupiter dipole wobbling. The azimuthal magnetic field variations are phase shifted with respect to the radial variations by a quarter of the period. The azimuthal magnetic field has maximum in the magnetotail neutral sheet and its amplitude is comparable with the amplitude of the radial magnetic field. We suggest that azimuthal variations represent the manifestation of shear waves standing along magnetotail flux tubes and driven by the dipole wobbling. The large amplitude of observed azimuthal variations could be attributed to the shear wave standing along the resonant flux tube. We have found that azimuthal magnetic field variations are associated with flat plasma density profiles across the magnetotail current sheet. We suggest that the flattening of the plasma density profile is due to the action of the ponderomotive force induced by standing shear waves.

# CHEMICAL COMPOSITION OF TITAN'S ATMOSPHERE: OBSERVATIONS AND THE PHOTOCHEMICAL MODEL

**Vladimir A. Krasnopolsky[1,2],**
*[1]Catholic University of America, Washington, DC 20064, USA; [2] PhysTech, Moscow, Russia.*
*Contact: vlad.krasn@verizon.net*

**Introduction:**

The last version of the self-consistent photochemical model of Titan's atmosphere and ionosphere [1] is a convenient tool for various aspects of Titan's chemical composition. Here the model results will be compared with observations, including the recent detection of propylene [2], some results from Hershel [3-5], and previous retrievals [6-12].

**Main Features of the Model:**

The model is aimed to reduce the numbers of species and their reactions to those that are essential and involves 420 reactions of 83 neutrals and 33 ions. The initial data are restricted to temperature and eddy diffusion profiles and $N_2$, $CH_4$, and Ar densities near the surface.

Photochemistry is driven by the solar EUV and UV, magnetospheric electrons, protons, $O^+$, meteorite $H_2O$, and cosmic rays. Vertical transport involves eddy, molecular, and ambipolar diffusion. Thermal escape and escape of ions by the rotating magnetosphere of Saturn are the upper boundary conditions. The model accounts for polymerization and condensation of species. Vertical profiles of all neutrals and ions up to 1600 km are the modle products.

**Model Results and Observations**

Propylene $C_3H_6$ abundances recently retrieved [2] from the CIRS limb spectra are in excellent agreement with the model prediction. Chemistry of $C_3H_6$ involves 23 reactions in our model, and 5 main processes are shown in the figure. The production peaks at 150 km, where chemistry is determined by transport of photochemical products from ≈500 km, cosmic rays, and condensation. The model agrees with the INMS as well.

Basic observational data on hydrocarbons, nitriles, and ions on Titan are compared with predictions of the photochemical model. Uncertainties of the observed abundances and differences between the data from different instruments and observing teams are comparable with the differences between the observations and the model results. Main reactions of production and loss for each species are quantitatively assessed and briefly discussed. Formation of haze by polymerization of hydrocarbons and nitriles and recombination of heavy ions is calculated along with condensation of various species near the tropopause. Overall deposition is a layer of 300 m thick for the age of the Solar System, and nitrogen constitutes 8% of the deposition. The model reproduces the basic observational data and adequately describes basic chemical processes in Titan's atmosphere and ionosphere. The presented model results and the observational data may be used as a reference to chemical composition of Titan's atmosphere and ionosphere.

**References:**

[1] Krasnopolsky V.A. (2012) *PSS 73*, 318-326. [2] Nixon C.A. et al. (2013) *ApJ 776,* L14. [3] Moreno R. et al. (2012) *Icarus 221,* 753-767. [4] Teanby N.A. et al. (2013) *PSS 75*, 136-147. [5] Rengel M. et al. (2014) *A&A 561*, A4. [6] Koskinen T.T. et al. (2011) *Icarus 216*, 507-534. [7] Niemann H.B. et al. (2010) *JGR 115*, E12006. [8] Kutepov A.A. et al. (2013) *DPS abstract.* [9] Vinatier S. et al. (2010) *Icarus 205*, 559-570. [10] Magee B.A. et al. (2009) *PSS 57,* 1895-1916. [11] Cui J. et al. (2009) *Icarus 200*, 581-615. [12] Vuitton V. et al. (2007) *Icarus 191,* 722-742.

# IS THERE LIFE IN SUBSURFACE OCEANS OF JOVIAN MOONS? THE BOREHOLE FROZEN WATER OF THE SUBGLACIAL LAKE VOSTOK (EAST ANTARCTICA) AND ITS MICROBIAL CONTENT

**S. Bulat[1], M. Khilchenko[1], D. Karlov[1], L. Demchenko[1], M. Doronin[1], D. Marie[2],**
*[1]Petersburg Nuclear Physics Institute, NRC "Kurchatov Institute", St. Petersburg-Gatchina, Russia;*
*[2]Station Biologique de Roscoff, Roscoff Cedex, France.*
*Contact: bulat@omrb.pnpi.spb.ru*

The objective was to estimate microbial content and diversity in the subglacial Lake Vostok (buried beneath 4-km thick East Antarctic ice sheet) by studying the uppermost water layer which entered the borehole upon lake entry (February 5, 2012) and then shortly got frozen within. The samples of so-called drillbit water frozen on a drill bit upon lake enter (RAE57) along with re-drilled so-called borehole-frozen water (RAE58) were provided for the study with the ultimate goal to discover the life in this extreme icy environment.

The comprehensive analyses (constrained by Ancient DNA research criteria) of the first lake water samples - drillbit- (one sample) and borehole-frozen (3 different depths 5G2-1N-3425, 3429 et 3450m), are got finished. If the drillbit water sample was heavily polluted with drill fluid (at ratio 1:1), re-drilled borehole-frozen samples were proved to be rather clean but still strongly smelling kerosene and containing numerous micro-droplets of drill fluid giving the 'milky' ice.

The cell concentrations measured by flow cytofluorometry showed 167 cells per ml in the drillbit water sample while in borehole-frozen samples ranged from 5.5 (full-cylinder 3429m deep frozen water ice core) to 38 cells per ml (freeze-centre of 3450m deep moon-shape ice core).

DNA analyses came up with total 49 bacterial phylotypes discovered by sequencing of different regions (v3-v5, v4-v8, v4-v6 et full-gene) of 16S rRNA genes. Amongst them all (*Alphaproteobacteria* (7 phylotypes, mostly *Rhizobiaceae*), *Betaproteobacteria-Burkholderiales* (7 phylotypes), *Gammaproteobacteria* (19 phylotypes, mostly *Pseudomonadaceae*, *Moraxellaceae* and *Enterobacteriaceae*), *Actinobacteria* (6 phylotypes, mostly *Micrococcaceae* and *Microbacteriaceae*), *Firmicutes-Bacilli* (7 phylotypes), *Bacteroidetes-Flavobacteriaceae* (1 phylotype)) but two were considered to be contaminants (were present in our contaminant library, including drill fluid findings).

The 1st remaining phylotype successfully passing all contamination criteria proved to be hitherto-unknown type of bacterium (group of clones, 3 allelic variants) showing less than 86% similarity with known taxa. Its phylogenetic assignment to bacterial divisions or lineages was also unsuccessful despite of the RDP has classified it belonging to OD1 uncultured Candidate Division. The 2nd phylotype was less remarkable and still dubious in terms of contamination. It was presented by just one clone and showed 93% similarity with *Janthinobacterium sp* of *Oxalobacteraceae* (*Beta-Proteobacteria*) — well-known 'water-loving' bacteria. No archaea were detected in lake water frozen samples.

Thus, the unidentified and unclassified bacterial w123-10 phylotype for the first time discovered in the uppermost water layer in subglacial Lake Vostok might represent ingenious cell populations in the lake, making the life in the lake less elusive. The proof may come (as well as other discoveries) with farther analyses (e.g., sample screening with w123-10-specific primers) of newly requested moon-shape samples of borehole-frozen water analyses of which are ongoing. The findings will be discussed in terms of cryoastrobiology.

# NEW METHODOLOGY FOR STUDY OF THE BASIC GEODETIC PARAMETERS AND RELIEF OF OUTER PLANETARY BODIES: GALILEAN SATELLITES AND ENCELADUS

**A. Zubarev[1], I. Nadezhdina[1], V. Patraty[1], I. Karachevtseva[1], A. Kokhanov[1], N. Kozlova[1],andJ. Oberst[1,2,3]**
*[1]Moscow State University of Geodesy and Cartography (MIIGAiK), MIIGAiK ExtraterrestrialLaboratory (MExLab), Gorokhovskiy per., 4, 105064, Moscow, Russia; [2]German Aerospace Center (DLR);[3]Technical University of Berlin, Berlin, Germany, Contact: I_karachevtseva@miigaik.ru*

**Introduction.**

We have developed new methodologyto produce three-dimensional geodetic control point networks of theouter satellites.3D-networks will be used as a basic framework to obtain the fundamental geodetic parameters of the planetary bodies and study size, shape, and spin parameters, which provide studies of their surface.These results are highly significant because reliable and accurate geodetic data on global topography and spin of theouter satellitescurrently just do not exist. Obtaining quantitative constraints on libration of Galilean satellites and Enceladuswill be of especial significance, because they will give exceptionally valuable eagerly wanted information on their internal structure.

The Galilean satellites are of great interest because of the upcoming JUICE (ESA) and Laplace-P (ROSKOSMOS) missions. The control point networks and basic maps will provide the needed reference and coordinate framework to support the missions[Zubarev et al., 2014]. The creation of a control network for Enceladus is of special scientific interest because of the ongoing Cassini mission. The spacecraft collected a large number of images during a long time interval, sufficient to derive complete shape models for Enceladus and track the satellite's rotation. Currently, topographic models and basic map have been prepared only for small local and regional areas of this satellite [Nadezhdina et al., 2012, Lazarev et al., 2012].

**Methodology.**

The novelty of the proposed approach is defined by innovative solutions of several problems with unique methods based on a new automated technique for generation of 3D geodetic control networks with images from different sensors, of different scales, and taken under different illumination and observation geometry, including oblique view. For the first time global 3D control networks will be generated for satellites of the outer planets using all available data and their rotation models (rotation axis orientation and libration) will be estimated.

**Summary.**

For future mission Laplace-P [Zeleniy et al., 2013]we mainly focused on Ganymede which coverage is nearly complete except for polar areas (which includes multispectral data). Updated data collection, including new calculation of elements of exterior orientation, provides new image processing of previous missions to outer planetary system. Using our new techniques we have generated a new control point network in 3D and global orthomosaic for Ganymede. Based on improved orbit data for Galileo we have used larger numbers of images than were available before, resulting in a more rigid network for Ganymede. The obtained results we used for further processing and improvement of the various parameters: body shape parameters and shape modeling, libration, as well it will be needed for further studying of the surface interesting geomorphological phenomena, for example, distribution of bright and dark surface materials on Ganymede and their correlations with topography and slopes [Oberst et al., 2013].

We willuse the proposedmethodology for careful evaluation of all available data from the previous Voyager and Galileo missions to re-determine geodetic control and rotation model for other Galilean satellites – Calisto and Europe.

**Acknowledgements:** This work was carried out in MIIGAiK and supported by Russian Science Foundation, project #14-22-00197.

**References:** Lazarev et al.,(2012) Izv.Vyssh.Uchevn.Zaved.,Geod. Aerofotos"emka,6, pp. 9-11 (In Russian); Nadezhdina et al., (2012) Vol. 14, EGU2012-11210; Oberst et al., (2013) GLCW_3_07; Zeleniy et al, (2013) GLCW_01; Zubarev et al., (2014) B0.3-0013-14

# GRAVITY-INERTIAL MEASUREMENTS ON EUROPA- JUPITER'S MOON

**A.B. Manukin, O.N. Andreev, I.I. Kalinnikov**

If you organize Gravity-inertial measurements on the surface of Europe, could be:

- Get data on the variations of the gravitational field in Europe, on which to estimate the period and the amplitude of its libration oscillstions.
- According to the projections of changes in gravity on the axis of sensitivity of the instrument can estimate its incline, and to evaluate the deformation of the ice cover in Europe.
- Measurement of $10^{-2}$ - 10 Hz could identify inertial signals related to several factors:

a) Commencement of seismic vibrations in the ice cover Europe movement of ocean waters.
b) vibrational excitation of forming new cracks the ice cover.
c) vibrational excitation of ice cover colliding meteorites.

- Installation of a high-frequency type sensor geophone would assess the intensity of the formation of microcracks in the immediate vicinity of the lander

These tasks allow us to formulate the basic requirements for the sensitivity of the sensors, their dynamic and frequency range.

In the low frequency range ($10^{-6}$–$10^{-4}$Hz) when the device is used as a gravity meter and inclinometer sensor sensitivity should be at the level of $10^{-7}$ g, which will measure the relative measurements of the gravitational acceleration on Europe ~ $10^{-6}$ m/s$^2$ and variations of the inclination angle of about 0.2 arcsec.

Seysmogravimetr for measurements on Europe will be developed on the basis of the experience gained in the design and creation of similar devices in the "Solar Sail», «Met-net», «Phobos - Grunt".

Principle of construction may remain the same: the test mass is placed in a cylindrical shape coaxial dielectric tube and the rod with the necessary bending stiffness is connected to a part rigidly attached to the dielectric base.

For the measurements of the two horizontal components of the seismic waves and surface slope caused by including tidal processes can be virtually unchanged development of sensors for use of the "Phobos-Grunt".

In the measurement of the vertical component at the level of $10^{-7}$g requires that the natural frequency of the oscillator mechanical sensing system $\omega_0$ was about 30 rad/s. Using the same scheme of the accelerometer to measure the vertical component of the surface of Europe is impossible: the proof mass oscillator simply rested in the fixed plate measuring container.

Consider another variant of the device, similar to that used in the project Luna-Resource, with a system of putting on the local gravitational vertical.

Implementation seismogravitational measurements Europe has its own characteristics. In particular, it presents estimates of the impact of the fuel elements in the SC parasitic tilts the body.

The main expected characteristics seysmogravimetr are presented.

The possibility of using penetrators to study seismic activity in Europe.

The main parameters determining the overload impact penetrator on the planet's surface, is the speed of the penetrator $V_0$ at the surface and the path length S, where the inhibition of the penetrator. In this path length includes both the penetration of the penetrator into the soil by the amount $S_1$, and the deformation amount on the penetrator housing $S_2$, so that $S = S_1+S_2$.

The estimates of congestion, the pressure force on the dielectric test mass sensor housing and duration of exposure, dynamic load during braking penetrator are presented. It has been shown that the rate of the penetrator in contact with the surface of the satellite can not exceed a few hundred m/s ( S~1m).

It is shown that a small gap d in the capacitive sensor provides not only high steepness of the transformation of small mechanical vibrations of the proof mass into an electrical signal, but does not give enough weight to buy more speed at impact and vibration loads.

The estimates of the possibility of using a sufficiently rigid mechanical sensing systems allowing to abandon the system of putting the device on the local gravitational vertical. In this case, the sensitivity to measure the variation of the gravitational acceleration will be $\Delta g \sim 2 \cdot 10^{-5} \div 10^{-6}$ m/s$^2$, and a minimum resolution of changes in the angles of inclination of the axes of sensitivity of the instrument: $\Delta\beta \approx 1{,}7 \cdot 10^{-7}$rad$\approx 3 \cdot 10^{-2}$ arc. sec.

Response to the events of a quasi-independent of the frequency of exposure. For example, at a frequency of exposure $\Omega = 2\pi$ rad/s (1 Hz), while the natural frequency of the sensing system $\omega_0 \sim 2{,}35 \cdot 10^2$ rad/s, the minimum detectable amplitude of the oscillations base $A_{min} \approx 5.4 \cdot 10^{-9}$ m. In this case, the dynamic range of the measured oscillation housing unit at a frequency of 1 Hz is ~1.6cm.

Installing multiple penetrators could solve a number of fundamental problems, including the objectives of the study of the internal structure of Europe.

# QUASI-CAPTURE IN HILL PROBLEM

**A.B. Batkhin[1]**
*[1]Keldysh Institute of Applied Mathematics, Miusskaya sq. 4, Moscow, Russia.
Contact: batkhin@gmail.com*

**Stickiness phenomenon:**

The stickiness phenomenon occurs when an orbit positioning in the immediate vicinity of the last invariant torus remains rather close to this torus for long time before leaving it into the chaotic sea. It is a well known fact [1] that stickiness phenomenon takes place due to the presence of so called cantori which are the remain parts of the invariant tori. These tori are destroyed by the perturbation and form the Cantor sets of points on the section surface. The rotation number of cantorus is equal to the rotation number of the corresponding invariant torus and thus it is possible to approximate this cantorus with resonances of suitable multiplicity.

A cantorus forms only a partial barrier to chaotic orbits, which can penetrate into and abandon the vicinity of the last invariant torus passing through the gaps of the cantorus. Such a behavior of the chaotic orbits can be exploited for the explanation of temporary capture phenomenon[2] which we call there quasi-capture.

There are some reasons of chaotic ux minimization. The first reason is the rotation number of a cantorus. If the rotation number of a cantorus is equal to the value representing with the continued fraction of the form

$$a = \left[a_1, a_2, \ldots\right] \equiv \cfrac{1}{a_1 + \cfrac{1}{a_2 + \ldots}},$$ where $a_i=1$ for all $i>N$,

then the flux is minimal (see [1] for further references). The second reason is the presence in the vicinity of cantorus the stability islandsof the nearest resonances, which cover the gaps in it and thus forms the aditional obstacles to the flux.

**Hill problem:**

We investigate the stickiness phenomenon in the vicinity of stability islands of the family *g'* of satellite periodic orbits in planar Hill problem. This problem is an effective model using for investigation of satellite dynamic [3].

The dynamics of phase trajectories is fully determined by Hill problem Hamiltonian:

$$H(q,p) = \frac{1}{2}(p_1^2 + p_2^2) + q_2 p_1 - q_1 p_2 - q_1^2 + \frac{1}{2} q_2^2 - \frac{1}{\sqrt{q_1^2 + q_2^2}}$$

The canonical equations of motion have the only firstrst integral and they are invariant under discrete group of phase space transformations with reverse of time.

With the help of numerical simulation the stickiness region was found out in Hill problem.This region is placed in the outer space of last invariant curve and has trajectories, which make more then $10^5$ revolutions around the origin. Due to the time-reversal symmetry of equations of motion one can state that these trajectories have penetrated earlier into the stickiness region and stay there for a long time. Thus we have a basic model of quasi-capture, which is used to investigate the parameters of motion of the outer satellites of giant planet.

**Natural satellites investigation:**

The contemporary data of natural satellites of Solar system giant planets were used from the Natural Satellite Data Center of IMCCE, Paris and SAI, Moscow and from database of NASAJPL. The main parameters of the satellite orbits such as semi-major axis, eccentricity and orbit inclination were computed into the corresponding Hill unit of length equals to $\mu^{1/3}a'$, where $\mu$ isthe ratio of the mass of the planet to the total mass of Sun and the planet, *a'* is the semi-majoraxis of the planet's orbit. We have checked parameters of 59 Jupiter's outer satellites, 38 outerSaturn's outer satellites, 9 Uranus' outer satellites and 5 Neptune's outer satellites. There was found only one Jupiter's satellite S/2003 J2 which orbital motion is near the inner boundary of stability island around the family *f* of retrograde satellite orbits.

**References:**

1. C. Efthymiopoulos, G. Contopoulos and N.Voglis. Cantori, islands and asymptotic curves in the stickiness region // CM&DA, 73: 221-230, 1999.
2. G. M. Zaslavsky. Physics of Chaos in Hamiltonian Systems. Imperial College Press, 1998.
3. A. B. Batkhin, N. V. Batkhina. Hill Problem, Volgogradskoe Nauchnoe Izdattel'stvo, 2009 (in russian).

# CLASSIFICATION OF METEOR EVENTS IN THE MARTIAN ATMOSPHERE

**D. Kuznetsova[1,2], M. Gritsevich[3,4,5,2],**
*[1] Institute of Mechanics of Moscow State University, Moscow, Russia;*
*[2] Moscow State University of Geodesy and Cartography (MIIGAiK), Moscow, Russia;*
*[3] Finnish Geodetic Institute, Masala, Finland;*
*[4] Ural Federal University, Ekaterinburg, Russia;*
*[5] Dorodnicyn Computing Centre RAS, Moscow, Russia.*
*Contact: morven9@yandex.ru*

**Introduction.** Nowadays, the considerable attention is given to the studies of meteor impacts at Mars. A number of meteorites has been found on the surface of Mars [1-4]. Some attempts were made to observe meteor events in the atmosphere [5]. Moreover, in October 2014 a meteor shower on Mars is predicted [6-7]. Several studies provide the estimations of the flux rate [8-9]. The theoretical study of meteor events in the Martian atmosphere can help to obtain more details on this subject and provide new material for comparing with the future observations.

In this study, we develop the model which describes meteoroids entering the atmosphere and categorizes different possible consequences of meteor events. We focus the attention on two types of results: (1) meteorite fall, when a fragment of a meteoroid can be found on the surface, and (2) full ablation of a meteoroid in the atmosphere.

**Mathematical model and results.** The model is based on the analytical solution of the classical equations of meteor body deceleration [10-11]. The dimensionless solution for mass and height as velocity functions can be expressed using two main dimensionless parameters: the ballistic coefficient, which shows the ratio between the mass of the atmospheric column along the trajectory and the body's pre-entry mass, and the mass loss parameter, which is proportional to the ratio between the initial kinetic energy of the body and energy required to insure total mass loss of the body due to ablation and fragmentation [12-13].

As the meteorite fall condition we use the criterion that the terminal mass of a meteoroid exceeds or is equal to a certain chosen value. This condition can be written using the parameters introduced above, giving a curve in the parameter plane which divides the plane by two regions, one corresponding to meteorite fall, second to full ablation.

We consider the meteoroid entry into the Martian atmosphere. To apply our theory, we take two meteoroid types as an example: a chondrite with the entry velocity 10 km/s, and an iron meteoroid with the entry velocity 15 km/s. For each case, we take several pre-entry mass values and show the result on the parameter plane. These results are also compared with the meteoroid entries into the terrestrial atmosphere with the same pre-entry characteristics. It is shown that for some pre-entry mass range, a meteoroid would be fully ablated for the case of Earth, but a fraction of it would reach the surface for the case of Mars.

**Acknowledgements.** The development of the analytical model for Martian meteor events was carried out by DK and MG under support of the Academy of Finland No. 260027 (MG) and Russian Foundation for Basic Research, projects No. 13-07-00276 (MG) and 14-08-00204 (DK and MG). The numerical simulations and the determining of necessary parameters were done out by DK and MG at MIIGAiK and supported by the Russian Science Foundation, project No. 14-22-00197.

**References:**

[1] Beech M. and Coulson I.M. Mon. Not. R. Astron. Soc. 2010, 404, 1457-1463.
[2] Chappelow J.E. and Sharpton V.L. Geophys. Res. Lett. 2006, 33, L19201.
[3] Chappelow J.E. and Golombek M.P. Event and conditions that produced the iron meteorite Block Island on Mars. Journal of Geophys. Res. 2010, 115, E00F07.
[4] Schröder C. et al. Meteorites on Mars observed with the Mars Exploration Rovers. J. of Geophys. Res. 2008, 113, E06S22. [5] Domokos A. et al. Measurements of the meteoroid flux on Mars. Icarus. 2007, 191, 141-150. [6] Vaubaillon J. et al. Meteor hurricane at Mars on 2014 October 19 from comet C/2013 A1. Mon. Not. R. Astron. Soc. 2014, 439, 3294-3299. [7] Moorhead A.V. et al. The meteoroid fluence at Mars due to comet C/2013 A1 (Siding Spring). Icarus. 2014, 231(1), 13-21. [8] Davis, P.M. Meteoroid impacts as seismic radiation sources on Mars. Icarus, 1993, V. 105, pp. 469-478. [9] Bland, P.A., Smith, T.B. Meteorite accumulations on Mars. Icarus, 2000, V. 144, pp.21-26. [10] Stulov V.P. Applied Mechanics Reviews. 1997, 50(11), 671-688. [11] Ceplecha et al. Space Science Reviews. 1998, 84, 327-471. [12] Gritsevich M.I. et al. Cosmic Research. 2012, 50(1), 56-64. [13] Gritsevich M.I. Advances in Space Research. 2009, 44(3), 323-334.

# CALCULATION OF LINE BROADENING COEFFICIENTS AND TEMPERATURE EXPONENTS FOR CO-$CO_2$ COLLIDING SYSTEM

**N.N. Lavrentieva[1,2], B.A. Voronin[1], A.A. Fedorova[3,4],**
*[1]V.E. Zuev Institute of Atmospheric Optics SB RAS, 1, sq. Academician Zuev, 634021, Tomsk, Russia;*
*[2]National Research Tomsk State University, 36, Lenina av., 634050, Tomsk, Russia; [3]Space Research Institute, 84/32, str. Profsoyuznaya, 117997, Moscow, Russia;*
*[4]Moscow Institute of Physics and Technology, Institute lane, 9, 141700, Dolgoprudnyi, Russia.*
*Contacts: vba@iao.ru, lnn@iao.ru, fedorova@iki.rssi.ru*

The atmospheres of Mars are composed of $CO_2$ predominately. CO is directly produced by the photolysis of $CO_2$. The processes of production and recycling of CO on Mars have been studied in detail in photochemical models [1]. As a condensable species, the abundance of carbon monoxide and its variation with season and location as well as vertical distribution provide important keys about atmospheric transport dynamics [2]. Therefore, CO will be one of the minor atmospheric species measured by high resolution MIR echelle spectrometer as a part of ACS (Atmospheric Climate Suite) onboard Exomars 2016 orbiter [3]. For accurate measurement of the CO abundance with high spectral resolution precise information about line spectroscopic parameters, especially, CO-$CO_2$ line broadening is needed.

Here we present calculations of vibration-rotation line broadening coefficients for CO due to pressure effects of $CO_2$ at the room temperature using semiempirical method [4]. This method is based on the impact theory which is modified to widen the use of empirical data by introducing additional parameters. These model parameters are determined by fitting the broadening and shifting coefficients to experimental data. Semiempirical technique remains the main of the cut-off method: clear physical meaning and the possibility to calculate separately the contributions of different types of intermolecular interactions and different scattering channels to the contour parameters. The last aspect allows us to analyse the vibration-rotational dependence of line broadening and shifting coefficients. Semiempirical approach gives the possibility to make numerous calculations of the line contour parameters without a noticeable loss of precision.

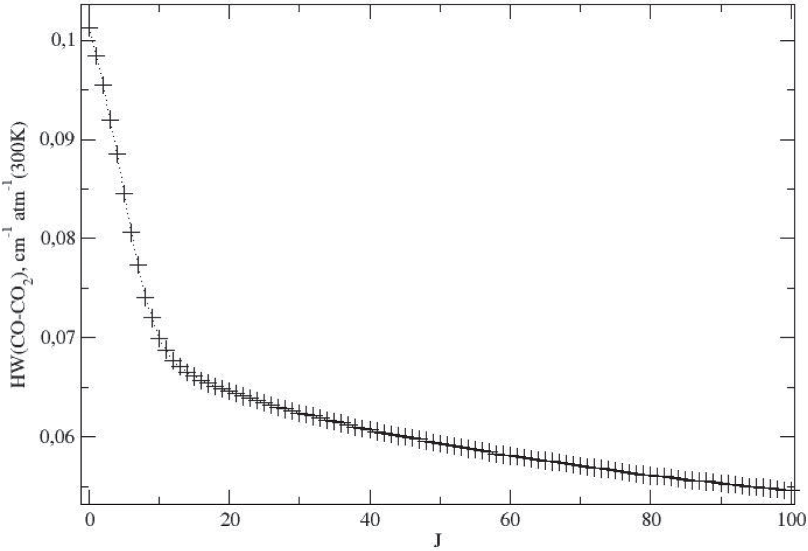


**Fig. 1.** Calculated *J*-dependences of room-temperature CO-$CO_2$ broadening coefficients.

Calculations were performed for wide ranges of rotational quantum numbers 0<*J*<100. Calculated values of the CO-$CO_2$ broadening coefficients, obtained at the temperature are presented in the Fig.1. We can see the sharp slope at small values of Rotational quantum numbers J (up to 10) the widths change from 1.1 to 0.7 cm/atm. And there is slow change till 0.54 cm/atm when numbers J are in the range of 10-100.

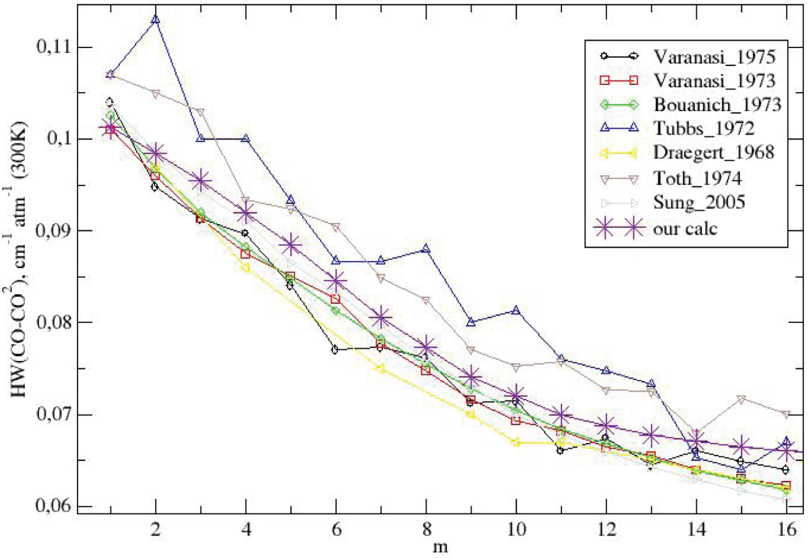


**Fig. 2.** Comparison of theoretical and experimental [5-11] *J*-dependences of room-temperature CO-$CO_2$ broadening coefficients.

Our theoretical results were compared with available experimental data [5-11]. The results of comparison are presented in the Figure 2. It is seen that the semiempirical results agree well with the measurements and provide identical values for high *J*. The computed values can be therefore considered as reliable and worthy of use in the spectroscopic databases. Moreover, because of the insignificant vibrational dependence of CO-$CO_2$ broadening coefficients, the calculated values can be safely used for different vibrational bands.

1. Krasnopolsky V.A.// Icarus. 1993. V.101. P.313-332.
2. Nelli S.M. et al.// JGR. 2007. V.112. E08S91.
3. Korablev O.I. et al.// JARS 2014. V. 8, id. 084983.
4. Bykov A., Lavrentieva N., Sinitsa L. // Mol. Phys. 2004. V. 102. P. 1653-1658.
5. Varanasi P. // JQSRT 1975.V.15, P. 191-196.
6. Tubes L.D., Williams D. // J. opt. Sot. Am. 1972. V.62, P.423-427.
7. Rothman L.S.et al. // JQSRT 2010.V.111, P.2139–2150.
8. Goorvitch D. // Astrophys J Suppl Ser. 1994. V.95, P.535-552.
9. **Varanasi** P., Tejwani G. D. T. // JQSRT **1971**. V.**11**, P. **255.**
10. **Lowry** H. S. III, **Fisher**, C. J. // JQSRT **1984**.V.**31**, P.**575.**
11. Sung K., Varanasi P. // JQSRT. V. 91, Iss. 3, 2005, P. 319–332.

# LONG-TERM NADIR OBSERVATIONS OF THE $O_2$ DAYGLOW BY SPICAM IR

**S. Guslyakova[1,2], A. Feforova[1,2], F. Lefevre[3], O. Korablev[1,2], J.-L. Bertaux[3], F. Montmessin[3], F. Forget[4]**
*[1]Space Research Institute, 84/32, str. Profsoyuznaya, 117997, Moscow, Russia;*
*[2]Moscow Institute of Physics and Technology, Institute lane, 9, 141700, Dolgoprudnyi, Russia;*
*[3]LATMOS – UVSQ/UPMC/CNRS, 11 bd d'Alembert, 78280 Guyancourt, France;*
*[4]Laboratoire de Meteorologie Dynamique, Institut Pierre Simon Laplace, Universite Paris 6 Boite Postale 99, 75252 Paris cedex 05, France.*
*Contact: guslyakova@iki.rssi.ru*

The $O_2(a^1\Delta_g)$ dayglow on Mars is produced during ozone photodissociation by solar UV radiation. The excited $O_2$ molecule, formed during this process, can emit photon at 1.27 μm or can be quenched by $CO_2$, the last process dominates at altitudes below 20 km. Ozone concentration has been considered to anticorrelate with water vapor abundance, as was first observed by Mariner 9 [1]. Consequently, the $O_2(a^1\Delta_g)$ dayglow emission should be also sensitive to the $H_2O$ distribution in the atmosphere of Mars.

We present results of 5 Martian years nadir measurements of the $O_2(a^1\Delta_g)$ dayglow made by the SPICAM IR instrument [2,3]. Its comparison with the GCM simulations [4,5] allows us to derive constraints for the quenching rate of excited $O_2$ molecules by $CO_2$ gas. The continuity of measurements during a long period of time gives an opportunity to investigate the interannual variability of the $O_2(a^1\Delta_g)$ dayglow and its connection with simultaneously observed water vapor. In most cases the revealed $O_2(a^1\Delta_g)$ dayglow variations truly depend on the water vapor variations, and their anti-correlation prediction is clearly confirmed. The comparison with ground based observations [6] is also presented.

**References:**

[1] Barth, C. A.; Hord, C.W, Mariner 9 Ultraviolet Spectrometer Experiment: Seasonal Variation of Ozone on Mars, 1973, Science, Volume 179, Issue 4075, pp. 795-796.
[2] Korablev O., J. L. Bertaux, A. Fedorova , D. Fonteyn, A. Stepanov, Yu. Kalinnikov, A. Kiselev, A. Grigoriev, V. Jegoulev, S. Perrier, E. Dimarellis, J.P. Dubois, A. Reberac, E. Van Ransbeeck, B. Gondet, F. Montmessin, A. Rodin. SPICAM IR acousto-optic spectrometer experiment on Mars Express, *J. Geophys. Res., 111, E09S03,* doi:10.1029/2006JE002696, 2006.
[3] Fedorova A., O. Korablev, S. Perrier, J. L. Bertaux, F. Lefevre, A. Rodin.Observation of $O_2$ 1.27 μm dayglow by SPICAM IR: seasonal distribution for first Martian year of Mars-Express, *J. Geophys. Res.,* **111**, E09S07, doi:10.1029/2006JE002694, 2006.
[4] Lefevre, F., Lebonnois, S., Montmessin, F., Forget, F., 2004. Three-dimensional modeling of ozone on Mars. J. Geophys. Res. 109, E07004.
[5] Lefevre, F. et al., 2008. Heterogeneous chemistry in the atmosphere of Mars. Nature 454, 971–975.
[6] Krasnopolsky, V. 2013. Night and day airglow of oxygen at 1.27 μm on Mars, Planet. Space Sci. 85, 243–249.

# ANOMALOUS INTERNAL STRUCTURE OF THE TERRESTRIAL PLANETS FROM GRAVITATIONAL FIELD AND TOPOGRAPHY: FIRST RESULTS OF THE EXPLORATION OF MARS

**N. A. Chujkova, L. P. Nasonova, T. G. Maximova**
*Sternberg Astronomical Institute, MoscowStateUniversity, Universitetskii pr. 13, Moscow, 119991 Russia*

In this paper we apply a new technique that we have developed earlier [1,2]for solving incorrect problem of determining the internal structure of the planets based on space research of the gravitational field and relief.The essence of this method is the determination of possible depths of compensation for expansion harmonics of topographic heights relative to the equilibrium ellipsoid for different-order and different-degree harmonics.The solution of this problem should satisfy a system of two equations. The first equation represents the consistency between the contribution of topographic and compensating masses to the gravity and the observations. The second equation represents the fact that the pressures below the compensation depth are equal to the pressures of the equilibrium model.Since each topographic heterogeneity is characterized by a certain set of the harmonics therefore the maximal concentration of compensation of this set within a certain limited depth interval may indicate the most probable depths of compensation of the considered topographic heterogeneity .

The paper also carried out a comparative analysis of the internal structure of the Earth and Mars, in order to identify the reasons for the differences in their geophysical and geodynamic features, such as: the distribution and level of isostatically unaligned stresses, the nature of convective motions caused by anomalies in the internal gravitational field, the existence of the magnetic field on the Earth and the lack of the magnetic field in Mars.To do this, on the basis of the analysis of the distribution histograms for the depths of compensation determined the most likely levels of compensation of topographic irregularities. On the selected depths , we constructed the maps of lateral distributions of the compensating masses. It is shown that the observed anomalous structures generate the anomalies in the internal gravity field, which may be the cause of convective motion in the mantle and core of the planet [3].

**References**

1.*Chuikova N.A., Nasonova L.P. , and Maksimova T.G.*Anomalous structure of the Crust and Mantle of Mars. ISSN 0027-1349, MoscowUniversity Physics Bulletin, 2011, Vol.66, No. 1, pp. 64-71

2.*Chuikova N.A., Nasonova L.P. , and Maksimova T.G.* Anomalies of Density, Stresses, and the Gravitational Field in the Interior of Mars. ISSN 0027-1349, MoscowUniversity Physics Bulletin, 2012, Vol.67, No. 2, pp. 218-225

3. *Chuikova N.A., Nasonova L.P. , and Maksimova T.G* Density, Stress, and Gravity Anomalies in the Interiors of the Earth and Mars and the Probable Geodynamical Implications: Comparative Analysis. ISSN 1069_3513, Izvestiya, Physics of the Solid Earth, 2014, Vol. 50, No. 3, pp. 427–443.

# AN ASSESSMENT OF SOURCE TO SINK MINERALOGY FOR THE JEZERO CRATER, MARS PALEOLAKE SYSTEM

**T.A. Goudge[1],J. W. Head[1], J. F. Mustard[1],C. I. Fassett[2]**
*[1]Dept. of Earth, Environmental and Planetary Sciences, Brown University, Providence, RI, USA; [2]Dept. of Astronomy, Mt. Holyoke College, S. Hadley, MA, USA.*
*Contact: Tim_Goudge@Brown.edu.*

**Introduction:**

Aqueous alteration minerals identified inancient deposits on Mars have been used to suggesta warmer, wetter early Mars [e.g., 1,2]. However, recent work has hypothesizedthat the hydrated minerals may have formed in the martian subsurface [3]. Nonetheless, there is abundantgeomorphic evidence for at least a transient period of surface fluvial activity early in Mars' history [e.g., 4-8]. Therefore, it remains an open question as to whether this period of fluvial activity is genetically linked to the formation of the observed alteration minerals.

Here we present work aimed at addressing this question through the study of the source to sink mineralogy of the Jezero crater (18.38°N, 77.70°E) paleolake system [7,9], which has previously been observed to contain alteration minerals in its two depositional fans [10,11]. The alteration minerals observed within the fans have previously been suggested to be primarily transported in nature [10,11], a hypothesis that is further tested here.

**Methods:**

The source to sink mineralogy of these fan deposits is investigated with a combined approach of geomorphic mapping and mineralogicanalysis with visible to near-infrared (VNIR) hyperspectral reflectance data. We created a geomorphic map of the Jezero crater paleolake basin and watershed as defined by topography from High Resolution Stereo Camera (HRSC) images [12,13]. Mapping was doneat a scale of 1:100,000 using a mosaic of ~6 m/pixel Context Camera (CTX) images [14]. The mineralogy of the major identified units was studied with Compact Reconnaissance Imaging Spectrometer for Mars (CRISM) VNIR reflectance data [15].

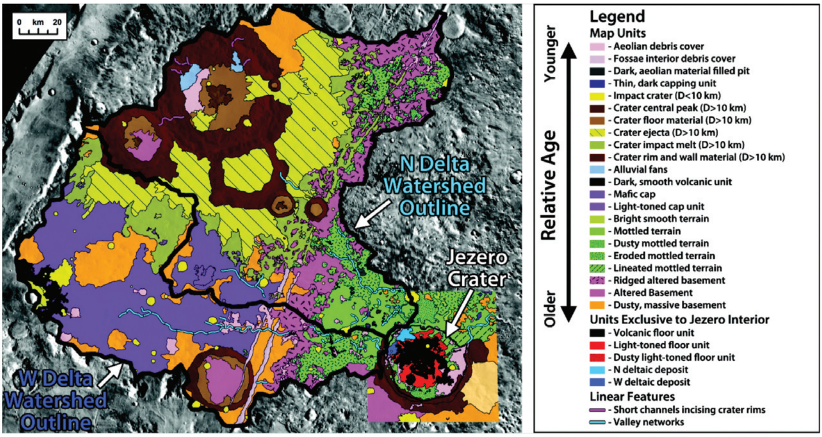


**Fig. 1.** Geomorphic map of the Jezero crater paleolake basin (indicated by labeled arrow) and its surrounding watershed (indicated by thick, black outlines). Legend for all map units is shown on the right, listed in relative stratigraphic order with the youngest units at the top. Background is the global Thermal Emission Imaging System (THEMIS) 100 m/pixel daytime infrared mosaic [21]. See text for discussion of major units.

**Major Geomorphic Units:**

*Intra-basin Units.* The mainunits of interest within Jezero crater are the two fandeposits (**Figure 1**), located at the mouths of the north(N) and west(W) inlet valleys [7,9]. These two depositsalso have distinct spectral signatures [10,11] (**Figure 2**).The N fandeposit shows spectra with a broad absorption feature centered near ~1 μm, as well as an absorption feature centered near ~1.92 μm, and a paired set of absorptions centered near ~2.31 and ~2.51 μm **(Figure 2**). We

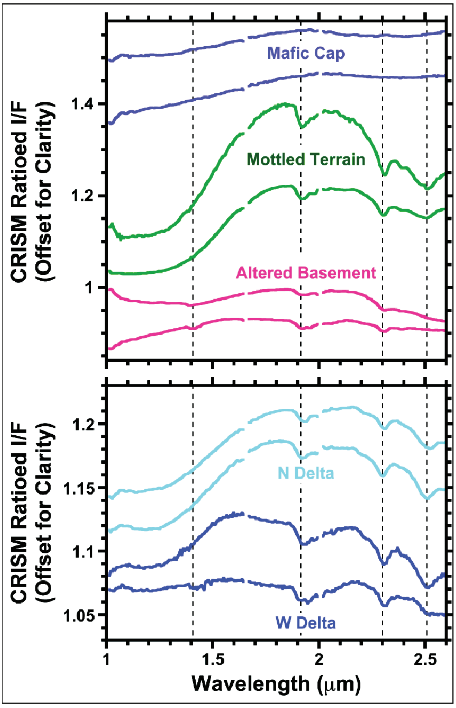


**Fig. 2.** Representative CRISM spectra of the major geomorphic units in the Jez-ero crater paleolake watershed (top plot) and of the two fandeposits in the Jezero crater basin (bottom plot). Dashed lines are at ~1.4, 1.92, 2.3 and 2.5 μm.

interpret the~1 μm absorption to be due to a crystal field electronic transition from $Fe^{2+}$ in olivine [16,17], andthe paired absorptions at ~2.31 and 2.51 μm to be due to an overtone of a fundamental vibrational mode of $CO_3$ in Mg-carbonate [18,19]. The ~1.92 μm absorption is caused by a combination tone of structural $H_2O$ [20]. This spectral signature of a mixture of olivine and Mg-carbonate is observedeverywhere on the exposed portions of the N fandeposit.

The W fandeposit spectral signature varies across its surface. Some locations show spectra indicating a mixture of olivine and Mg-carbonate, as is seen on the N fandeposit; however, the main spectral signature observed shows narrow absorptions centered near ~1.42, 1.92 and 2.31 μm (**Figure 2**), interpreted to be due to the first overtone of the OH stretch, a combination tone of OH stretch and H-O-H bend, and a combination tone of OH stretch and metal-OH bend respectively, in an Fe/Mg-bearing smectite [20,22]. These spectra also havea subtle spectral shoulder near ~2.51 μm, possibly due to an overtone of $CO_3$ from minor amounts of carbonate. We conclude that the W fandeposit is spectrally dominated by Fe/Mg-bearing smectite, with variable amounts of olivine and Mg-carbonate.

*Watershed Units.* The stratigraphically lowest majorunit in the watershed is the Altered Basement unit (**Figure 1**). This unit has a spectral signature with narrow, vibrational absorptions centered near ~1.41, 1.92 and 2.30-2.31 μm (**Figure 2**). We interpret this unit to be the source of the Fe/Mg-smectite in the fan deposits.

Two mapped units are emplaced directly upon the Altered Basement unit, and thus occupy the same stratigraphic level: the Mafic Cap unit and the Mottled Terrain unit (**Figure 1**). Spectra of the Mafic Cap unit arecharacterizedby broad absorptions centered near ~1 and 2 μm (**Figure 2**), which we interpret to be due to $Fe^{2+}$ in the mineral structures of pyroxene and olivine [16,17,23]. The Mafic Cap unit appearsthin, and in many locations the valley networks that feedJezero crater have eroded through this unit and down into the underlying Altered Basement unit.

Spectra of the Mottled Terrain unit have a broad absorption feature centered near ~1 μm, as well as narrower absorptions centered near ~1.92 μm, and near ~2.31 and 2.51 μm (**Figure 2**). We interpret this unit to be the source of the olivine and Mg-carbonate identified in the fan deposits.

**Discussion:**

The two fandeposits within the Jezero crater paleolake have distinct mineralogies based on their VNIR spectral signatures. If the alteration minerals identified inthese two fandeposits are primarily transported in origin, we suggest that it is likely that this difference in mineralogy is caused by a difference in the mineralogy of the units within the watersheds of the two fan deposits.

To test this hypothesis, we looked at the areal extent of exposureof the major identified geomorphic units in the different watersheds of the two fan depositsin Jezero crater (**Figure 1**). For this analysis, wedividedthe major geomorphic units into two groups: a Fe/Mg-smectite-bearing group, and an olivine- and carbonate-bearing group. The Fe/Mg-smectite-bearing group consists of the Altered Basement unit and the Mafic Cap unit, as this unit is cutinto by valley networks in many locations to expose the underlying Altered Basement unit. This group covers ~3685 km$^2$ in the N fan deposit watershed and ~5030 km$^2$ in the W fan deposit watershed. The olivine- and carbonate-bearing group consists of onlythe Mottled Terrain unit, and covers ~2275 km$^2$ in the N fan depositwatershed and ~725 km$^2$ in the W fan depositwatershed. Therefore, it is clearthat the difference in mineralogy between the two fan deposits is consistent with the difference inareal extentand mineralogy of the units within their respective watersheds. This supports a primarily transported origin for the alteration minerals within the two sedimentary fandeposits, consistent with previous work [10,11].

**Conclusions:**

Based on ourgeomorphic mapping and VNIR spectral analysis,we conclude that the alteration minerals observed within the two Jezero crater paleolake fandeposits are primarily transported in origin, as opposed to having forming *in situ*. Therefore, at this study site, the formation of the identifiedalteration minerals isnot genetically relatedto the fluvial activity that formed the Jezero crater paleolake.

**References:**

[1] Poulet, F., et al. (2005), *Nature,* **438**:623.
[2] Bibring, J.-P., et al. (2006), *Science,* **312**:400.
[3] Ehlmann, B., et al. (2011), *Nature,* **479**:53.
[4] Carr, M. (1987), *Nature,* **326**:30.
[5] Howard, A., et al. (2005), *JGR,* **110**:E12S14.
[6] Irwin, R., et al. (2005), *JGR*, **110**:E12S15.
[7] Fassett, C. and Head, J. (2005), *GRL*, **32**:L14201.
[8] Fassett, C. and Head, J. (2008), *Icarus,* **198**:37.
[9] Schon, S., et al. (2012), *PSS,* **67**:28.
[10] Ehlmann, B., et al. (2008), *Nat. Geosci.*, **1**:355.
[11] Ehlmann, B., et al. (2008), *Science*, **322**:1828.
[12] Neukum, G. *et al*. (2004) *ESA Spec. Pub,***ESA SP-1240**:17.
[13] Gwinner, K., *et al.* (2010) *EPSL,* **294**:506.
[14] Malin, M. *et al*. (2007) *JGR*. **112**:E05S04.
[15] Murchie, S. *et al*. (2007) *JGR*. **112**:E05S03.
[16] Burns, R. (1970) *Mineralogic Applications of Crystal Field Theory*. Cambridge Univ. Press. [17] King, T. and Ridley, W. (1987) *JGR,***92**:11,457.
[18] Hunt, G. and Salisbury, J. (1971), *Mod. Geol.,* **2**:23.
[19] Gaffey, S. (1987), *JGR*, **92**:1429.
[20] Clark, R., et al. (1990), *JGR,* **95**:12,653.
[21] Christensen, P. *et al*. (2004) *Space Sci. Rev*. **110**:85.
[22] Frost, R., et al. (2002), *Spec. Acta*, **58**:1657. [23] Adams, J. (1974) *JGR,***79**:4829.

# IMPACT EJECTA FROM MARS TO PHOBOS: REGOLITH BULK CONCENTRATION AND DISTRIBUTION, AND THE SUFFICIENCY OF MARS EJECTA TO PRODUCE GROOVES AS SECONDARY IMPACTS

**K.R. Ramsley, J.W. Head, III,**
*Department of Earth, Environmental and Planetary Sciences, Brown University, Box 1846, Providence, Rhode Island, 02912, USA.*
*Contact: james_head@brown.edu*

**Introduction:**

The surface of the martian moon Phobos is characterized by parallel and intersecting grooves that bear resemblance to secondary crater chains observed on planetary surfaces. Some researchers have hypothesized that Phobos grooves are produced by ejecta from martian primary crater impacts that intersects Phobos to produce parallel chains of secondary craters. To test this hypothesis we plot Keplerian trajectories of ejecta from Mars to Phobos. From these trajectories we: (1) set the fragment dispersion limits that are required to emplace the parallel grooves pits as observed in returned images from Phobos; (2) plot ejecta flight durations from Mars to Phobos; (3) map regions of exposure to secondary impacts and exposure shadows, and compare these to the observed grooves; (4) assess the viability of ejecta emplacing the large family of grooves covering most of the northern hemisphere of Phobos; and (5) plot the arrival of parallel lines of ejecta at oblique incident angles. We also assess the bulk volume of ejecta from large martian impact events and compute the total volume of Mars ejecta that intersects Phobos over geological time. On the basis of our analysis, we find that the predictions of this hypothesis (that Phobos grooves are produced by the intersection of ejecta from craters on Mars) are inconsistent with a wide range of Mars ejecta emplacement models and observations, and based on our analysis we conclude that the hypothesis is not valid.

We also apply modeling methods that predict the flight of ejecta from Mars to Phobos to the question of the bulk concentration and distribution of Mars ejecta that is deposited in the regolith of Phobos. The gravity of Mars and the observation of a thick Phobos regolith suggests that nearly all ejecta from impacts on Phobos is inserted into temporary orbits around Mars and remains trapped in these orbits for several days to several hundred years until it re-impacts with Phobos to produce new generations of ejecta. Due to orbital mechanics, Phobosejecta fragments typically re-impact on opposite hemispheres of Phobos from their previous impact sites, and when combined with the typical conical dispersion pattern of impact ejecta, this suggests that just two or three generations of re-impacts on Phobos are sufficient to uniformly disperse Mars ejecta fragments globally across the geographic surface of Phobos. For the present-day altitude of Phobos, we calculate a bulk concentration of Mars ejecta fragments in the regolith of Phobos of 250 ppm. Because Phobos has orbited at least 4,000 km farther from Mars during all but the most recent 500 Myr, this suggests that our prediction of 250 ppm for the bulk concentration of Mars ejecta will be found preferentially in the uppermost 0.5–1.0 meters of the Phobos regolith, and at depth, Mars ejecta fragments are likely to be found in bulk concentrations that are 10–60 x less than at the surface of Phobos.

# THE WATER VOLUME REQUIRED TO ERODE THE VALLEY NETWORKS ON MARS: IMPLICATIONS FOR LATE NOACHIAN CLIMATE

**E. N. Rosenberg, J. W. Head,**
*Department of Earth, Environmental, and Planetary Sciences, Brown University, Providence, RI 02912 USA.*
*Contact: james_head@brown.edu*

**Introduction:** The fluvially-formed martian valley networks, a majority of which are dated to the late-Noachian [1], are often cited as evidence that Mars' climate in this period must have been significantly warmer and wetter than at present [2]. Here, we attempt to determine the volume of water that was required to carve out the valleys, in anticipation that this may shed light on climatic conditions. Following Carr and Malin [3], we first estimate the total volume of sediment removed from the valleys and then estimate a water/sediment volume ratio.

**Sediment Volume:** Using the raw data collected by Williams and Phillips [4] from MOLA crossings and approximating the V-shaped profiles as triangles and the U-shaped profiles as trapezoids, we find a mean cross-sectional area of the valley networks. Then, as the Williams and Phillips [4] sample is taken from Carr's [5] mapping, we multiply this cross-sectional area by Carr's [5] total length to find the total cavity volume of the valley networks. Assuming a porosity of 0.3, the volume of sediment removed from the valleys that Carr [5] mapped is $1.03 \times 10^4$ km$^3$. Similarly, using the same porosity and the volumes found by Hoke, et al. [6] using stereo images, the volume of sediment removed from the eight valleys considered by Hoke, et al. [6] is $2.4 \times 10^4$ km$^3$.

**Water to Sediment Volume Ratio:** We use as a proxy for the ratio (*water volume*)/(*volume of sediment removed from valley*) the ratio mean((*fluid flux*)/(*sediment flux*)) = mean($Q_f/Q_s$), which we proceed to estimate. Instead of modeling the suspended flux directly, we account for it using the suspended-to-bedload ratio *k*. We use the Darcy-Weisbach equation for fluid flux and both the Wong and Parker (2006) and Parker [7] equations for sediment flux, (both of which can be found in Garcia [8]) assigning equal weight to both. Both of these sediment flux equations were derived from gravel-bed datasets. We let the boundary shear stress vary uniformly from 110% to 130% of the critical value, as Parker [1] found that, for gravel-bed rivers with stable widths, it is 120% of the critical value. Further, we assign values to variables as follows:

- The submerged specific gravity $R$ (equal to $\rho_s/\rho - 1$, where $\rho_s$ and $\rho$ are the sediment and fluid densities, respectively), is between 1.65, which is the value for quartz, and 2.4, which is the value for martian basalt [7]. We fix $R$ at 1.8.
- For Noachian terrain, the average slope $S$ is between 0.0052 and 0.007 [9]. As large valleys are associated with steep slopes, we fix $S$ at 0.007.
- Kleinhans [7] notes that Gilbert-type deltas, which are comprised of coarser sediment, typically have volumes approximately one-third the volume of their inlet channels. Therefore, we prefer $k = 2$. We let $k$ vary between 1 and 3 (i.e. we let $k$ be a normally-distributed random variable with a mean of 2 and a standard deviation of 0.5).
- Following Hoke, et al. [6], we use the White–Colebrook function to estimate the Darcy-Weisbach friction factor. The input to this function, the ratio (flow depth/bed roughness) is found from the ratio (shear stress)/(critical shear stress), $R$, and the critical Shields stress, which in turn, is found using Equation 2-59a from Garcia [8].

The above inputs produce a water/sediment flux ratio that is distributed as follows: 2.5th Percentile: 1570; 5th Percentile: 1710; 25th Percentile: 2690; 50th Percentile: 16200; 75th Percentile: 204000; 95th Percentile: 1470000; 97.5th Percentile: 2080000. This is significantly larger than the ratio of 100-1000 assumed by Carr and Malin [3]. The parameter to which the water/sediment ratio is most sensitive is the ratio (shear stress)/(critical shear stress), so better constraining this could yield great improvements.

**Water Volume and Implications:** Using the sediment volume from Hoke, et al. [6], and modeling the water/sediment ratio as above leads to total water volumes that are distributed as follows when expressed as global equivalent layers in meters: 2.5th Percentile: 260.; 5th Percentile: 283; 25th Percentile: 445; 50th Percentile: 2680; 75th Percentile: 33800; 95th Percentile: 244000; 97.5th Percentile: 344000. Thus, we are 95% confident that at least 283 m GEL of water was required to carve the valley networks, although much more may have been required. The current surface and near surface reservoir is ~30 m GEL [9], so this amount must have cycled through at least ~10 times. If the flow was subcritical for large amounts of time, then much more water could have flowed through without causing erosion. Further, if the flow was more intense than assumed here, i.e. if the ratio (shear stress/critical shear stress) were larger, then the erosion could have been accomplished with less water.

Fassett and Head [10] find the total volume of water necessary to fill the 220 open-basin lakes they identified to be 2.90 m GEL. Taking this to be exact, the ratio of this water to the minimum water required to carve the late-Noachian valleys is at most 1%. Fastook and Head [11] find that, given Late Noachian Icy Highlands conditions, a transient warming of +18 K for 2000 years or a single year of warming under special conditions could produce enough water to fill the open-basin lakes. Thus, it would take at least 100 such warmings (and possibly many more) to form the valley networks. If each warming lasts 2000 years, this is a total of 200,000 years. If the total time scale during which these melting events occurred was 1 Ma, then the intermittency was at least 20%. This intermittency seems unreasonably high when compared to that found by Buhler, et al. [12], so the line of reasoning used herein should be examined with scrutiny. Further, future studies should ascertain whether the fluid fluxes generated from melting events, such as those considered by Fastook and Head [11], are strong enough to transport sediment.

Segura, et al. [13] estimate that large martian impactors have produced a cumulative total of ~650 m GEL of rainfall. We are, as of yet, unable to determine whether this would have been enough water to carve the valleys. Further, in order to evaluate the giant impactors hypothesis, timing and fluxes must also be considered.

The reasoning outlined above suggests that either very large total volumes of long-term sustained flow, or shorter durations of very strong flows were required to carve the martian valley networks. Intermittent, catastrophic and non-catastrophic melting in a generally cold and icy climate and sustained rainfall are currently being evaluated in this context.

**References:**


[1] C. Fassett and J. Head, *Icarus,* vol. 195, p. 61, 2008.
[2] R. Craddock and A. Howard, *J. Geophys. Res,* vol. 107, no. E11, p. 5111, 2002.
[3] M. Carr and M. Malin, *Icarus,* vol. 146, p. 366, 2000.
[4] R. Williams and R. Phillips, *J. Geophys. Res,* vol. 106, p. 23737, 2001.
[5] M. Carr, *J. Geophys. Res,* vol. 100, p. 7479, 1995.
[6] M. Hoke, et. al, *Earth and Planetary Science Letters,* vol. 312, p. 1, 2011.
[7] G. Parker, *J. Fluid Mech.,* vol. 89, p. 127, 1978.
[8] M. Garcia, "Sediment Transport and Morphodynamics," in *Sedimentation Engineering: Processes, Measurements, Modeling, and Practice*, Reston, Virginia, American Society of Civil Engineers (ASCE), 2008, pp. 21-163.
[9] M. Carr and J. Head, *LPSC45,* 2014.
[10] C. Fassett and J. Head, *Icarus,* vol. 198, p. 37, 2008b.
[11] J. Fastook and J. Head, *Planetary and Space Science,* Submitted 2014.
[12] P. Buhler, C. Fassett, J. Head and M. Lamb, *Icarus,* vol. 241, pp. 130-147, 2014.
[13] T. Segura, B. Toon and A. Colaprete, *J. Geophys. Res,* vol. 113, p. E1107, 2008.

# STRATIGRAPHIC RELATIONSHIPS BETWEEN GULLIES AND THE LATITUDE DEPENDENT MANTLE ON MARS: EVIDENCE FOR CYCLICAL EMPLACEMENT, BURIAL, INVERSION AND REMOVAL OF YOUNG FLUVIAL FEATURES IN THE MID-LATITUDES

**J. L. Dickson[1],J. W. Head[1], T. A. Goudge[1], L. Barbieri[2]**
*[1]Dept. of Earth, Env. and Planet.Sci., Brown U., Providence, RI, USA.*
*[2]Rubenstein Sch. of Env. And Nat. Res., U. Vermont, Burlington, VT, USA*
*Contact: jdickson@brown.edu.*

**Introduction:**

Gullies have been proposed to represent evidence for localized flow of liquid water in very recent times on Mars [1-3]. Modification of gullies in the southern hemisphere, however, occurs under contemporary conditions [4-9] during seasons that are consistent with the removal of $CO_2$ frost at these locations [8]. Whether this activity is sufficient to erode channels to the depths observed in the southern hemisphere and to produce landforms characteristic of terrestrial fluvial erosion [3, 10] is a focal point of ongoing investigations. If $CO_2$ is not sufficient, then gullies likely formed under conditions different than the climate observed today.

Conditions for both the emplacement [11] and melting [2] of near-surface $H_2O$ ice in the latitudes where gullies are most common (30°-45° in each hemisphere [12]) were more favorable during the last 1-2 million years, when high-obliquity conditions [13-14] facilitated the emplacement of a latitude dependent mantle (LDM) [15-16]: an ice-rich layer in the top meter of the surface in the mid-latitudes. The LDM is no longer stable at lower latitudes and is thus dissected between 30°-45° [12, 15], though recent hyperspectral observations indicate that $H_2O$ ice is preserved on sheltered pole-facing slopes at these latitudes [17], where the majority of gullies occur [18-20]. In addition, gullies and $H_2O$-rich mantling units have been documented together at the local scale [21].

This leads to a two-stage hypothesis that we explore in this contribution: Gully channels are formed within ice-rich mantling units by the melting of that same unit during high-obliquity periods, then are modified by $CO_2$-related processes during mid- and low-obliquity periods. Context Camera (CTX) and High Resolution Imaging Science Experiment (HiRISE) data allow for the analysis of stratigraphic relationships between gullies and the LDM, and between successive episodes of gully activity. These relationships reveal a spectrum that ranges from (1) gullies that are dormant and buried by later mantling units, to (2) gullies that have been inverted to form sinuous ridges, to (3) gullies that have been nearly entirely removed from the surface.

**Gully Stratigraphy:**

*Modification.*The most common example of gullies occurring both above and below units of LDM occurs when older gully fans exhibit along-slope fractures,

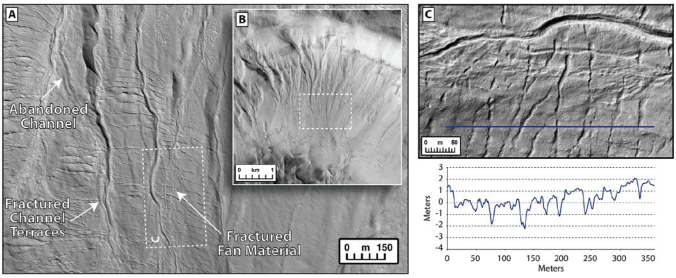


**Fig. 1.** Typical example of multiple episodes of gully activity, separated by periods of mantle degradation. (A) HiRISE image PSP_005943_1380 showing along-strike fracturing of the LDM. (B) Context showing the pole-facing wall of a ~15 km impact crater at 41.5°S, 202.3°E. (C) Subframe showing older gully fan material that is fractured adjacent to a younger gully channel that is not fractured. Pits are generally ~1 m to ~2 m in depth. Profile extracted from USGS HiRISE DEM of PSP_005943_1380 and ESP_011428_1380.

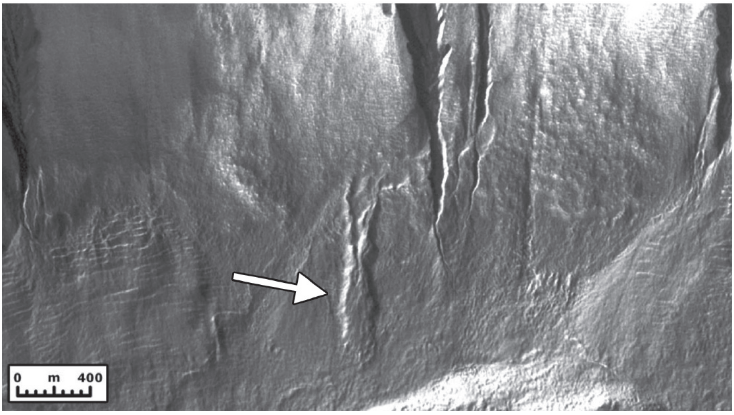


**Fig. 2.** CTX image (B03_010651_1398, 39.9°S / 174.3°E) of a gully fan in which the source channel and alcove have been almost entirely removed. This implies that gullies form within an easily removable layer.

and that fan material is cross-cut by younger gully channels and superposed by gully fans without fractures(Figure 1). This relationship is common in both hemispheres and provides evidence for multiple episodes of gully activity separated by at least enough time to degrade the initial fan to form the fractures. The LDM is considered to be ice-rich [16], and if these features are forming in the LDM, the rimless fractures are consistent with coalescence of sublimation pits with associated downslope movement on these steep slopes.

Recently acquired stereo image pairs from the HiRISE instrument allow for a quantitative assessment of the depth of these fractures (Figure 1), which provide a minimum estimate of LDM thickness. In the example provided in Figure 1, fracture depth ranges from sub-meter in pits that have not yet coalesced to form a continuous fracture, to 2.5 m at further developed fractures.

*Removal.*If gullies form within an ice-rich layer, this would then suggest that if that layer is removed through sublimation, evidence for older generations of gullies should be removed with it.

This process is observed in a few specific locations (Figure 2) where just the remnants of gully fans are preserved on the surface, while the gully channel and alcove have been almost entirely removed. Thus, this implies that gullies do not just undergo degradation (Figure 1), but can be entirely removed from the surface. If this sequence is accurate, this would mean that gully formation could have occurred not simply within the last million years, the record of which is preserved at the surface.

*Inversion.*A globally distributed feature indicative of multiple gully events are downslope ridges found on steep slopes in the mid-latitudes. These ridges share many of the morphological characteristics of gullies in addition to their similar distribution. As shown in Figure 3, these ridges are exposed in the walls of younger gullies and show that they were emplaced before the most recent deposition of LDM material.

If these ridges do represent inverted channels, then the ridge crest represents the floor of the channel when the gully was incised [e.g. 22]. Calculations made on DEMs of this site show that these ridges are ~10 m in height on average, providing a minimum thickness of the mantle that has been lost. Total LDM thickness at this location was likely considerably higher than this value, depending upon the maximum channel depth at the time of emplacement.

Further evidence for significant LDM removal at this site is found when measuring the azimuth of the ridges that represent older gully activity compared to the azimuth of the younger gully channels (Figure 3). While the fresh gullies reflect the azimuth of the host crater wall at this location, the ridges are rotated to the north by an average of 17.1°. Thus, gully orientation was controlled not by the underlying slope of the crater wall, but by the surface slope of the LDM itself. As the LDM degraded, gully azimuth eventually reflected the underlying host surface.

In the southern hemisphere, these ridges are concentrated in the 40°-50°S latitude band, which is the region where preserved LDM towards the pole transitions to dissected LDM towards the equator [16].

**Implications:**

The stratigraphic relationships documented here dictate that gullies form during successive emplacement and removal events of the LDM, thus within a dynamic Late Amazonian Mars of the last several million years. These events reflect periods when both $H_2O$-ice emplacement [11] and melting [2] were both more likely than today. Therefore, gullies are consistent with a Late Amazonian climate that promotes increased $H_2O$ activity under high-obliquity (> 30°) conditions followed by $CO_2$-dominated activity at mid- and low-obliquity.

**References:**

[1] Malin and Edgett, 2000, *Science*, 288, 2330. [2] Costard et al., 2002, *Science*, 295,110.[3] McEwen et al., 2007, *Science,* 317, 1706. [4] Diniega, S. et al, 2010, *Geology*, 38, 1047. [5] Dundas, C. et al., 2010, *GRL*, 37, L07202. [6] Reiss et al., 2010, *GRL*, 37, L06203.[7] Dundas et al., 2012, *Icarus*, 220, 124. [8] Dundas et al., 2014, *Icarus*, in press. [9] Raack et al., 2014, *Icarus*, in press.[10] Mangold et al., 2010, *JGR*, 115, E11001.[11] Madeleine et al., 2014, *GRL*, in press. [12] Milliken et al., 2003, *JGR*, 108, 5057.[13] Laskar et al., 2002, *Nature*, 419, 375.[14] Laskar et al., 2004, *Icarus*, 170, 343.[15] Mustard et al., 2001, *Nature*, 412, 411.[16] Head et al., 2003, *Nature*, 426, 797.[17] Vincendon et al., 2010, *GRL*, 37, L01202. [18] Heldmann and Mellon, 2004, *Icarus*, 168, 285. [19] Balme et al., 2006, *JGR*, 111, E05001.[20] Dickson et al., 2007, *Icarus*, 188, 315.[21] Christensen, 2003, *Nature*, 422, 45.[22] Williams et al., 2009, *Geomorphology*, 107, 300.

# NEW VERSION OF MARS GLOBE

**J. F. Rodionova[1], E. N. Lazarev[2], O. S. Nosova[2], V. V. Shevchenko[1],**
*[1]Sternberg Astronomical Institute, Department on Lunar and Planetary Research, Universitetskij pr., 13, Moscow, Russia.*
*[2]Lomonosov Moscow State University, Geographical Department, Chair on Cartography and Geoinformatics, Vorobjevi Gori, 1, Moscow, Russia;*
*Contact: jeanna@sai.msu.ru*

**Introduction:**

In Russia the first globe of Mars was issued in Sternberg Astronomical Institute in 1989. There were various Martian relief features (planitiae, dorsa, chasma, craters, fossae etc.) on this globe. During the last 25 years both a lot of new precise data and processing techniques were obtained. The main goal of this work is compiling of a new version of Martian globe with the use of unique hand-made hillshade segments of the globe (1989) and contemporary information about surface of the planet, landing sites etc.

**Technology:**

The DTM from Mars Global Surveyor with the resolution of 16 pix/deg (3,705 km/pixel) was used for mapping. To make hypsometric tints smoother heights of the DTM were averaged by ArcGIS Focal Statistics tool with rect-angle of 100 cellsize.

Each of the 12 hand-made hillshade segments having used for the globe of 1989 compiling were converted to digital raster format, colorized and referenced to GCS_Mars_2000 in Polyconic projection. Polar segments were references in equidistant azimuthal projection with the standard parallel 90 deg.

The result with Martian relief features names are represented on Figure 1.

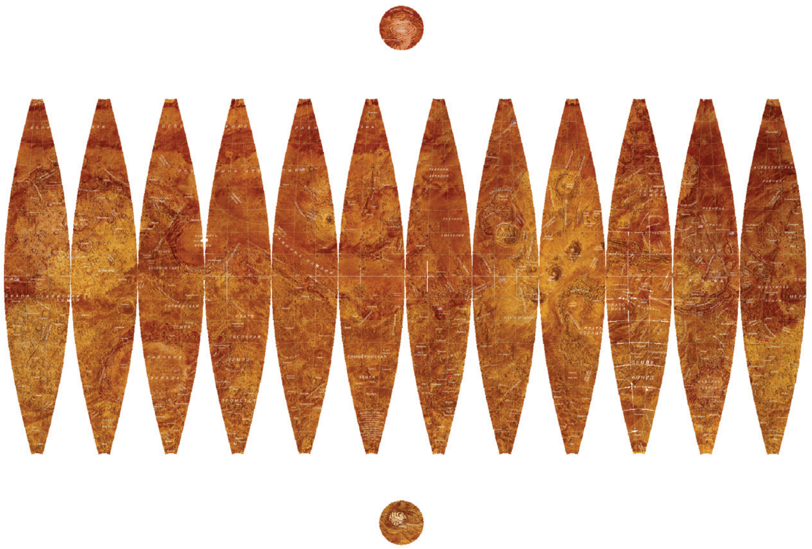

**Fig.1.** Segments of the new Mars globe (2014)

**Summary:**

The Mars globe (1989) is reissuing in digital format. The hypsometric tints, feature names, landing sites and marks of height are joined with the unique hand-made hillshade segments.

# MAPPING AND DATING THE RESURFACING EVENTS ON MARTIAN OUTFLOW CHANNELS: A CASE STUDY OF HARMAKHISVALLIS IN THE EASTERN HELLAS RIM REGION

**S. Kukkonen, V. –P. Kostama, A. I. Rauhalaand J. Raitala,**
*Astronomy, Department of Physics, P.O. Box 3000, FI-90014 University of Oulu, Finland.*
*Contact: soile.kukkonen@oulu.fi*

**Introduction:**

HarmakhisVallis is one of the four large-scale outflow channel systems (i.e. Dao, Niger, Harmakhis and Reull Valles) which cut the Late Noachian – Early Amazonian age volcanic, sedimentary and mixed material on the northeastern Hellas rim region of Mars [1–3]. Because it starts as a broad (38 x 90 km) and deep (in places > 1.6 km) depression without other fluvial features around it, it is suggested that the Harmakhis channel formed when the subsurface ice melted and the waterwas released due to theactivity of the nearby volcanoes and theproduced volcanic heat [1–7]. When the melted ice ran towards the lower topography of the Hellas basin, the surrounding surface eroded untilit collapsed and the now visible valley formed.

The varying structure of HarmakhisVallis indicates that the evolution of the channel has been complex. One of the most significant characteristics of HarmakhisVallis is that it is not a continuous channel. Instead, its head depression and main channel are separated by the ~ 80 km long and topographically higher part of the channel (thedifferenceis > 0.4 km) called "barrier surface" [8] (Fig. 1a), which probably represents the still existing subsurface part of the channel.

In this work we outline our results of mapping and dating the geologic activity on the HarmakhisVallis floor (see also our previous studies [9–11]). We focus especially on the possible ice-facilitated flow units which cover the channel floor almost entirely, and investigate when the processes that formed these units occurred.

**Data and methods:**

The used data consist of a full resolution CTX mosaic (~ 5 m/pixel) and separate HiRISE images (~ 0.3 – 0.5 m/pixel). In the case of mapping, images of MGS's MOC (~ 1.5 – 12 m/pixel), Mars Express' HRSC (~ 50 m/pixel) and Mars Odyssey's THEMIS infrared (day and night) camera were also used.

The age determinations were conducted inthe GIS environment by using the established crater counting methods [12–14] and the crater model ages were measured from the cumulative crater size-frequency distribution plots obtained with the Craterstats software.

**Results:**

MappingontheHarmakhisVallischannelindicatesthatthechannelisalmostentirely covered by the flows, the varying texture of which may indicate that they are ice-facilitated. On the head depression of the channel, the flows originate from the interior walls and the surrounding pitted plains and debris aprons, and theyare-directed towards the deepest part of the head depression. On the barrier surface and the main channel, on the other hand, the flows seem to originate only-from the interior walls andare directed towards the central part of the U-shaped channel.

The texture of the flow units also varies throughout the channel. Especially in the beginning of the main channel,the flows are smooth and continuous, cut only by the remnants of the wall collapses and mass movements. However, approximately in the middle of the main channel, the flows suddenly become clearly rougher and smaller in scale, and in many places the number of craters on the units is too small for reliable dating.

The results of the crater counts are seen in Fig. 1b. The figure shows that the cratering model ages measured on the flow units are relatively young. The oldest ages, only ~ 1 Ga, were found on the head depression and near the end of the main channel. Elsewhere, the oldest ages of the flows are between ~ 100 Ma – 1 Ga, exceptonthe units at the beginning of the main channel (the oldest preserved age is ~ 70 Ma) and near the terminus of the channel (the oldest age is ~ 15 Ma). In addition, all of the units show evidence of 1 – 3 resurfacing ages, which mainly correlate with each other on the different units.

**Conclusions and discussion:**

Most of the HarmakhisVallis floor has resurfaced due to the now visible flows which are possibly ice-facilitated. In most cases, the oldest measurable age of these flows varies from ~ 100 Mato1 Ga, which might be, however, only the youngest limits for the formation age due to the ice-facilitated nature of the flows and thus the intensive crater erosion caused by ice sublimation. However, in afew cases, the crater size-frequency distributions of the flow units do not show evidence of the ages of > 100 Ma at all.

All of the flows also have 1 – 3 resurfacing ages which correlate on different units. In addition, almost all of the craters on the channel floor seem to have sufferedonlyerosion processes (not deposition). Because of that, it seems implausible that the oldest ages (< 100 Ma) found on some units are the formation ages of these units, although the measured crater size-frequency distributions in these cases do not show evidence of older surface ages.

The correlation of the resurfacing ages might also indicate that on the channel, there have occurred several channel-scale resurfacing processes, the intensities and durations of which have varied on different parts of the long channel. This location-dependent intensity and duration of the resurfacing processes together with the possible uneven ice sublimation (and thus crater erosion) might also explain why some cratering model ages are missing from some units.

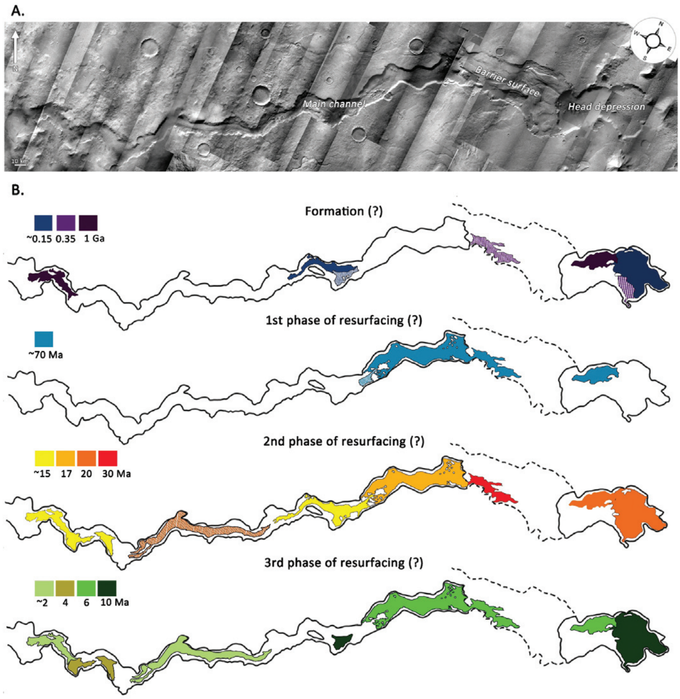


**Fig. 1**. A) A CTX mosaic shows the HarmakhisVallis channel and its different parts. B) An overview of the crater counting results for the flow units on the HarmakhisVallis floor. The dashed lines indicate the location of the barrier surface. The different colorsrepresent themeasured ages (see the labels).On the units filled with lines the number of fitted craters is<4.

**References:**

[1] Greeley R. and Guest J. E. (1987) USGS Misc. Invest. Ser. Map I–1802–B. [2] Crown D. A. and Greeley R. (2007) USGS Misc. Invest. Ser. Map 2936. [3] Price K. (1998) USGS Misc. Invest. Ser. Map I-2557. [4] Crown D. A. et al. (1992) Icarus, 100, 1-25. [5] Crown D. A. et al. (2005) JGR, 110, E12S22. [6] Harrison K. P. and Grimm R. E. (2009) JGR, 114, E04004. [7] Kostama V. -P. et al. (2010) EPSL, 294, 321-331. [8] Glamoclija M. et al. (2011) PSS, 59,1179-1194. [9] Kukkonen S. et al. (2014) LPS XLV, abstract #2596. [10] Kukkonen S. et al. (2013) LPS XLIV, abstract #2140. [11] Kukkonen S. et al. (2013), EPSC2013, #743. [12] CATWG (1979) Icarus, 37, 467-474. [13] Ivanov B. (2001) Space Sci. Rev. 96, 87-104. [14] Hartmann W. K. and Neukum G. (2001) Space Sci. Rev. 96, 165-194.

# TESTING THE GLACIAL SUBSTRATE MODEL FOR DOUBLE-LAYERED EJECTA CRATERS ON MARS

**D. K. Weiss [1],J. W. Head [1],**
*[1]Department of Geological Sciences, Brown University, Providence, RI 02912, U.S.A. (david_weiss@brown.edu)*

**Introduction:**

The martian layered ejecta craters possess unique characteristics relative to the ballisticallyemplaced ejecta of their lunar and mercurian counterparts: their ejecta deposits display distinct boundaries rather than gradational thicknesses and appear to have been fluidized upon emplacement [1]. The unique ejecta morphology associated with layered ejecta craters is typically attributed to sub-surface and/or surface volatiles [1-19] and/or atmospheric-vortex interactions [20-24].

Of the wide variety of layered ejecta craters (e.g. single-layered ejecta, multiple-layered ejecta, low-aspect-ratio layered ejecta, pedestal, double-layered ejecta (DLE) craters are a particularly unusual subclass. DLE craters (Fig. 1) range from ~1 to 35 km in diameter (~8 km on average) and exhibit two ejecta facies; the inner facies is characterized by a distinctive radial texture of parallel ridges and grooves, transverse fissures, and an annular depression at the base of the rim [1,15,19]. DLE craters are located in the mid-high latitudes in both hemispheres [15,19]. Ejecta mobility (EM; ratio of ejecta runout distance from the rim crest/crater radius) has been used to characterize the layered ejecta craters [1-5,25], which typically have EM values of ~1—2. DLE craters exhibit anomalously high EM values compared with other martian layered ejecta morphologies, displaying an average EM of ~3 for the outer ejecta facies, and ~1.5 for the inner ejecta facies[5].

DLE craters have been hypothesized to form through 1) interaction with the martian atmosphere [20,21]; 2) the incorporation of volatiles from within the target materials [5-9,14]; 3) some combination of these factors [5,14,17]; 4) a base surge [7,14, 26]; 5) impact melt overtopping the crater rim [9,27], 6) impact into a subsurface ice layer [15]; 7) impact into a volatile-rich substrate followed by a landslide of the near-rim crest ejecta [28]; or 8) impact and penetration through a surface snow and ice layer, followed by an ice-lubricated landslide off of the structurally uplifted rim-crest [19]. They [19] suggest that the landslide of the inner ejecta facies and the long runout distances of the outer facies are explained by ejecta sliding on a lubricating (low friction) icy surface layer.In the latter two landslide scenarios for DLE inner ejecta facies formation, the grooves on the DLE inner facies are analogous to longitudinal grooves formed on the surfaces of terrestrial landslides [30], particularly those that slide on snow and ice [29,30-32].

We use recently improved frictional models [33] to test the landslide hypothesis.

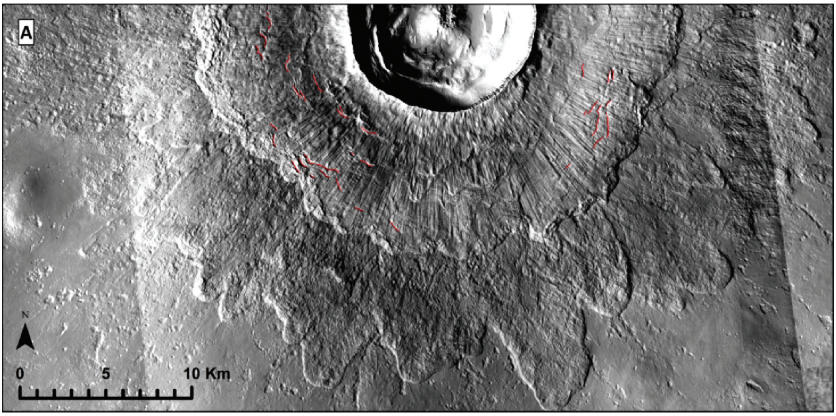


**Fig. 1.** Radial grooves and transverse fissures (red lines) on the southern inner ejecta facies of the martianSteinheim crater (190.6°E, 54.5°N; CTX im-age P21_009160_2348).

**Application of recent quantitative landslide models:** DLE inner facies have runout distances of ~2-20 km and initial (rim-crest) heights of ~10-100 m for craters 2 to 25 km in diameter, respectively. Can landslide scaling laws be reconciled with those large runout distances despite their low sliding angles and initial landslide heights? Are the speeds sufficient to form and preserve the grooves, which simultaneously require vertically unmixed flow, low degrees of movement perpendicular to the primary flow direction, low values of basal friction, and high speeds [30,32,34]? Furthermore, did the landslide occur on snow and/or ice (i.e. glacial-substrate model [19]) or rock [28]? In order to address these questions, we model the runout and sliding speeds of a landslide of near rim-crest ejecta. We use the equation of motion for a landslide center of mass (COM) (e.g. [34]) in cylindrical coordinates using the structural uplift height function of [35] and a new frictional weakening law [33].

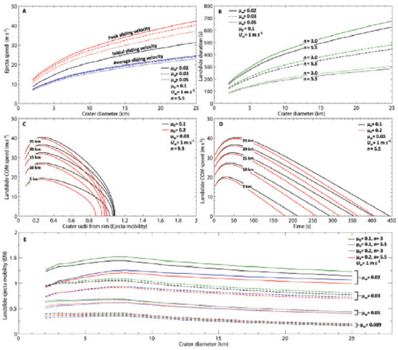

**Fig. 2.** Landslide model results.A) Sliding speed, B) Duration, C,D) Time evolution, E) Runout distance.

On the basis of this model, the landslide COM is predicted to have peak sliding speeds ranging between ~12 to 42 m $s^{-1}$, and average landslide COM speeds ranging between ~8 and 25 m $s^{-1}$(Fig. 2a). Under the same computational conditions, our results predict landslide durations of 75-675 s (Fig. 2b), depending on crater diameter, over the entire range of input parameters. We find that across the parameter space, the runout distance of the inner ejecta facies COM is predicted to range from 0.4-1.5R from the rim crest for craters between 2 and 25 km in diameter after correcting for crater collapse (Fig. 2e), and thus are in good agreement with observation. The high EM values of the DLE inner facies, despite low sliding angles and low initial heights, is a predicted consequence of the lubricating snow and ice substrate [4,19]. The average landslide COM speeds calculated (~8-25 m $s^{-1}$) are typical of, though somewhat lower than, terrestrial landslides overriding glaciers (~20-100 m $s^{-1}$), which were sufficient to form and preserve grooves. Thus, the presence of grooves on the inner ejecta facies of DLE craters is consistent with a landslide origin. Grooves form through a shear/splitting process [29,30,32,34] and can only be preserved throughout the landslide under conditions in which the flow is vertically unmixed. Longitudinal grooves (as opposed to more hummocky textures) form when the primary flow direction speed is much greater than the lateral flow speed[32]. We note that in the case of a near rim-crest landslide, azimuthal confinement from adjacent landsliding ejecta will prevent movement at right angles lateral to the primary flow direction, and will thus assist in groove formation Volume in the landslide is thus conserved by splitting, where expansion is accommodated by the longitudinal grooves. This is consistent with the observation that wider are grooves are present with increasing distance from the rim-crest [36].

**References**

1) Carr et al., JGR, 1977; 2) Mouginis-Mark, P., JGR, 1979; 3)Costard, F., Earth Moon and Planets, 1989; 4)Weiss, D. and J. Head, Icarus, 2014;5) Barlow, N., Large Met. Impacts III, 2005; 6)Barlow, N., and C. Perez, JGR, 2003; 7)Mouginis-Mark, P., Icarus, 1981; 8)Barlow, N. and T. Bradley, Icarus, 1990; 9)Osinski, G., MAPS, 2006; 10)Wohletz, K., Icarus, 1983; 11)Mouginis-Mark, P., Icarus, 1987; 12)Stewart et al., LPSC 32; 2090, 2001; 13)Baratoux, D., GRL, 2002; 14)Barnouin-Jha et al., JGR, 2005; 15)Boyce, J. and P. Mouginis-Mark, JGR:P, 2006; 16)Senft, L. and S. Stewart, MAPS, 2008; 17)Komatsu et al., JGR:P, 2007; 18)Oberbeck, V., MAPS, 2009;19)Weiss, D. and J. Head, GRL, 2013; 20)Schultz, P. and D. Gault, JGR: SE, 1979; 21)Schultz, P., JGR, 1992; 22)Barnouin-Jh, O. and P. Schultz, JGR:P, 1998; 23)Barnouin-Jha et al., JGR:P, 1999a; 24)Barnouin-Jha et al., JGR:P, 1999b; 25)Barlow, N. and A. Pollak, LPSC 39; 1322, 2002; 26)Harrison et al., LPSC 44; 1702, 2013; 27)Osinski et al., EPSL, 2011; 28)Wulf, G. and T. Kenkmann, LPSC 45; 1792, 2014; 29)Shreve, R., Science, 1966; 30)Dufresne, A. and T. Davies, Geomorph., 2009; 31)Shugar, D. and J. Clague, Sediment., 2011; 32)De Blasio, F.,

# FREE OSCILLATIONS FOR INTERIOR STRUCTURE MODELS OF MARS

**T. V. Gudkova[a], V. N. Zharkov[a], Ph. Lognonné[b], S. Raevskiy[a]**
*[a] Schmidt Institute of Physics of the Earth RAS, B.Gruzinskaya 10, Moscow 123995 Russia.*
*[b] Institut de Physique du Globe de Paris, Paris Sorbonne Cité, Univ. Paris Diderot, UMR CNRS 7154, 39 Rue Hélène Brion Paris 75013 France*
*Contact: gudkova@ifz.ru*

At present we are on the threshold of seismic experiment on Mars: a broadband seismometer is the primary instrument in the InSight project planned by NASA [1, 2].

Since the outer shells of Mars are very inhomogeneous, a global, spherically symmetric model of its interior structure is difficult to construct by using only seismic body-wave data. Free oscillations, if they are excited, are indeed particularly attractive to probe beneath the surface of an extraterrestrial body into its deep interiors. Interpretation of data on free oscillations does not require knowledge of the time or location of the source, thus the data from a single station are sufficient. Since the planet has finite dimensions and is bounded by a free surface, the study of the free oscillations is based on the theory of vibration of an elastic sphere. The planet reacts to a quake (or an impact) by vibrating as a whole, vibrations being the sum of an infinite number of modes that correspond to a set of frequencies. The important feature of free oscillations is that they concentrate towards the surface with increasing the degree number. Therefore different regions of interiors are sounded by different frequency intervals.

Mars is assumed to be an active planet, most theoretical models of the seismic activity on Mars, which are based on the thermoelastic cooling of the lithosphere [3, 4, 5], predict a total of 10-100 quakes per year with seismic moments larger than $10^{22}$ dyne cm. Taking into account the fact that one can see giant faults on the surface of Mars (within Tharsis region, Tempe Terra, Valles Marineris, Olimpus region), it is not possible to rule out large seismic events.

Mars' internal density distribution is constrained by the recent estimates of the moment of inertia and the Love number $k_2$ characterizing the tidal response of the planet [6]. The model is usually described by a restricted set of parameters: the thickness of the crust, the location of phase transitions, the core radius. Our analysis is based on a seismic model M14 3 from [7] and the model A of [8] ($R_c$=1468 km; the density of 110-km thick crust is 2810 kg/m$^3$). The model M14_3 [7] is shown in the Fig. 1. The parameters of M14_3 model are the following: the crust is 50 km thick (with density of 2.9 g/cm3), the molar ratio Fe/(Fe+Mg) in the mantle is 0.20, the Fe-Ni core contains 70 mol % H in addition to 14 wt % S with radius of 180 km, the bulk Fe/Si ratio is close to chondritic 1. Water content should also be considered as a compositional variable in the mantle. Olivine and its high pressure phases, wadsleyite and ringwoodite are particularly important as they constitute about 60 wt% of the Martian mantle and have probably large capacity for water in the Martian mantle [9].

On the basis of the interior structure models of Mars described above (M14_3 model with and without water traces in mantle minerals and model A) torsional (Fig. 2) and spheroidal (Fig. 3) oscillation periods are calculated.

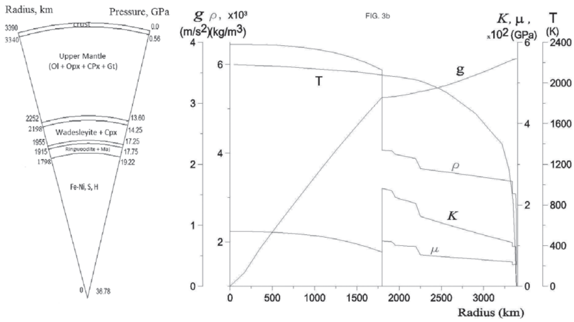


**Fig. 1.** Schematic figure of the Martian internal structure (M14_3 model [7] and the distribution of density ρ, gravity g, tem-perature T, elastic modulus K and the rigidity μ as a function of radius through the planet for the trial M14_3 model (Fe# 20, 50 km crust thick with density of 3000 kg/m3). Acknowledgments.

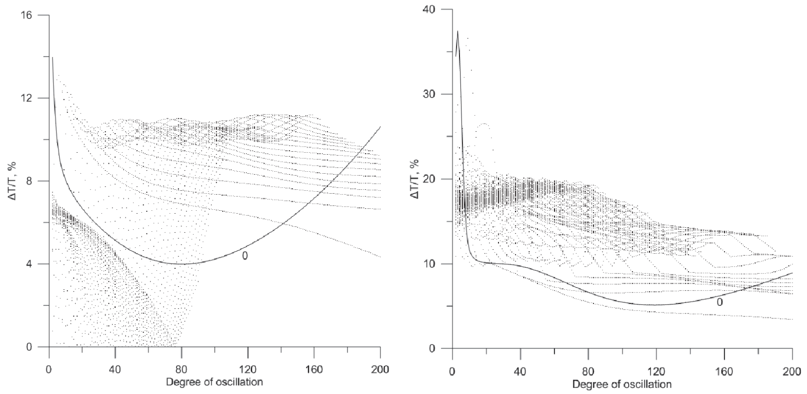


**Fig. 2.** The relative difference of periods (%) between the model M14_ 3 [7] and the Model A [8] as a function the degree of oscillation (solid line – fundamental tones) for torsional (left) and spheroidal (right) oscilations.

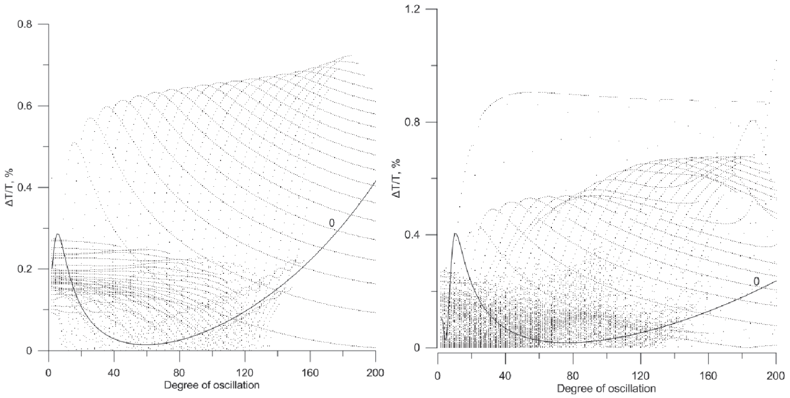


**Fig. 3.** The relative difference of periods (%) between the model M14_ 3 [7] with and without water traces in mantle miner-als as a function the degree of oscillation (solid line — fundamental tones) for torsional (left) and spheroidal (right) oscila-tions.

The study was supported by the Russian Foundation for Basic Research (project no. 12-02-00378).

**References**

[1] Banerdt B. et al. (2010) *Proc.Am.geophys.Union Fall meeting*, San Francisco.
[2] Lonnonné Ph. et al. (2012) *Proc. 3rd Moscow Solar System Symp*. Moscow.
[3]Phillips,R.J,Grimm,R.E.(1991)*LPS*XXXII,1061.
[4] Solomon, S.C. et al. (1991) *LPI Tech.Rpt.* 91-02.Lunar and Planetary institute, Houston, 51 pp. [3] Golombek. et al. (2002) *Science*, 258, 979-981.
[5] Knapmeyer M. et al. (2006) *JGR*, 111, E11006, doi:10.1029/2006JE002708.
[6] Konopliv A.S. et al. (2011) *Icarus,* 211, 401-428.
[7] Zharkov,V.N. et al. (2009) *PEPI*, 172, 324-334.
[8] Sohl, F., Spohn.T. (1997) *JGR*,102, 1613-1635.
[9] Zharkov V.N., Gudkova T.V. (2013) *Proc. 4th Moscow Solar System Symp*. Moscow

# ON NON-HYDROSTATIC DEVIATIONS IN THE CORE-MANTLE BOUNDARY OF MARS

**V. N. Zharkov, T. V. Gudkova ,**
*Schmidt Institute of Physics of the Earth RAS, B.Gruzinskaya 10, Moscow 123995 Russia.*
*Contact: zharkov@ifz.ru*

In a static approach the calculations for the non-hydrostatic deviations in the core-mantle boundary have been performed for a trial interior structure model of Mars with a crust of 50 km thick (Fig.1). Mars departs from hydrostatic equilibrium to significant extent. It is seen if we compare the first even gravitational moments $J_2^0$ and $J_4^0$ for the Martian models in hydrostatic equilibrium state with gravitational moments of the planet [1].

The definition of the "topography" needs the choice of a reference surface. Usually the "topography" is referenced to the areoid determined from the gravity field. As we want to know how nonhydrostatic contributions influence the dynamic flattening at the core-mantle boundary and the amplitudes of the nutations of Mars, the areoid does't fit. To avoid uncontrollable stresses and deformations in the mantle of the planet due to the significant deviation of Mars from hydrostatic equilibrium state, we do not consider the areoid as the reference surface. An outer surface of a hydrostatical model is taken as a reference surface [2, 3].

$$r(s_1,\theta) = s_1\{1 + s_0(s) + s_2(s)P_2(t) + s_4(s)P_4(t) + ...\},$$

where $s_1$ is the mean radius (the radius of an equivolume sphere) and $P_2(t)$ and $P_4(t)$ are the first even ordinary Legendre polynomials, which depend on even degrees of $t$=cos$\theta$ , $\theta$ is the polar distance.

The joint analysis of second-degree harmonics of the topography and the non-equilibrium part of the gravitational potential of the planet has been made. The anomalous density field is represented in the form of two weightable thin layers positioned on the surface and on the interior level – the crust-mantle interface and extended in terms of spherical harmonics, the amplitudes being selected so that the anomalous gravitational field can be produced. The problem is reduced to the determination of Green's response functions for the case of a single anomalous density wave (ADW) located at two depth level [4, 5, 6]. For the case when one ADW is on the surface $x_1$=1 and the other ADW is on the interior level $x_2$<1 the relation between the gravitational moments $\bar{C}_{inm}$ , the amplitudes $R_{inmj}$ and the loading coefficients $k_{n,j}$ and $\bar{k}_{n,j}$ has the form [5]:

$$\bar{C}_{inm} = \frac{3}{2n+1}\frac{1}{R_0\rho_0}\left[(1+k_n)R_{inm,1} + (1+\bar{k}_{n,2})x_2^{n+2}R_{inm,2}\right] =$$
$$\frac{3}{2n+1}\frac{\rho_1}{R_0\rho_0}\left[(1+k_n)H_{ginm,1} + (1+\bar{k}_{n,2})\frac{\rho_2}{\rho_1}x_2^{n+2}H_{ginm,2}\right]$$

where we introduce the corresponding heights of layers $H_{ginm,1} = R_{inm,1}/\rho_1$ — the harmonic coefficients in the expansion of relief. The level $x_2$, in particular, may play the role of level of isostatic compensation or crust-mantle boundary. Only $H_{ginm\,2}$ will be unknown, since $k_n$ and $\bar{k}_{n,2}$ may be calculated for the particular planet model (Fig. 2).

To calculate the amplitudes of ADW, the data on martian topography [7] and gravity [1] have been used. Only unequilibrium components of gravity and topography fields have been considered: surface relief (or topography) was referenced to the standard equilibrium spheroid in the first approximation, and the hydrostatically equilibrium field of Martian spheroid was subtracted from the full potential

$$T(r,\varphi,\lambda) = R_{Mars}(r,\varphi,\lambda) - r(R,\theta), \quad T_g(r,\varphi,\lambda) = V(r,\varphi,\lambda) - V_0(r,t),, \quad \varphi + \theta = \pi/2,$$

where $t$=cos$\theta$ = sin $\varphi$.

Using the amplitudes of ADW as boundary conditions the displacements at the mantle-core boundary and the ellipticity of this level have been estimated.

Two types of models have been considered. We started with a simple model —

an elastic model. Then the models with an elastic lithosphere and weakened layers below it (relaxed values of shear moduli) were calculated: the effective shear modulus (rigidity) of the mantle is reduced in comparison with an elastic one and in extreme case is approaching zero everywhere except the elastic lithosphere. The thickness of the elastic lithosphere was varied from 50 to 300 km (Fig. 3 ). Non-equilibrium state of Mars results in three-axiality of the core-mantle boundary. For an elastic model the deviation of Mars from hydrostatic equilibrium state leads to the large decrease of the semiaxe b of CMB , going through the central region of Tharsis rise, by 660-780 m, and the increase of both the equatorial semiaxe a by 240-300 m, and the polar axe c by 400-490 m. We also have studied the effects of the relaxation of shear modulus on the obtained results.

The mean equatorial flattening $e^{-1}_{ab(c-m)}$ of the core-mantle boundary under given loading for a trial model with different reology is plotted in Fig.3. These results are used to compute amplitudes of forced nutations that is important for future observations of Mars's rotation state [8].

**Acknowledgments.**

The study was supported by the Russian Foundation for Basic Research (12-02-00378).

**References**

[1] Konopliv et al, 2011. Icarus, 211: 401-428; [2] Zharkov, V.N., Gudkova, T.V., 2000. PEPI, 117: 407-420. [3] Zharkov, V.N., Gudkova, T.V., 2005. Solar System Res., 39: 343-373; [4] Marchenkov, K. et al., 1984. Doklady Akad. Nauk, SSSR, Earth Science Sections, 279: 14-16; [5] Zharkov, V.N. et al., 1986. Astron. Vestn., 20: 202-211 (in Russian); [6] Zharkov, V.N.et al., 1991, 25: 515-547; [7] Smith, D.E. et al., 2001. J.Geophys. Res., 106 (E10): 23689-23722; [8] Molodensly, S.M. et al., 2009. PEPI, 172, 335-344.

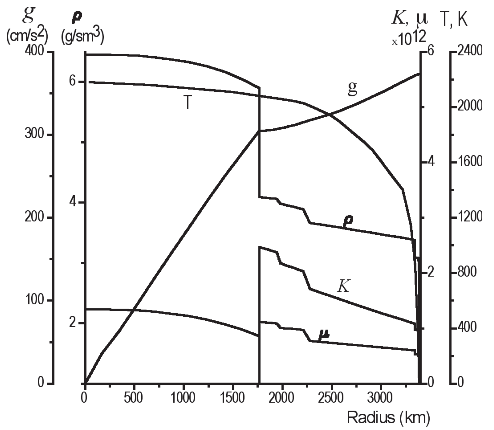


**Fig. 1.** The distribution of density ρ, gravity *g* , temperature *T*, bulk modulus *K* and the rigidity μ as a function of radius through the planet for a trial interior model of Mars

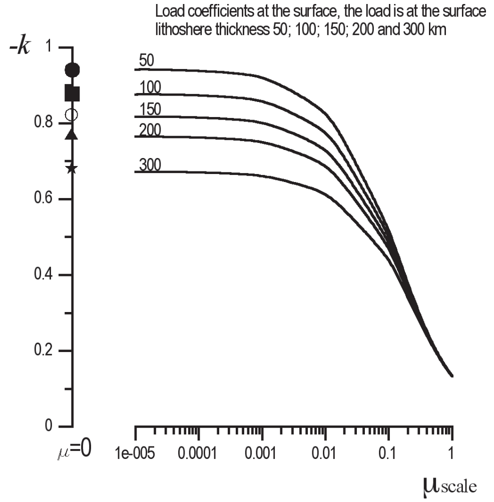


**Fig. 2.** Load coefficients at the surface for different lithosphere thickness.

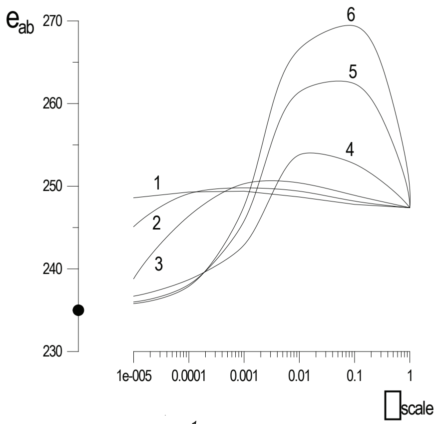


**Fig. 3.** The mean equatorial flattening $e^{-1}_{ab(c-m)}$ of the core-mantle boundary under given loading for a trial model with different reology (μ is multiplied by the coefficient from 1 to $10^{-5}$ in 50 km (1), 100 km (2), 200 km (3), 500 km (4), 1000 km (5) thick astenosphere layers and everywhere (6) under the elastic lithosphere). The elastic lithosphere is 300 km thick. The solid point is the value for μ=0.

# NEW APPROACHES FOR THE ANALYSIS OF GEOMAGNETIC DATA

**L. Vázquez[1], M. Ramirez[1], B. Sánchez-Cano[1], R. Caro[2], C. Aguirre[3], R. V. Mendes[4], S. Jiménez[5]**
*[1]Universidad Complutense de Madrid (UCM), Spain,*
*[2]Universidad Pontificia de Comillas, Spain,*
*[3]Universidad Autónoma de Madrid (UAM), Spain,*
*[4]University of Lisbon, Portugal, 5Universidad Politécnica de Madrid (UPM), Spain*

In this work, we present the preliminary results regarding to the analysis of the magnetic field data from San Pablo de los Montes Observatory (Toledo, Spain) by using Analysis of Variance (ANOVA). This technique provides a statistical test of whether or not the means of several groups are equal. In addition, within descriptive statistics box plots have allowed one to visually estimate various L-estimators. A box plot is a convenient way of graphically depicting groups of numerical data through their quartiles indicating variability outside the upper and lower quartiles. In our study, we have analyzed the three components of the Earth magnetic field for the year 2012. In particular, we carried out a detailed analysis during the period 8th-23rd of July.

The preliminary results show that with our techniques it has been possible to identify different magnetic events related with the solar activity. Such techniques are used usually in other research areas such as economy, marketing or engineering. We also have applied new tomographic techniques.

# AN APPROACH TO CALCULATE SOLAR RADIATION FLUXES ON THE MARTIAN SURFACE

**A. Vicente-Retortillo[1], F. Valero[1], L. Vázquez[1], G. M. Martínez[2]**
*[1]Universidad Complutense de Madrid (UCM), Madrid, Spain).*
*[2]University of Michigan, Ann Arbor, USA.*

MetNet is an atmospheric science mission to Mars, which includes a Solar Irradiance Sensor (MetSIS), designed to measure solar radiation in several bands below 1200 nm. Here we present some preliminary results of a radiative transfer model that we have developed to simulate the solar radiation on the Martian surface in the same spectral bands measured by MetSIS.

# PHOBOS' ORIGIN: REVISITING THE CAPTURE SCENARIO. TIDAL EVOLUTION OF THE POST-CAPTURE ORBIT

**P. Rosenblatt[1], B. Pinier[2],**
*[1]Royal Observatory of Belgium, Avenue circulaire, 3, 1180 Uccle, Belgium; [2]Université de Rennes 1, UFR de Mathématiques, 35065 Rennes cedex, France. Contact: rosenb@oma.be*

**Introduction:**

The origin of Phobos and Deimos is still an open issue. Two families of scenario have been proposed: Either both moons were formed away from Mars' orbit and then captured by Mars gravitational attraction or both moons were formed in orbit, for instance, by re-accretion of debris from a giant impact on Mars (see Rosenblatt, 2011 for a recent review). Recent works on accretion have shown that Phobos and Deimos-like bodies could be formed in Mars' orbit but they cannot be maintained in Mars' orbit over more than some hundreds of millions of years (Rosenblatt and Charnoz, 2012). On another side, a recent study of the Mars' orbit insertion of an asteroid, has shown the capture possible with a large number of initial conditions (Pajola et al., 2012). However, this study has not re-investigated the modeling of the long-term evolution of the post-capture orbit, which has been performed already 30 years ago. These studies have shown the difficulty to produce, by tidal interactions between Mars and its moons, the orbital changes required by the capture scenario to match the current orbit of both moons. Indeed, Deimos' orbit could not be changed by tidal effects over the age of the solar system and the change in orbital inclination of Phobos requires tidal dissipation rate inside Phobos that are not compatible with a rocky body (see Rosenblatt, 2011 and references therein).

Here, we revisit the modeling of the post-capture orbit evolution due to tidal dissipation of the orbital energy. Indeed, the estimation of the current tidal properties of Mars has been improved since the last 30 years and its relationship with the tidal frequency (related to the orbital period of the moons) has been reinvestigated (Efroimsky and Lainey, 2007). The impact of these updated tidal dissipation properties on the long-term evolution of Phobos' orbit is the main focus of this study.

**Model of orbit evolution:**

We have developed a model of the long-term evolution of the orbit of Phobos on the basis of Kaula's (1964) approach and considering the variation of orbital energy due to tidal dissipation inside Mars and inside Phobos. We thus model the secular variations of the semi-major axis, the eccentricity and the inclination of the orbit due to tidal dissipation. The evolution of the inclination of the orbital plane is formulated with respect to the Laplace plane (see Mignard, 1981). Under this formulation, the evolution of this plane with time provides the evolution of the orbital plane inclination with regard to the Mars' equatorial plane and to the ecliptic plane. It thus allows studying the required conditions to change a post-capture orbit in the ecliptic plane into the current equatorial plane of Mars.

The tidal dissipation is introduced following a frequency dependent model of the tidal lag or of the quality factor Q, following a power-law of the orbital frequency of the Mars-Phobos system, with the following values for the power-law exponent $\alpha$: -1, 0, 0.2, 0.3 and 0.4 (Efroimsky and Lainey, 2007). The values from -1 to 0.4 are for increasing tidal dissipation rate, respectively. This dissipation law is applied for Mars as well as for Phobos. The quality factor of Mars at the frequency corresponding to the current orbit of Phobos is taken as the last updated value derived from Phobos ephemerides, i.e. 80 (Lainey et al., 2007; Jacobson, 2010) instead of 50 as in previous studies (see for instance Lambeck, 1979). The same value for Phobos is varying since neither measurements nor theoretical estimation of this parameter has been done so far. The preliminary results presented hereafter have been obtained with values of 10 and 2 for Phobos quality factor in order to compare with previous studies. The frequency dependency has already been introduced in previous studies but primarily with the value of -1 for $\alpha$ (except in Lambeck (1979) who took roughly the same values considered in this study). Other parameters related to secular variations of the orbit are the $k_2$ tidal Love number; the orbital changes being actually proportional to $k_2/Q$. The $k_2$ value is taken as 0.16 for Mars (Konopliv et al., 2006) and as $10^{-4}$ for Phobos as in Lambeck (1979) since no new theoretical estimates have been done for it neither.

**Results:**

As in previous studies, we have run the numerical integration of our model of orbital evolution backwards in time with the initial conditions corresponding to current Phobos orbit (i.e. near-circular and near-equatorial orbit with a semi-major axis of 2.7 Martian planetary radii, or 2.7 Rm) till 4.5 Ga ago.

For a Phobos Q value of 10, the semi-major axis does not almost change till about 20 Ma ago. Then, it exponentially increases and reaches almost 10 Rm about 4.5 Gy ago for the less dissipative law (i.e. $\alpha$=-1). More dissipative law allows for reaching a semi-major axis of up to 16 Rm for $\alpha$=0.4. The eccentricity almost does not change till about 10 Ma ago, and then it abruptly increases between 20 Ma and 200 Ma to reach values of 0.7. It more slowly increases till 4.5 Gy ago to finally reach values as high as 0.8 for $\alpha$=-1 and almost 0.9 for the other values of $\alpha$. The Laplace plane slowly evolves and cannot reach the ecliptic plane of Mars 4.5 Gy ago. It reaches an inclination in between the ecliptic and the Mars' equator (i.e. about 12-13 degree off each plane).

For a Phobos Q value of 2, the secular changes of the orbit are faster since there is more dissipation inside Phobos. The evolution of the semi-major axis follows the same trend as above but it reaches larger values 4.5 Gy ago (up to 15 Rm and 35 Rm for $\alpha$=-1 and $\alpha$=0.4, respectively). The eccentricity reaches the value of 0.7 only 10 Ma ago but it finally reaches the same value 4.5 Gy ago as for a Q of Phobos equal to 10. The Laplace plane evolves in a position in between the ecliptic plane and the equatorial plane for $\alpha$=-1 and $\alpha$=0 but it is almost shifted from the ecliptic to the equatorial plane 4.5 Gy ago for a more dissipative law (i.e. $\alpha$=0.2, 0.3 and 0.4).

**Conclusion and discussion:**

The new value of the Q of Mars (i.e. 80) is less dissipative than the previous one (50) used in previous studies. It thus slows down the secular changes of the post-capture orbit of Phobos with regard to previous results. Nevertheless, the more dissipative law we have used ($\alpha$=0.2, 0.3, 04 instead of -1) accelerates the orbital evolution. Roughly, both effects compensate and we obtain similar results as previously published. Therefore, the evolution of the post-capture orbit to the current orbit requires too much high dissipation inside Phobos, especially to shift the orbital plane from the ecliptic plane to the Mars' equatorial plane. A value of 2 for the Q of Phobos is indeed more relevant for icy material than for rocky material (Rosenblatt, 2011).

Moreover, we have also studied the evolution of the altitude of the periapse of the orbit. This altitude starts at the current value, almost 2.7 Rm, and then it slowly increases to almost 2.8 Rm at 10 Ma ago, for a Q of Phobos of 10 while it decreases to 1.7 Rm for a Q of Phobos of 2. Then, this altitude continues to decrease and reaches 1.8 Rm and 1.4 Rm at 4.5 Gy ago, for Q of Phobos of 10 and 2, respectively. This evolution of the periapse of Phobos' orbit makes it to pass below the Roche limit (2 Rm for a porous Phobos, Sharma, 2009). It does not nevertheless mean that Phobos could have been broken apart by large Mars' tidal forces because for those low altitude periapse passes the orbit is already highly elliptical, and Phobos is most of the time well above the Roche limit.

This low altitude of the periapse of Phobos' orbit put, however, several constraints on the capture scenario that has not been discussed in previous studies. First, the orbit just after capture has to have a periapse at low altitude that make an ad-hoc initial condition and may make the capture even more unlikely, except if another process might help to get rapidly this low-altitude of the periapse. Second, the repeated passes close to or even below the Roche limit might have affected the internal structure of Phobos by shaking its interior (Sharma, 2005). A consequence would be an increase of macro-porosity, which would decrease the bulk rigidity, and thus increases the $k_2$ tidal Love number. The tidal quality factor might also be decreased but in a way still challenging to model. The net effect would be an increase of the k2/Q ratio of Phobos, thus an acceleration of the orbital evolution in a way that has not been taken into account in any computation.

The results of our study confirm the difficulty to change a post-capture orbit into the current orbit of Phobos, especially the shift of its orbital plane from the ecliptic plane to the equatorial plane. However, our results also suggest that the study of the tidal evolution of the post-capture orbit of Phobos would require more complex modeling in order to take into account physical evolution of Phobos that could accelerate the orbital changes.

**References:**

Efroimsky M. and Lainey V., 2007, J. Geophys. Res., vol. 112, doi:10.1029/2007/JE002908; Jacobson R.A., 2010, Astron. J., vol. 139, p. 668-679; Kaula, W.M., 1964, Rev. of Geophys., Vol. 2., 661-685; Konopliv et al., Icarus, 2006, doi:10.1016/j.icarus.2005.12.025; Lainey V. et al., 2007, Astron. & Astrophys., vol. 465, doi:10.1051/0004-6361:20065466.; Lambeck K., 1979, J. Geophys. Res., vol. B 84, p. 5651-5658; Mignard F., 1981, Mon. Not. R. Astron. Soc., vol. 194, p. 365-379; Pajola M., et al., Mon. Not. R. Astron. Soc., 2012, vol. 427, p. 3230-3243; Rosenblatt P., 2011, Astron. & Astrophys. Rev., vol. 19, p. 19-44; Rosenblatt P. and Charnoz S., 2012, Icarus, vol. 221, P. 806-815; Sharma, et al., 2005, Icarus, vol. 183, p. 312-330; Sharma, I., 2009, Icarus, doi:10.1016/j.icarus.2008.11.027.

# THE DRIFT AND STEPS OF THE CENTER OF MASS OF THE MOON WITH RESPECT TO THE CRUST AND INTERPRETATION OF UNEXPLAINED SECULAR CHANGES OF THE LUNAR ORBIT

**Yu. Barkin[1], H. Hanada[2], M. Barkin[3]**
*[1]Sternberg Astronomical Institute, Moscow, Universitetskii pr-t, 13, Russia;*
*[2]National Astronomical Observatory of Japan, Mizusawa, Japan;*
*[3] Bauman Moscow State Technical University, 2 Baumanskaya, Moscow, Russia. Contact: barkin@inbox.ru*

**Introduction:**

We have previously predicted and studied a step (abrupt) shift of the center of mass of the Earth in 1997 - 1998 years relatively to the mantle (Zotov, Barkin, Lubushin, 2009). In accordance with the basic provisions of the geodynamic model of excitation of planets and satellites shells (Barkin, 2002) we expected and we expect similar displacements of the centers of mass for other bodies in the solar system (for Mercury, Moon, Sun, Titan, Mars, etc.). Moreover, according to our hypothesis these abrupt geodynamic phenomena for solar system bodies are synchronous (Barkin, 2000) and, in particular, it should appear in 1997-1998. On the Earth, the similar jumps in 1997-1998 were observed in many planetary processes (Barkin, 2009). In the case of the Moon similar jump of center of mass obtains a confirmation in the data of laser observations and accounts for a specified period of time 1997-1998 (Barkin, 2013).

**The jump (step) in the center of mass of the Moon in 1997 on data of laser ranging of reflectors on the lunar surface.** On the basis of current laser measurements of distances to reflectors mounted on the Moon the preliminary estimates of the parameters of drift, oscillations and jump of the center of mass of the Moon were obtained. Their dynamic interpretation on the base of a geodynamic model of forced relative oscillations of the shells of planets and satellites has been done (Barkin, 2002). In the paper of G.A. Krasinskii (2003) from the analysis of lunar laser range measurements (or rather their residual differences compared with the theoretical celestial-mechanical design values of ranges) an abrupt (step) changes (in 1997 - 1998) in the coordinates of reflectors on the very substantial distances of about 15 -25 cm in selenographic coordinate system of the epoch have been discovered. Since jumps of coordinates for all four observed reflectors were quite close, it is natural to assume that the jump occurred in the position of the center of mass of the Moon by about 25-35 cm relatively to the lunar crust (in direction from the Earth).

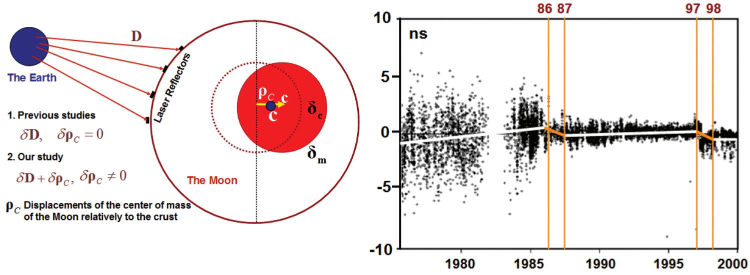


**Fig. 1.** (left) Possible mechanism of the drift of center of mass of the Moon and their manifestations in variations O-C distances to lunar reflectors. Fig. 1 (right) Hypothetical drifts and jumps in values mean laser distances to reflectors on the Moon (in EPM residuals) in 1986 - 1987 and 1997 - 1998 (Barkin, 2013). In ordinate axis are nanoseconds (ns).

Extremely important here is the fact that the jumps occurred in 1997-1998, as it was predicted by the theory of the unified geodynamic synchronous rhythms in variations of the activity of natural processes on the bodies of the solar system (Barkin, 2000). For the mean values of displacements of reflectors the following values were obtained (in meters): -0.15 ± 0.04 m (offset along x coordnate — from the Earth), 0.23 ± 0.07 m (offset on y - east), - 0.23 ± 0.07 m (offset along z - to the north). Thus in 1997, the center of mass of the Moon abruptly shifted to a geographical point on the lunar surface with coordinates 40.0º N, 32.1º W approximately on distance in 0.36 ± 0.11 m. According to the Krasinskii work (2003) we have identified trends in the changes of distances to reflectors and their abrupt changes before 1997 and after 1998, with rates of about 0.036 ns / year (before the jump) and at a rate of 0.128 ns / year (after the jump ). If we consider only the drift relatively to the axis x, then estimates the drift velocities decrease: 0.98 cm / year - until 1997 and 1.47 cm / year - since 1998. It is expected to perform a spectral analysis of the residual differences of distances in order to identify their cyclic variations (with lunar months periods and with multiple periods).

"We find that all the results of obtained from satellite ocean tidal solutions are systematically smaller than the values from LLR. The difference between this study with an average value of 38.45 mm/yr for and the results of LLR with an average value of 37.52 mm/yr needs to be explained in further studies. Thus, a difference of 0.93 mm/yr between our result and the average LLR results still exists." (Williams et al., 2008). Unexplained secular effects in the orbital motion of the Moon are consequences of the observed phenomenon of remove of the center of mass of the Moon relatively to its mantle and crust toward the backside. An explanation of anomalous part of secular variation in the longitude of the Moon and in the eccentricity of the lunar orbit has been obtained.

**Unexplained secular variation of the eccentricity of the lunar orbit.** In the works of James Williams and his colleagues showed that the observed rate of secular change of the eccentricity of the orbit of the Moon in $2.3\times10^{-11}$1/yr can not be explained within the framework of the classical model of the tides. Earth tides give only a fraction of the value specified in $1.3\times10^{-11}$1/yr and lunar tides result even effect with the opposite sign and give part of the acceleration in $-0.6\times10^{-11}$1/yr. Remains unexplained an anomalous part of the secular change in the eccentricity $(1.6\pm0.4)\times10^{-11}$1/yr. This value corresponds to abnormal changes in the distances to the perigee and apogee at 6 mm / year. "Abnormal speed distances to the perigee and apogee of the lunar orbit is up to 6 mm / year and its cause is unknown" (Williams J., Brower lecture, 2006).

Tidal acceleration and evolution of the Moon's orbit. Laser ranging method proved to be very sensitive to the tidal acceleration of the Moon. Tides on the Earth dominate in the transfer of angular momentum, and energy in the orbital motion, in particular in the removal of the Moon from the Earth. Tidal effects on the Moon are separable from the effects of Earth tides in laser range measurements to the Moon (Chapront et al., 2002; Williams et al., 2009). Full tidal acceleration in the mean orbital longitude (due to the tides of the Earth and the Moon) is estimated at -25.85'' 1/cy², corresponding to the removal of the Moon from the Earth at a speed of 3.81 cm / year (Williams et al., 2009). The rate of secular variation of the eccentricity of the lunar orbit $e=(9\pm3)\times10^{-12}$1/year also detected on the basis of long laser observations over a period of 38.7 years (March 16, 1970 - November 22, 2008) (Williams, Boggs, 2009). The basis of dynamical studies makes a precision lunar ephemeris DE421, taking into account all of Newtonian and Einsteinian effects. The authors believe that the study of the evolution of the lunar orbit is an important and surprisingly difficult task. Lunar laser ranging provides the numerical values for the two sources of dissipation on the Earth and the Moon.

Recently, the main features of the anomalous secular in reases of both the astronomical unit and the lunar eccentricity attracted the attention of many scientists dealing with them in different contexts (Ni, 2005; Kopeikin, 2007, 2010; L¨ammerzahl & Dittus, 2007; Carrera & Giulini, 2010; Li et al., 2010; Goldhaber & Nieto, 2010; Sharma, 2010; Speliotopoulos2010; Zhang et al.2010; L¨ammerzahl, 2011; Zhang& Kaley, 2011). Thus, several more or less sound attempts to find, or to rule out, possible explanations (Krasinsky & Brumberg, 2004; Iorio, 2005; Mashhoon & Singh, 2006; Østvang, 2007; Mashhoon et al., 2007; Khokhlov, 2007; Noerdlinger, 2008; L¨ammerzahl et al., 2008; Verbiest et al., 2008; Amin, 2009; Arakida, 2009; Miuraetal,2009; Ito, 2009; Li & Chang, 2009; L¨ammerzahl, 2009; Brumberg, 2010; Nyambuya, 2010; Bel, 2010; Arakida, 2010, 2011; Anderson & Nieto, 2010; Rasor, 2010; Iorio, 2011) for both anomalies have been proposed so far, both in terms of standard known gravitational physical phenomena and of long-range modified models of gravity (Iorio, 2012). For preliminary introduction to discussed non-trivial problems we recommend to read mentioned papers Williams et al., 2008; Iorio, 2012 and oth.

Explanation of the pointed anomalous effects in orbital motion of the Moon in our work is given on the base of mechanism of forced relative displacements of the center of mass o f the Moon which we found by interpretation of laser observations.

**Possible secular drift of the center of mass of the Moon relative to its crust and mantle toward the back side and an explanation of the anomalies of the orbital motion.** In this report we give some first estimations of the possible rate of the secular drift of the Moon center of mass with respect to its crust and mantle in the 10 - 15 mm / year toward the back-side of the satellite. This secular drift of the center of mass of the Moon should be considered by the studying of the orbital motion of the Moon on laser-based observations. Namely, to add to the value obtained by laser observations. The result will be an estimate of the secular increasing of semi-major axis is the center of mass of the Moon. It should be expected that this will obtain the interpretation and explanation of the unexplained part of the secular acceleration of the Moon orbit and the anomalous part of the secular variation of the eccentricity of the lunar orbit, identified according to the perennial laser observations of the Moon. An anomalous part of the orbital acceleration (unexplained) of the Moon is 0.7''/cy$^2$, and the anomalous part of the secular variation of the eccentricity is characterized by rate in $1.23\times10^{-11}$1/yr (Williams et al., 2011). Found offset - drift of the center of mass of the Moon (12 - 15 mm / yr) is explained by the mechanism of excitation and the relative displacements of the shells of the Moon (solid core, liquid core, mantle) (Barkin, 2002).

# THE UNIFIED THEORY OF NATURAL PROCESSES OF PLANETS, SATELLITES AND THE SUN

**Yu. Barkin,**
*Sternberg Astronomical Institute, Universitetskii pr-t, 13, Moscow, Russia.*
*Contact: barkin@inbox.ru*

The key issue of the theory of natural planetary processes on the Earth and other celestial bodies, is the question about the sources of endogenous activity and the underlying mechanism of energetic excitation of celestial bodies. We offer a solution to this difficult question on the basis of the mechanism of excitation of the shells of a celestial body by gravitational attraction of the external celestial bodies. The main provision of the developed geodynamic concept lies in the fact that the planets, moons and the Sun are the define system of shells (of the core, the mantle, and others), which make to each other a translational-rotational motion and deformation changes under the influence of others external celestial bodies (Barkin, 2002). Main exciting factors of systems of shells of the celestial body (planets, satellites, stars, pulsars, etc.) are their non-sphericity and eccentricity of their mutual positions.

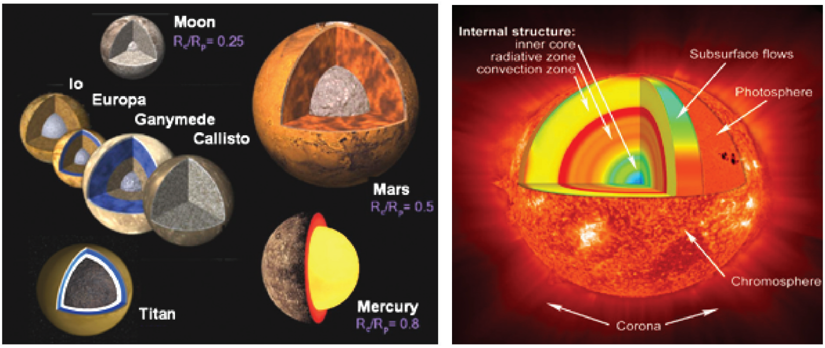


**Fig.1.** The fundamental feature of the structure of the planet and satellites (left) and the Sun (right) is their inner shell structure.

We have developed the fundamentals of this geodynamic model of the forced and free oscillations of the shells. In particular, the tides in the viscous-elastic mantle of the planet, which are generated by the gravitational forces of interaction with the movable core. They change over time leads to the dissipation of the mechanical energy in the material of planet, which is transformed into heat and generates the temperature field inside the planet. As a model of the non-deformed planet e consider viscous elastic homogeneous sphere, the material behavior is described by the Kelvin - Voigt model. It is determined by the strain rate tensor of deformations of rotating planet and the average temperature field inside the planet. The integral heat flow as global so in the northern and southern hemispheres of the Earth are determined. The most important question, of course, at all times in the history of geosciences was the question about the source of energy (Khain, Lomize, 2005), which provides unprecedented activity of the Earth, and it is now known that many other celestial bodies. The known energy mechanisms such as radiogenic heat, tidal friction and others can not explain either by a total energy or cyclical processes, not to mention the above fine planetary phenomena of inversion, step-by-step phenomena, the activity of the polar regions and others (Barkin, 2002). The current research clearly shows that tidal friction gives only a small contribution to the total observed heat flow of the Earth (~ 0.4 TW) across the surface of the Earth, which is currently estimated at 46 ± 3 TW, i.e. order of one percent. The dissipation of tidal energy on Enceladus can explain only 1 part of 27 of the observed heat flow. The dissipation of tidal energy in the satellite Io explains only a small part of the observed heat flow and the endogenous activity of the satellite (Barkin, 2011). All these problems are solved with the help of the geodynamic mechanism of the forced relative oscillation of the core and mantle of the Earth (Barkin, 1999, 2002). These displacements of the core lead to a shift of the center of mass of the Earth relative to the mantle, which is currently available for the study of space geodetic techniques (satellite methods). Currently, revealed a wide range of oscillations of the center of mass of the Earth (Barkin et al., 2007; Gobinddass et al., 2009;) and discovered his secular trend towards the north (the area of the Taimyr Peninsula) (Barkin, 1995). On the other hand, the displacements of the center of mass of the Earth can restore the style and features of the relative displacements of the core and mantle of the Earth, to study geodynamic consequences of these shifts, such as physical fields, the redistribution fluid masses and other studies carried out effectively solve the energy issue in the life of deformation of the mantle, the variations of its elastic energy, power dissipation and heat flux of the planet, the other the planets and satellites.

In particular the power of dissipation of the elastic energy of the mantle for the observed oscillations of the core and according to our estimates may be 1000 — 10.000 terawatt (TW). This is a huge value of power with a vengeance explains all the endogenous activity of the Earth. Regarded geodynamic model of the relative displacements and oscillations of the core and mantle explains all the fundamental properties of planetary processes on Earth and other planets, satellites and Sun: cyclicality, unity, synchronicity, inversion, polar activity, step-by-step phenomena (Fig.2), saw-toothed, orderliness, twisting of layers of the mantle, the pear-shaped, versatility.

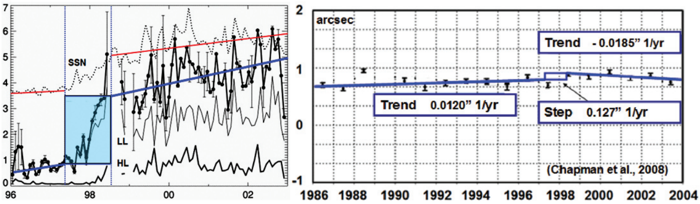


**Fig. 2.** Synchronous steps in natural processes on the Sun in 1997 – 1998: (left) rates of coronal mass ejections (CMEs), obtained by coronagraphs SOHO / LASCO (solid line with black circles) in compared with daily values of SSNs. (on the paper Gopalswamy et al., 2003); (right) trend and step changes of mea radius of the Sun (on Chapman et al., 2008).

After 10-15 years of our studies the mentioned above phenomena and properties of endogenous activity of the celestial bodies have been obtained wide development in geosciences and planet science. Some from them are illustrated in report on the examples of natural processes on the Earth, the Sun, the Moon, Enceladus, Titan, Mars, etc.

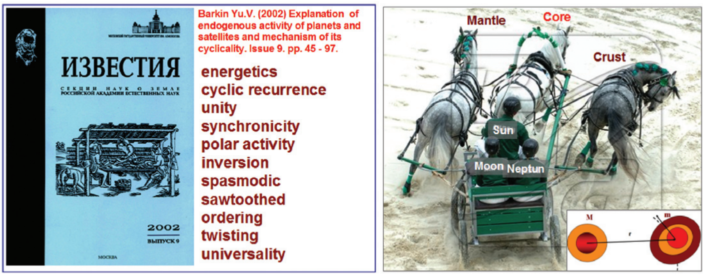


**Fig. 3.** Main publication on mechanism of endogenous activity of celestial bodies and discussed properties of natural processes (left); schematic illustration of the gravitational excitation of the Earth's shell system (right).

### References

Barkin Yu.V. (2002) Tectonic activity of the planets and satellites: mechanism and nature of cyclicity. In: Earth-like planets and moons. Proceedings of the 36th ESLAB Symposium, 3 - 8 June 2002, ESTEC, Noordwijk, The Netherlands. Eds.: B. Foing, B. Battrick. ESA SP-514, Noordwijk: ESA Publications Division, ISBN 92-9092-824-7, 2002, p. 201 – 207.

Zotov L.V., Barkin Yu.V., Lubushin A.A. (2009) Geocenter motion and its geodynamical contents // "Space Geodynamics and Modeling of the Global Geodynamic Processes", Novosibirsk, Russian Federation, 22-26 September, 2008; Russian Academy of Sciences, Trofimuk Inst. Of Petrol. Geol. And Geophys., SB RAS. – Novosibirsk: Academic Publishing House "Geo". 2009. P. 98-101

Barkin Yu.V. Synchronous jumps in the processes and phenomena on the Earth, Moon and Sun in 1997-1998 and a unified mechanism // Geology of seas and oceans: Proceedings XX International Scientific Conference (School) in marine geology. Vol.5. - M .: GEOS. 2013. c. 21 -25. In Russian.

Barkin Yuri (2013) Unified theory of planetary processes of planets, satellites and the Sun. International Symposium & Summer School on Planetary Science (IAPS 2013) July 1-7, 2013, Shanghai, China. 2p.
http://202.127.29.4/meetings/iaps2013/Program_IAPS2013.pdf

# NEW SPECTRAL FEATURES OF SOME ASTEROIDS

**V. V. Busarev[1,2], S. I. Barabanov[2], V. B. Puzin[2], F. A. Musaev[3, 2],**
*[1] Moscow Lomonosov University, Sternberg Astronomical Institute, University Av. 13, 119992 Moscow, Russia, Contact: busarev@sai.msu.ru;*
*[2]Institute of Astronomy of Russian Academy of Science (IA RAS), Pyatnitskaya St. 48, 109017 Moscow, Russia;*
*[3]Special Astrophysical Observatory of Russian Academy of Science, 357147 Nizhnij Arkhys, Karachai-Circessia Republic, Russia*

**Introduction:**

We have performed spectrophotometry of (32) Pomona, (704) Interamnia, (779) Nina, (330825) 2008 XE3, and 2012 QG42 accessible for observation in September 2012 including two NEAs, one of which is PHA, to study absorption features in their reflectance spectra with the aim to get new mineralogical information on the surface matter and its correspondence to a spectral type. The obtained results could be useful in investigations of Moon and other atmosphereless bodies at identification of residues of fallen asteroids.

**Observations and data reduction:**

Low-resolution spectrometry of (32) Pomona, (704) Interamnia, (779) Nina, (330825) 2008 XE3 and 2012 QG42 has been performed on 2-m telescope at Terskol Observatory (3150-m above sea level) operated by IA RAS. As is follows from the practice of observations, the more the height, the better spectral transparence of terrestrial atmosphere, especially, in the short-wavelength range. The telescope is equipped with a prism CCD-spectrometer (WI CCD 1240 x 1150 pix.) working in the range 0.35 - 0.97 μm with $R \approx 100$ resolving power. Asteroid reflectance spectra were computed according to a conventional method based on observations of a solar analog star (e. g., [18, 10]). HD10307 was used as a standard and solar analog star [14]. To extract the asteroid spectra, standard processing of CCD-data and the Dech spectral package [13] were employed.

**Results:**

*(32) Pomona.* Pomona's average diameter and geometric albedo are 80.76 km and 0.256 [26] or 78 km and 0.27, respectively, according to WISE data [2]. It rotates with a period of $9.448^h$ [15]. The asteroid observational spectra were obtained for ~1.5 hours corresponding to ~1/5 of the period of asteroid rotation on the night 19/20 in September 2012. The asteroid average reflectance spectrum is close in shape to those obtained previously [28, 5] and corresponds to an S-type asteroid which mineralogy is dominated by pyroxenes, olivines and other high-temperature minerals (e. g., [12]). Reflectance spectra of the asteroid normalized at a wavelength of 0.55 μm are presented in chronological order in Figure 1. Spectrum 2 is arbitrarily shifted relative to 1 by 0.3 unit for clarity. Spectra 1 and 2 are averages of 6 and 2 similar in shape consecutive reflectance spectra, respectively.

We registered two relatively weak and broad absorption bands at 0.49-0.55 μm and 0.73-0.77 μm on the reflectance spectra of Pomona (Fig. 1). We suppose that the first one, at 0.49-0.55 μm, has a complex nature. It may be a superposition of two or three features. It is established that electronic spin-forbidden crystal-field transitions in $Fe^{2+}$ ions in M2 crystallographic sites of clinopyroxenes are responsible for a couple of weak bands near 0.505 and 0.550 μm (e. g., [20, 19, 8, 17]). If the asteroid surface matter consists of a clinopyroxene and Fe-orthopyroxene mixture, then additional weak band of spin-forbidden crystal-field transitions in $Fe^{2+}$ ions in M1 crystallographic sites of Fe orthopyroxenes could origin at 0.525 μm. Moreover, the common absorption band at 0.49-0.55 μm could be widened because of crystal structure disordering at the process of space weathering of the asteroid surface (e. g., [9]). At the same time, as shown for terrestrial and meteoritic analog samples [9, 21, 7, 3, 19, 16, 25], more intense absorption bands take place in the same positions as spin-forbidden crystal-field features of $Fe^{2+}$ and $Fe^{3+}$ ions. Probable mechanisms of a such intensification could be electronic transitions in magnetic exchange-coupled pairs of neighboring cations, $Fe^{2+}$ - $Fe^{3+}$ [22, 19] or $Fe^{3+}$- $Fe^{3+}$ [11, 21, 24, 25].

*(704) Interamnia.* The average diameter and geometric albedo of Interamnia are 316.62 km and 0.074 [26] or 361 km and 0.06 according to WISE data [2]. It rotates with a period of $8.727^h$ [15]. It is classified as F-type asteroid by

Tholen [27] and as B-type by Bus & Binzel [6] characterized by a wide absorption behind ~0.5 μm with a common negative gradient. Five observational spectra of Interamnia were obtained for ~3/4 hour corresponding to ~1/10 of its rotation period. Normalized (at 0.55 μm) and averaged reflectance spectrum of the asteroid is shown in Fig. 2. We have discovered three prominent absorption bands in the reflectance spectra of Interamnia. The strongest one is in the range 0.54-0.83 μm arising possibly due to electronic intervalence charge transfer (IVCT) $Fe^{2+} \rightarrow Fe^{3+}$ in hydrated and/or oxidized silicates [20, 3, 8]. The second is at 0.42-0.49 μm originating probably at electronic transitions in exchangeable pairs of $Fe^{3+}$ ($^6A_1(^6S) \rightarrow {}^4T_2(^4G)$) [21, 24, 3, 16]. The third could be at 0.36-0.40 μm (Fig. 2), though it is distorted by influence of observational errors in the range. The last may appear because of electronic transitions in exchangeable pairs of $Fe^{3+}$ ($^6A_1(^6S) \rightarrow {}^4E(^4D)$) [21, 24, 3, 16].

*779 Nina*. It is a 76.62-km asteroid having geometric albedo of 0.144 [26] and rotating with a period of 11.186$^h$ [15]. It was classified as M-type by Tholen [27] and as X-type according to SMASSII taxonomy [6]. Normalized (at a wavelength of 0.55 μm) reflectance spectra of Nina are presented in chronological order in Fig. 3. Spectra 1, 2 and 3 are arbitrarily displaced for clarity. Each of the spectra 1 and 2 is the average of five, and the spectrum 3 – of two similar in shape consecutive reflectance spectra. As it turned out, reflectance spectra of the asteroid representing ~1/2 part of its surface are very similar to the obtained spectrum of Interamnia (Fig. 2). There are almost the same absorption bands in the reflectance spectrum of Nina (at 0.37, 0.44 and 0.7 μm) as ones of Interamnia (especially in 2 and 3 spectra, Fig. 3). Some differences of the Nina's absorption features (Fig. 3) are their slightly larger width comparing with those of Interamnia. Thus, the same interpretations of the absorption bands of Nina could be given. We speculate that considerable parts of both asteroids are covered with a similar matter corresponding to B-type. However, there is a substantial difference in geometric albedo of Interamnia (0.60-0.074) and Nina (0.144). This suggests that the material (lower albedo) can be distributed unevenly on Nina. Yet, radar observations of Nina showed that its albedo is typical for a primitive type asteroid [23].

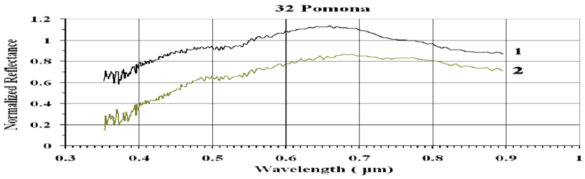


**Fig. 1.** .

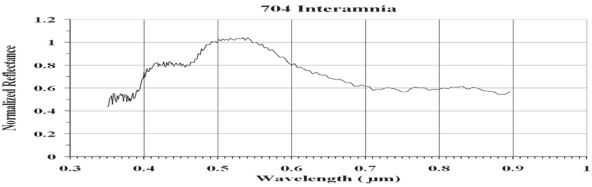


**Fig. 2.**

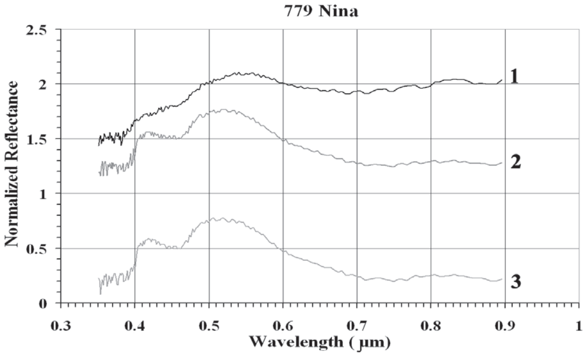


**Fig. 3.**

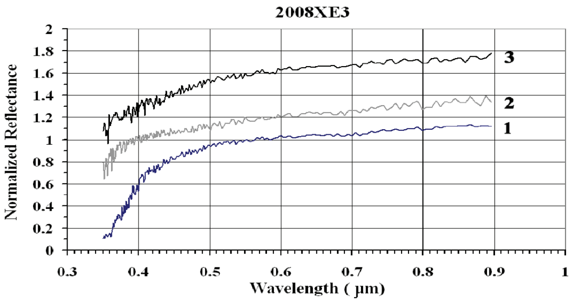


**Fig. 4.**

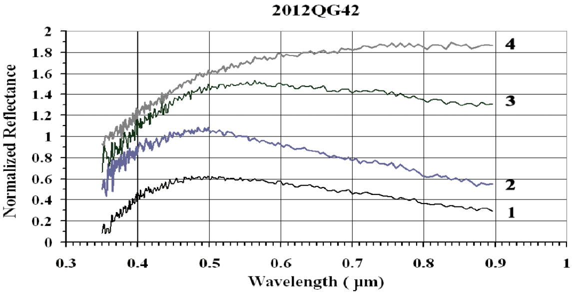


**Fig. 5.**

*330825 (2008 XE3) and 2012 QG42.* The asteroids (330825 (2008 *XE*3) is a member of Amor group and 2012 QG42 is a member of Apollo group) have rotational periods of 4.409$^h$ [29] and 24.22$^h$ [30], respectively. Observational spectra of 330825 were registered for about 2.5 hours, which corresponds to ~3/5 of its rotational period. Normalized (at 0.55 µm) reflectance spectra of the asteroid are shown in Fig. 4. Spectra 2 and 3 are arbitrarily displaced relative to the first to facilitate their comparison. Spectrum 1 is calculated as the average of three and spectrum 3 of two similar in shape consecutive reflectance spectra. Reflectance spectrum 2 is calculated only from one registered spectrum obtained with exposure time of 30 minutes. A relatively short rotational period of 330825 could be considered as an indicator of its monolithic structure and a dense structure of matter. On the contrary, a relatively long rotational period of 2012 QG42 could be a sign of porous and/or low density interiors. Observational spectra of the asteroid were obtained for about 2 hours, which corresponds ~1/10 part of its rotational period. Normalized (at 0.55 µm) reflectance spectra of the asteroid are shown in chronological order in Fig. 5. The spectra arbitrarily displaced for clarity. Spectrum 1 of 2012 QG42 is the average of three, and spectrum 4 – of two similar in shape consecutive reflectance spectra. Reflectance spectra 2 and 3 are calculated from single observational spectra obtained with 20-minute expositions. As seen from Figs 4 and 5, both asteroids demonstrate featureless reflectance spectra typical for C-B-type bodies. This may be a consequence of darkening agents presence (provisionally carbonaceous compounds and/or magnetite) in their surface matter. Relying on taxonomy of spectrally similar bodies [6], we preliminary assess spectral type of 330825 as “C” and that of 2012 QG42 as “B”.

**References:**

[1] Adams J. B. 1974, J. Geoph. Res., 79, 4829. [2] Ali-Lagoa V. et al. 2013, A&A, 554, id.A71, 16 pp. [3] Bakhtin A. I. 1985, Rock-forming minerals: Spectra, crystal chemistry, coloring regularities, and typomorphysm, Kazan: Kazan. Univ. Press (in Russian). [4] Bell J. F. et al. 1989, Asteroids: The big picture, in Asteroids II (Eds R. P. Binzel, T. Gehrels & M. S. Mattews (Tucson: Univ. of Arizona Press), 921. [5] Bus S. J., & Binzel R. P. 2002a, Icarus, 158, 106. [6] Bus S. J., & Binzel R. P. 2002b, Icarus, 158, 146. [7] Burns R. G. 1981, Ann. Rev. Earth Planet Sci., 9, 345. [8] Burns R. G. 1993, Mineralogical Applications of Crystal Field Theory. 2nd ed., 1993, Cambridge: Cambridge University Press. [9] Charette M. P. et al. 1974, J. Geoph. Res., 79, 1605. [10] Chapman C. R. et al. 1973, Astron. J., 78, 126. [11] Ferguson J. et al. 1966, J. Phys. Soc. Jap., 21, 347. [12] Gaffey M. J. et al. 1989, Asteroids II / Eds Binzel R. P., Gehrels T. & Mattews M. S. Tucson: Univ. of Arizona Press, 98. [13] Galazutdinov G. A. 1992, Preprint Special Astrophys. Observ., 92, 27 (in Russian). [14] Hardorp J. 1980, A&A, 91, 221. [15] Harris A.W. et al., Eds., 2012, Asteroid Lightcurve Derived Data V13.0. EAR-A-5-DDR-DERIVED-LIGHTCURVE-V13.0. NASA Planetary Data System. [16] Khomenko V. M., & Platonov A. N. 1987, Rock-forming

pyroxenes: Optical spectra, colouring, and pleochroism/ Kiev: Naukova Dumka Press (in Russian). [17] Klima R. L. et al., 2006, 37th Lunar Planet. Sci. Conf., # 1637. [18] McCord T. B. et al. 1970, Science, 168, 1445. [19] Matsyuk S. S. et al. 1985, Optical spectra and coloring of mantle minerals in kimberlites, Kiev: Naukova dumka (in Russian). [20] Platonov A. N. 1976, The nature of mineral coloring, Kiev: Naukova dumka (in Russian). [21] Rossman G. R. 1975, Americ. Mineralogist, 60, 698. [22] Robbins D. W., & Strens G. G. 1968, Chem. Communs, 5, 508. [23] Shepard M. K. et al. 2010, Icarus, 208, 221. [24] Sherman D. M. 1985, Phys. Chem. Minerals, 12, 161. [25] Taran M. N., & Rossman G. R. 2002, Americ. Mineralogist, 87, 1148. [26] Tedesco E. F. et al., Eds. 2004, IRAS minor planet survey V6.0. IRAS-A-FPA-3-RDR-IMPS-V6.0. NASA Planetary Data System. [27] Tholen D. J. 1989, Asteroids II (Eds Binzel R. P., Gehrels T. and Mattews M. S.), Tucson: Univ. of Arizona Press, 1139. [28] Tholen D. J., & Barucci M. A. 1989, Asteroids II (Eds Binzel R. P., Gehrels T. and Mattews M. S.), Tucson: Univ. of Arizona Press, 298. [29] Warner B.D. 2013, Minor Planet Bul. 40, 71. [30] Warner B.D. et al. 2013, Minor Planet Bul. 40, 25.

# LUNOKHOD 1 ANDCHANG'E 3 LANDING SITES: COMPARATIVE CHARACTERISTICS

**V.V. Shevchenko[1], Lu Yangxiaoyi[2],**
*[1]Sternberg State Astronomical Institute, Moscow University, 119991 Moscow, Universitetsky pros. 13, Russian Federation;*
*[2]Beijing Planetarium, Building B, Room 606.*
*No. 138 Xizhimenwai Main Street, Xicheng District, Beijing, China, 100044.*
*Contact: vladislav_shevch@mail.ru*

**Introduction:**

Both devices are landed and carried out a series of active measures in the northern part of the Mare Imbrium. Landing sites of the vehicles are separated from each other by nearly 400 km, however, are in areas of similar morphology, topography and spectral characteristics of the surface layer. If we compare the traces of the chassis units, it is possible in the first approximation to conclude that the mechanical properties of the soil in both areas are about the same.

**Positions of the Lunokhod 1 and Chang'e 3 in Mare Imbrium:**

Figure 1 shows northern part of the Mare Imbrium.The figure enhanced color contrast that highlights the area of the surface ofMare Imbrium, having spectral differences from the surrounding countryside. The positionsof theboth vehicles indicates that both Lunokhod 1 and Chang'e3 are located on the surface with the same spectral characteristics.

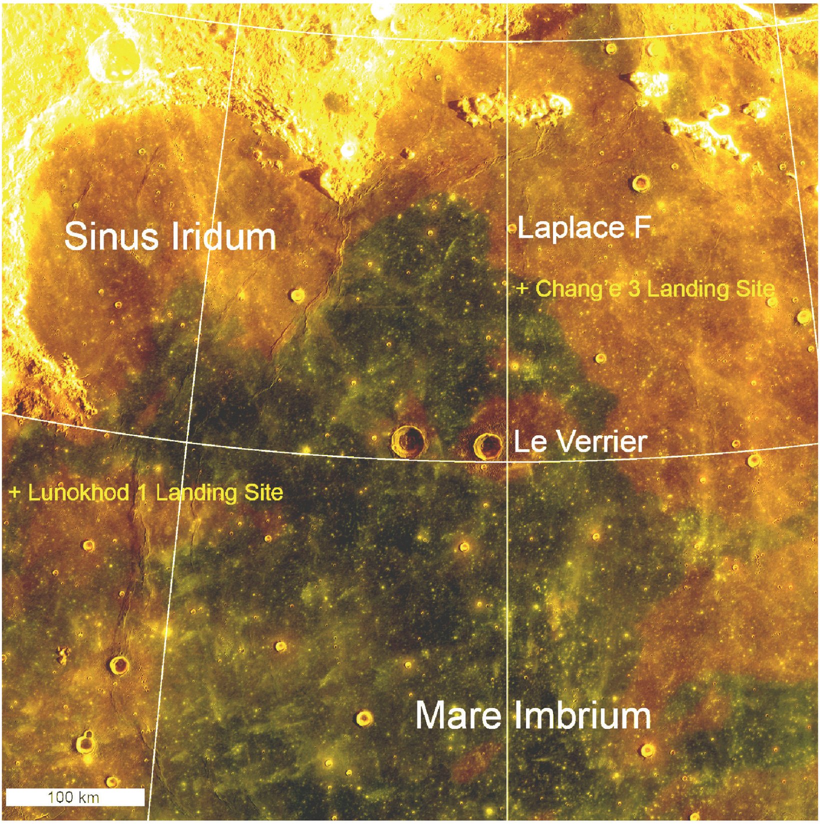


**Fig.1.** (NASA/GSFC/Arizona State University).

According to compositional remote sensing data from Lunar Prospector Gamma Ray Spectrometer and Clementine high-alumina basalts in the lunar surface for the regions correspond to the intersection of three compositional constraints taken from values of sampled basalts: 12–18 wt% FeO, 1.5–5 wt% $TiO_2$, and 0–4 ppm Th (Kramer et al., 2008). Spectrally resemble high-alumina basalts are consistent with the compositional and relative age of the Luna 16 samples. General morphological situation for landing sites are in Figure 2 (area of the vehicleLunokhod 1) and Figure 3 (area of the vehicleChang'e 3). Large-scale images with a resolution of about 0.5 m per pixel obtained satellite camera from Lunar Reconnaissance Orbiter (NASA/GSFC/Arizona State University).

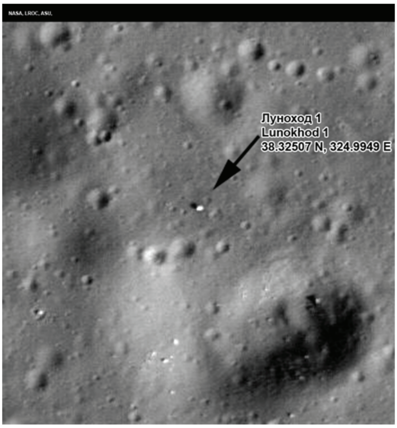


**Fig. 2.**

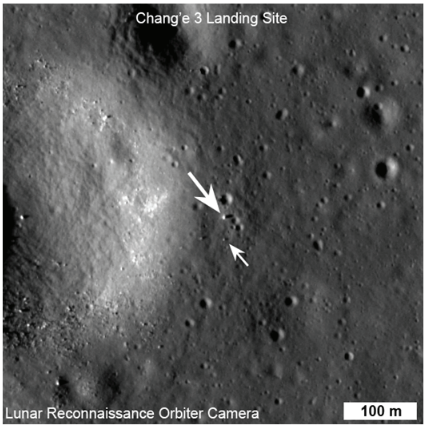


**Fig. 3.**

**Bright Fragments:**

A characteristic feature of the surface layer of lava in both areas is the presence of light-colored debris. Figure4 and Figure5show typical areas with high incidence of light debris on panoramas obtained from Lunokhod 1 and Chang'e 3.

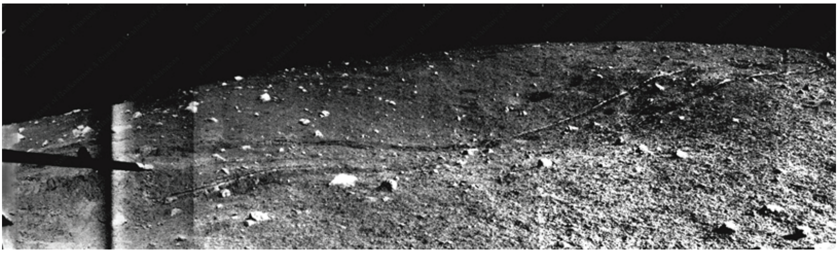

**Fig. 4.**

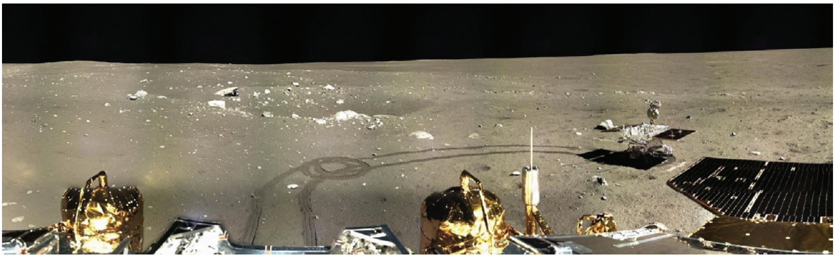

**Fig. 5.**

**Reference**

Kramer et al., Icarus, V. 198, Iss.1, P 7–182008, 2008.

# KREEP-LIKE TERRAINS RISING IN WIDE SUBSIDED BASALT FILLED HEMISPHERIC EXPANSES OF EARTH, MARS, AND MOON: A COMMON REASON

**G.G. Kochemasov;**
*IGEM of the Russian Academy of Sciences, 119017 Moscow, 35 Staromonetny , kochem.36@mail.ru*

Wave planetology [1-5] divides cosmic globes into two halves –hemispheric segments. They regularly appear in the bodies due to a warping action of inertia-gravity waves arising due to regularly changing cosmic accelerations of bodies moving in non-circular keplerian orbits. Angular moments of the two hypsometrically different hemispheric segments must be equal (or nearly so) to bring a rotating body to a smooth rotation and minimize its energy. That is why bodies lowlands are filled with dense basalts and highlands are built by less dense lithologies like granites, andesites, plagioclasites and so on. The wave planetology distinguishes along with the segments-hemispheres ($2\pi R$-structures) superimposed on them less large and amplitudinal structures of the harmonic row. One of them complicates subsided basaltic segments by bulges (“superswells” in the terrestrial terms). But rising (uplifted) blocks, according to the rotating bodies tectonics, must be less dense than surrounding subsided basaltic spaces. To fulfill this purely physical demand the uplifted blocks extract from the mantle depths less dense alkali rich but still basaltic material. Alkali enrichment brings with it a number of small elements like radioactive elements, strontium, rare earth elements, and volatile elements like phosphorus. Having at Earth, Mars and Moon some peculiar features these light alkali rich basaltic formations (KREEP and KREEP-like terrains) show remarkable common characteristics discovered by remote sensing and on land studies.

Terrestrial South-Pacific “Superswell” under French Polynesia is marked by chains of basaltic islands with peculiar geochemical characteristics and deep mantle roots (Fig. 1, 2). Basalts often are of alkaline type and enriched with K, Na, U, Th, Sr, Ba, REE, P - a kind of terrestrial KREEP.

The central part of the lunar Procellarum Ocean has geochemically anomalous area with elevated concentrations of potassium and thorium – so called Procellarum KREEP Terrain (PKT) (Fig. 3). Morphologically it is slightly elevated area and discovered on land basaltic fragments have distinctive KREEP characteristics (K, Th, REE, P).

On the whole similar with the lunar and terrestrial alkali rich terrains in the middle of the vast basaltic lowlands ($2\pi R$-structures) the martian case is somewhat different. The K-Th anomaly (Fig. 4, 5) is not underlined by a topographic “swell”. It occurs in the deepest part of the Vastitas Borealis (Acidalia Planitia), but presents the north-eastern continuation of the Tempe Terra – the most protruding into lowlands the north-eastern corner of the huge Tharsis Montes (Fig. 5, 6). The Tempe Fossae strike NE and partly cover the K-Th anomalous area. Why there is such detachment between the anomalies and “related” upwarp is not known but one might presume (as one of the reasons) that waters of the ancient ocean washed off a soft K-Th enriched basaltic tuff and deposited debris on the oceanic bottom near by. But more fundamental reason might be in the martian planetary tectonics. The striking NE crest of the most prominent positive geoid anomaly (Fig. 5) goes through Arsia, Pavonis, and Ascraeus Mons, Uranius Patera, Tempe Terra and Tempe Fossae. Farther this NE tectonic direction crosses the dichotomy boundary and enters the Acidalia Planitia where it is marked by the prominent K-Th geochemical anomaly (Fig. 4, 6). The Tempe landscape is marked by several extensive valley systems [6, 7]. Long grabens upto 1 km wide witness crustal extension. Belonging the geochemical anomaly to the NE edge of the most prominent geoid uplift should provoke melting out the lighter alkali fraction of the basaltic mantle of the northern hemisphere. In the southern highland hemisphere this wave induced uplift provokes appearance of the lighter lithologies (Tharsis itself and huge volcanoes).

Thus, the origin of the KREEP-like terrains in comparable situations of three different celestial bodies indicates that common reasons related to the wave-induced tectonics actually exist.

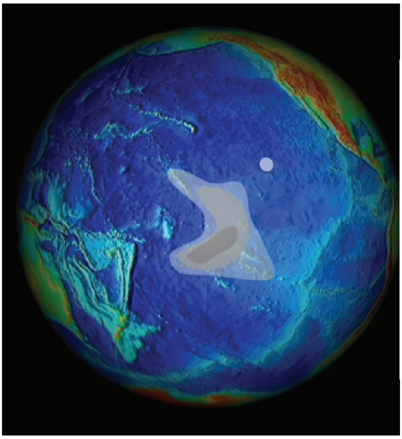

Fig. 1. Earth. The South Pacific "Superswell"

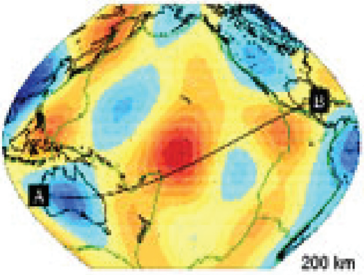


**Fig. 2.**. South Pacific "Superswell" at 210 km depth, seismic tomography [8]..

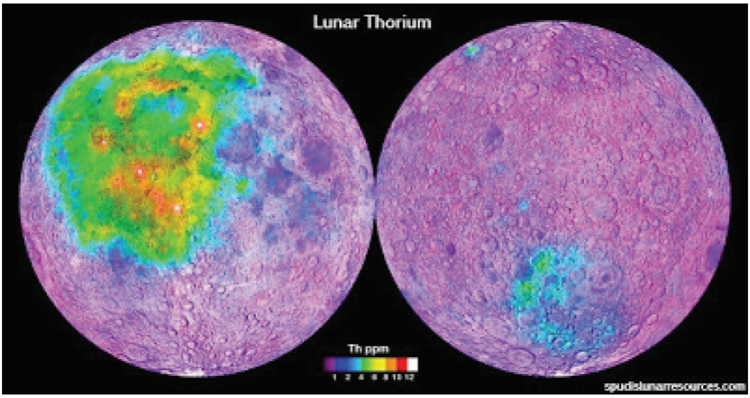


**Fig. 3**. Moon. Procellarum KREEP terrain.

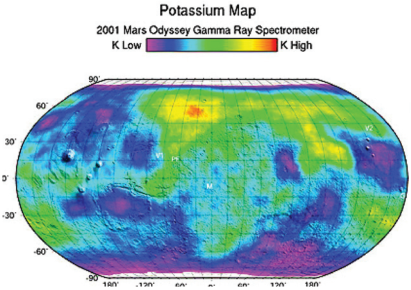


**Fig. 4.** Martian geochemistry

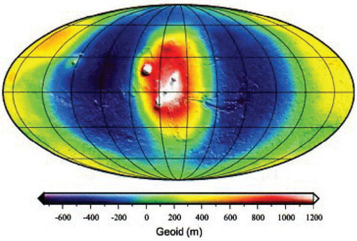


**Fig. 5**. Martian-geoid-j2002_jpg

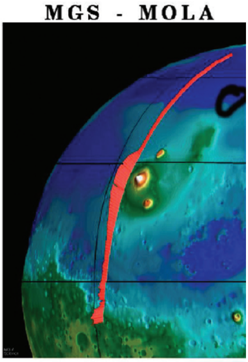


**Fig. 6.** Tharsis bulge. Black line-western part of the K-Th anomaly. mgs_n_hemisphere1_jpg

**References:**

[1] Kochemasov G.G. (1992) Concerted wave supergranulation of the solar system bodies // 16th Russian-American microsymposium on planetology, Abstracts, Moscow, Vernadsky Inst. (GEOKHI), 36-37.
[2] Kochemasov G.G. (1998a) Sectoral tectonics of the Earth's eastern hemisphere and its crucial role in localization of giant ore deposits, prominent rift systems and large flood basalt provinces // Global Tectonics and Metallogeny, V. 6, # 3 & 4, 195-197.
**[3]** Kochemasov G.G. (1998b) Tectonic dichotomy, sectoring and granulation of Earth and other celestial bodies // Proceedings of the International Symposium on New Concepts in Global Tectonics, "NCGT-98 TSUKUBA", Geological Survey of Japan, Tsukuba, Nov 20-23,1998, p. 144-147.
**[4]** Kochemasov G. G. (2004) Mars and Earth: two dichotomies – one cause // In Workshop on "Hemispheres apart: the origin and modification of the martian crustal dichotomy", LPI Contribution # 1203, Lunar and Planetary Institute, Houston, p. 37.
**[5]** Kochemasov G.G. (2014) Earth and Moon: similar structures – common origin // NCGT Journal, v. 2, # 2, 28-38.
**[6]** Fernãndez C. and Anguita F. (2007) Oblique rifting at Tempe Fossae, Mars // JGR, v. 112, E09007, doi 10.1029/2007JE002889, 2007.
**[7]** Golombek M.P., Tanaka K.L., Franklin B.J.(1996) Extension across Tempe Terra, Mars, from measurements of fault scarp widths and deformed craters // JGR, v. 101, 26, 119-26, 130.
**[8]** Gung Y. and Romanovicz B. (2004) Q tomography of the upper mantle using three component long period waveforms // Geophys. J. Int., v. 157, 813-830.

# A NEW PLANETOLOGICAL THINKING: ORBITS CREATE STRUCTURES

**G.G. Kochemasov;**
*IGEM of the Russian Academy of Sciences, 119017 Moscow, 35 Staromonetny ,*
*Contact: kochem.36@mail.ru*

The theorem 3 of the comparative wave planetology ("Celestial bodies are granular"[1-3]) connects sizes of tectonic granules of cosmic bodies with their orbital frequencies. Granules form regular grids of shoulder-to-shoulder evenly sized ring structures (Fig. 1-6). The sizes depend on orbiting frequencies: the higher frequency – the smaller "rings", and vice versa, lower frequency – larger rings. Figures 1 to 8 represent a row of some full disk images of celestial bodies having a large difference in orbital frequencies: from satellite Triton (1/5,9 days) and Titan (1/15,9 days) through satellite Callisto (1/16,7), satellite the Moon (1/27,3), planet Mercury (1/88), planet Earth (1/365) and Mars (1/687) to asteroid Ceres (1/1680). Sizes of granules are: Triton $\pi R/250$, Titan $\pi R/91$, Callisto $\pi R/88$, Moon $\pi R/48$, Mercury $\pi R/16$, Earth $\pi R/4$, Mars $\pi R/2$, asteroids $\pi R/1$. Triton' s granules, not resolved in the whole disk image 1, are shown in Fig. 9- average diameters about ~17-18 km (5-25 km). Another two-segments asteroid Vesta is in Fig. 10.

The whole disk images clearly demonstrate the fundamental for the comparative planetology conclusion resolving the question of origin of structuring cosmic bodies energy. Neither impacts nor plate movements play the main role in this sense. Only standing inertia-gravity waves is an adequate solution. An important verification of this conclusion is a comparison of two globes with equal orbiting frequencies. The images of the Moon and the solar photosphere (orbits the center of the solar system) having equal frequencies show similarity of their granulations (Fig. 13). Also, an intriguing similarity of tectonic granulations is between two very different bodies: Earth and satellite Nereid (Fig. 11, 12). What is common – their orbital frequencies: Earth 1/365 days, Nereid 1/360 (a very rare Earth's counterpart!). Due to this one could expect a relative similarity of their tectonic granules sizes. This is the case, though the only image of Nereid has bad quality (Fig. 11, 12).

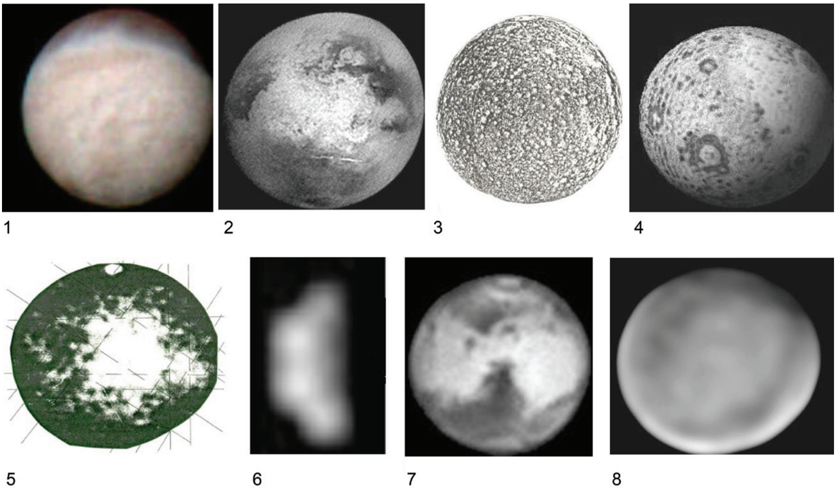

**Fig. 1-8.** Full disk images of celestial bodies in order of diminishing orbital frequencies. **Fig. 1**.Triton, PIA02246, 5.4 mln. km.**Fig. 2.** Titan, PIA06154; **Fig. 3.** Callisto (Voyager image); **Fig. 4.** Moon, Kaguya mission, forum.worldwindcentral.com; **Fig. 5.** Mercury [5]; **Fig. 6.** Earth, PIA04159, (the MRO image from the distance of 1.2 mln.kms); **Fig. 7.** Mars (image 314_2, Jaime Fernández, telescope Clestron 9.25, Valdemorillo, Spain); **Fig. 8.** Ceres ( Credit: Dumas C. et al.NASA-JPL).

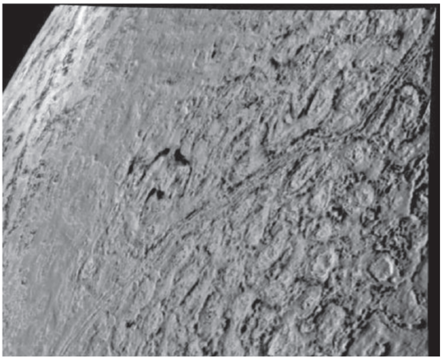

**Fig. 9**. Triton, “Cantaloupe” texture, PIA00061, frame 220 km long

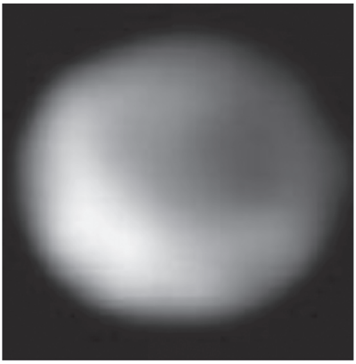

**Fig. 10**. Vesta, PIA17467, HST image

**Fig. 11**. Nereid, PIA00054 R= 170 km

**Fig. 12**. Earth, PIA04159

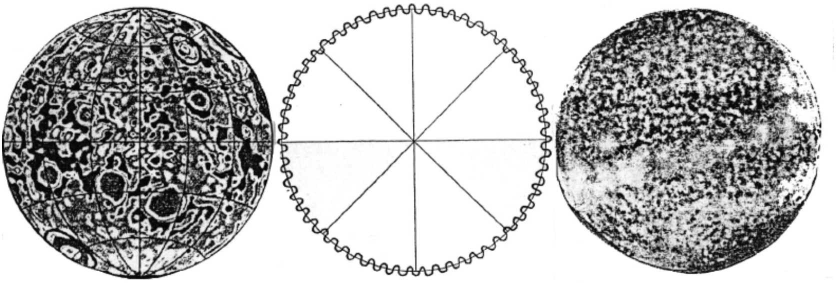

**Fig. 13**. Comparison of lunar (left, [4]) and solar photosphere wave tectonic granulations ($\pi$R/48-60). Similar wave structuring of solid and gaseous media.

**References:**

**[1]** Kochemasov G.G. Concerted wave supergranulation of the Solar system bodies // 16th Russian-American microsymposium on planetology, Moscow, Vernadsky Inst. (GEOKHI), Abstracts, 36-37, 1992. **[2]** Kochemasov G.G. Sectoral tectonics of the Earth's eastern hemisphere and its crucial role in localization of giant ore deposits, prominent rift systems and large flood basalt provinces // Global Tectonics and Metallogeny, V. 6, # 3 & 4, 195-197, 1998. **[3]** Kochemasov G.G. Tectonic dichotomy, sectoring and granulation of Earth and other celestial bodies // Proceedings of the International Symposium on New Concepts in Global Tectonics, “NCGT-98 TSUKUBA”, Geological Survey of Japan, Tsukuba, Nov 20-23, 1998, p. 144-147, 1998. **[4]** Konopliv A.S. et al. Clementine: gravity survey of the Moon // Science, v. 281, # 5382, 1476-1480, 1998. **[5]** Slade M.A. et al. Mercury: the radar experiment from Earth // Science, v.258, 635-640, 1992

# ANCIENT VOLCANISM ON THE MOON: THE GLOBAL DISTRIBUTION AND COMPOSITION OF CRYPTOMARIA

**J.L. Whitten[1], J.W.Head[1],**
*[1]Brown University, Providence, RI, USA.*
*Contact: jennifer_whitten@brown.edu.*

**Introduction:**

Cryptomaria (Head and Wilson, 1992) are mare deposits that have been obscured by impact crater and basin ejecta deposits. This obscuration produces high-albedo smooth plains. Deposits with a high-albedo and smooth surface, also known as Cayley Plains, are found across the Moon and many are hypothesized to form from the ponding of impact basin ejecta into topographic lows (Oberbeck et al., 1974). Therefore, the buried maria can easily be misinterpreted as Cayley Plains deposits. Several different identification techniques have been employed over the last 50 years to determine the location of lunar cryptomaria including the identification of dark-halo impact craters (DHCs), geochemical anomalies the surface regolith, a surface albedo intermediate between exposed maria and lunar highlands materials, and gravity anomalies. Approximately 21 different cryptomaria locations have been proposed across the lunar surface (e.g., Schultz and Spudis, 1979; Hawke and Spudis, 1980;Bell and Hawke, 1984; Head et al., 1993;Antonenko et al., 1995; Blewett et al., 1995; Mustard and Head, 1996;Giguere et al., 2003; Hawke et al., 2005;Lawrence et al., 2008). Most proposed cryptomaria are associated with ancient impact basins and, thus, many are believed to be ancient volcanic deposits. These most ancient volcanic deposits available for analysis provide a glimpse of the earliest volcanic history of the Moon, helping to address several key questions listed below.

The distribution of volcanic deposits reveal information for understanding the thermal history of any planetary body, such as the rate of cooling and the amount of melting that occurred in the interior. On the Moon, it is critical to determine the onset of mare volcanism and its timing relative to other volcanic processes (e.g., the intrusion of the Mg-suite); were mare basalts being emplaced onto the surface of the Moon as soon as the lunar anorthositic crust was solidified or was there a delay? In addition,measuring the mineralogy of ancient volcanic deposits can aid in determining temporal or spatial mineralogicvariations in surface deposits and also any mantle heterogeneities. In order to address these questions we begin with a study of the distribution of lunar cryptomaria.

**Methods:**

In order to fully characterize the distribution of volcanic deposits on the surface of the Moon we mapped the distribution of cryptomaria using several lunar datasets, including the Moon Mineralogy Mapper ($M^3$) visible to near infrared spectral data, Lunar Orbiter Laser Altimeter (LOLA) topography and surface roughness, Diviner rock abundance, and Lunar Reconnaissance Orbiter Camera (LROC) visible imagery. Here we searched for a high concentration of basaltic DHCs, small impact craters the form on high-albedo surfaces and excavate low-albedo material from the subsurface, and regolith with a high mafic (e.g., pyroxene) content using $M^3$ spectral data. The boundaries of cryptomaria were refined using LOLA topography and LROC visible imagery. Then the identified cryptomaria were analyzed to determine their characteristic rock abundance, surface roughness, and ages. Based on our analysis, we were able to determine that the most reliable tool to identify cryptomaria is a high concentration of DHCs. DHC spectra were collected using the $M^3$ dataset in order to determine the mineralogy of cryptomaria. The collected $M^3$ spectra were processed using the Modified Gaussian Model (Sunshine et al., 1990) to accurately determine the position of the pyroxene mineral absorptions and to analyze for temporal or spatial variations.

**Results:**

Of the 21 proposed cryptomaria locations, we were able to identify 18 regions of cryptomare deposits. No new deposits were detected. Cryptomaria follow the same distribution as exposed maria (Fig. 1, orange) and have increase the total surface area of the Moon covered with mare basalts by ~2%. The identified cryptomaria are concentrated on the lunar nearside and are typically associated with younger exposed mare basalts (Fig. 1, compare orange with grey). The largest cryptomaria occur in ancient impact basins, such as Schiller-Zucchius and Lomonosov-Fleming basins (Fig. 1, numbers 8 and 12). The largest increase of surface area occurs on the eastern nearside of the Moon. Analysis of DHC spectra indicates that the cryptomaria are basalts and have the same mineralogy as exposed maria in the same study region. Crater counts of the largest cryptomaria indicate that the surface of the deposits date between 3.8 and 4.0 Ga; this time period coincides with the formation of the Nectaris, Serenitatis, Crisium, Imbrium, and Orientale basins (Stöffler et al., 2006). It is probable, therefore, that the dated cryptomaria (Table 1) formed prior to many of these impact basins. Clustering with later mater deposits of similar mineralogy suggests that the cryptomaria are similar in age. These cryptomaria model ages also indicate that the process controlling the distribution of mare basalts (concentrating them on the farside) was in place early in lunar history.

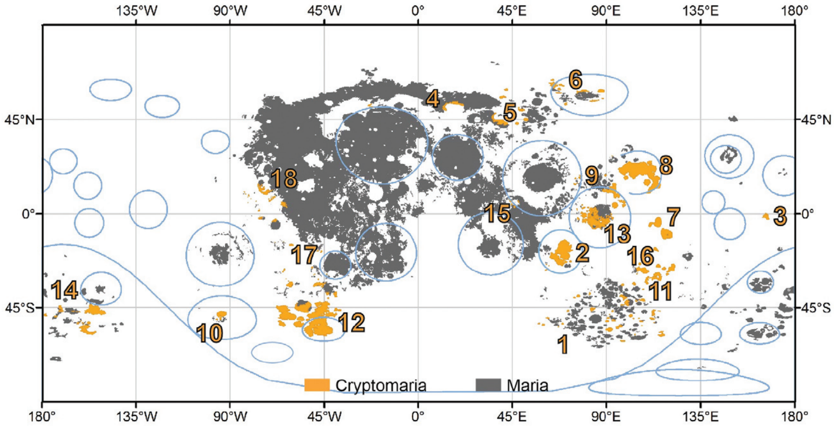


**Fig. 1.** The distribution of cryptomaria deposits (orange), as mapped in this study. With the addition of cryptomaria, the total surface area of the Moon covered with mare basalts increases from ~16% to ~18%. Blue circles represent identified impact basins on the Moon (e.g., Wilhelms, 1987). The numbers correspond to the cryptomaria listed in Table 1.

**Table 1.** Identified cryptomaria characteristics.

| Region[1] | Average Topography (m) | Average Albedo (1489 nm) | Model age | Associated ancient impact basin[2] |
|---|---|---|---|---|
| Australe (1) | -1952 | 0.12 | - | s |
| Balmer (2) | -987 | 0.14 | 3.84 +0.05/-0.07 | Balmer-Kapteyn |
| Dewar (3) | 542 | 0.13 | - | Keeler-Heaviside |
| Mare Frigoris (4) | -2413 | 0.12 | - | - |
| Hercules (5) | -1789 | 0.14 | - | - |
| Humboldtianum (6) | -3645 | 0.14 | - | s |
| Langemak (7) | 1627 | 0.15 | - | - |
| Lomonosov-Fleming (8) | -947 | 0.15 | 4.01 +0.02/-0.03 | s |
| Marginis (9) | -1928 | 0.12 | 3.88 +0.06/-0.12 | - |
| Mendel-Rydberg (10) | -1765 | 0.15 | - | s |
| Milne (11) | -1036 | 0.14 | - | - |
| Schiller-Schickard (12) | -666 | 0.14 | 3.77 +0.05/-0.07 | Schiller-Zucchius |
| Smythii (13) | -3119 | 0.12 | 3.90 +0.05/-0.07 | s |

| | | | | |
|---|---|---|---|---|
| South Pole-Aitken (14) | -4666 | 0.11 | 3.88 +0.06/-0.10 | s |
| Taruntius (15) | -1793 | 0.10 | - | - |
| Lacus Solitudinis(16) | -1036 | 0.14 | - | - |
| W. Humorum (17) | -557 | 0.15 | - | Humorum |
| W. Procellarum (18) | -1606 | 0.12 | - | - |

[1]Numbers in parentheses correspond to the numbered deposits in Fig.1.
[2]The letter 's' means that the name of the region is the same as the containing basin. No 's' or a '-' means that the cryptomaria is not in an obvious impact basin.

**References:**

Antonenko I. et al. (1995) *Earth Moon Planets, 69*, 141. Bell J.F. & Hawke B.R. (1984) JGR, 89, 6899-6910. Blewett, D.T. et al. (1995) *JGR, 100*, 16959.Giguere, T.A. et al. (2003) *JGR, 108*, 5118.Hawke B.R. &Spudis, P.D. 1980. Proc. Conf. Lunar Highlands Crust, 467–481.Hawke B.R. et al.(2005)*JGR, 110,* E06004.Head J.W. & Wilson L. (1992) *GCA, 55,* 2155. Head J.W. et al. (1993) *JGR, 98*, 17149. Lawrence S.J. et al. (2008) JGR, 113, E02001.Mustard J.F. & Head J.W. (1996) *JGR, 101*, 18913.Oberbeck V.R. et al. (1974) *The Moon, 12,* 19. Schultz P.H. &Spudis P.D. (1979) *Proc. LPSC X,*2899. Stöffler D. et al. (2006) Rev. Min. Geochem.519—596.Sunshine J.M. et al. (1990) *JGR, 95*, 6955—6966.Wilhelms, D.E. (1987) USGS Special Pap.1348.

# FIGURES OF EQUILIBRIUM OF SELF-GRAVITATING INHOMOGENEOUS MASS

**S. A. Voropaev**
*GEOKHI RAS, 119991 Moscow, Kosygina Str. 19,*
*Contact: voropaev@geokhi.ru*

**Introduction:**

The standard theory suggests precipitation of dust particles in the central plane of the solar nebula resulted in the formation of a thin, dense sub-disk, the dusty material of which probably gave birth to solid-state evolution. It is possible that the solar nebula decomposed to local clumps, which could assemble to large but, in the scale of solar system, rather compact gas-dust bodies. E.M. Galimov suggested applying this mechanism to the formation of the Earth-Moon system involving serious arguments of geochemistry and computational modeling using particle dynamics [1]. But, the question of stability of this model and its steady evolution remains open.

**Results and discussion:**

We consider the inhomogeneous self-gravitating gas-dust spheroid with stratification and a non-zero vorticity which rotates around the minor semiaxis and is in equilibrium. General relationships for pressure, angular velocity and gravitational potential of the spheroid with specified density function are obtained. Special cases of piecewise constant and continuous density functions are analyzed. Joint solution of hydrodynamic Euler equations for compressible medium, the Poisson equation for the gravitational potential, and the equation of state of the environment was analyzed at a reasonable restrictions following from the Galimov's concept of the Earth-Moon origin.  Exact solutions are possible for simple special cases, for the general case analyzed the boundaries of existence of stable solutions.

**References:**

[1] E.M. Galimov, A.M. Krivtsov. Origin of the Moon. New concept. De Gruyter, 2012, ISBN 978-3-11-028628-1.

# LUNAR FLOOR-FRACTURED CRATERS: PROBES OF SHALLOW CRUSTAL MAGMATISM ON THE MOON

**L.M. Jozwiak[1],J. W. Head[1], G. A. Neumann[2]**
*[1]Brown University, Department of Earth, Environmental, and Planetary Science, 324 Brook St. Box 1846, Providence, RI, 02912, USA;*
*[2]NASA Goddard Space Flight Center, Solar System Exploration Division, Mail Code 698, Greenbelt, MD, 20770, USA.*
*Contact: lauren_jozwiak@brown.edu*

Lunar floor-fractured craters (FFCs) are a class of 170 lunar craters characterized by shallow, fractured floors and associated morphologic features such as moats, mare deposits, and pyroclastic deposits. These craters are formed by stalling of a dike beneath the crater, and subsequent sill formation which uplifts and deforms the overlying crater floor. The geographic distribution of FFCs indicates that they preferentially form near the edges of lunar basins, although a subset of the FFC population is located in highland areas. The nature of FFC intrusions is an important factor to the understanding of the intrusive volcanic history of the Moon. Here, we investigate the temporal distribution of FFCs and the spatial distribution of FFCs as it relates to crustal thickness. The stratigraphic ages of the FFC host craters span from the pre-Nectarian through the Eratosthenian. The majority of the host craters are Nectarian to Imbrian in age. Host crater age places an older bound on the intrusion age for a given intrusive event. In Pre-Nectarian and Nectarian aged host craters the fractures appear less degraded than the host crater, suggesting the magmatic intrusion and subsequent deformation did not occur in response to the crater forming event. We conclude that the intrusions beneath FFCs are broadly consistent with having been formed during the main stage of mare volcanism.

A map of the spatial distribution of FFCs reveals a close association between FFC location and the location of mare deposits and basins. Plotting FFC distribution on a map of lunar crustal thickness (derived from GRAIL measurements) reveals that FFCs form predominately in crust of intermediate thickness, about 20-30 km (figure 1). This is in contrast to typical mare deposits, which form in shallow crust, generally thinner than 10 km. These relationships begin to suggest a process by which local crustal thickness influences the observed volcanic/magmatic morphologies. We establish a paradigm in which lunar dikes have a distribution of overpressurizations such that the small percent of dikes with the highest overpressurization may reach the surface in a thin crustal environment. By then imposing this paradigm on a variety of crustal thickness environments (figure 2) we are able to make predictions about the volcanic/magmatic features, and compare these predictions to actual observations. When compared to lunar features, our established paradigm is able to explain the observed distribution of FFCs, and also suggests that the deep lunar crust should be rich with stalled and solidified dikes. Thus the magmatic intrusions beneath FFCs present a link between the Moon's deeply stalled dikes and the surface mare basalts, and can serve as probes into magmatic evolution processes in the shallow lunar crustal environment.

# LOW PRESSURE AS EXTRATERRESTRIAL FACTOR INFLUENCING ON THE VIABILITY OF MICROORGANISMS

**V.S. Cheptcov[1], E. A Vorobyova[1,2]. V.S. Soina[1], I. A Shashkova[2], I. A. Kuznetsov[2] , A. V. Zakharov[2], G. G. Dolnikov[2], A.K. Pavlov[3], M.A. Vdovina[3] , V.N. Lomasov[4],**
*[1]Lomonosov Moscow State University, GSP-1, Leninskie Gory 1-12, Moscow, 119991, Russia;*
*[2]Space Research Institute (IKI), 84/32 Profsoyuznaya Str, Moscow, 117997, Russia;*
*[3]Ioffe Inst. Physics and Technology, S.-Petersburg, Polytechnicheskaya str. 26, Russia;*
*[4]S.-Petersburg State Polytechn. University; 195251, S.-Peterburg, Polytechnicheskaya str. 29, Russia.*
*Contact:cheptcov.vladimir@gmail.com*

The present work is focused on the study of the survival of native Earth like microbial systems in the dust layer and regolith of the moon and Mars, meteorites, and cosmic dust. As a potential habitat for putative extraterrestrial organisms or microorganisms introduced from the Earth alien regolith has the characteristics of fundamental importance for the interaction of mineral components with microbial cells. Creating an environment is defined by a wide range of planetary characteristics. This study covers the response of bacterial populations (community) adapted to the earth extreme habitats to the influence of low pressure as potential extraterrestrial environment-forming factor.

As model objects the samples from the extreme environments of Earth, considered as terrestrial analogues of Mars were used: permafrost sediments (Antarctic Dry Valleys) and gray-brown soils from the mountainous desert of Morocco, and also bacterial strains isolated from extreme ecotopes: Kocuria rosea SN_T60, Micrococcus luteus 49, Xantomonas sp.26, Cellulomonas sp. 15. Bacterial biomass was immobilized in clay mineral montmorillonite or analogues of the lunar regolith: 1) mixture of glass microspheres which considered as the analogues of the lunar regolith in granulometric characteristic; 2) lunar analogue LGA-St developed in the Institute for Geochemistry RAS. Biological samples were incubated under low pressure up to 1 torr (133 PA) using specially designed climatic chamber (Ioffe PTI RAS) and up to 1.4 PA in the chamber for deep vacuum (IKI RAS).

After a short (2 hours) exposure of bacterial strains Kocuria rosea SN_T60 and Cellulomonas sp. 15 at a pressure of 1 torr (133 PA) and the temperature of-50 C (model of the surface of Mars) inhibiting of bacteria was not observed. On the contrary, bacteria revealed increasing reproductive and metabolic activity, Inhibiting effect was fixed in all cultures of bacteria which have been tested (Kocuria rosea SN_T60, Micrococcus luteus 49, and Xantomonas sp.26) when the pressure decreased up to 1.4 PA and the time of exposure increased to 75 days. However, bacterial resistance to the low pressure remained at the high level, more than 50% of populations have kept viability.

Even more high viability under long-term influence of low pressure (1,4 PA) have revealed microbial communities of ancient Antarctic permafrost and dry desert soils. A slight decrease in the number of proliferating bacteria was detected. However, the total content of bacterial cells in the samples counted by direct microscopic epifluorescence technique remained at the initial level ,which indicates the transition of bacterial cells from the active state to hypobiosis. The functional state of microbial communities have changed: metabolic tests testified about activating consumption digestible high energetic substances

The study gives grounds for asserting that low pressure is not fatal for viable status and potential metabolic activity of putative Earth like microorganisms in extraterrestrial regolith.

The work is supported by RFBR №13-02-90441 Ukr-f-a and RFBR №13-04-a.

# CERES AS A TARGET FOR THE IMPACT CRATERING

**B. A. Ivanov,**
*[1]Institute for Dynamics of Geospheres RAS, Leninsky prospect 38-1, Moscow, Russia.*
*Contact: baivanov@idg.chph.ras.ru, boris_a_ivanov@mail.ru*

**Introduction:**

Recent robotic space mission to the second largest asteroid Vesta (DAWN [1]) delivered a lot of new observational data including images and gravity anomaly measurements. These data create the new database for planetological analysis including the re-iteration of previously elaborated models. A set of studies use these data to compare with numerical models to understand the specific of the impact cratering processes on Vesta and to support the data interpretation (e.g. [2, 3, 4]). The DAWN arrival to the first largest asteroid Ceres promises us the new data. The presentation describes the specifics of the impact modeling for Ceres and displays preliminary results.

**Ceres as a target:**

The preliminary models of Ceres' interiors are based at the astronomical data and geochemical modeling [5, 6, 7]. The low average density and spectral data allow us to assume that Ceres is a volatile rich (in comparison to Vesta), differentiated body. Temperature at the center may be estimated in the vicinity of ~400 K with the gradual decay to the surface. The ice cover ("crust") of ~100 km is possible [5]. The unknown additions to the ice may control the presence or absence of a thin liquid layer ("mantle") near the surface to the silicate core. The core may be also layered due to presence of hydrated minerals in the outer rocky shell [7] – details are highly depending on the fracture state of the core and its permeability [7].

Before better models we assume here the simplest model close in spirit to published results [5, 6, 7]: the water ice crust above a silicate core. With this simplest approximation we can use available equations of state (EOS) for $H_2O$ [8] and granite (as a proxy for a rocky material with the density of 2700 kg $m^{-3}$). Both EOS'es are tested previously [9, 10].

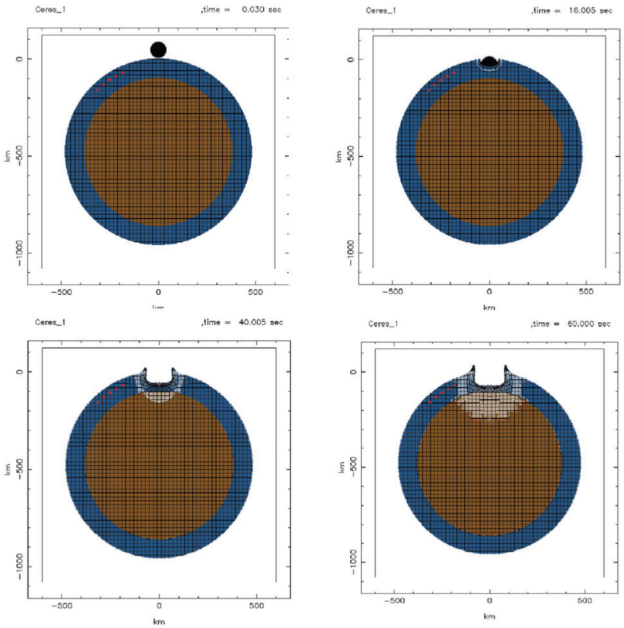


**Fig. 1.** The first minute after an impact of a slow projectile ($v_{imp}$ =4 km $s^{-1}$, $D_{projectile}$ =80 km) at the model "Ceres". The silicate "core" (brown) is modeled as a "granite", the outer shell (blue) is constructed of water ice. Various colorizations indicate density changes (including melting) for $H_2O$, and the inelastic deformations (including fracturing) for the silicate core. The thermal profile in spirit of [5] was chosen to get the ice melting point at the ice/silicate boundary.

**Preliminary results:**

Preliminary results are shown in Fig. 1. Here the projectile with the diameter of ~80 km penetrates the ice shell of ~100 km thickness. The impact velocity is assumed to be close to the average impact velocity for Ceres at the current position in the main belt [11]. The shock wave is not a strong one here (~10 GPa and below). However the reflection at the ice/rock boundary results in the secondary compression of ice in the reflected wave. The shock wave decay in the silicate core starts from the same pressure level and decays below 1 GPa at the depth of ~300 km below surface. Hence the direct shock heating of rocks is not possible. However the shock stresses are above the strength level (cohesion plus dry friction) and some frictional heating here is also available.

**Outlook:**

Before the wide range modeling we can formulate some selected questions which could be answered with the numerical modeling. (1) The impact depression in ice has good chances to be heeled with the ice plastic flow [10]. The question is how large should be an "initial" crater to be recorded in the surface topography of the Ceres core? (2) If outer layers of the core are filled with the ice/liquid [7], how to estimate shock loading of this "permafrost" layer? (3). However the real problems will be delivered soon from the orbit around Ceres.

**Acknowledgments:**

The work is supported by the Program 22 "Fundamental Problems of Solar System Research" (Project 8.3).

**References:**

[1] Russell C. T. et al. (2012) *Science*, **336**(6082), 684–686.
[2] Ivanov B. A. and H. J. Melosh (2013) *JGR-Planets*, v. **118**, 1545-1557.
[3] Ermakov, A.I., et al. (2014) Constraints on Vesta's Interior Structure Using Gravity and Shape Models from the Dawn Mission, *Icarus* (in press).
[4] Bowling, T.J., et al. (2013) *JGR-Planets*, **118**, 1821-1834, 2013.
[5] McCord, T.B., and C. Sotin (2005) Ceres: Evolution and current state, *JGR-Planets*, **110** (E5), E05009, 1-14, 2005.
[6] Castillo-Rogez, J.C., and T.B. McCord (2010), *Icarus*, **205**, 443-459.
[7] Zolotov, M.Y. (2009) *Icarus*, **204** (1), 183-193.
[8] Ivanov, B.A. (2005) *Lunar and Planetary Conference 36th*, abs. #1232.
[9] Ivanov, B.A., and E. Pierazzo (2011) *Meteoritics and Planetary Science*, **46**, 601-619.
[10] Ivanov, B.A., H.J. Melosh, and E. Pierazzo (2010) In: *GSA Special Papers 465*, edited by R.L. Gibson, and W.U. Reimold, pp. 29-49, Geological Society of America, Boulder, Colorado, USA.
[11] O'Brien D. and M. V. Sykes (2011) *Space Sci. Rev.* **163**, 41-61.
[12] Bland, M.T. (2013) *Icarus*, **226**, 510-521.

# THE NATURE OF NSR N1 AREA IN THE CRATER PEARY

**E. A. Feoktistova,**
*Sternberg Astronomical Institute, Moscow State University, Universitetskij pr., 13, Moscow, Russia,*
*Contact: Hrulis@yandex.ru*

**Introduction:**

The data from LEND (neutron spectrometer probe LRO) on the hydrogen content in the surface layer of the Moon showed that areas of high hydrogen content do not always coincide with the permanently-shaded areas (Mitrofanov I.G. et al., 2010, 2012). One such area is located in the crater Peary near the north pole of the Moon (Mitrofanov I.G. et al., 2012) (Fig. 1). The high hydrogen content in this region (145 ppm at the average level on the Moon - 50 ppm) was observed by probe Lunar Prospector, explored the Moon in 1998-1999 (Feldman et al., 2001). These results may indicate the presence in the soil not only deposits of water ice, but other hydrogen-containing volatile compounds, such as H2, $H_2S$, $NH_3$, $C_2H_4$, $CH_4$. These substances have been found in the LCROSS impact plume in 2009 (Gladstone et al., 2010, Colaprete et al., 2010). We studied the possibility of the existence of such substances in the crater Peary and its surroundings.

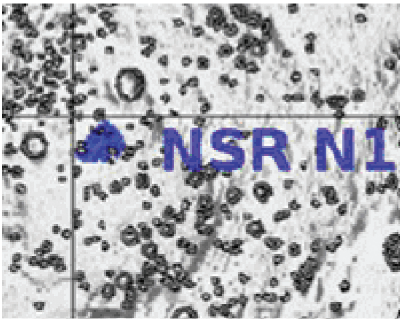


**Fig.1.** The crater Peary and NSR N1(Mitrofanov I.G. et al., 2012).

**Model:** Since the evaporation rate of substances is a function of temperature (Watson et al., 1961), we investigated the illumination conditions and temperature regime in the area of crater Peary during the lunar year. For our calculations we used the model described in (Berezhnoy et al., 2011) and topographic data from altimeter LOLA working on board the probe LRO (). Our results show (Fig.2), that the permanently shaded areas exist in this region. These areas are located in small impact craters. The maximum temperature in such craters does not exceed 70-120 K. The coldest region of Peary is its southern part: the maximum temperature here ranges from 120 to 220 K. The maximum temperature in the central part of the crater does not exceed 120-170 K. In NSR1 area the maximum temperatures reaches 170- 220 K. At such maximum temperatures, water ice may remain stable only under a regolith layer.

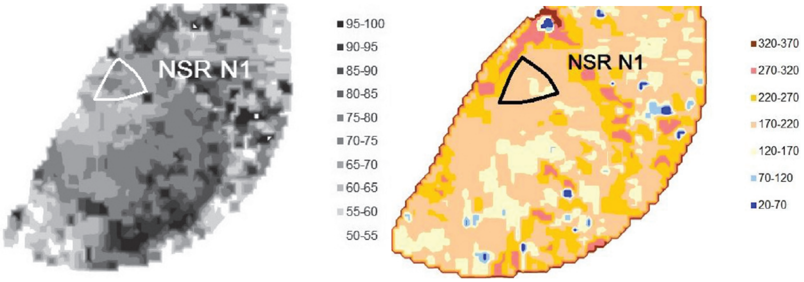


a b

**Fig.2.** Illumination conditions (a) and maximum temperatures (b) in the crater Peary region.

According to (Zang and Paige, 2009), deposits of volatile compounds are stable relatively evaporation if the vapor pressure is less than $10^{-16}$ bar. We calculated the evaporation rates of volatile substances as a function of temperature and the depth according to approach of (Schorghofer and Taylor2007). For our calculations, we chose the thickness of the regolith layer 10, 30 and 50 cm. Dependence of vapor pressure on temperature for $H_2O$, $CH_4$, $C_2H_4$, and $H_2S$ was taken from (Fray.and Schmitt, 2009).

According to our calculations deposits of water ice may exist in the NSR 1 only in small shaded areas (Fig 3a). However, the presence of the shielding layer of regolith greatly expands the area where possible existence of volatile compounds (Fig 3b). The deposits of NH3 and H2S may exist in this area with regolith layer thickness of about 30 and 50 cm, respectively.

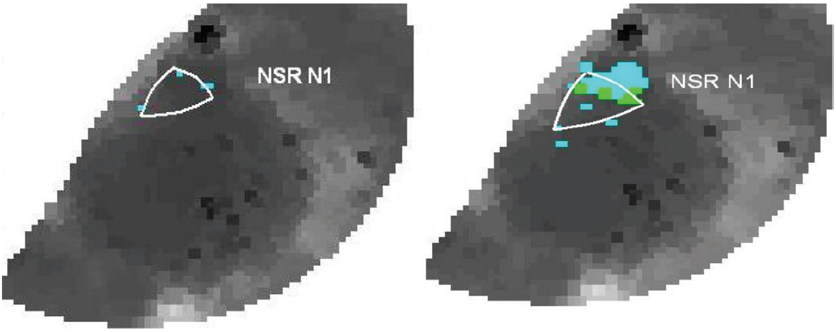


a b

**Fig. 3.** Water ice (blue) and NH3 (green) deposits at the surface and at the depth 30 cm in the NSR N1 area.

Thus, the presence of the shielding layer of regolith may be the main condition for the existence of volatile compounds in this area.

http://ode.rsl.wustl.edu/moon/
Berezhnoy A. A., Kozlova E. A., Shevchenko V.V. et al // Origin and Stability of Lunar Polar Volatiles. ASR 50, c. 1581 - 1712, 2011
Colaprete A., Schultz P., Heldmann J. et al. // detection of water in the LCROSS ejecta plume. Science 330, 463-468, 2010
Gladstone G.R., Hurley D.M., Retherford K.D. et al.// Corrections and Clarifications: LRO-LAMP Observations of the LCROSS Impact Plume. Science 333, 1703, 2010
Mitrofanov I.G. et al. Hydrogen Mapping of the Lunar South Pole Using the LRO Neutron Detector Experiment LEND, Science, Vol. 330, No. 6003, p. 483 – 486, 2010
Mitrofanov I.G. et al. Solar Water Permafrost: is it detected on the Moon? Is it expected on the Mercury? Lunar Planet. Sci. Conf. 43, 2083, 2012.
Feldman W.C., Maurice S., Binder A.B., Barraclough B.L., Elphic R.C. and D. J. Lawrence. Evidence for water ice near the lunar poles. J. Geophys. Res., V. 106, p. 23231-23252, 2001
Fray, N., Schmitt, B. Sublimation of ices of astrophysical interest: A bibliographic review. Planet. Space Sci. 57, 2053-2080, 2009.
Schorghofer N., Taylor G.J. Subsurface migration of $H_2O$ at lunar cold traps // JGR. V. 112. E02010, 2007
Vasavada A.R., Paige D.A. and S.E. Wood. Near-Surface Temperatures on Mercury and the Moon and the Stability of Polar Ice Deposits // Icarus V. 141. p. 179-193, 1999
Watson K., Murray B.C., Brown H. The Behavior of Volatiles on the Lunar Surface // JGR V. 66. N 9. p. 3033-3045, 1961
Zhang, J.A., Paige D.A. Cold-trapped organic compounds at the poles of the Moon and Mercury: implications for origins // Geophys. Res. Lett. 36, CiteID L16203, 2009.

# NEW TECHNIQUES OF LUNAR IMAGE PROCESSING AND ARTIFICIAL MODELING OF SURFACE.

**A. Zubarev[1], N. Kozlova[1], V. Patraty[1], A. Kokhanov[1], E. Matveev[1], L. Mitrokhina[1], I. Nadezhdina[1], I. Karachevtseva[1], and J. Oberst[1, 2,3]**
*[1]Moscow State University of Geodesy and Cartography, (MIIGAiK), MIIGAiK Extraterrestrial Laboratory (MExLab), Russia*
*[2]German Aerospace Centre (DLR), Berlin, Germany;*
*[3]Technical University of Berlin (TUB), Berlin, Germany*
*Contact: natally.ko@gmail.com*

**Introduction:**

Nowadays there is a lot of information on lunar relief in form of global and local DEMs as well as lunar high-resolution imagery derived from modern missions to the Moon. All these data have to be processed to provide accurate and safe landing as well as operation on the surface. This is especially important for preparation of future Russian missions Luna-25 and -26 which are planned as a continuation of glorious Soviet Lunar missions, among which were first images of the far side of the Moon, soft landing and first lunar rovers – Lunokhods. Ongoing Lunar Reconnaissance Orbiter (LRO - http://lroc.sese.asu.edu/) mission provides images of the lunar surface with resolution up to 0.3 m/pixel, however, on panoramas obtained by Soviet Lunokhods we can study details up to several cm in size. These images complement each other and their joint processing provide unique information about the Moon and can be used for developing and testing of different approaches and techniques.

**Methodology:**

We have developed a unique technique of lunar data processing and artificial modeling of surface images based on fusion of orbit and surface data. Now we are testing/implementing it on regions of Soviet Lunokhod-1 (Luna-17, 1970-1971) and -2 (Luna-21, 1973) missions, as for these areas we have a combination of stereo orbital images (LRO NAC) and surface archive panoramas obtained by Lunokhods. The first step is to analyze and select LRO NAC images for stereo photogrammetric processing and create DEMs for the study area. We select images with best resolution and illumination and orthorectify them using the created DEM (Zubarev et. al., 2012).

Next step — GIS-analysis of the rover tracks and the territory based on high-resolution DEMs and orthomosaics — provides different types of spatial data like crater density, morphometry parameters of craters, surface roughness (Karachevtseva et al., 2013a).

Thirdly, we have made new photogrammetry processing of archive data, including panoramas and images obtained by navigation cameras of Lunokhods. During the two Lunokhod missions about 300 high-resolution panoramic images were obtained but, unfortunately, information about shooting points (coordinates and exterior orientation of images) was lost (Karachevtseva et al., 2013b).

To recover lost information (step four) we suggest artificial modeling of the surface images based on LRO NAC DEM and orthomosaic (first step) and possible observation points on the digitized Lunokhod traverse (second step). For this purpose special software has been developed which provides obtaining all necessary exterior orientation parameters which characterize the image and are essential for future processing. Comparison of the produced image with the original one (horizon line, craters, prominent relief features, etc.) we can state that the original image was obtained from the point which was used for the modeling (Kozlova et al., 2014).

Finally, these results will be used for morphologic analyses of the lunar surface (Abdrakhimov et al., 2013). Identification of observation points is important for accurate and detailed morphometric studies (Basilevsky et al., 2014).

The proposed technique suggests different types of products (depend on level of processing, projection, etc.), so to storage the results we have developed a special lunar data model which provides description (metadata) and easy access to our geodatabase (Karachevtseva et al., 2013c). External users have free access via MIIGAiK Planetary Data Geoportal (http://cartsrv.mexlab.ru/geoportal/).

**Conclusions:**

For Lunokhod areas we have a very good data set (detailed DEMs and images with resolution up to 0.3 m/pixel) as well as real surface images obtained in-situ during the Lunokhod missions. It is the best way to test and improve the developed technique for fusion of orbit and surface data. Our methodology and specially created software can be used for modeling of Moon surface images for candidate landing sites for Luna-25 and Luna-26 and determination of exact coordinates of the landing module based on the transmitted surface images.

**Acknowledgments:**

Works on Lunokhod panoramic image processing are supported by European Community's 7th Framework Programme (FP7/2007-2013) under agreement No 312377 PRoViDE. We would like to thank Russian State Archive of Scientific and Technical Documentation which provided image fragments of archive panoramas for the research.

**References:**

Abdrakhimov A.M., Basilevsky A.T., Karachevtseva I.P., Geological review of Lunokhod 1 area, The Fourth Moscow Solar System Symposium (4M-S3), IKI RAS, Moscow, Russia, 14-18 October 2013.

Basilevsky A.T., Kreslavsky M.A., Karachevtseva I.P., Gusakova E.N. Morphometry of small impact craters in the Lunokhod-1 and Lunokhod-2 study areas. Elsevier, Planetary and Space Science 92, 2014, pp. 77-87. http://dx.doi.org/10.1016/j.pss.2013.12.016.

Karachevtseva I., Oberst J., Scholten F., Konopikhin A., Shingareva K., Cherepanova E., Gusakova E., Haase I., Peters O., Plescia J., Robinson M. Cartography of the Lunokhod-1 Landing Site and Traverse from LRO Image and Stereo Topographic Data. 2013 Elsevier, Planetary and Space Science, Vol.85, p. 175-187. http://dx.doi.org/10.1016/j.pss.2013.06.002.

Karachevtseva I., Kozlova N., Nadezhdina I., Zubarev A., Abdrakhimov A., Basilevsky A., and Oberst J. New processing of Luna archive panoramas and geologic assessment of the Lunokhod landing sites. European Planetary Science Congress, September 08-13, 2013, London, United Kingdom, [EPSC2013-532].

Karachevtseva I., Matveev E., Kokhanov A., Kozlova N., Garov A. Development of a planetary data storage system and access to it by means of GIS (Geoportal). Modern problems of remote sensing of the Earth from space, Moscow, IKI, 2013, V.10, № 4. C. 89-97. http://d33.infospace.ru/d33_conf/sb2013t4/89-97.pdf (in Russian).

Kozlova N., Zubarev A., Karachevtseva I., Nadezhdina I., Kokhanov A., Patraty V., Mitrokhina L., and Oberst J. Some aspects of modern photogrammetric image processing of Soviet Lunokhod panoramas and their implemenation for new studies of lunar surface. ISPRS Archives MTSTC4-2014-103, Volume XL-4, 2014, pp. 121-126. doi:10.5194/isprsarchives-XL-4-121-2014.

Zubarev A., I. Nadezhdina, N. Kozlova, I. Karachevtseva, J. Oberst, M. Robinson "High-resolution terrain models from LRO stereo images for Luna-Glob landing site selection" The Third Moscow Solar System Symposium (3M-S3), Space Research Institute, Moscow, Russia, October 8-12, 2012. http://ms2012.cosmos.ru/sites/ms2012.cosmos.ru/files/3m-s3-abstracts.pdf.

# LUNAR CAVING AND LAVA TUBES

**R. R. Chau, A. A. Mardon,**
*The Antarctic Institute of Canada, 11919-82 Street NW, Edmonton, Alberta, Canada;*
*[2]The Antarctic Institute of Canada, 11919-82 Street NW, Edmonton, Alberta, Canada.*
*Contact: aamardon@yahoo.ca*

**Introduction:**

With what little information we have about the surface of the moon, there is very little documentation detailing much about the surface of the moon apart from images we obtain from satellites. Lunar caves are more of a prediction than actual knowledge not be- cause of how much we know but how little we know. However, there have been few predictions of the existence of lunar lava tubes and caves stemming from pictures taken by various satellites. This includes rilles on the surface as well as what is predicted to be a lava tube skylight. One major prediction of the formation of rilles is the flowing of a liquid, most likely lava from a volcano or other source as there is no evidence of water or other liquid. Flowing liquid erosion also accounts for the fact that many rilles have walls that run parallel as opposed to a more erratic shape [1]. Another pieceof evidence for lunar caves is the picture taken by SELENE Terrain Camera. It shows a hole on the surface of the moon that is unlike many of the craters that dot the surface of the moon [2]. Whereas many craters on the moon show definite illumination on both sides of the depression, the photograph of the skylight only has half of the circumference illuminated suggesting that there is a possibility that this depression has more depth.

**References:**

[1] Harold Masursky et al. (1978) NASA SP-362, page 193.
[2] Junichi Haruyama et al. (2009) Possiblelunar lava tube skylight observed by SELENE cameras. Geophysical Research Letters., Volume 36, issue 21.

# MAPPING AND THE MORPHOMETRIC MEASUREMENTS OF SMALL LUNAR CRATERS

**A. A. Kokhanov[1], M. A. Kreslavsky[1,2], J. Oberst[1,3,4], I.P. Karachevtseva[1]**
*[1]Moscow State University of Geodesy and Cartography (MIIGAiK), MIIGAiK Extraterrestrial Laboratory (MExLab), Gorokhovskiy per., 4, 105064, Moscow, Russia ;*
*[3]University of California - Santa Cruz, 1156 High Street, Santa Cruz, CA, 95064, USA,*
*[3]Technical University of Berlin, Berlin, Germany,*
*[4]German Aerospace Center (DLR), Rutherfordstr. 2, D-12489 Berlin.*
*Contact: s_kokhanov@mexlab.ru*

**Introduction:** Small impact craters are the dominant landform on the Moon. They have long been known to be in dynamic equilibrium: their formation is balanced by obliteration; this phenomenon is also known as "empirical saturation". The dominant mechanism of crater degradation and obliteration is transport of the uppermost disintegrated layer of lunar surface, so-called regolith. This transport (also dubbed regolith gardening) is primarily caused by micrometeoritic bombardment. Some other processes like electrostatic dust levitation, thermal contraction effects, ejecta from distal large craters make poorly known contribution to regolith gardening. The new data set resulting from recent missions to the Moon, primarily, LRO mission, give principally new possibilities to study regolith properties in detail. We are conducting studies of alteration of small impact craters (~20 – 1000 m in diameters) to gain new knowledge about formation, modification and transport of lunar regolith.

**Survey:** The data set we used for this study is the digital terrain models created by photogrammetric methods from stereo image pairs acquired by camera LROC NAC onboard LRO mission to the Moon. With this data we created catalogs of small impact craters for several selected areas on the Moon. The catalogs contain morphometric characteristics of craters, such as crater depth, wall slopes, etc. The catalogs are used for further analysis of statistical distributions of crater sizes and morphometric parameters. The inferences about the dominant mechanisms of the regolith mobility will be made through comparison between the observed and modeled frequency distributions of small craters.

**Automation:** The crater catalogs were created using ArcGIS software complex. To facilitate and accelerate massive morphometric measurements of the craters we developed a set of supporting automated procedures. They combine certain ArcGIS tools and are controlled by user-defined parameters. The developed instrumentation enables calculation of topography statistics inside craters, along their rims, create center lines of craters with different direction for the further simultaneous generation of several topographic profiles.

**Study sites:** In this work we mapped small craters at the vicinities of Luna-20 landing site. This is a rather typical highland area in the central eastern lunar nearside. We selected it to obtain data that would be complimentary to previous research of small craters (Basilevsky et al, 2013) on the mare surfaces. On the LRO NAC image M152505885, which covers LUNA-20 landing site we catalogued 1911 craters with 20 m < $D$ < 730 m. Measured with NAC DTM LUNA20 (Tran et al., 2010) morphometric parameters includes: diameter, maximum depth, mean depth, maximum slope, mean height of the rim.

**Future work:** Measured values will be used for classification craters according to their stage of degradation, comparative analysis of surface dynamic on the highland and mare terrains. For the similar analysis of the other chosen regions of interests, including subpolar areas, the new DTMs will be specially created (Zubarev et al., 2012).

**Acknowledgements:** This work was carried out in MIIGAiK and supported by Russian Science Foundation, project #14-22-00197.

**References:**

Basilevsky et al., Morphometry of small impact craters in the Lunokhod-1 and Lunokhod-2 study areas. Elsevier, PSS 92, 2014, pp. 77-87. http://dx.doi.org/10.1016/j.pss.2013.12.016.
Tran et al., Generating Digital Terrain Models Using LROC NAC Images,ASPRS/CaGIS, 2010.
Zubarev et al., High-resolution terrain models from LROC stereo images for Luna-Glob landing site selection. The 3-rd Moscow Solar System Symposium, Space research institute, Moscow, 8-12 October, 2012.

# LUNAR INTERNAL STRUCTURE MODELING USING APOLLO SEISMIC TRAVEL TIME DATA AND THE LATEST SELENODETIC DATA

**K.Matsumoto[1], R. Yamada[1], F. Kikuchi[1],S. Kamata[2],Y. Ishihara[3],T. Iwata[3], H. Hanada[1], S. Sasaki[4]**

*[1]National Astronomical Observatory of Japan, Japan,*
*[2]University of California Santa Cruz, U.S.A.,*
*[3]Japan Aerospace Exploration Agency, Japan,*
*[4]Osaka University, Japan. Contact:koji.matsumoto@nao.ac.jp*

**Introduction:**

Internal structure and composition of the Moon provide important clue and constraints on theories for how the Moon formed and evolved. The Apollo seismic network has contributed to the internal structure modeling. Efforts have been made to detect the lunar core from the noisy Apollo data (e.g., [1], [2]), but there is scant information about the structure below the deepest moonquakes at about 1000 km depth. We tried to constrain lunar internal structure by combining the Apollo seismic travel time data and selenodetic data including potential Love number k2 which has been greatly improved by recent GRAIL mission.

**Internal structure modeling:**

We used a seven-layer model consisting of crust, upper mantle, middle mantle, lower mantle, low-velocity layer (LVL), fluid outer core and solid inner and core. The model is constrained by the following observations; four selenodetic data of mean radius, mass, mean moment of inertia (MOI), degree-2 potential tidal Love number k2 from [3], and Apollo seismic travel time data from [4]. The latter includes 318 P and S travel time data from 59 sources (24 deep sources, 8 shallow sources, 8 artificial impacts, 19meteorite impacts) recorded at 4 surface stations. Markov Chain Monte Carlo (MCMC) method is used to infer the model parameters. We collected about 100 million samples from 10 chains.The basic idea is to constrain the crust and the mantle mainly by the seismic data and to infer the deep interior so that the selenodetic data are satisfied.Viscosity is not taken into account in this calculation.

**Results:**

Mean crustal thickness of 46 ± 4 km is estimated by fitting a normal distribution curve to the posterior distribution. This is to be compared to the previous estimate of 34 - 43 km from GRAIL gravity and LOLA topography [5]. Major part of crustal densities is sampled between 2500 and 2600 kg/m$^3$, which is consistent with the value of 2550 kg/m$^3$reported by [5]. There is a trade-off between crustal and mantle densities. The estimated mantle densities are a little larger than those of previous studies [1], [2] in which larger crustal density about 2800 kg/m$^3$ was assumed. In general, seismic wave velocities in the mantle are consistent with the previous estimates.

Given that the structures of the crust and mantle are estimated to be consistent with previous studies, next we look into the structure of deeper part. The ranges of size and density of the outer core which satisfy the observation are relatively wide and it is difficult to tightly constrain them. Strong correlation between outer core size and LVL thickness is observed. The smaller outer core should be accompanied by thick LVL and vice versa. When we take into account the upper bound of the fluid core size of 400 km which is predicted by magnetic observation [6], the thickness of the LVL is at least about 100 km. The S-wave velocity within this low-velocity layer is estimated to be less than about 3 km/s,and the probability of the considerably small Vs of 1 - 2 km/s (corresponding to the shear modulus value of about 5 - 15 GPa) is high.The effect of low viscosity [7] may change the estimate of the Vs in the LVL.The inner core radius is expected to be smaller than 265 km. The lunar displacement Love number is predicted to be $h_2$ = 0.0423 ± 0.0004..

**References**

[1] Weber et al. (2011), Science, 331, 309-312, doi:10.1126/science.1199375
[2] Garcia etal. (2011), PEPI, doi:10.1016/j.pepi.2011.06.015
[3] Williams et al. (2014), JGR, doi:10.1002/2013JE004559
[4] Lognonne et al. (2003), EPSL, 211, 27-44
[5]Wieczorek et al. (2012), Science, doi:10.1126/science.1231530
[6] Shimizu et al. (2013), Icarus, doi:10.1016/j.icarus.2012.10.029
[7] Harada et al. (2014),

# COMPARISON OF LOCAL GEOLOGY OF CHANG'E 3 LANDING SITE AND IN THE MIDDLE OF LUNOKHOD-1 TRAVERSE

**A. M. Abdrakhimov[1], A. T. Basilevsky [1],**
*[1]Vernadsky Institute, Russia, 111538, Kosygina 19, atbas @ geokhi.ru*

**Introduction:**

On Dec. 14, 2013, Chang'e 3 (CE-3) successfully landed in Mare Imbrium (44.13°N, 19.50°W) on the rim of ~450-m bowl-shaped crater (Fig. 1) [1,2]. The CE-3 landing site is about 500 km NE from the landing site of Luna 17/ Lunokhod-1 [3].

The geologic setting of the CE-3 landing site, as it is seen in LROC NAC images [2], is close to that in the middle part of the Lunokhod-1 (L-1) rover traverse. The L-1 route there crossed the rim of similarly large bowl-shaped crater Borya (Fig. 2, 38.284 N, -35.007 W, D=470 m) [4]. The slopes of the Borya inner walls are steep (reaching >20°) [5] and covered with rock boulders. The crater is characterized by a depth/diameter ratio h/D=0.12 [5]. The characteristics of crater Borya resemble those of 450-m crater (19.524W, 44.120N) near CE-3 landing site: h/D=0.11, 30° rocky wall [1] (Fig. 1). These characteristics permit to classify both craters as belonging to morphologic class B, according classification [6].

L-1 (803-08) panorama [7] was chosen to illustrate the geologic context as for L-1 (Fig. 3), which could be considered as some analog for the CE-3 landing site, and. It was compared with CE-3 panorama (Fig. 4) in geological terms of [7], with classification of craters and rock fragments.

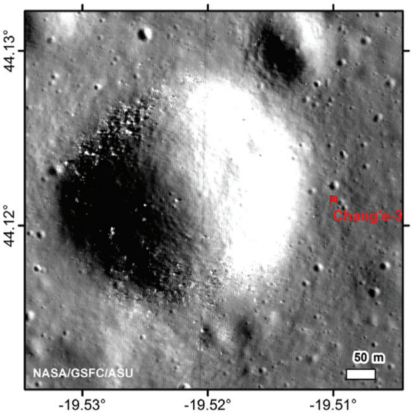


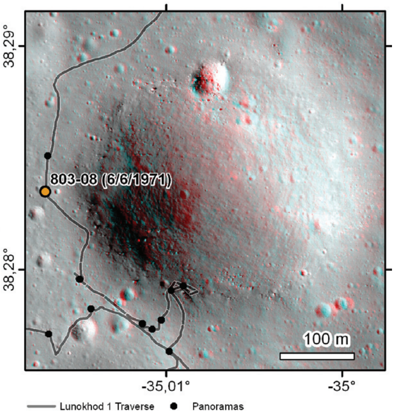


**Fig. 2.** Anaglyph showing crater Borya and the route of Lunokhod-1 [4]. Composed of LRO NAC images M150749234LC and M166072850LC (NASA/GSFC/ ASU).

**Fig. 1.** Fragment of LRO NAC M1811302794LE (NASA/GSFC/ASU) showing the crater on the eastern rim of which CE-3 landed [1,2].

**L-1 Panorama 803-08. On the rim of Borya crater:**

On the panorama taken June 6, 1971 (Session 803, panorama 08), during the 8th lunation of the L-1 traverse, the crest of the western part of Borya crater rim is seen (Fig. 3). It can be observed here that as the distance from the 470-m crater increases, the spatial density of rock fragments is rapidly decreasing. On the left side of the panorama the intercrater surface of the mare plain is observed and on the right is seen the Borya crater northern inner slope covered with rock fragments. In the right-center part of the panorama ~2 m from the rover there is a small fresh crater about 1 m of class B with a sharp rim crest and steep internal walls. On the right, 3-7 m towards Borya crater, there are several prismatic and angular rocks of about 20-30 cm (class 1-2, type IV, by [7]). Small rocks (<5 cm, a class 2, type I-II) are observed in the surroundings, with the spatial density ~10/sq.m. Toward Borya crater the spatial density and sizes of rock fragments are increasing. The surface structure near the rover looks cloddy, with small, decimeters sized craters.

**CE-3 Panorama. On the rim of crater B ~ 450 m:**

On the panorama taken by CE-3 at the landing place among the smooth mare plain on the outer rim slope of crater B ~ 450 m, with the depth ~50 m [1]. In E-S-W direction the horizon is almost even, only in the W it is limited by the crest of crater B ~ 450 m and in the NW by the crest of the almost invisible adjacent large crater BC ~ 125 m. The mare plain is covered mainly by gentle craters C~0.5-4 m. In ~30 m to the W the bowl-shaped crater B~450 m with gentle crest is partly seen. Its inner walls are covered by piles of boulders and relatively smooth areas, apparently related to landslides. The vertical zoning of rock fragment distribution is observed. The maximum of quantity and size of rocks is reached at the steepest (> 30°) middle part of the wall, where D ~ 1-5 m. Below and above the zone the number and size of rocks are falling sharply. The rocks are more rounded on the rim crest, and the rock's density is lower: N (10-20 cm) /sq.m~ 5-10. The big angular boulder is noticed in 40 m SW with D ~ 4 m. The bowl-shaped crater B ~ 13 m is observed in 20 m N. There are dozen mainly angular-rounded prismatic rocks with D~0.5-2 and many cobbles on its walls and rim, but its floor and eastern wall are almost free of large stones. The depth of observed traces of Yutu rover in the north is about 1 cm. The footprints of wheel tracks are unclear, that could point to reduced adhesive local regolith properties.

**Discussion:**

L-1 and CE-3 sites show their similarity. Two geologic settings are observed by panoramas: on the rim and on the inner crater walls. The differences between them are rather steep slope and the presence of numerous rock fragments on steep inner walls, and gentle-sloping to horizontal surface with rare and small rock fragments on the crater rim. It is obvious that the elements of this crater formed simultaneously. If we apply the technique of [6], it has happened approximately 150-200 Ma ago and then the settings evolved due to ongoing surface processes.

One of the obvious surface processes – small-scale meteorite bombardment — had to be working in practically the same way in both situations. On the rim of crater Borya, which initially had to be very rocky (because it certainly penetrated through preexisting regolith into the bedrock) the meteorite bombardment destroyed the rocks. According to estimates of [8] for the time 150-200 Ma more than 90% rocks of the initial population should have been destroyed.

The original population of rock fragments on the inner walls of crater Borya was exposed to the same destruction process and had to be destroyed too. The rocks which are now seen there are obviously those which were sitting safe from breakdown in the local regolith layer and were recently exposed by the regolith local overturn due to down-slope material movement. The same situation could be seen and for CE-3 450 m crater

**Fig. 4.** *Lunokhod-1.* Session 803. Panorama 08. June 6, 1971. Site 2. On the crest of the Borya crater rim.

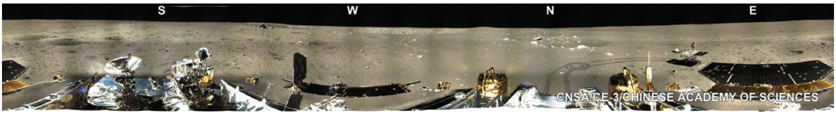


**Fig. 5.** Chang'e 3 panorama (CNSA/Chinese Academy of Science).

**Conclusions:**

CE-3 encountered the situation similar to that described for the Lunokhod-1 on the rim regional Borya crater. In fact, the local settings in the Chang'e-3 landing site described by [1] are practically the same: rather steep rocky slope of the inner walls of the 450-m crater and much less rocky crater rim with superposed small craters, some of which excavated the rock fragments. The chemical analyses of outcropped rocks and regolith should provide the ground truth about compositions of local younger high-Ti basalts and, possibly underlying them, older low-Ti basalts [9,10].

**References:**

[1] Zhao J N et al. (2014) *Sci China-Phys Mech Astron*, 57. 569-576. doi: 10.1007/s11433-014-5399-z.
[2] Robinson M. (2013) NASA/GSFC/ASU, LROC Report 30.12.2013.
[3] Florensky C.P. et al. (1972) *Space Research XII*, 107-121.
[4] Gusakova E. N. et al. (2012) *LPS 43*, Abstract #1750.
[5] Gusakova E. N. et al. (2013), *LPS 44*, Abstract #1174.
[6] Basilevsky A.T. (1976) Proc. *LPSC 7.* 1005-1020.
[7] Barsukov V.L. et al. (1978) Lunokhod-1, a mobile laboratory on the moon. Volume 2. Moscow. Nauka press. 183 p.(in Russian).
[8] Basilevsky A.T. et al. (2013) *Planet. Space Sci. 89*. 118-126. [9] Hiesinger H. et al. (2000) *JGR*, *105*. E12. 29,239-29,275. [10] Wu Y. Z. (2014) *LPS 45*, abs. 2613.

# DEFLECTION OF SOLAR WIND PROTONS FROM THE LUNAR MAGNETIC ANOMALIES

**A.M. Sadovski, A.A. Skalsky,**
*[1]Space Research Institute of Russian Academy of Sciences, Profsouznaya str., 84/32, Moscow, Russia,*
*Contact: asadovsk@iki.rssi.ru*

The first measurements, was made on the lunar orbits, has shown that Moon has no its intrinsic dipolar magnetic field. However the residual magnetization in returned lunar samples and also the anomalous magnetization of lunar surface (till several hundred nT) was found even in Apollo missions.

Observations of Kaguya and Chandrayaan reveal the significant solar wind protons deflection from the lunar surface in particular from the magnetic anomalies regions. These observations implies that the magnetic anomalies may act as magnetosphere-like obstacles (mini-magnetospheres), modifying the upstream plasma.

We examined the conditions in solar wind for the anomaly observation on 29 of April 2009 and estimated plasma parameters in solar wind and in crustal magnetic field. The estimates of the deflection from the anomaly (taking into account also the ambipolar electric field) suggest that it is possible to make some shock structure and deflection of electrons. However the estimations of the proton energy have shown that protons should fill the cavity and additional factors are needed to be taken into account.

# RADIOLOCATION AS AN EFFECTIVE TOOL FOR REMOTE SENSING OF THE SUBSURFACE STRUCTURE OF THE LUNAR SOIL

**O.V.Yushkova, O.I.Yakovlev, A.G.Pavelyev, V.M. Smirnov, V.N. Marchuk**
*Kotel'nikov Institute of Radio Engineering and Electronic of Russian Academy of Sciences, Fryazino Branch, Russia;*
*Contact: y.o.v@mail.ru*

Accurate study of the composition and structure of the lunar ground is one of the most important problem of comparative planetology both from scientific and practical point of view. Especially a problem of existence of water ice deposits, their location and volume is of particular interest. Radar remote sensing is the most efficient non-contact method of studying the subsurface structure of the Moon. Radar remote sensing can be carried out with two modes: (i) regime of bistatic radar when a powerful terrestrial transmitter emits radio waves, and a lunar artificial satellite is receiving signals reflected from different parts of the Moon's subsurface, and (ii) monostatic regime of radio location, when the emission and reception is conducted from orbit.

The theoretical analysis and methods created to solve the inverse problem of radar remote sensing, including formulation of the fundamental requirements for the selection of the frequency range of the radio waves, selecting the type of signal modulation, evaluation of the necessary power of terrestrial transmitters, determination of the technical characteristics of the transmission system, with aim to provide a study of ground to depths of 1 km, with the highest possible spatial resolution in depth are discussed in the report. The dependences of the reflected signal, spatial resolution of the method, the accuracy of determining the density and dynamic characteristics of the lunar ground relevant to the existing domestic radio transmitters are described.

**Acknowledgements.**

This study has been partially supported by the Program 22 of the Presidium of RAS "Fundamental Problems of research and exploration of the Solar System."

# THE GAS-ANALYTICAL-COMPLEX FOR ANALYSIS OF VOLATILES IN THE LUNAR POLAR REGOLITH DURING THE LUNA-RESOURCE MISSION (2019)

**S.A.Aseev[1], M.V.Gerasimov[1], M.A.Zaitsev[1], A.G.Sapgir[1], + GAC team**
*[1]Space Research Institute of Russian Academy of Sciences (IKI RAS), 117997, 84/32 Profsoyuznaya str., Moscow, Russia*
*Contact: Ser.aseev@iki.rssi.ru*

**Introduction:**
The Roscosmos will launch two landers: «Luna-Glob» (2017) and «Luna-Resource» (2019) aimed on detail investigation of the lunar polar environment. These missions are of great scientific interest since all previous numerous landings on the Moon were performed in areas close to the equator. The study of the lunar regolith at the poles will help to answer on a set of important questions among which the most fundamental one is the inventory of Lunar polar volatiles with their possible utilization during future exploration of the Moon.

In the frame of preparation for the experiment **ALPOL** (**A**nalysis of **L**unar **P**olar v**OL**atiles) on «Luna-Resource» mission, IKI RAS develops Gas-Analytical-Complex (GAC) in collaboration with scientific institutes of France and Switzerland. The GAC consists of three instruments: Thermal Analyzer (TA-L), Gas Chromatograph (GC-L), and Neutral Gas Mass Spectrometer (NGMS). The TA-L and the GC-L instruments are manufactured at IKI and the NGMS — in the Physics Institute of the University of Bern. The GC-L instrument is developed in collaboration of IKI with LATMOS (France). The main scientific objective of the GAC is the comprehensive analysis of volatile compounds in the regolith in the polar regions of the Moon.

The TA-L instrument performs pyrolysis of a portion of lunar regolith delivered by the manipulator and/or drilling device. The heating of a regolith sample up to 1000°C results in release of volatile compounds which are transferred via a system of capillaries into the GC-L and the NGMS for chemical analysis. The GC-L uses a complex system of capillaries, valves, and adsorption traps to collect, separate, and concentrate gases and volatiles for analysis. The GC-L also has a Tunable Diode Laser Absorption Spectrometer (TDLAS) for precise measurement of isotopic composition of carbon, hydrogen, and oxygen in $H_2O$ and $CO_2$ molecules. The GC-L uses two capillary chromatographic PLOT-columns (Molsieve 5A and PoraPlot Q) which can work in a serial or parallel mode depending on the valves configuration.

Neutral Gas Mass Spectrometer (NGMS)is a time-of-flight type mass spectrometer with a grid-less ion mirror (reflectron). The ions are generated from the neutral gas by electron impact ionisation. The high cadence of recorded mass spectra allows the accumulation of mass spectra with a large dynamic range of up to $10^6$ within 1s integration time.

The GAC is able to detect concentrations of volatile species in the soil sample of about 0.2 ppb of mass for hydrocarbons and 2ppb of mass for noble gases. An additional feature of NGMS is that it can be operated as a standalone instrument for sampling the tenuous lunar exosphere.

# DUSTY PLASMA SHEATH NEAR THE LUNAR SURFACE (NUMERICAL SIMULATION)

**E.A. Lisin[1], V.P. Tarakanov[1], O.F. Petrov[1,2], S.I. Popel'[2-4] G.G. Dol'nikov[3], V.V. Afonin[3], A.V. Zakharov[3], L.M. Zelenyi[2,3]**
[1]*Joint Institute for High Temperatures of the Russian Academy of Sciences*
[2]*Moscow Institute of Physics and Technology (State University)*
[3]*Space Research Institute of the Russian Academy of Sciences*
[4]*Institute of Geosphere Dynamics of the Russian Academy of Sciences*

One of the main challenges of future missions to the Moon is associated with lunar dust. The lunar surface is exposed to both the solar wind and solar UV radiation causing electron photoemission. As a result, there is a substantial surface change and a near-surface plasma sheath. Dust particles from the lunar regolith, which turned in this plasma as a result of any mechanical processes, can levitate above the surface, forming dust clouds.

In 2016-2019 Russia plans to launch the spacecrafts "Luna-25" and "Luna-27". For experimental investigations of the lunar dusty plasma exosphere of the polar regions, it is planned to equip "Luna-25" and "Luna-27" stations with instruments both for direct detection of dust particles over the surface and for optical measurements [1, 2].

We have carried out numerical calculations of the near-surface plasma sheath in the alleged places of landing of "Luna-25" and "Luna-27". The calculations have been performed by the PiC-code KARAT which is developed for solving nonstationary electrodynamic problems with complex 3D geometry and relativistic particle dynamics [3]. Here we present some new results of PiC simulation of the plasma sheath formed near the sunlit surface of the lunar polar regions as a result of interaction of the solar wind and UV radiation with the lunar surface. As a data source of the photoelectron energy spectrum we used photoelectron distribution function calculated recently by S. Popel' et al. [2].

The conditions of charging and stable levitation of dust particles in plasma above the lunar surface are also considered.

*This work was supported by the Program 22 of the RAS Presidium and the Russian Foundation for Basic Research (13-02-90441).*

[1] E. A. Lisin, V. P. Tarakanov, O. F. Petrov, S. I. Popel' G. G. Dol'nikov, A. V. Zakharov, L. M. Zelenyi, and V. E. Fortov, JETP Letters 98, 664 (2013)
[2] S. I. Popel, A. P. Golub', Yu. N. Izvekova, V. V. Afonin, G. G. Dol'nikov, A. V. Zakharov, L. M. Zelenyi, E. A. Lisin, and O. F. Petrov, JETP Letters 99, 115 (2014)
[3] Tarakanov V. User's Manual for Code KARAT (VA, USA: Berkeley Res. Ass., Inc. 1992)

# DUST PARTICLES INVESTIGATION FOR FUTURE RUSSIAN LUNAR MISSIONS

**A. Zakharov[1], I. Kuznetsov[1], G. Dolnikov[1], A. Lyash[1], V. Afonin[1], F. Esposito[2], E. Seran[3], M. Horaniy[4], M. Koepke[5], V. Gotlib[1]**
*[1]Space Research Institute (IKI), Russian Academy of Sciences, Moscow, Russia,*
*[2]INAF - Osservatorio Astronomico di Capodimonte, NAPLES, Italy*
*[3]Laboratoire Atmospheres, Milieux, Observations Spatiales, Paris, France*
*[4]University of Colorado, Boulder, Colorado, United States*
*[5]West Virginia Univeristy, Morgantown, West Virginia, United States*
*Contact: kia@iki.rssi.ru*

One of the complicating factors of the future robotic and human lunar landing missions is the influence of the dust. Meteorites bombardment has accompanied by shock-explosive phenomena, disintegration and mix of the lunar soil in depth and on area simultaneously. As a consequence, the lunar soil has undergone melting, physical and chemical transformations.

Recently we have the some reemergence for interest of Moon investigation. The prospects in current century declare USA, China, India, and European Union. In Russia also prepare two missions: Luna-Glob and Luna-Resource. Not last part of investigation of Moon surface is reviewing the dust condition near the ground of landers. Studying the properties of lunar dust is important both for scientific purposes to investigation the lunar exosphere component and for the technical safety of lunar robotic and manned missions.

The absence of an atmosphere on the Moon's surface is leading to greater compaction and sintering. Properties of regolith and dust particles (density, temperature, composition, etc.) as well as near-surface lunar exosphere depend on solar activity, lunar local time and position of the Moon relative to the Earth's magneto tail. Upper layers of regolith are an insulator, which is charging as a result of solar UV radiation and the constant bombardment of charged particles, creates a charge distribution on the surface of the moon: positive on the illuminated side and negative on the night side. Charge distribution depends on the local lunar time, latitude and the electrical properties of the regolith (the presence of water in the regolith can influence the local distribution of charge).

On the day side of Moon near surface layer there exists possibility formation dusty plasma system. Altitude of levitation is depending from size of dust particle and Moon latitude. The distribution dust particle by size and altitude has estimated with taking into account photoelectrons, electrons and ions of solar wind, solar emission. Dust analyzer instrument PmL for future Russian lender missions intends for investigation the dynamics of dusty plasma near lunar surface. PmL consists of three parts: Impact Sensor and two Electric Field Sensors.

Dust Experiment goals are:

1) Impact sensor to investigate the dynamics of dust particles near the lunar surface (speed, charge, mass, vectors of a fluxes) a) high speed micrometeorites b) secondary particles after micrometeorites soil bombardment c) levitating dust particles due to electrostatic fields. PmL instrument will measure dust particle impulses. In laboratory tests we used: min impulse so as $7\cdot10^{-11}$ N·s, by $SiO_2$ dust particles, 20-40 m with velocity about 0,5 -2,5 m/s, dispersion 0.3; max impulse was $10^{-6}$ N·s with possibility increased it by particles Pb-Sn 0,7 mm with velocity 1 m/c, dispersion 0.3. Also Impact Sensor will measure the charge of dust particle as far as $10^{-15}$ C (1000 electrons). In case the charge and impulse of a dust particle are measured we can obtain velocity and mass of them.

2) Electric field Sensor will measure the value and dynamics of the electric fields near the lunar surface. Two Electric Field Sensors both are measured the concentration and temperature of charged particles (electrons, ions, dust particles). Uncertainty of measurements is 10%. Electric Field Sensors contain of Langmuir probes. Using Langmuir probes near the surface through the lunar day and night we can obtain the energy spectra photoelectrons in various periods of time.

PmL instrument is developing, working out and manufacturing in IKI. Simultaneously with the PmL dust instrument to study lunar dust it would be very important to use an onboard TV system adjusted for imaging physical properties of dust on the lunar surface (adhesion, albedo, porosity, etc), and to collect dust particles samples from the lunar surface to return these samples to the Earth for measure a number of physic-chemical properties of the lunar dust, e.g. a quantum yield of photoemission, what is very important for modeling physical processes in the lunar exosphere.

# ELECTRIC CHARGING OF DUST PARTICLES: IMPACT ON THE VARIATIONS OF ELECTRIC FIELD AND ELECTRIC RESISTIVITY OF AIR

**E. Seran[1], M. Godefroy[1], A. Zakharov[2], G. Dolnikov[2]**
*[1] LATMOS, France, [2] IKI, Russia*

Short Dipole Antenna is proposed in the frame of the Dust Package onboard the ROSCOSMOS- ESA ExoMars Lander. The SDA is developed to measure the electric field from few $\mu$V m$^{-1}$ to few tens kV m$^{-1}$ in the frequency range form DC to few kHz. The SDA concept and the model of its electric coupling with the air were tested and justified in the Nevada desert, in the conditions of dust devils generation. We illustrate our presentation with few examples of earth's observations, present simple models that explain the measured electric field and its correlation with the electric charge of the dust/sand particles, their density and motion. Comparative analysis between Earth and Mars cases is discussed.

# PHOTOLUMINESCENCE OF SILICON-VACANCY DEFECTS IN METEORITIC NANODIAMONDS

**A. A. Shiryaev[1], A. V. Fisenko[2], L. F. Semjonova[2], A. A. Khomich[3], I. I. Vlasov[3],**
*[1]Institute of physical chemistry and electrochemistry, Leninsky pr. 31, Moscow, Russia;*
*[2]Vernadsky Institute, Moscow, Russia;*
*[3]General Physics Institute, Moscow, Russia.*
*Contact: shiryaev@phyche.ac.ru*

**Introduction:**

Nanodiamonds present in meteorites are an enigmatic substance. Their abundance may reach 2000 ppm, thus constituting up to 3% of total carbon inventory of a given meteorite. Despite long history of active research the formation process(es) and astrophysical source(s) of meteoritic nanodiamonds (MND) remain highly debatable. Whereas isotopic composition of noble gazes and in particular of Xe indicates that a fraction of nanodiamonds might be related to Supernovae type II explosions, isotopic composition of matrix carbon and of the principal chemical impurity — nitrogen — are less conclusive and may support hypothesis of MND formation in the Solar system (e.g., Dai et al., 2002). Processes of MND formation are also debatable, but combined analysis of information about structure and chemical impurities (Shiryaev et al., 2011) suggests that the growth process of (at least) N-containing grains should be very fast. The CVD-like (Chemical Vapour Deposition) process (Daulton et al., 1996), possibly triggered by a shock wave, looks plausible, but other processes cannot be excluded. Investigation of defects in nanodiamonds structure is very important for deciphering process of MNDs formation.

Recently we have reported observation of an important point defect — a silicon-vacancy complex (SiV) — in nanodiamonds from Efremovka (CV3) and Orgueil (CI) chondrites (Shiryaev et al., 2011). Subsequent studies (Vlasov et al., 2014) demonstrated that the SiV luminescence is confined to the smallest grains (≤2 nm). We present here results of investigation of the SiV defects in size fractions of nanodiamonds extracted from meteorites of various chemical classes and groups.

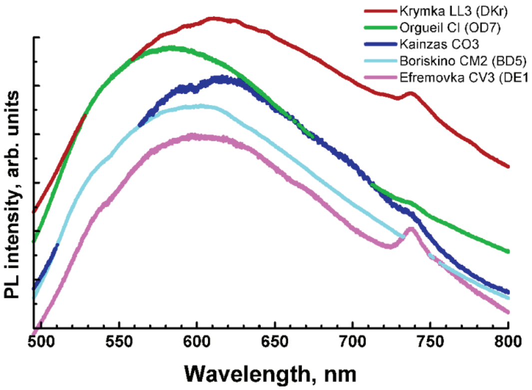


**Fig. 1.** General view of photoluminescence spectra of nanodiamonds from various meteorites

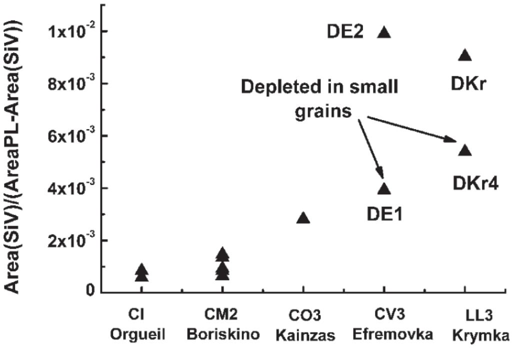


**Results:**

Nanodiamonds (ND) were extracted from Orgueil (CI), Boriskino (CM2), Efremovka (CV3), Kainsaz (CO3), and Krymka (LL3.1) chondrites. The extraction was performed according to standard protocol involving acid dissolution of a meteorite piece at temperatures up to 220 °C (Tang et al., 1988). Colloidal ammonia solutions of nanodiamonds of some meteorites were further separated into grain size fractions by ultracentrifugation at various accelerations and duration.

Typical photoluminescence spectra of studied nanodiamonds are shown in Fig. 1. The spectra are normalised to the maximum of the broad band and displaced vertically. The maximum of the broad structureless band lies between 590 and 610 nm. This band is due to overlapping signals from non-diamond $sp^2$-carbon and defects on the surfaces of diamond grains. The variations in its maximum position are due to differences in surface structure of nanodiamond grains. The SiV band is clearly seen as a feature at 737 nm.

Figure 2 shows that the relative area of the SiV band depends on chemical class and group of meteorite and on nanodiamond grains sizes. As shown by us earlier (Vlasov et al., 2014) the SiV luminescence is observed in the grains with sizes ≤2 nm, which are smaller than the median MND size of 2.6-2.8 nm (Daulton et al., 1996; Lyon, 2005). The size separation depletes the “bulk” sample in smaller grains, therefore the SiV intensity for the coarse grain fractions for Krymka and Efremovka meteorites decreases. In the same time, for the Orgueil and Boriskino samples the size effect is small and probably not significant (Fig. 2).

We believe that behaviour of SiV luminescence intensity presented at Figure 2 could be explained by two principal factors: 1) existence of several nanodiamonds populations, and 2) thermal history of meteorites parent bodies.

Isotopic measurements suggested existence of several independent populations of nanodiamonds (e.g., Huss and Lewis, 1994). If true, parent meteorite bodies may have sampled different proportions of Si-containing nanodiamonds population. The uneven sampling may be explained by formation of meteorites of different clans at different parts of protoplanetary nebula and/or at different times. In addition thermal stability of the populations may play an important role.

It is possible however, that the total Si content in ND grains of different meteorites is roughly similar and observed scatter of the SiV intensity is due to thermal history of the meteorites. Indeed, the lowest intensity of the SiV defects are observed for nanodiamonds of Orgueil (CI) and Boriskino (CM2) meteorites which underwent low temperature (~100 °C) metamorphism only. The SiV is stronger in MND from Efremovka (CV3) and Krymka (LL3.1), with temperature of metamorphism of at least 300-400 °C.

Oxidative annealing of meteoritic NDs enhanced the SiV photoluminescence. Most likely the effect is due to partial removal and reconstructs of the $sp^2$-carbon superficial layer. Remarkably, the tendency of changes of the SiV relative intensity shown on Fig. 2 for carbonaceous meteorites correlates with concentration of P3 noble gases, which might be related to disordered carbonaceous phase on surfaces of nanodiamond grains (Fisenko et al., 2014 and refs. therein). In the studied meteorite set the concentration of P3 noble gases in NDs of Orgueil and Boriskino is the highest, whereas for Efremovka NDs it is the lowest (Huss and Lewis, 1994; Verchovsky et al., 1998; Fisenko et al., 2004).

**Conclusions:**

A band of silicon-vacancy (SiV) defect in diamond lattice is observed in photoluminescence spectra of different size fractions of nanodiamonds extracted from chondrites of various groups. At present our statistics includes the following classes and groups: CI, CM2, CO3, CV3, and LL3. The concentration of silicon in NDs lattice may reach hundreds of atomic ppm, which makes this element important for identification of astrophysical sources and formation processes of meteoritic nanodiamonds.

The variations of the SiV luminescence intensities for nanodiamonds extracted from meteorites of different classes are due to variations of thermal metamorphism temperature of their parent bodies and/or uneven sampling of nanodiamonds populations. The silicon impurity is preferentially incorporated into the smallest grains (less than 2 nm). Thermal metamorphism of parent meteorite bodies is an important factor for enhancement of the luminescence of trapped Si atoms promoting formation of specific lattice defect and by modification of nanodiamonds surfaces. Strong and well-defined luminescence and absorption of the SiV defect may allow detection of cold nanodiamonds in space.

# THE EXOLIFE: NEW FACTORS

**Oleg B. Khavroshkin, Vladislav V. Tsyplakov**
*Institute of Physics of the Earth, RAS, Moscow, Russia*
*Contact: khavole@ifz.ru*

**Introduction**

The hypothesis that bacteria and protozoa microorganisms are able to travel from one planet to another and become of exolife was not taken seriously by the scientific community for a long time. However at the end of the XX century the situation changed dramatically. Firstly, in 1990, meteorites consisting of Martian rocks were found. Secondly, it became clear that many microorganisms especially bacteria spores have an uncanny ability to endure the rugged environment of the outer space for a long time and then re-activate in a more favorable environment. If we compare these findings, the idea of interplanetary transmigration of the simplest forms of life on meteoroids ceases to look so illusory. The final dot in this issue was made by the works of academician Rozanov, and later Hoover (Professor Richard B. Hoover) through the discovery of fossilized microbes inside of a meteorite massif, that is to say seeds of life. However, to tie only the simplest forms of life to meteorites or comets are to introduce strong constraints on the likelihood of delivery of seeds (spores of life) to Earth for many obvious reasons. Besides exobiology does not negate the problem of origin of life, and transfers it into the era of the young universe. Therefore, it is necessary to consider in detail the essence of seeds of life or cosmic particles of dust and gas-dust streams as their carriers, their penetration path to Earth and forms of their existence.

**Gas-dust streams from the nearest multiple of some stellar systems**

As is well known, close multiple star systems form powerful gas-dust disks. A flow of matter spreading from the central zone of a system may have relativistic velocities and modulates on the rotation periods of components. On further distributions the flux of stellar matter is transformed into a gas-dust stream producing plasma crystals which prevent smoothing modulation perturbations. The estimates show that as compared to the solar system fluxes, the density of which exceeds the density of gas and dust flows from multiple systems by an order of magnitude or more, the latter due to the high velocities put pressure on the lunar surface comparable to the impact of fluxes of the solar system. This agrees well with the results of the statistical analysis of lunar seismicity: apart from periodicities from modulated flows of the solar system periodicities of nearest binary stars (see Table 1) are observed. These effects should be observed in the Earth’s atmosphere. However, initially let us try to find a connection between gas-dust flows of the solar system and the processes in the Earth’s atmosphere, since only by demonstrating the connection of dust flows and the Earth`s atmosphere, it can be argued that the possibility of penetration of the spores of life on the Earth exists.

**Seeds of life and gas-dust plasma form generation**

Gas-dust plasma in outer space, in weightlessness and specific local conditions, in accordance with the theoretical and experimental research, is capable of generating 3D-forms (V.N. Tsytovich et al). These forms as granules (grains) can be formed in the space from the background dust or gas-dust streams and under simulation using special cameras.

# NONLINEAR DUST ACOUSTIC WAVES IN A DUSTY PLASMA OVER THE MOON

**T. I. Morozova, S. I. Kopnin, S. I. Popel,**
*Space Research Institute RAS, 84/32 Profsoyuznaya Str., Moscow 117997, Russia. Contact: timoroz@yandex.ru*

Plasmas over the lunar dayside contain electrons, ions, neutrals, and fine dust particles [1–5]. Dusts located on or near the surface of the Moon absorb photons of solar radiation, electrons and ions. All these processes lead to the charging of dust particles, their interaction with the charged surface of the Moon, rise and levitation of dust. Despite the existence of neutrals in the lunar atmosphere on the lunar dayside (~$10^5$cm$^{-3}$), the long photo-ionization time-scales (~10–100 days) combined with rapid ion pick-up by the solar wind (~1 s) should limit the associated electron and ion number densities to only ~1 cm$^{-3}$. However, there are some indications on larger electron number densities in the lunar ionosphere. In particular, the Soviet Luna-19 and Luna-22 spacecrafts conducted a series of radio occultation measurements to determine the line-of-sight electron column number density, or total electron content, above the limb of the Moon as a function of tangent height [6]. From these measurements they inferred the presence of a “lunar ionosphere” above the sunlit lunar surface with electron number densities reaching 1000 cm$^{-3}$. Electrons over the lunar dayside appear [2] due to the photoemission from the lunar surface as well as from the surfaces of dust particles levitating over the Moon, while the photoelectron emission is due to the solar vacuum ultraviolet (VUV) radiation. The electron distributions can be represented in the first approximation as a superposition of two Maxwellian those characterized by different electron temperatures [5, 7].

The dust acoustic waves propagate in a lunar dusty plasma when $kv_{Td} \ll \omega \ll kv_{TiS}$. In this case (with taking into account the characteristic parameters of the dusty plasma constituents) the dispersion equation takes the form

$$1 + (1/k^2\lambda_{De1}^2) - (\omega_{pd}^2/\omega^2) = 0 \tag{1}$$

where, $v_{Td}$ is the thermal dust speed, $v_{Ti}$ is the ion thermal velocity, $\omega_{pd}$ is the dust plasma frequency, $\lambda_{De}$ is the electron Debye length, the subscript $S$ characterizes a physical value determined by the solar wind parameters, the subscript 1 fits the photoelectrons produced by photons with the energies close to the work function of lunar regolith [7]. The excitation of the dust acoustic waves can take place in the vicinity of the lunar terminator. The terminator’s speed (several hundred cm/s) is several times larger than the dust acoustic velocity. Correspondingly, the instability resulting in the excitation of the dust acoustic oscillations can develop.

Growth of the dust acoustic waves, which occurs in the terminator region, can lead to the formation of dust acoustic nonlinear structures. Solitons play an important role among them. The behavior of the dust acoustic solitons is governed by the conservation equations, Boltzmann distributions, and the Poisson equations

$$\partial_t n_d + \partial_x(n_d\nu_d) = 0,\ \partial_t\nu_d + \nu_d\partial_x\nu_d = \frac{Z_d e}{m_d}\partial_x\varphi,$$
$$n_e = n_{e0}\exp\left(\frac{e\varphi}{T_e}\right),\ n_{i0}\exp\left(-\frac{e\varphi}{T_i}\right),\ \partial_x^2 = 4\pi e(n_e + Z_d n_d - n_i) \tag{2}$$

where $\varphi$ is the electrostatic potential; $x$ and $t$ are the space and time variables; $n_\alpha$ and $n_{\alpha 0}$ ($\alpha$ = $e,i,d$) are the density and the unperturbed density of the electrons, ions and dust particles; $m_d$, $v_d$, and $Z_d$ are the mass, velocity, and charge number of a dust particle, $-e$ is the electron charge; and $T_{e(i)}$ is the electron (ion) temperature. The equations are valid if the characteristic velocity of the process is larger than the dust thermal speed and much less than the ion thermal speed.

The main contributions to the terms of the above equations containing the electron parameters are made by photoelectrons, while to those containing the ion parameters are made by solar wind ions. The role of ions in the formation of the dust acoustic structures in dusty plasmas over the illuminated part of the Moon is negligibly small. Thus below the ion contribution is omitted. Furthermore, we neglect dust charge variations within the soliton.

We now look for solutions of (2) in the form of localized wave structures propagating with constant velocities M in the x-direction. Thus, all the parameters involved depend on x and t only through the variable $\xi = x - Mt$. We assume that all perturbations vanish for $\xi \to \pm\infty$. We use the standard Sagdeev potential approach and reduce the problem to the analysis of the effective energy integral

$$\frac{1}{2}\left(\varphi\xi\right)^2 + V(\varphi) = 0, \tag{3}$$

where the normalizations $e\varphi/T_e \to \varphi$ and $M/c_d \to M$ have been used, and

$$v\left(\varphi\right) = 1 - exp + \left|M\right|d\left(\left|M\right| - \sqrt{M^2 - 2Z_d\varphi}\right). \tag{4}$$

Here, $c_d^2 = T_i/m_d$ and $d = n_{d0}/n_{e0}$. Fig. 1 shows examples of dust acoustic solitons at to be 0.15 eV. For the existence of the dust acoustic solitons, the Sagdeev potential $V(\varphi)$ must have a local maximum at $\varphi = 0$, and the equation $V(\varphi) = 0$ must have at least one more real solution $\varphi_0$. A local maximum of the Sagdeev potential $V(\varphi) = 0$ at the point $\varphi_0$ exists if

$$M^2 > Z_d^2 d/(1 - Z_d d). \tag{5}$$

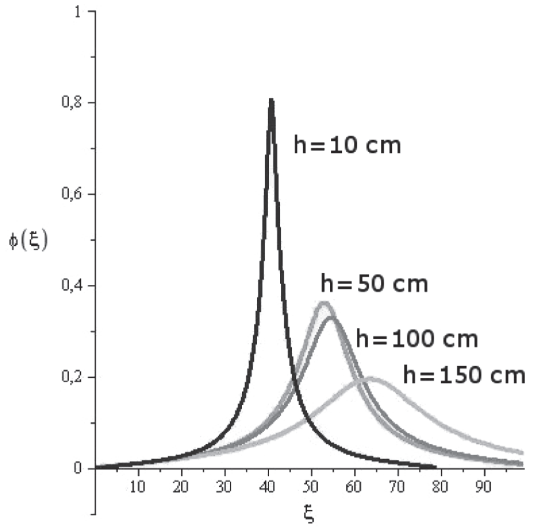


**Fig. 1.** The $\varphi(\xi)$ profiles for the dust acoustic solitons at different heights (h).knowledges the financial support of the Dynasty Foundation

In addition to the solitons dust acoustic shocks can exist. Indeed, by analogy with the active space experiments which involve the release of some gaseous substance in Earth's ionosphere [8], the motion of the terminator can be associated with the propagation of dust acoustic shock: the terminator treated as the shock front distinguishes sharply the dusty plasma parameters before and behind it and moves with the Mach number M > 1.

This work was carried out as part of the Russian Academy of Sciences Presidium program no. 22 "Fundamental problems of Research and Exploration of the Solar System" and was supported by the Russian Foundation for Basic Research, project no. 12-02-00270-a. T.I. Morozova acknowledges the financial support of the Dynasty Foundation and S.I. Kopnin acknowledges the financial support of the RF President Grant Council for support of young scientists and leading scientific schools (grant no. MK-3764.2013.2).

**References:**

1. A.P. Golub', G.G. Dol'nikov, A.V. Zakharov, et al., JETP Lett.95, 182 (2012)
2. S.I. Popel, S.I. Kopnin, A.P. Golub', et al., Solar Syst. Res. 47, 419 (2013)
3. S.I. Popel, L.M. Zelenyi, J. Plasma Phys. 79, 405 (2013)
4. E.A. Lisin, V.P. Tarakanov, O.F. Petrov, et al., JETP Lett. 98, 664 (2013)
5. S.I. Popel, A.P. Golub', Yu.N. Izvekova, et al., JETP Lett. 99, 115 (2014)
6. T.J. Stubbs, D.A. Glenar, W.M. Farrell, et al., Planet. Space Sci. 59, 1659 (2011)
7. S.I. Popel, G.E. Morfill, P.K. Shukla, H. Thomas, J. Plasma Phys. 79, 1071 (2013)
8. S.I. Popel, V.N. Tsytovich, Astrophys. Space Sci. 264, 219 (1999)

# A TOOLKIT FOR METEOR ORBIT DETERMINATION USING NUMERICAL INTEGRATION OF EQUATIONS OF MOTION

**V. Dmitriev [1], V. Lupovka[1], M. Gritsevich[2,3], J. Oberst [4,5]**
*[1]State University of Geodesy and Cartography (MIIGAiK), Gorokhovskiy per., 4, 105064, Moscow, Russia;*
*[2] Finnish Geodetic Institute, Geodeetinrinne2, P.O. Box 15, FI-02431 Masala, Finland;*
*[3]Russian Academy of Sciences, Dorodnicyn Computing Centre, Department of Computational Physics, Vavilova40, 119333 Moscow, Russia;*
*[4]TechnischeUniversität Berlin, Institute for Geodesy and Geoinformation Science, Planetary Geodesy, Strasse des 17. Juni 135, 10623 Berlin, Germany;*
*[5]German Aerospace Centre, Institute of Planetary Research, Rutherfordstrasse 2, D-12489 Berlin, Germany*
*Contact: v.lupovka@miigaik.ru*

**Introduction:**

A traditionalapproachto meteoroid orbit computation assumes a set of corrections applied tothe observed velocity vector, see e.g. [1, 2, 3].In particular, apopular concept of “zenith attraction” is used to correct the direction of ameteor trajectory and its apparent velocity in the Earth’s gravity field.In this study, we review this and more explicit approaches to orbit determination.We develop and describe a new technique and softwaretodetermine meteoroidorbitbased on ground-based meteor observations.We use strict coordinate transformations and integration of differential equations of motion.We compareresults obtained for the selected fireball data usingthe proposed technique with corresponding results obtained by other authors.

**The Technique**

Specifically, the following transformations are in use:

A velocity vector is transformed from the topocentric to the geocentric coordinate system with account fordiurnal aberration.

The beginning point coordinate and velocity vectors are transformed from the Earth-fixed geocentric coordinate system ITRF2000 to the Geocentric Celestial Reference System (GCRS) realization ICRF2 (J2000) according to [4]. JPL ephemeris DE421 are used for transformation of meteoroid position and velocity vectors from the geocentric to the heliocentric coordinate system:

$$\vec{r}_{J2000} = \vec{R}_0 + \vec{R}_{in},$$
$$\dot{\vec{r}}_{J2000} = \vec{V}_0 + \vec{V}_{in}$$

here $\vec{r}_{J2000}$, $\dot{\vec{r}}_{J2000}$ are therequired initial conditions for numerical integration,

$\vec{R}_0$, $\vec{V}_0$ - Earth position and velocity vectors from JPL DE421 ephemeris [5],

$\vec{R}_{in}$, $\vec{V}_{in}$ - meteoroid position and velocity vectors in celestial geocentric coordinate system ICRF2 (J2000).

Backward integration of equations of perturbed meteoroid motion:

$$\ddot{\vec{r}} = \frac{GM_{Sun}}{r^3}\vec{r} + \ddot{\vec{r}}_{Earth}(C_{nm}, S_{nm}, \vec{r}, t) + \ddot{\vec{r}}_{Moon}(r, t) + \sum \ddot{\vec{r}}_{planets}(\vec{r}, t) + \ddot{\vec{r}}_{atm}(\vec{r}, t)$$

was performed by implicit single-sequence numerical method [6].

The equations of perturbed meteoroid motion include central body (Sun) attraction, perturbations from Earth gravity field, Moon, other planets, and atmospheric drag.For obtaining undistorted heliocentric orbit backward integration was performed within the Hill sphere (i.e. about 4 days backward in this case).

**The Tools**

This techniquehas been implementedin softwareto determine theorbitsof meteoroids. The graphical interfaceof this applicationis shown in Figure1.Using this software,it is possible toperform an analysisof the orbital motionof ameteoroidbefore it enters into the Earth’s atmosphere. The forwardnumericalintegration of the equationsof motionup to the possible impact point on the ground, can be performed to estimatethe locationof the associated meteorites, when applicable [7].This feature is useful forefficient meteorite detection, and shields the light onmore general problem of determinationof the characteristics for possible impacts between near-Earth objects and the Earth.

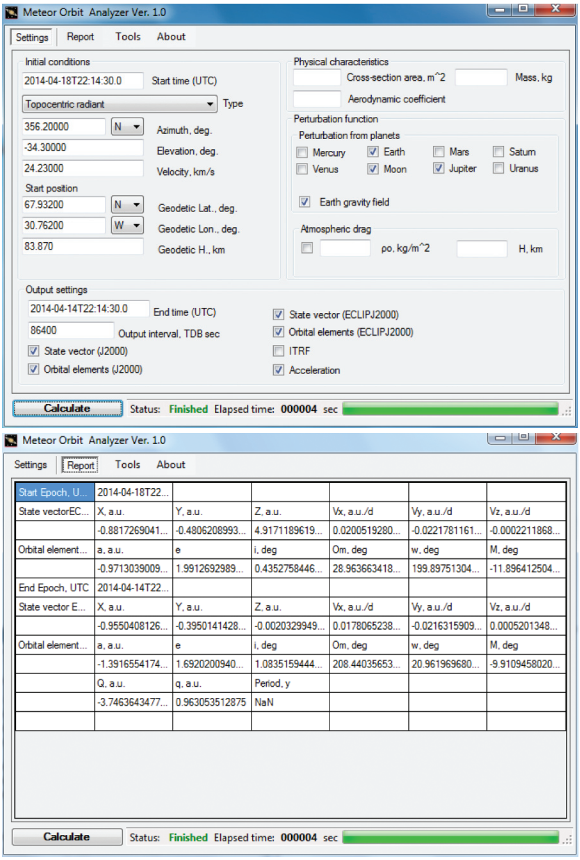


**Fig.1.**GUI of the described software fororbit determination.


**References**

[1] Ceplecha Z. Geometric, dynamic, orbital and photometric data on meteoroids from photographic fireball networks. Astronomical Institutes of Czechoslovakia, Bulletin, vol. 38, 1987, pp. 222-234.
[2] Andreev G. The Influence of the Meteor Position on the Zenith Attraction. Proceedings of the International Meteor Conference, Violau, Germany, September 6-9, 1990, Eds.: Heinlein D.; Koschny D., International Meteor Organization, 1990, pp. 25-27.
[3] Langbroek M. A spreadsheet that calculates meteor orbits. WGN, Journal of the International Meteor Organization, vol. 32, no. 4, 2004, pp. 109-110.
[4] IERS Conventions. IERS Technical Note No. 36, 2010, 160 p.
[5] Folkner W., Williams J., Boggs D. The Planetary and Lunar Ephemeris DE 421. IPN Progress Report 42-178, 2009, 34 p.
[6] Everhart E. Implicit single-sequence method for integrating orbits. Celestial Mechanics, vol.10, 1974, pp. 35-55.
[7] Gritsevich M. I., Stulov V. P., Turchak L. I. Consequences of collisions of natural cosmic bodies with the Earth's atmosphere and surface. Cosmic Research, vol. 50, pp. 56–64.

# CLOUD TOP AND WATER VAPOR VARIATIONS IN THE VENUS' MESOSPHERE FROM THE SPICAV OBSERVATIONS

**A. Fedorova[1,2],E.Marcq[3], F. Montmessin[3], M.Luginin[2,1],O. Korablev[1,2], J.L.Bertaux[3],**
[1]Space Research Institute(IKI), 84/32, Profsoyuznaya str., Moscow, 117997, Russia;
*[2]Moscow Institute of Physics and Technology (MIPT), 9 Institutsky dr., 141700 Dolgoprudny, Moscow Region, Russia;*
*[3]LATMOS-UVSQ, 11 Bdd'Alembert, F-78280 Guyancourt, France. Contact: fedorova@iki.rssi.ru*

*SPICAV VIS-IR* is an AOTF (acousto-optical tunable filter) spectrometer working in the spectral range of 0.65-1.7 µm onboard the *Venus Express* mission [1]. It provides measurements of the $H_2O$ abundance above Venus' clouds based on the 1.38-µm band and the cloud top altitude based on the $CO_2$ bands in the range of 1.4-1.6 µm. The new calibrations of the instrument in 2010-2012 allowed updating of results reported earlier.

The cloud top altitude has been routinely retrieved for all dataset from 2006 to 2014 (4350 nadir series from orbit 30 to 2900) taking into account multiple-scattering in the cloudy atmosphere. The $\tau$=1 level at 1.48 µm varies from 69 to 73 kmat lower latitudes and from 64 to 68 kmat high latitudes near the Poles assuming a constant scale height of upper clouds equal 4 km. Local time variations in the middle latitudes have been observed which are sensitive to the scale height assumption. There is no prominent long-term variation.

The $H_2O$ mixing ratio from the 1.38 µm band varies from 3 to 13 ppm. The variations are higher than $H_2O$ mixing ratio variations at altitudes of 68-70 km observed by *VIRTIS-H/Venus Express* [2] from 2.56 µm. The 1.38 µm $H_2O$ band is sensitivity to altitudes of 55-70 km and a vertical gradient of water within the upper clouds can be responsible for the water behavior. There is a maximum of the $H_2O$ mixing ratio at the lower latitudes (injection of water from lower atmospheric levels?) and an increase to the Poles. Local time and long-term variations of water vapor in upper clouds were not found for period from 2007 to 2014. The spot pointing observations for wide variations of viewing angle in the near-IR spectral range are useful to determine the vertical gradient of water within the clouds.

**References:**

[1] Korablev, O., Fedorova, A., Bertaux, J.-L. et al., SPICAV IR acousto-optic spectrometer experiment on Venus Express, Planetary and Space Science 65, 38–57, 2012.
[2] Cottini, V., Ignatiev, N., Piccioni, G. et al., Water vapor near the cloud tops of Venus from Venus Express/VIRTIS dayside data, Icarus, Volume 217, Issue 2, p. 561-569,2012

# MORPHOMETRY OF RIFT-ASSOSIATED VOLCANOES ON VENUS AND EARTH

**Guseva E.N.**
*Vernadsky Institute, Moscow, 11999, Russia.*
*Contact: guseva-evgeniya@ya.ru*

**Introduction:** Volcanism on Venus appears as both the extended lava plains and large and small volcanic edifices [1; 2]. The edifices are classified by size into three categories: small (<20 km), average (20-100 km) and large (>100 km) [3]. The large volcanic edifices (shield volcanoes) spatially associated with rift zones [2; 4] and are located mainly in the areas of their triple junction [5]. The highest concentration of volcanic structures observed in the region of BAT (Beta-Atla-Themis region), where they are associated with positive gravity anomalies [6; 2]. Composition of volcanics on Venus is mostly basaltic [7].

Continental volcanism on Earth is characterized by the fracture-related (basalt plateau) and the central types of eruptions [8]. The volcanoes of the central type are divided into monogenic and polygenic [9] and are often spatially associated with large areas of rifting, for example with the East African Rift System (EARS) [10]. The thermal and seismic anomalies characterize the lithosphere beneath the rifts of EARS [11; 12]. EARS is characterized mainly basaltic volcanism [13].

The goal of this study was to determine the morphometric characteristics (diameter, height, volume, ratio of height/diameter, K) volcanoes of Venus and Earth that are in association with the major areas of extension (rifts of Venus and EARS). The lateral dimensions and structure of these zones [14-18] suggest that they occur in similar geodynamic settings. The quantitative parameters of volcanoes associated with the rifts on Venus and Earth are important for the comparison of these geodynamic settings and understanding of their similarities and differences on both planets.

**Results:** For Venus, the large volcanoes with diameter >100 km were analyzed. Of all the studied volcanoes, eleven are located in rift zones: Theia, Maat, Ozza, Gula, Innini, Hathor, Uretsete, Polik-mana, Olesnicka, Mem Loimis, Yunya-mana (tabl.1). The Theia volcano has an irregular shape (volume of the volcanic edifice was not estimated), because the volcano is at the center of the triple junction of the large rifts of Beta Regio. The updoming and rifting have largely affected the volcano shape in this area [19]. The other studied volcanoes have the shape of either cones or truncated cones. Diameters of the volcanoes vary from 89 to 410 km, the height varies from 0.9 to 5.9 km, the height/diameter ratio (K=H/D) is from 0.004 to 0.023 (tabl.1). As the diameter of the volcanoes increases, the K value is decreases (Fig.1). The volumes of the venusian volcanoes is from $5.8\times10^3$ to $202.3\times10^3$ $km^3$ (tabl.1). These estimates of the volumes are consistent with the literature data.

For the Earth, twenty-nine of the studied volcanoes are located either on the flanks (Kilimanjaro, Kenya, Elgon) or directly within the rift zones of EARS. The volcanic edifices are presented the stratovolcanoes, often having the shape of truncated cones; less frequently they have a conical or irregular shape. Diameters of the studied volcanoes vary from 4 to 107 km, the height varies from 0.3 to 4.8 km (tabl.1). The K value is from 0.03 to 0.24 (tabl.1). As for Venus, with increasing of the diameter, the value of K decreases (Fig.1). The volumes of terrestrial volcanic edifices range from $0.002\times10^3$ $km^3$ to $10.4\times10^3$ $km^3$ (tabl.1).

**Conclusions:** The relationships of the morphometric parameters of the volcanoes on Venus and Earth suggest the presence of two distinct groups of edifices. (1) The venusian volcanoes are characterized by the larger diameters and the lower height/diameter ratios and have the general shape of the flattened cones with very shallow slopes on their flanks. (2) Most of the studied terrestrial volcanoes are characterized by the smaller diameters, the larger height/diameter ratios and are presented by stratovolcanoes with steeper slopes. The three largest volcanoes of EARS, Kilimanjaro, Kenya, and Elgon, which are located on the flanks of the Kenya rift, occur near the group of the venusian volcanoes (Fig.1). The volume of the venusian volcanoes is on the order of magnitude larger than the volume of the terrestrial volcanoes of the group 2. The differences in the shape and volume of volcanic edifices of Venus and Earth are probably related to: (a) the different viscosity of lavas (low-viscosity, more fluid on Venus) and (b) with the different productivity of volcanism (the higher eruption rates on Venus).

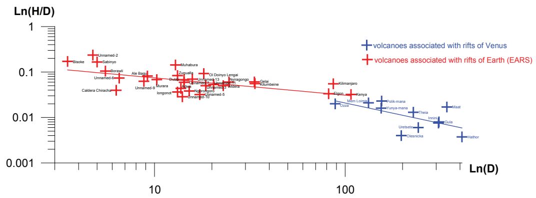


**Fig. 1.** Relationships between the height/diameter to diameter for volcanic edifices of Venus and Earth.

**Table 1.** Morphometric characteristics rift-associated volcanoes of Venus and Earth (EARS).

| **Rift region** | **Volcano** | **Volume (10^3 km^3)** | **Mean heigth (km)** | **Diameter (km)** | **H/D** |
|---|---|---|---|---|---|
| **Beta** | Theia | not estimated | 3,0 | 227,8 | 0,013 |
| **Atla** | Maat | 202,3 | 5,88 | 341,5 | 0,017 |
| | Ozza | 5,8 | 1,78 | 88,6 | 0,020 |
| **W. Eistla** | Gula | 74,5 | 2,59 | 310,3 | 0,008 |
| **Dione** | Innini | 58,1 | 2,33 | 308,6 | 0,008 |
| | Hathor | 67,2 | 1,53 | 409,6 | 0,004 |
| **Rabie Chasma** | Uretsete | 29,8 | 1,5 | 241,8 | 0,006 |
| **Hecate Chasma** | Polik-mana | 22,4 | 3,55 | 155,3 | 0,023 |
| **Tkashi-mapa Chasma** | Olesnicka | 17,4 | 0,85 | 196,9 | 0,004 |
| **Zewana Chasma** | Mem Loimis | 15,5 | 2,75 | 132,6 | 0,021 |
| **Pinga Chasma** | Yunya-mana | 15,8 | 2,53 | 154,3 | 0,016 |
| **Afar** | Afdera | 0,159 | 1,15 | 22,9 | 0,05 |
| | Dubbi | 0,052 | 0,97 | 14,3 | 0,07 |
| | Ale Bagu | 0,018 | 0,75 | 9,2 | 0,08 |
| | Unnamed-3 | 0,088 | 0,93 | 18,6 | 0,05 |
| | Unnamed-5 | 0,055 | 0,55 | 17,3 | 0,03 |
| | Adwa | 0,039 | 0,60 | 13,8 | 0,04 |
| | Borawli | 0,005 | 0,58 | 5,5 | 0,10 |
| **Ethiopian rift** | Elgon | 5,452 | 2,73 | 81,9 | 0,03 |
| | Unnamed-6 | 0,005 | 0,48 | 6,5 | 0,07 |
| | Unnamed-7 | 0,046 | 0,85 | 14,3 | 0,06 |
| | Unnamed-9 | 0,011 | 0,55 | 8,8 | 0,06 |
| | Caldera Chiracha | 0,003 | 0,25 | 6,3 | 0,04 |
| | Zuqualla | 0,057 | 1,10 | 13,2 | 0,08 |
| | Unnamed-10 | 0,021 | 0,40 | 14,0 | 0,03 |
| | Unnamed-11 | 0,118 | 1,08 | 20,4 | 0,05 |
| **Kenyan rift** | Kilimanjaro | 9,677 | 4,78 | 86,7 | 0,06 |
| | Kenya | 10,365 | 3,44 | 107,3 | 0,03 |
| | Ol Doinyo Lengai | 0,153 | 1,68 | 18,1 | 0,09 |
| | Kitumbeine | 0,648 | 1,87 | 33,6 | 0,06 |
| | Gelai | 0,610 | 2,03 | 33,4 | 0,06 |
| | longonot | 0,025 | 0,48 | 13,2 | 0,04 |
| | Unnamed-13 | 0,078 | 1,10 | 15,8 | 0,07 |
| | Ngorongoro | 0,054 | 0,58 | 15,2 | 0,04 |
| **Tanganyika rift** | Nyiragongo | 0,311 | 1,48 | 24,6 | 0,06 |
| | Unnamed-1 (Murara) | 0,024 | 0,70 | 10,3 | 0,07 |
| | Unnamed-2 | 0,007 | 1,12 | 4,8 | 0,24 |
| | Muhavura (Muhabura) | 0,080 | 1,84 | 12,9 | 0,14 |
| | Sabinyo | 0,005 | 0,83 | 5,0 | 0,17 |
| | Bisoke | 0,002 | 0,60 | 3,5 | 0,17 |

**References:**

[1] Barsukov, Basilevsky, Burba et al. JGR, 1986. V.91. D378-D398;
[2] Head, Crumpler, Aubele et al. JGR, 1992. V.97. 13,153-13,197;
[3] Crumpler, Aubele, Senske et al. 1997. 697-756;
[4] Basilevsky, Head, JGR, 2000. V.105. 24583-24611;
[5] Senske. E., M., and Plan., 1990. 50/51, 305-327;
[6] Smrekar, Phillips, EPSL, V. 107, № 3-4. 582-597;
[7] Barsukov, Surkov, Moscaleva et al. Geochemistry, 1982. №7. 899-919;
[8] MacDonald, Volcanoes, 1975. 261-275;
[9] Ritman, Volcanoes and their activity, 1964. 171-225;
[10] Frolova, Soros Educ. Journ., №2, 1996. 74-81;
[11] Ebinger., Karner and Weissel, Tectonics, 1991. V.10, 1239-1256;
[12] Condie, Mantle plumes and their record in Earth history, 2001. 306.;
[13] Frolova, Burikova, Magmatic formations of modern geotectonic environments, 1997. 249-295;
[14] Solomon, Head, Rift Systems on Venus... abst. “Terrestrial Planets: Comparative Planetology”. 1985. 138;
[15] Foster, Nimmo, EPSL, 1996. V.143;
[16] Chorowicz J.J. of Afr. Earth Sci, 2005. V.43. 379-410;
[17] Guseva, 39th LPSC, 2008.1063;
[18] Guseva, 4th MSSS, 2013.4MS3-PS-43;
[19] Stofan and Smrekar, Bindschadler, Senske, JGR, 1995. V.100. 23,317-23,327

# VISCOPLASTIC MEDIUM ON THE SURFACE OF VENUS

**L.Ksanfomality,**
*Space Research Institute of the Russian Academy of Sciences (IKI RAS), 117997, 84/32 Profsoyuznaya Str., Moscow, Russia*

On March 1 1982, experiment in television photography instrumented by the lander VENERA-13, yielded panoramic images of the Venus surface at the landing site. Over the past 32 years, no similar missions have been made. Using a modern technique the VENERA images' clarity was greatly improved which made it possible to study their details. An interesting object has the form of a low long wall of a relatively thin layer, disposed vertically. The wall extends along the periphery of 1.5-2 meter rounded feature, placed on a laminate surface. Location of the wall suggests that its material is extruded from under the plate surrounding rounded feature. Part of the wall, which resembles the incident wave, bent and partially lies on the surface, forming strata. The object is apparently formed by a material that remains at a semi-softened state at Venus' temperatures (about 740 K). It is assumed that on the basis of physico-chemical settings on the planet together with data on the composition of the Venus surface one can make assumptions about the nature of the observed viscoplastic medium, that even could be modelled in a laboratory.

# VARIATIONS OF THE ZONAL FLOW AT VENUS CLOUD TOPS FROM VMC/VEX UV IMAGES IN PERIOD FROM 2006 TO 2014

**Khatuntsev I.V.** [1,2], **Bertaux J-L.**[3], **Patsaeva M.V.** [1,2], **Hauchecorne A.**[3], **Titov D.V.**[4], **Marcq E.**[3], **Ignatiev N.I.** [1,2], **Markiewicz W.J.**[5], **Turin A.V.** [1], **Lebonnois S.**[3]
*[1]Space Research Institute (IKI), Russian Academy of Sciences, Moscow, Moscow, Russia;*
*[2]Institute of Physics and Technology, Dolgoprudny, Russia; Moscow, Russia;*
*[3]CNRS LATMOS, 11 bd d'Alembert, 78280 Guyancourt, France;*
*[4]ESA/ESTEC, PB 299, 2200AG Noordwijk, The Netherlands;*
*[5]Max-Planck-Institute for Solar System Research, Max-Planck-Str. 2, 37191 Katlenburg-Lindau, Germany*
*Contact: khatuntsev@gmail.com*

Abstract: Venus Monitoring Camera onboard Venus Express made long-term UV observations (2006-2014) of upper cloud of Venus. Out of the 3000 orbits of Venus Express over which the images used in the study cover about 13 Venusian years. We tracked cloud features in UV images obtained in 140 orbits by a manual cloud tracking technique and by an automated digital method in 690 orbits. Both methods and main results are described in detail in [3]. The VMC observations indicate a long term trend for the zonal speed of the flow at low latitudes to increase from 85 m/s in the beginning of the mission to the maximum (about 110 m/s) by the middle of 2012 and decreasing up to 97 m/s at present time (middle of 2014). VMC UV observations also showed significant short term variations of the mean flow in low latitudes with a period of 4.1-5 days (4.83 days on average) that is close to the super-rotation period at the equator. The wave amplitude is ±4-17 m/s and decreases with latitude, a feature of the Kelvin wave. The VMC observations demonstrated a clear diurnal signature. A minimum in the zonal speed was found close to the noon (11-14 h) and maxima in the morning (8-9 h) and in the evening (16-17 h). The meridional component peaks in the early afternoon (13-15 h) at around 50ºS latitude. The minimum of the meridional component is located at low latitudes in the morning (8-11 h). Here we present the latest update of our result.

It was the correlation between relief of the Venusian surface and the zonal flow speed. The global averaged field of the zonal wind speed was constructed in coordinates "latitude vs longitude" (Fig. 1). Spatial wind speed structure corresponding to Aphrodite Terra is discovered westward in 35-45 longitude.

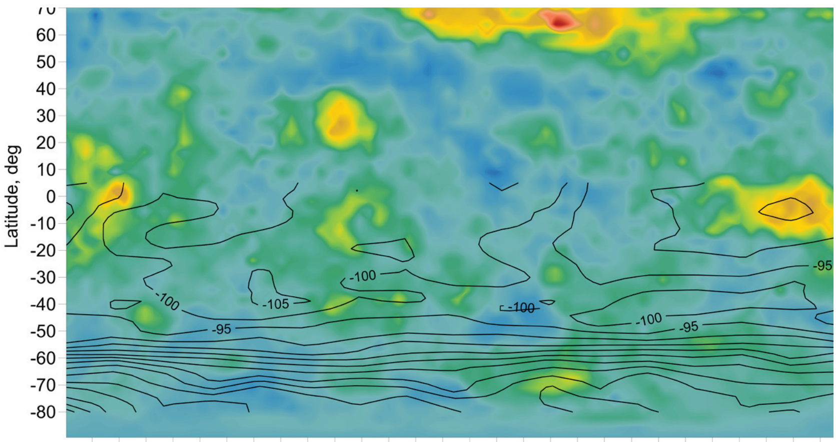


**Fig. 1.** Correlation between zonal flow speed and venusian relief.

# CORRELATION OF THE CLOUD TOP WIND PATTERN WITH CLOUD MORPHOLOGY AT THE UPPER CLOUD LEVEL OF VENUS AT 25°S-75°S FROM VMC/VENUS EXPRESS

**M. V. Patsaeva[1,2], I. V. Khatuntsev[1,2], D. V. Patsaev[1], D. V. Titov[3], N. I. Ignatiev[1,2], W. J. Markiewicz[4], A. V. Rodin[1,2]**
*[1]Space Research Institute (IKI), Russian Academy of Sciences, Moscow, Russia;*
*[2]Moscow Institute of Physics and Technology, Dolgoprudny, Russia;*
*[3]ESA/ESTEC, PB 299, 2200AG Noordwijk, Netherlands;*
*[4]Max Planck Institute for Solar System Research, Justus-von-Liebig-Weg 3, 37077 Göttingen, Germany.*
*Contact: marina@irn.iki.rssi.ru*

## Introduction:

The Venus Monitoring Camera (VMC) obtained a set of UV images of the upper cloud level during the Venus Express mission. The images were processed by a digital tracking method which analyses correlations between pairs of UV images separated in time. The method allows us to track displacements of cloud features and compute wind velocities.

The set of 257 orbits for the period from May 2006 to September 2013 providing the best spatial coverage has been analyzed. Areas where the wind velocity deflects from the zonal direction were of special interest. We searched for the maximum deflection angle in each orbit using regions 2h×15° in size. Depending on the orbit, the deflection angle changes from -18.5° ± 2.4° to -0.4° ± 2.1° (the sign "-" means the poleward flow, the standard error is given). 30 orbits with the deflection angle below -13° were found. All the analyzed orbits exhibited relations between the angle value and the cloud morphology at the middle latitudes. It can be attributed to the motion of global cloud features, like the Y-feature, due to the super-rotation of the atmosphere. The position of the area where the wind velocity has maximum deflection depends on the position of a sharp streak (if present) in the image. The area can lie within the local time interval from 12:00 to 15:00 and the latitudinal range from 40˚S to 55˚S.

The maximum for averaged deflection angle was found at 14:00 local time in 50°S. In the sub-polar region the flow slightly deflects to the equator at morning hours. This deflection we attribute to activity of the polar vortex. The latitude 60°S corresponds to the lower (high-latitude) streak boundary and separates the motion in sub-polar and middle latitudes.

# THE MARTIAN GAS-ANALYTIC PACKAGE FOR THE LANDING PLATFORM EXPERIMENTS OF THE EXOMARS 2018

**M. V. Gerasimov[1], A. G. Sapgir[1], M. A. Zaitsev[1], S. A. Aseev[1], I. I. Vinogradov[1], C. Szopa[2], P. Coll[3], M. Cabane[2], D. Coscia[2], F. Goesmann[4], P. Wurz[5], D. Lasi[5], and M. Tulej[5],**
*[1]Space Research Institute of the RAS, 84/32 Profsoyuznaya, 117997, Moscow, Russia,*
*[2]LATMOS, Univ. Pierre et Marie Curie, Univ. Versailles Saint-Quentin & CNRS, 75005 Paris, France,*
*[3]LISA, Univ. Paris-Est Créteil, Univ. Denis Diderot & CNRS 94010 Créteil, France*
*[4]Max Planck Ins. for Solar System Res., Katlenburg-Lindau, Germany,*
*[5]Physikalisches Institut, University of Bern, Sidlerstrasse 5, CH-3012, Bern, Switzerland*
*Contact: mgerasim@mx.iki.rssi.ru,*

**Introduction:**

The Martian Gas-Analytic Package (MGAP) is an assemblage of instruments designed to investigate dynamics of atmospheric major and trace species and surface-atmosphere interaction. MGAP is planned to be delivered to the martian surface as a part of the Russian scientific payload on the Landing Platform of the ExoMars mission. The Landing Platform is designed to deliver the European ExoMars rover and to act as a surface station after release of the rover. The rover is focused mainly to explore the past or present habitability of Mars by exploring carbon chemistry and search for organic compounds at different geologic units and subsurface. The station has limited possibilities for life search, but is appropriate for atmosphere monitoring and investigation of surface-atmosphere interaction as well as seismology.

**Scientific Goals of the MGAP:**

The main scientific goal of the MGAP is to investigate the dynamics of atmospheric gases at the martian surface and their interaction with the soil. Experiments will include:

- measurements of diurnal and seasonal variations of water vapor and other volatiles concentration in the soil at depths accessible to the manipulator;
- measurements of diurnal and seasonal variations of major and trace components of the martian atmosphere near the surface;
- measurements of isotopic ratios of the main volatile elements: H, O, C, S, Cl, in different reservoirs;
- measurements of elemental composition and isotopic ratios of noble gases in the atmosphere;
- investigation of reactivity of martian soil.

**MGAP Instruments and Subsystems:**

MGAP consist of four main instruments and two subsystems. The instruments are the Thermal Analyzer for Mars (TAM), the Gas Chromatograph for Mars (GCM), the Neutral Gas Mass-Spectrometer (NGMS), and the Martian Tunable Diode Laser Absorption Spectrometer (MTDLAS). Subsystems are the soil sample transfer system (SSTS), the atmospheric gases sampling system (AGSS), and the enrichment trap system (ETS).

*The Thermal Analyzer for Mars (TAM) instrument.* The TAM provides thermal analysis of solid soil samples. The TAM also provides sampling of both solid soil portions and atmospheric gases. Solid soil samples are loaded into ovens for pyrolysis and thermal analysis using SSTS. TAM experiments are performed using fine-grained solid material. There are two multiuse ovens in the TAM. Targeted temperature of heating of ovens is ~1000°C. One oven is used for analysis of volatiles in the martian samples, and the second has a possibility to perform chemical reactions between martian solid samples and probing gases. Manipulator drilling and sampling system sieves fine-grain material from the drilling debris or from the regolith and delivers it to the ovens. The drilling system is aimed to drill stony objects to a depth about 10 cm. The TAM houses AGSS for sampling of atmospheric gases. It consists of a pump and a gas volume. The sampling is performed via a tube which end is located at the end of the manipulator for the possibility to sample gases at heights varying from several centimeters to about 2 m above the surface. Pumped gases can pass the enrichment trap system before analysis. The ETS produces enriched concentration of trace gas components using their accumulation on different adsorbents with a focused release for analysis.

*The Gas Chromatograph for Mars (GCM) instrument.* The GCM separates complex mixtures of gases into molecular components with their subsequent measurements with the thermal conductivity detectors and MS analysis. GC is focused on separation of permanent and noble gases using two SS capillary columns: one with molecular sieves 5A and another with PoraPlot Q. Only light organic molecules (C1 to C7) can be measured by the GCM. The GCM instrument has two injection traps (IT), the first one collects gases for analysis on the column with molecular sieves 5A and the second collects gases for analysis on the column with PoraPlot Q. The GCM has a carrier gas transfer system with heated micro valve manifolds and transfer capillaries to send gases through the MGAP. The GCM electronics controls the main chronogram sequence for the MGAP experiments.

*The Neutral Gas Mass-Spectrometer (NGMS) instrument.* The NGMS is a time-of-flight type mass spectrometer (TOF-MS) with a grid-less ion mirror (reflectron). The ions are generated from the neutral gas inside ion source by electron impact ionization. The high cadence of recorded mass spectra allows the accumulation of mass spectra with a large dynamic range of up to 106 within 1s integration time. The source of gas being either from the output of the GCM instrument (GC-mode) or directly from the martian atmosphere (atmosphere mode). The NGMS is built by the Physics Institute of the University of Bern. Measuring range of the NGMS is 1 – 1000 amu with a resolution ~1000, sensitivity for trace gas measurements – 1ppbv. The sensitivity can be increased by use of the ETS. The detection limit of the combined TAM/GCM/NGMS work exceeds the part per billion for any volatile component in the soil. The prototype of the NGMS is the same-name instrument of the Luna-Resource lander but equipped with a highvacuum turbo-molecular-pump for work in martian atmosphere.

*The Martian Tunable Diode Laser Absorption Spectrometer (MTDLAS) instrument.* The MTDLAS is an autonomous instrument to monitor water vapor and methane in the atmosphere. The MTDLAS incorporates a separate optical cell of the MGAP which can be purged by gases from the GCM via transfer capillaries. The cell has optical windows on both sides to pass a beam of four lasers through it. The MTDLAS is capable to measure D/H and $^{17}O/^{16}O$, $^{18}O/^{16}O$, $^{13}C/^{12}C$ in water and carbon dioxide molecules. The accuracy of 1.0% to measure $H_2{}^{17,18}O$ and HDO will be available at water concentration over 400 ppm in the soil.

MTDLAS can operate in the following modes of work:

- active measurements in a Herriot multi-pass optical cell, co-axially combined with an ICOS (Integrated Cavity Output Spectroscopy) cell which are directly linked to the ambient atmosphere;
- active measurements in a closed optical capillary cell, which is linked to a pyrolytic cell of the MGAP, in a similar way as it was earlier developed for the Phobos-Grunt Lander mission;
- passive heterodyne measurements at the Solar occultation free atmosphere optical path, which is codirectional with the optical path of the FAST (Fourier spectrometer for Atmospheric Species and Temperature) experiment.

**The Atmospheric Gases Analysis:**

MGAP will perform regular direct atmospheric sampling which will enable diurnal and seasonal variations measurement over the period of the two year mission. Most of the measurements will be performed using NGMS and some of them will involve GC separation for precise isotopic measurements. Specialized gas sampling experiments will be performed using enrichment traps to accumulate trace gases and to remove the major components ($CO_2$, $N_2$, Ar, etc.). Enriched trace gases can be analyzed using both GCMS and MTDLAS (water vapor). The noble gas enrichment experiment removes out chemically reactive gases to provide noble gas enriched samples for the MS for isotope and noble gas elemental ratio analysis. The gas sampling tube being mounted on the manipulator can provide sampling of gases from the close vicinity at the surface to investigate UV-induced decomposition of salts.

**Analysis of Soil Samples:** Experiments with soil samples include:

1. Measurement of volatiles composition of the soil sample
2. Probing of the soil interaction with labeled gases. In sequence 1, several

hundreds of cubic millimeters of a fine-grain soil sample are deposited into one of the ovens and heated with a programmed ramp from ambient to ~1000°C while the evolved gas continuously pass through the MTDLAS tube and is accumulated in the injection traps of the GC for later release and GCMS analysis. Small portions of the evolved gas is periodically sent into NGMS for on-line MS analysis. In sequence 2, labeled by isotopes gases are added to the sample in the oven and the sequence of analysis 1 is repeated.

# DIODE LASER SPECTROSCOPY FOR THE EXOMARS-2018 MISSION STATIONERY LANDING PLATFORM

**I. Vinogradov[1,2], A. Rodin[2,1], V. Barke[1], A. Fedorova[1], M. Gerasimov[1], N. Ignatiev[1], A. Kiselev[1], O. Korablev[1], Yu. Lebedev[1], O. Roste[1], A. Sapgir[1], A. Venkstern[1], M. Zaitsev[1],O. Benderov[2], D. Churbanov[2], I. Filatov[2], A. Klimchuk[2], V. Krasnopolsky[2],N. Pereslavtseva[2],O. Grigoryan[3], A. Kal yuzhnyi[3],A. Titov[3], A. Nadezhdinskii[4], M. Spiridonov[4], Ya. Ponurovskiy[4], G. Durry[5], L. Joly[5], J. Cousin[5], N. Amarouche[6],L. Labadie[7], M. Sornig[7], R. Thomson[8],**

*[1]Space Research Institute of the Russian Academy of Sciences (IKI RAS), 117997, 84/32 Profsoyuznaya Str., Moscow, Russia; Moscow Institute of Physics and Technology (MIPT), Institutsky Dr. 9, Dolgoprudny, Moscow Region, Russia;[3]Special Design Bureau of Space Device Engineering of IKI RAS, 249100, Tarusa, Kaluga Region, Russia;[4]Prokhorov General Physics Instituteof the Russian Academy of Sciences (GPI RAS), 119991, Vavilov Str., 38, Moscow, Russia;[5]GSMA, UMR CNRS 7331, Université de Reims, BP 1039, 51687 Reims, Cedex 2, France;[6]Division Technique de l'Institut National des Sciences de l'Univers, CNRS, 92195 MeudonCédex, France.[7]I. PhysilalishesInstitut, UniversitaetzuKolen, Koeln, Germany;[8]Scottish Universities Physics Alliance (SUPA), Institute of Photonics and Quantum Sciences, Heriot-Watt University, Edinburgh, United Kingdom.*

*Contacts: imant@iki.rssi.ru , alexander.rodin@phystech.edu*

A concept of Martian atmosphere and soil volatiles studywas developed on the basis of diode laser spectroscopy by collaborationof participants from IKI RAS, MIPT, GPI RAS, University of Reims (France), University of Cologne (Germany), and University of Edinburgh (Great Britain). An experiment, named as M-DLS, has been proposed for the stationery Landing Platform scientific payload of the ExoMars-2018mission.

The M-DLS instrument is targeted for long-term studies of:

- chemical and isotopic composition of atmosphere near the Martian surface, and its diurnal and seasonal variations,
- chemical and isotopic composition of Martian soil volatiles at the location of the Landing Platform, and its diurnal and seasonal variations,
- integral chemical and isotopic composition of Martian atmosphere at low scales of altitude at the Landing Platform location area, and its variations in respect to local time at the light time of a day,
- thermal and dynamic structure of the Martian atmosphere at low scales of altitude at the Landing Platform location, and its variations in local time at the day-light time.

The M-DLS studies are based on of regular periodic measurements of molecular absorption spectra in the Infra-Red range along several optical path trajectories, including:

- a suite of several ICOS optical cells of up to ~1 km effective optical path, which are directly linked to the ambient atmosphere,
- closed-volume optical capillary cell, which is linked to a pyrolytic cell of a proposed MGAS instrument (Martian Gas Analytic Suite), in a similar way as it was earlier done for the Phobos-Grunt expected Lander mission,
- direct Solar observationopen atmosphere path of passive heterodyne measurements, co-directional with the open optical line of sight of a proposed FAST instrument (Fourier spectrometer for Atmospheric Components and Temperature).

The M-DLS measurements will take place in series of narrow-band intervals of 2 $cm^{-1}$ wide, with spectral resolution of ~3 MHz (~0.0001 $cm^{-1}$), providing for detailed recording of absorption line contours. By measurement of diurnal and seasonal variations of $H_2O$ and $CO_2$ main molecules and their isotope ratios D/H, $^{18}O/^{17}O/^{16}O$,$^{13}C/^{12}C$, of soil volatiles $H_2S$, $NH_3$, $C_2H_2$ and others,we expect to get data forspecifying of physical and chemical interactions between surface and atmosphere of Mars. Datarelated to seasonal variations of $H_2O$ and $CO_2$ molecular concentration vertical profiles, as well as other atmospheric parameters, will be obtained by detailed recording of molecular absorption line form factors during one Martian year. Continuous measurements near the surface and in the atmospheric column at the fixed point of landing will provide for contribution into the campaign of methane search in the Martian atmosphere.

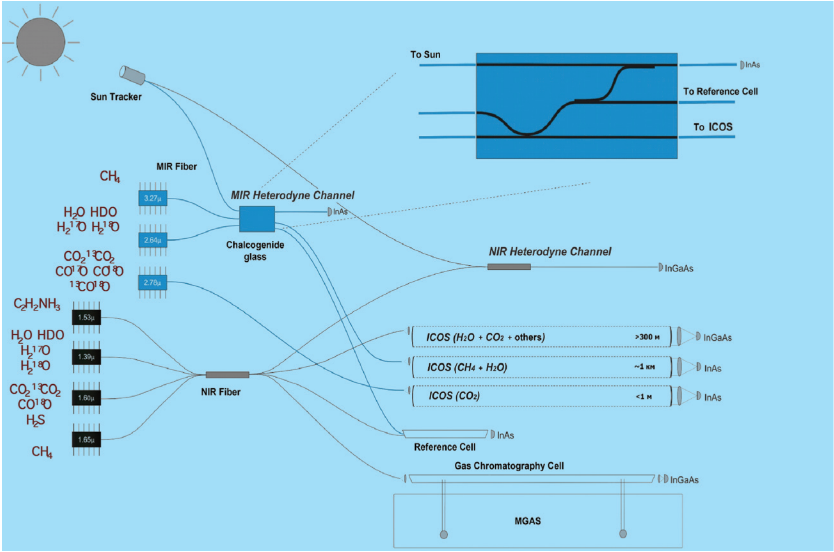


Basic optical layout of the proposed M-DLS instrument is shown in the context figure. Butterfly packaged single mode (SM) optical fiber pigtailed DFB-laser modules are schematically shown for the near-IR region around 1.5 microns (in grey) and for the medium-IR region around 3 microns (in blue). A bundle of SM optical fibers and directional couplers efficiently distributes monochromatic laser output across analytical and reference optical channels,providing for versatility of the M-DLS instrument parts use. Direct Solar observation through the total Martian atmosphere depth, and radically enhanced effective optical path for the ambient atmosphere, sampled inside the ICOS cells, provide for an outstanding optical accumulation of the absorption signal, and high resulting sensitivity of the M-DLS instrument for all the considered molecular targets and isotopic ratios.

The M-DLS experiment basics, M-DLS instrument realization issues, forthcoming M-DLS team activity planning, and other moments of the mission are discussed in the report.


I. Vinogradov, A. Rodin,A. Klimchuk,M-DLS team, M-DLS - a multichannel diode laser spectrometer for Martian studies. 40th COSPAR Scientic Assembly, report #B0.2-0038-14 STW-L-118, M. V. Lomonosov Moscow State University, Moscow, Russia, 2-10 August2014.
http://smiswww.iki.rssi.ru/d33_conf/thesisshow.aspx?page=78&thesis=4157

I. Vinogradov, A. Rodin, O. Korablev, V. Barke, A. Klimchuk, M. Gerasimov, N. Ignatiev, A. Fedorova, A. Stepanov, I. Filatov, A. Titov, A. Venkstern, M. Barke, A. Sapgir, M. Zaitsev, O. Roste, Yu. Lebedev, A. Kalyuzhnyi, O. Grigoryan, A. Nadezhdinskii, M. Spiridonov,.Ya. Ponurovskiy, G. Durry, L. Joly, J. Cousin, N. Amarouche, Diode Laser Spectroscopy for Martian studies, The Fourth Moscow Solar System Symposium, Space Research Institute, Moscow, Russia, 14-18 October 2013.
http://ms2013.cosmos.ru/sites/ms2013.cosmos.ru/files/4m-s3_program-10-07.pdf

# PROPOSAL OF THE DUST COMPLEX ONBOARD THE EXOMARS-2018 LANDER

**A. Zakharov[1], I. Kuznetsov[1], G. Dolnikov[1], A. Lyash[1], V. Afonin[1], F. Esposito[2], E. Seran[3], M. Horaniy[4], M. Koepke[5], V. Gotlib[1]**
*[1]Space Research Institute (IKI), Russian Academy of Sciences, Moscow, Russia, kia@iki.rssi.ru*
*[2]INAF - Osservatorio Astronomico di Capodimonte, NAPLES, Italy*
*[3]Laboratoire Atmospheres, Milieux, Observations Spatiales, Paris, France*
*[4]University of Colorado, Boulder, Colorado, United States*
*[5]West Virginia Univeristy, Morgantown, West Virginia, United States*

The load of suspended dust in the Martian atmosphere varies dramatically but never drops entirely to zero. Effects of airborne dust contribute to the dynamic and thermodynamic evolution of the atmosphere and its large-scale circulation processes on diurnal, seasonal and annual timescales. Suspended dust plays a key role in determining the present climate of Mars and probably influenced the past climatic conditions and surface evolution. Atmosphere dust and wind-blown dust are responsible for erosion, redistribution of dust on the surface, and surface weathering.

The mechanisms for dust entrainment in the atmosphere are not completely understood, as the current data available so far do not allow us to identify the efficiency of the various processes. Dust-grain transport on the surface of Mars has never been directly measured despite great interest in and high scientific and technological ramifications of the associated phenomena. This paper describes planned, future investigations of the Martian dust environment made possible by the proposed scientific payload \Dust Complex" (DC) of the ExoMars-2018 mission's landing platform.

DC is a suite of four sensors devoted to the study of Aeolian processes on Mars with a primary aim of monitoring the diurnal, seasonal, and annual dust-environment cycles by Martian-ground-based measurements of dust flux in situ, i.e., in the near-surface atmosphere of Mars.

This suite includes:

1) an Impact Sensor, for the measurement of the sand-grain dynamics and electrostatics,
2) a particle-counter sensor, MicroMED, for the measurement of airborne dust size distribution and number density,
3) an Electric Probe, for the measurement of the ambient electric field,
4) a radiofrequency antenna.

Besides outlining design details of DC and the characterization of its capabilities, this presentation reviews various dust effects and dust phenomena that are anticipated to occur in the near-surface environment on Mars and that are possible to observe with DC. The negative consequences of these effects and phenomena may limit the ExoMars-2018 mission and future human development of Mars. Mechanisms

associated with the influence of dust in atmosphere processes are discussed. Scientific outcomes of DC have future meteorological and environmental applications on Mars, for example, for the study of the evolution dynamics of the atmospheric aerosols and near-ground stratification. The primary objective of DC is to provide direct measurements of atmosphere aerosols parameters not attainable by other techniques. The following goals have secondary priority:

- Measurement of the daily and seasonally variability and dynamic of the atmosphere dust;
- Detection of the windblown particles and their parameters such as mass distribution and possible charge appearance;
- Measurement of the electrostatic field, electric conductivity of the Martian Detection of micro discharges and electric perturbations in the radiofrequency range.

# SEISMIC AND GRAVITY MEASUREMENTS ON MARS WITHIN THE "EXOMARS"

**A.B.Manukin, O.N. Andreev, A.V. Kalyuzhni**

Seismic and gravity measurements on Mars within the "Exo-Mars" will provide information about the internal structure of the planet, its level of seismicity, about tidal effects

The main difficulty — wind effects that almost was not allowed to obtain reliable seismic recording apparatus Viking. We discuss the possibility of obtaining records using two identical devices. One is mounted on RTD lander and the other — on the surface of Mars. To ensure contact with the ground the second unit is pressed him a ladder to exit the rover. The information from the first device on the machine will be used to account for the effects of wind loads on the lander in the processing of readings mounted on the surface.

A new option to create a vertical channel seysmogravimetra feedback using magnetic suspension. Applied design, provides a system with a dedicated axis sensitivity. Conducted to evaluate the ultimate sensitivity of such a system. It is shown that it is ~ 10-9 m / s 2. A new scheme for constructing seismic gravimeter, including three single-axis sensing elements mounted at the same angle relative to the longitudinal axis of the instrument. This scheme does not require a system of putting the device on the local gravitational vertical

# MASS-SPECTROMETRIC METHOD FOR UNVEILING SIGNS OF LIFE VIA ANALYSIS OF THE ELEMENTAL COMPOSITION OF THE SUPPOSED BIOMASS EXTRACTED FROM REGOLITH OF MARS

**Luchnikov K.A., Managadze G.G., Vorobyova E.A., Chumikov A.E., Safronova A.A. Managadze N.G., Bondarenko A.L., Saralidze G. Z., Kusnetsov A.I.**
*Space Research Institute of the Russian Academy of Sciences, str. Profsoyuznaya 84/32, GSP-7, Moscow 117997, Russia.*
*Contact: luchnikov@iki.rssi.ru*

**Introduction:**

New results on the development of the technique of revealing extraterrestrial microorganisms are presented. The technique is based on the measurement of elemental composition of the sample and the choice of certain chemical elements as biomarkers.

The instrument and technique proposed can be used to analyze the element composition of the supposed extraterrestrial biomass and compare it to the element composition of terrestrial microorganisms. Biomass is to be identified by a number of criteria: the presence and abundance ratio of matrix biogenic elements – H, C, N, O; abundance ratios of biogenic markers like P/S, K/Ca, the presence of other biologically important elements (e.g., Cl) and microelements, such as Mg, Fe, Cu, Zn, and F.

The element composition of the sample studied is to be performed using the onboard LASMA time-of-flight laser mass-reflectron similar to the instrument developed for the «Phobos-Grunt» mission however after significant improvement. The system of sample preparation is based on the separation of the microorganisms from regolith. After extraction of microorganisms with water the solution obtained must be desalted. Sample for investigation is produced by drying the solution on the holder being the target for laser ablation.

The results of measurements performed on microorganisms and soil samples confirm the applicability of this solution. Various methods of extracting the biomass from different space bodies are discussed.

Experimental result has shown that previously chosen biomarkers - P/S and K/Ca ratios do not provide high authenticity of biomass detection. These ratios for some soils and rocks were shown to be close to biological area and can be falsely attributed to biomass. In order to increase reliability of identification, it was decided to use another criterion - the content of nitrogen and carbon. Points corresponding to the microorganisms and soils or rocks are spread from each other on the N-C graph (Fig. 1) forming distinct areas thus increasing reliability of the technique.

The method can be used to search for and identify biomass in different samples including ice retrieved from the subsurface layer of Solar-System planets or satellites, e.g., Europa or Enceladus.

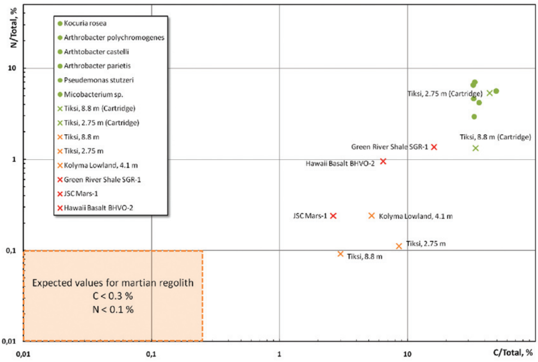


**Fig. 1.** Measured abundances of carbon and nitrogen in samples of soils and microorganisms.

# CHARACTERIZATION OF ION FORMATION CONDITIONS IN LA TOF MS BY VIRTUE OF INDIRECT MCP DETECTOR ILLUMINATION

**Luchnikov K.A., Managadze G.G., Chumikov A.E.**
*Space Research Institute of the Russian Academy of Sciences, str. Profsoyuznaya 84/32, GSP-7, Moscow 117997, Russia.*
*Contact: luchnikov@iki.rssi.ru*

**Introduction:**

Characterization of ion formation conditions in laser ablation time-of-flight mass spectrometers (LA TOF-MS) is crucial for precise spectra interpretation. These conditions strongly influence relative sensitivity coefficients (RSC) of the instrument.

A signal originating from indirect illumination of microchannel plate detector is observed during the operation of LA TOF-MS. This illumination originate from optical emission of laser plume itself formed above the target under investigation and indicates the properties of plasma that generates ions for further time-of-flight separation.

We suppose this signal can provide substantial data for diagnostics of the laser plume itself complementing information from integrated solutions like laser pulse energy measurement module. Thus it can increase the accuracy of determining RSC for each spectrum.

# CORRELATED STUDY OF PARTICLES RETURNED BY THE HAYABUSA SPACE PROBE FROM THE 25143 ITOKAWA ASTEROID BY SRXTM, NG-MS, IR AND RAMAN MICROSCOPY

**S. G. Pavlov[1], C. Alwmark[2], S. Bajt[3], U. Böttger[1], H. Busemann[4], W. Fujiya[5], J. D. Gilmour[4], U. Heitmann[6], P. Hoppe [5], H.-W. Hübers[1,7], F. Marone[8], M. M. M. Meier[2], U. Ott[5], U. Schade[9], N. H. Spring[4], M. Stampanoni[8,10], I. Weber[6],**
*[1] Institute of Planetary Research, German Aerospace Center (DLR), Rutherfordstr. 2, 12489 Berlin, Germany;*
*[2] Department of Geology, University of Lund, Sölvegatan 12, 223 62 Lund, Sweden;*
*[3] Photon Sciences, DESY, Notkestr. 85, 22607 Hamburg, Germany;*
*[4] University of Manchester, School of Earth, Atmospheric and Environmental Sciences (SEAES), Oxford Road, Manchester M13 9PL, UK;*
*[5] Max-Planck-InstitutfürChemie, Hahn-Meitner-Weg 1, 55128 Mainz, Germany;*
*[6] InstitutfürPlanetologie, WestfälischeWilhelms-UniversitätMünster, Wilhelm-Klemm-Str. 10, 48149Münster, Germany;*
*[7]Institutfür Optikund Atomare Physik, Technische Universität Berlin, Straße des 17. Juni 135, 10623 Berlin, Germany;*
*[8] Swiss Light Source, Paul Scherrer Institut, 5232 Villigen PSI, Switzerland;*
*[9] Helmholtz-Zentrum Berlin für Materialien und Energie, Albert-Einstein-Str. 15, 12489 Berlin, Germany;*
*[10]Institute for Biomedical Engineering, ETH Zurich and the University of Zurich, Gloriastr. 35, 8092 Zurich, Switzerland.*
*Contact: sergeij.pavlov@dlr.de*

A correlated study with Raman micro- and infraredspectroscopy, noble gas mass spectroscopy (NG-MS) and Synchrotron Radiation X-ray Tomographic Microscopy (SRXTM) has been implemented for the determination of cosmic-ray exposure (CRE) ages and trapped Xe content in a few particles returned by the JAXA's Hayabusa space probe from the near-Earth asteroid 25143 Itokawa, the first successful sample return mission to an asteroid [1]. We analysedsix olivine-rich particles allocated for the study by JAXA [2]. The CRE age gives information about asteroid dynamics as well as surface processes. Raman (DLR Berlin, Germany) and SRXTM (TOMCAT beamline of the Swiss Light Source at PSI Switzerland) microscopy revealed mineral composition, particle volume, and the density distribution of the material. The helium and neon analysis was done on the compressor-source noble gas mass spectrometer at ETH Zurich. The correlated study by Raman spectroscopy and X-ray tomography allows reconstruction of spatially resolved mineral topographic images of individual particles (Fig. 1), including mineral orientation. The particles have volumes between 17800±900 µm$^3$ (RA-QD02-0187, #0187) and 442700±5900 µm$^3$ (#0049-1) [3]. Theforsteritecontent (#Mg) as determined by Raman spectroscopy is between 58±10 (#0049-1) and 72±8 (#0158), compatible with LL chondrite chemistry within errors [4]. A CRE age of 1.5±0.4 Ma, calculated from cosmogenic He and Ne, for the surface of Itokawa is very short compared to the CRE ages of most LL chrondrites, which are typically 5-50 Ma [5].

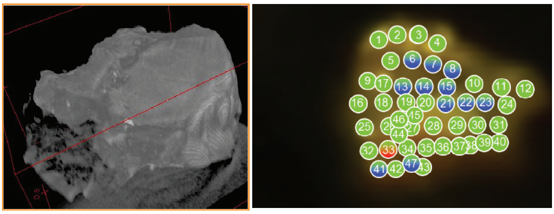

**Fig. 1.** Left: SRXTM image of the sample # RA-QD02-0197 showing the different density distribution; right: localization of Raman spectra, showing different mineral phases in the particle.

[1] T. Nakamura et al., Science 333, 1113-1116 (2011).
[2] H. Busemann et al., LPSC XLIV, Abstract #2243 (2013).
[3] M. M. M. Meier et al., LPSC XLV, Abstract #1247 (2014).
[4] U. Böttger et al., LPSC XLV, Abstract #1411 (2014).
[5] K. Marti and T. Graf, Ann. Rev. Earth Planet. Sci. 20, 221-243 (1992).

# SELF-DESTRUCTING SMALL COSMIC BODIES: CHURYUMOV-GERASIMENKO COMET AND SOME EARLIER EXAMPLES

**G.G. Kochemasov;**
*IGEM of the Russian Academy of Sciences, 119017 Moscow, 35 Staromonetny ,*
*kochem.36@mail.ru*

The classical planetology considers impacts as a main source of energy reworking celestial bodies. However a region or regions of impacting objects affecting all planetary bodies everywhere in the Solar system is poorly understood. But now planetologists have several tens of images of full discs of these bodies. Distribution patterns of “impact traces” – craters in many of them are surprisingly regular. They show alignments, regular grids not related to random hits expected from impacts but rather require more regular and ubiquitous structuring force. Moreover, such regular patterns appear in the outer gaseous spheres of some bodies including the Sun’s photosphere.

t was shown earlier [1-3] that such regular patterns appear due to warping action of inertia-gravity waves affecting all bodies moving in keplerian elliptical orbits. Periodically changing accelerations of celestial bodies cause their wave warping having in rotating bodies (but all bodies rotate!) four ortho- and diagonal directions. An interference of 4 directions of standing waves brings about a regular net of uprising, subsiding and neutral tectonic blocks. Naturally polygonal in details they appear as rings in cosmic images (Fig. 4). This is one of reasons why they are often confused with round impact craters and essentially disfigure their statistics. Figures 1-3 show the Rosetta ‘s images of the Churyumov-Gerasimenko comet core.

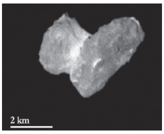


1

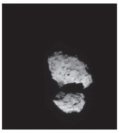

2

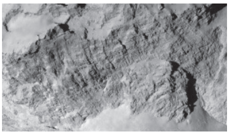

3

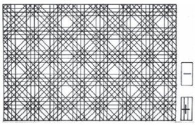

4

**Fig. 1.** Churyumov-Gerasimenko comet.  comet29July2014fromRosetta.jpg
**Fig. 2.** Comet_on_10_August_2014_NavCam_node_full_image_2.jpg
**Fig. 3.** Churyumov-Gerasimenko comet. A portion of “Comet_on_7_August_b_node_full_image_2.jpg”.
**Fig. 4.** Scheme of interference of 4 direction waves. Ring structures appear on scheme and in Fig. 3.

A fundamental nature of the wave woven nets of evenly sized round “craters” (granules) is dependence of their sizes on orbital frequencies of bodies [1-3]. The lower frequency the larger sizes, the higher frequency the smaller granule sizes.  The correspondence between orbital frequencies and tectonic granulations proving the structuring role of the orbital energy was earlier noted in comparative planetology of the terrestrial planets. The row of Mercury, Venus, Earth, Mars, asteroids (Fig. 5) with decreasing orbital frequencies is remarkable by increasing relative sizes of tectonic granules, relief ranges, iron content in lowland basalts and decreasing atmospheric masses from Venus to Mars.

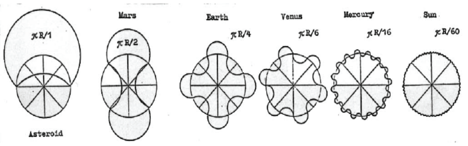


5

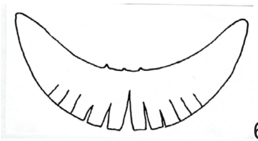

6

**Fig. 5.** Geometric presentation of warping waves in the planetary system.
**Fig. 6.** Geometrical model of convexo-concave oblong shape of a small celestial body caused by the wave1 warping. Deep cracks of the convex hemisphere and the concave hemisphere cause development of a “waist” or ‘neck” and finally lead to a body breakage

In this spectacular row the position of asteroids is especially remarkable. The strongest amplitude fundamental wave1 embraces an asteroid body making it strongly bent. Its extended convex hemisphere is deeply cracked and the concave one from the opposite site approaches the deepest fissures (Fig. 6, 9). As a result the body disintegrates and two or several pieces move as binaries, polycomponent asteroids, asteroids with satellites (Fig. 10-12). Dumb-bells shapes often are observed. Examples of various stages of destruction are asteroids Eros, Toutatis, Braille, Castalia, Hector, and recently observed P/2013R3 that shows enormous volumes of gas-dust clouds accompanying the process (Fig. 12). The orbiting clouds in the past may have been a media for gravity separation of M-, S-, and C-asteroids. Various stages of the destruction are in Fig. 1, 2, 7-12.

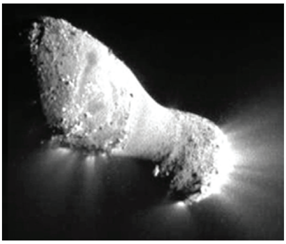
7

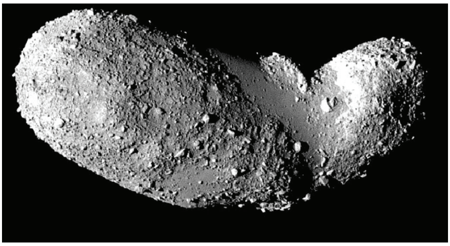
8

**Fig. 7.** 103P/ Hartley, 2, 2 km long, Comet 103P/Hartley exhibits the concave side (up), destroyed convex side (down) and “waist”. Credit: NASA/JPL-Caltech/UMD.
**Fig. 8.** Apollo asteroid 25143 Itokawa. 535 x 294 x 209 m. Itokawa07 Hayabusa. Jpg.

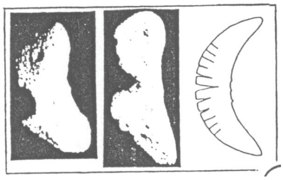
9

.10


11

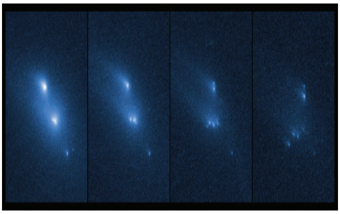
12

**Fig. 9.** Asteroid Eros, 33 km long, and a scheme of process of its destruction
**Fig. 10.** Asteroid 9969 Braille (“Deep space 1” mission), 2.2 km long, Pia01345.gif.
**Fig. 11.** Asteroid 4769 Castalia (Radar observations, S.J. Ostro, J.F. Chandler, 1990), 1.8 km long.
**Fig. 12.**.Hubble witnesses an asteroid mysteriously disintegrating (heic 1495-Science release, 6 March 2014). Asteroid P/2013R3. Ten fragments; the four largest rocky fragments are up to 200 m in radius. Credit: NASA, ESA, and D. Jewitt (UCLA).

**References:**

**[1]** Kochemasov G.G. (1992) Concerted wave supergranulation of the solar system bodies // 16th Russian-American microsymposium on planetology, Abstracts, Moscow, Vernadsky Inst. (GEOKHI), 36-37.
**[2]** Kochemasov G.G. (1998) Tectonic dichotomy, sectoring and granulation of Earth and other celestial bodies // Proceedings of the International Symposium on New Concepts in Global Tectonics, “NCGT-98 TSUKUBA”, Geological Survey of Japan, Tsukuba, Nov 20-23, p. 144-147.
**[3]** Kochemasov G.G. (1999) Theorems of wave planetary tectonics // Geophys. Res. Abstr., V.1, №3, p.700.

# COMET CHURYUMOVA-GERASIMENKO IS NOT ICE

**O. S. Potashko**
*Scientific Training Center of Applied Informatics NASU,prospect Glushkova 40, Ukraine.*
*Contact: tumburland@gmail.com*

First obtained data near 67P demonstrates that comet is not icy in fact. “the Alice team discovered that the comet is unusually dark in the ultraviolet and that the comet’s surface – so far – shows no large water-ice patches. Alice is also already detecting both hydrogen and oxygen in the comet’s coma, or atmosphere.” The VIRTIS team “see some strong hints of carbon-bearing compounds”. What is the comet like – it looks like a volcano – produces water, gases, dust but isn’t ice itself. 67p/C-G has many features common with underwater volcanoes – chimney, carbon-bearing walls. So one may wait to find life-components structures.

# FTES IN THE MERCURY MAGNETOSPHERE: DEPENDENCE ON IMF

**E. S. Belenkaya[1], I. I. Alexeev[1],**
*[1]Skobeltsyn Institute of Nuclear Physics Lomonosov Moscow State University (SINP MSU), 1(2), Leninskie gory, GSP-1, Moscow 119991, Russian Federation*
*Contact: elena@dec1.sinp.msu.ru*

**Introduction:**

IMF plays significant role for Mercury, as this planet is located close to the Sun and obtains a week own magnetic field. At the Mercury orbit the radial IMF component dominates. The topology of Mercury magnetosphere for strong radial IMF leads to formation of a quasi-neutral line in one of the cusps and neutral point of magnetic field in the other. FTEs generation may be associated with this quasi-neutral line. Thus, depending on the sign of  radial IMF component, FTEs may be connected with one or the other cusp. This result was supported by MESSENGER observations.

# SOME PRINCIPLES OF CREATING ASTROMETRIC OBSERVATORY ON THE MOON TERRITORY

**M.I. Shpekin**
*Kazan Federal University, Russia, Kazan, Kremlevskaya str. 18,*
*Contact: MichaelS1@yandex.ru*

**Introduction.** The creation of astrometric observatory on the Moon territory discusses. We consider some of the scientific objectives of applied and fundamental nature which are available for such an observatory. The observation program includes such tasks as selenodesy (determination of the parameters of physical libration and coordinates of the mass center), fundamental astrometry (accurate determination of the relative positions of stars ecliptic belt), the theory of relativity (gravitational deflection of light in the field of the Sun), as well as high-precision measurements of light diffraction on the lunar horizon. The issues of site selection for the observatory, the technical aspects of the astrometric observation method.

**On the choice of location.** As is well known the analysis of astroclimatic conditions in the preparation site for Earth-based observatories plays important role. If we talk about the moon astroclimate, the situation is considerably different from the Earth-based observatories. Firstly, there is no need to have an observatory in the mountains. Moreover, the position of the observatory in low-lying areas may be preferable embodiment of the mountain. In this case, the location is easier to protect against external influences by the comet and asteroid impacts, as well as from the sun and cosmic radiation. Secondly, do not have to worry about the transparency of the atmosphere and image stability. This factor may need to put in the first place, because the nature of extra-atmospheric images just brings major benefits of the observatory on the lunar surface. The third factor that seems to be the place to put selenographic position observations. Given the nature of the regime, in which resides the Moon orbits the Earth, there are several options. It is a choice between the visible, the reverse side as well as the Marginal Zone. It is a choice between the sea and the mainland part of the surface. The choice between the lunar poles. Here, apparently crucial belongs range of problems which observatory destination.

The connectivity with Earth is important when choosing a place. The observatory control, of course, easier to organize when it is located in the zone of direct visibility from Earth. That is, either on the visible side, or in the Marginal Zone. Observatory on the far side will require additional management costs and the transfer of results to Earth. However, in the presence of the space station at the Lagrange point L2, the draft of which has recently appeared in Internet, and this problem will be overcome. From the point of view of availability of celestial bodies on the lunar sky version with the reverse side is not the best, as in this case, the Earth is not visible and cannot be turned it into the measurements.

An important requirement for the choice of the place is illumination from the Sun because the main source is likely to be solar panels.

With the goal of long-term astrometric observations, the requirements for the stability of the observatory base should be increased. The problem of the stability of the base is dictated by the presence of meteorite bombardment, emissions of boulders, moonquakes, diurnal temperature difference, tectonic faults, the aftereffects of young impact craters, glacial-like movements of the rocks, the influence of cosmic radiation and so forth.

Separately it is necessary to analyze the presence and dynamics of the lunar dust. New studies graduate from the United States, who drew attention to the unusual properties of the dust particles and their motion, force to take these factors seriously.

**Objectives and methods of observation.** Do observer of Moon-based observatory there are quite a few temptations to implement these or other astrometric observations. After many years of experience of Earth-based observations — especially. For example, the lack of atmosphere offers a great opportunity to observe near the Sun, and near the lunar horizon.

Measuring the exact positions of stars near the Sun will allow directly determine the gravitational light deflection. There is no need to measure when the Sun is above the horizon, but rather wait for him sunset or use the “window” before sunrise.

Observations near the visible lunar horizon, which for obvious reasons are "not interested" in the case of Earth-based observatories, may be of practical interest for Moon-based observatory. Registration of the process of the star approaching to the lunar horizon, made with sufficient time resolution, opens the possibility of measuring the Fresnel diffraction for a large number of stars. Geometrical and physical foundations of these measurements in many ways similar to the Earth-based observations of star occultations by the Moon, which are used to evaluate the angular diameters of stars. In contrast to the Earth-based occultation method, the velocity of the moon's shadow across the aperture of the telescope to an observer on the Moon is much smaller. This is due to the fact that on the Moon this rate is "free" from the component caused by the motion of terrestrial observer. The truth and the size of the first Fresnel zone becomes less, as an opaque screen (lunar horizon) becomes closest to the telescope. In this scheme of the measurement the choose a place for the observatory becomes important, which would be best suited to the task. It would be possible to use the visible horizon formed, for example, by the crest of the crater wall of a sufficiently large crater, placing itself observatory near the center of the crater. They would then be measured as well setting as rising stars.

If you pick a place with a good visible lunar horizon in the Marginal Zone of the Moon, the composition will include observations of the Earth. Measuring the image of the Earth on the background stars will clarify the orientation of the lunar coordinate system relative to the inertial coordinate system, which is an important result for spacecraft navigation in the near-moon space.

Conclusion. The report covers only certain aspects of the lunar astrometric observatory.

Outside abstract are such important issues as the problem of ephemeris support observational programs and maintain the health conditions of the lunar observatory in climate, numerical estimates of the expected performance of the astrometric observatory, as well as a priori estimates of the accuracy of the physical parameters derived from observations, storage and transmission of measurements to the Earth, development of the light receiving devices, etc...

Detailed study of the task of creating an observatory on the Moon requires the participation of experts in various fields. Submitted proposals are merely an invitation to discuss the problem.

# TWO GAMMA – RAY RADIATION SOURCES: ELEMENTS SYNCHRONIZING, SOLAR PERIODICITY

**Khavroshkin O.B., Tsyplakov V.V.**
*Institute of Physics of the Earth. RAS*
*Contact: khavole@ifz.ru*

**Introduction.** There were before discovered few peculiarity interaction between radioactive nucleus and solar neutrino stream. For example: the spectrum of temporal variations in the activity of the sample radioactive ore contains peaks which coinciding with the period of natural oscillations of the Sun. The capture cross section of the radioactive heavy deformed nucleus in time decay increases by in many orders and is able to interact with the stream of solar neutrinos which are modulated by own oscillations of the Sun. The picks of spectrum of long-period oscillations of the Earth exceeding its own and contains peaks that match the value with an accuracy of 1-3% with peaks of its own oscillations of the Sun. The mechanism of excitation of these oscillations is similar to the nature of variations in the activity of a radioactive sample of ore. These effects are included in the mechanisms of interaction of the Earth - the Sun systems and the impact on seismicity; search problem of existing natural nuclear reactor inside Earth core.

In continuation of these studies conducted synchronous recording gamma variations isotope cesium Cs137 and uranium ore. Isotope Cs137 beta - radioactive but the resulting barium Ba 137 gives gamma radiation in a narrow energy band Cs137 at 661 keV. Uranium ore which was in a closed metal container highlights the various radioactive isotopes including radium, radon and its decay isotopes, which are in equilibrium. Synchronous recording of $\gamma$- variations activities Cs137 and cesium ore Ur carried radiation detectors that were created on the basis of Geiger type detector. This resulted in the implementation of the two synchronous variations entries $\gamma$ radioactivity of cesium ore and lasting more than 13 days. Research of the results of that recording is given next: mmaximum of cross-correlation function is shifted by 28 minutes; correlation between the variations of $\gamma$ radioactivity Cs137 and uranium ore with probability P> 0.99 exists, there is and can be represented as an element of synchronicity analyzed processes; on the level of radioactive cesium and uranium ore is an external influence. To identify the source of external influence on the observed realization of the studied $\gamma$ radioactive cesium and uranium ores and their cross-correlation (FCC) were identified by their energy spectra. Found by the observed spectral peaks coincide with the theoretical solar data to 3 inclusive sign. Thus, we can assume that the main agent, affecting Cs137 and uranium ore $\gamma$ radioactivity is the sun, which is consistent with previous results.

# MENTAL HEALTH CARE CONSIDERATIONS FOR LONG TERM SPACE MISSIONS

**R. R. Chau, A. A. Mardon,**
*[1]The Antarctic Institute of Canada, 11919-82 Street NW, Edmonton, Alberta, Canada;*
*[2]The Antarctic Institute of Canada, 11919-82 Street NW, Edmonton, Alberta, Canada*
*Contact: aamardon@yahoo.ca*

**Introduction:**

Mental health care currently uses vast amounts of resources and despite being more technologically advanced than our counterparts centuries or even decades ago, we still do not have a very solid grasp on ways to take care of those with mental health illnesses. Thus when going on long term space missions, mental health care should be considered and proper precautions should be taken to take care of those who suddenly may acquire these problems. This is particularly since that said individual or individuals become a liability and there is no other organization that they can be handed to and be dealt with like that on earth. It's not uncommon for the human mind to break when put under strenuous activity as this is particularly evident when exposed to extreme events or placed into uncomfortable situations and going into space is no exception. Proper accommodation should be brought such as proper restraints for those who suffer from psychotic episodes or proper medication should be brought in the event that such a disorder could be treated and suppressed. Unfortunately other measures may have to be considered if it so jeopardizes the mission. This is particularly important since, as mentioned before, the affected members become a liability to all others.

# THE CONTENT OF HELIUM AND MOLECULAR HYDROGEN IN ACCRETION ICE OF THE SUBGLACIAL LAKE VOSTOK, EAST ANTARCTICA

**Yu.O. Chetverikov[1], V.F. Ezhov[1], V.A. Solovei[1], V.Ya. Lipenkov[2], N.N. Aruev[3], I.L. Fedichkin[3], R.V. Tyukaltcev[3], S.N. Klyamkin[4], S.A. Bulat[1]**
*[1]PNPI, NRC "Kurchatov Institute", St. Petersburg-Gatchina,Russia;*
*[2]AARI, St. Petersburg, Russia;*
*[3]IPTI, St. Petersburg, Russia;*
*[4]MSU, Moscow, Russia.*
*Contact: yurka@lns.pnpi.spb.ru*

The content of light gases helium and molecular hydrogen dissolved in the matrix of the accretion type 2 ice cores extracted from the deep borehole 5G-3 at the Russian station Vostok, East Antarctica was investigated. The ice cores under studies were obtained from the depth range 3596-3699 meters. The gases were collected into special vacuum glass containers during 3-day degassing by diffusion at minus temperature of ice cores just recovered from a borehole. During this time period most of the helium and hydrogen was released from ice core into the sample container. To reduce the pressure of background gases the container with a core was sealed and evacuated before to allow gases to diffuse. The analysis of gas samples was carried out by TOF mass spectrometry 6 months later at laboratory conditions.

As a result, the detected concentration of hydrogen in accretion ice type 2 averaged 3 μM per liter of ice, while helium concentration was about 0.53 μM/l. These values are by several orders higher than the equilibrium concentration of helium and hydrogen in meteoric ice (for helium - 0.01-0.02 μM/l, hydrogen-0.001-0.002 μM/l). However, in the previous studies of helium content in accretion ice from similar depth range (3530-3610 meters) the measured total helium concentrations were much less (0.01-0.04 μM/l) [1] than in current work. This discrepancy is now under discussion.

Thus, the data obtained could testify for a kind of hydrothermal activity in the subglacial Lake Vostok earlier predicted from biology data [2]. To clarify this issue the helium isotope studies are ongoing.

[1] Philippe Jean-Baptiste et. al, Nature, **411**, 460-462 (2001)
[2] S.O.Bulat et.al, International Journal of Astrobiology, **3**, 1, p 1-12 (2004)

# ICE/ROCK RATIO IN GANYMEDE AND TITAN IN THE CONTEXT OF THEIR INTERNAL STRUCTURE, ORIGIN AND EVOLUTION

**A. N. Dunaeva, V. Kronrod, O. Kuskov**
*Vernadsky Institute of Geochemistry and Analytical Chemistry, Russian Academy of Sciences, Kosygin Str., 19, 119991 Moscow, Russia, Contact: dunaeva@kmail.ru*

**Introduction:**

In this paper the values of $H_2O$ (water, ice)/rock ratio in the large icy moons of Jupiter and Saturn have been examined. The models of internal structure of the largest icy satellites, Ganymede and Titan, were considered in details. It has been shown that the model of fully differentiated Ganymede, as well as the model of partially differentiated Titan (Titan with rock-ice mantle), are in a good agreement with available theories of the satellites' formation and evolution in Jupiter and Saturn accretion discs. These models provide the ice/rock ratio in the satellites close to 1, whereas a model of Titan with hydrated (serpentine) mantle (fully differentiated Titan) gives the lower ice/rock ratio equal to 0.5-0.6.

**Problem's description and results:**

In general case the satellites Ganymede and Titan are described by three-layer models including: 1) the outermost water-ice shell (high pressure ices ± water internal ocean with any salt composition), 2) the central rock-iron or Fe-FeS core and 3) intermediate mantle [1-5]. Depending on a chosen satellite and corresponding model the mantle is assumed to be composed of either anhydrous [1-3] or hydrous silicates (serpentine, antigorite) [4], or ice-rock homogeneous mixture [5]. Models of the satellites, reviewed in this paper, were based on the previously developed approaches [1-2, 5] and continue them. In these models we additionally estimated the heterogeneity of the satellites' interiors which can be due to a change of phase composition within a local structural layer or owing the substance's density change with depth. To do this, the special subroutine which includes equations of state of all $H_2O$ phases, silicate and hydrous silicate minerals, and also the special procedure describes the convective regime in mantle's reservoir were developed. This allowed us to calculate more detailed the density of the satellite's substance in changing P-T conditions, to improve the boundaries between the structural zones, and also to estimate the $H_2O$ content in the water-ice-containing interiors of satellites.

*Internal structure of Ganymede*

Based on a large number of theoretical works, Ganymede can be considered as a completely differentiated satellite, in which the outer water-ice shell with an internal ocean, silicate mantle and the central Fe-FeS core were fully separated [1-2, 6]. Using revised data on the physical characteristics of Ganymede (R=2631.2 km, $\rho$ = 1942.0 kg/m$^3$, I/MR$^2$=0.312 [6]), and the value of the satellite's heat flux ~5 mW/m$^2$ the Ganymede's internal structure was recalculated. The values of core density were chosen in the range of 5.15-6.50 g/cm$^3$. When calculating, we additionally estimated the progressive change in the mantle density with depth in accordance with the equations of state of silicates [4].

The results of calculations showed that the radius of Ganymede's central Fe-FeS core does not exceed a value of 630-760 km. The maximum thickness of the outer water-ice shell is about 910 km (100 km of Ih-icy crust + 200 km of water internal ocean + 50 km of ice V + ice VI). The density of the mantle's silicates under standard conditions was determined from calculations, and it was found to be equal to 3.15-3.50 g/cm$^3$, which is in a close agreement with the density of ordinary L/LL chondrites. Taking into account silicates compressibility under pressure, the mantle's density varied with depth between 3.19 and 3.74 g/cm$^3$. The total $H_2O$ content in Ganymede is estimated as 43.3-50.4% which is slightly lower than our previous assessments [1] and corresponds to the satellite's water/rock ratio of 0.8 – 1.0.

*Internal structure of Titan*

There are two competitive models of the internal structure of Saturn's icy moon, Titan: 1) a model of partially differentiated satellite, with a large internal region composed by homogeneous rock and ice mixture (rock-ice mantle) [5], and 2) a model of fully differentiated Titan (Ganymede's like structure), in which a complete separation of rock from ice occurred, and an intermediate mantle composed of hydrous minerals was formed [3, 4].

The model of Titan with undifferentiated rock-ice mantle was thoroughly investigated in [5]. The main calculation results for this model are as follows: 1) The maximum thickness of the satellite's water-ice shell is 450-470 km. The maximum size of the central rocky core is 1300 km.; 2) The density of rock-ice mantle is about 1.22-2.64 g/cm$^3$ with the $H_2O$ content of 24-70%; 3) The total $H_2O$ content in Titan is 45-51% (ice/rock ratio is close to 1), which is similar to Ganymede and Callisto (49-55%) [1-2, 5], (Fig. 1).

The main calculation results for the Titan's model with hydrous silicate mantle indicate that the maximum thickness of the water-ice shell is 430-480 km, and maximum size of the central Fe-Si core is 930 km. The $H_2O$ content of Titan's hydrated mantle was taken as 13% - typical value for serpentine group minerals. This assumption led to the related estimates of the bulk amount of $H_2O$ in Titan as 35-38% (Fig. 1, red color), which reflect the $H_2O$/rock ratio in the satellite equal to 0.5-0.6.

**Conclusions:**

Revealed features of the Ganymede and Titan internal structures, as well as their bulk amount of $H_2O$, calculated from different models, should reflect the specific conditions of the satellites' formation and evolution. Our results have shown that the internal structure and composition of Ganymede are consistent with a theory of the regular satellites' formation in the jovian accretion disk, according to which Ganymede was formed in the relatively warm subnebula ~250 K during 10$^4$ yrs - the shortest accretion time comparing with Callisto and Titan. This has led to the fact that Ganymede could heated up sufficiently for melting its inner layers and following differentiation. It is likely that Titan was formed during ~10$^6$ yrs at lower temperatures 60–90 K in the saturnian accretion disk [7]. This has lead to incomplete differentiation of the satellite, conforming to the Titan's model with ice-rock mantle.

It should also be noted that the same ice/rock ratio (close to 1) in fully differentiated Ganymede and in partially differentiated Titan and Callisto could indicate that these satellites could be formed from the planetesimals with a composition similar to the composition of ordinary L/LL-chondrites. In another words, it is logical to assume that Jupiter and Saturn satellite systems were made up of the substance with the similar composition. In connection with this the $H_2O$ content in Titan obtained by "hydrous silicate mantle" model which is found to be more than 10% lower than the values typical for all large Jupiter and Saturn satellites (Fig.1) is quite difficult to explain, even in general terms.

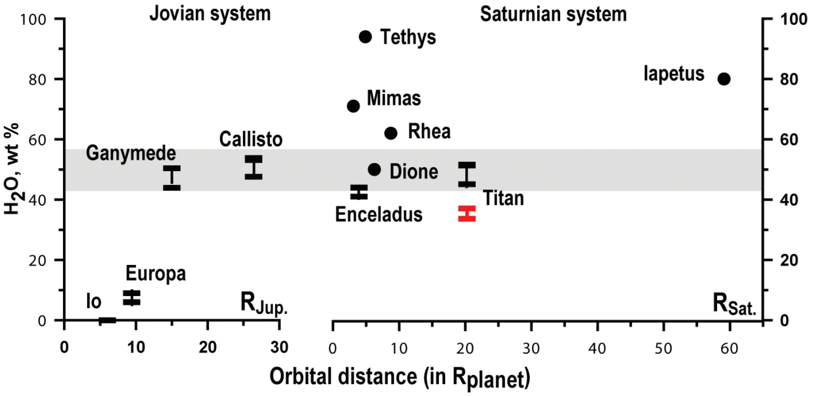


**Fig. 1.** $H_2O$ content in the icy satellites of Jupiter and Saturn [1-2, 5, 8]. The red symbol indicates a model of Titan with hydrous silicate mantle (13 wt % $H_2O$). Shaded area shows the area in which the ice/rock ratio values in satellites are close to 1.

**Acknowledgements:**

This research was supported by the Russian Academy of Sciences under Program 22 and by the RFBR grants 12-05-00178 and 12-05-00033.

**References:**

[1] Kuskov, O.L., Kronrod, V.A.: Core Sizes and Internal Structure of Earth's and Jupiter's Satellites, Icarus, V. 151, pp. 204–227, 2001.

[2] Kuskov, O.L., Kronrod, V.A.: Internal structure of Europa and Callisto, Icarus, V. 177, pp. 550–569, 2005.

[3] Castillo-Rogez, J. and Lunine, J.: Evolution of Titan's rocky core constrained by

Cassini observations, Geophys. Res. Lett., Vol. 37, L20205, 2010.
[4] Fortes, A.: Titan's internal structure and the evolutionary consequences, Planet. Space Sci., Vol. 60, pp. 10–17, 2012.
[5] Dunaeva, A.N., Kronrod, V.A., Kuskov, O.L.: Models of Titan with water–ice shell, rock–ice mantle, and constraints on the rock–iron component composition, Doklady Earth Sciences, Vol. 454, Part 1, pp. 89–93, 2014.
[6] Schubert, G., Anderson, J.D., Spohn, T., McKinnon, W.B.: Interior composition, structure and dynamics of the Galilean satellites. Jupiter. The Planet, Satellites and Magnetosphere, pp. 281-306, 2004.
[7] Makalkin, A.B., Dorofeeva, V.A.: Accretion Disks around Jupiter and Saturn at the Stage of Regular Satellite Formation, Solar System Research, Vol. 48, No. 1, pp. 62–78, 2014.
[8] Sekine, Y., Genda H.: Giant impacts in the Saturnian system: A possible origin of diversity in the inner mid-sized satellites, Planetary and Space Science, V. 63-64, pp. 133-138, 2012.

# EXPERIMENTAL STUDY OF THE SHOCK-EVAPORATIVE TRANSFORMATION OF METEORITIC ORGANICS DURING HYPERVELOCITY IMPACTS FOR THE CHARACTERIZATION OF EXOGENOUS ORGANIC MATTER ON THE SURFACES OF ICY SATELLITES

**M. A. Zaitsev[1], M. V. Gerasimov[1], M. A. Ivanova[2], C. A. Lorenz[2], A. V. Korochantsev[2],**
*[1]Space Research Institute of Russian Academy of Sciences (IKI RAS), 117997, 84/32 Profsoyuznaya str., Moscow, Russia;*
*[2]Vernadsky Institute of Geochemistry and Analytical Chemistry of Russian Academy of Sciences (GEOKHI RAS), 119991,19 Kosygin str., Moscow, Russia.*
*Contact: mzaitsev@iki.rssi.ru*

**Introduction:**

The main goal of planned missions to Jupiter's Galilean satellites Ganymede or Europa is the search for extraterrestrial life, which could potentially be revealed by characterization of surface organics at the landing site. It is well known that planets and satellites are exposed to steady meteoritic and cometary bombardment which delivers exogenous organic matter. The exogenous organic matter on the satellite surfaces may include both unaltered organics of in falling meteorites and comets, and organics synthesized from organic and/or inorganic and mineral components of the incoming bodies during impacts. Biologically important molecules such as amino acids and nucleobases also could be delivered by carbonaceous chondrites/comets. To adequately interpret organic compounds (OC) on the surface of Ganymede or Europa, we must take into account the presence of this exogenous organic matter.

The quantitative composition of exogenous organics is difficult to predict. It depends on the frequency of meteoritic/cometary bombardment, conditions and efficiency of potential synthesis of organics in the water mantles below the satellites' icy crusts, speed of crustal renovation, and other factors. However, the qualitative composition of exogenous organics can be described through the study of organic matter in different classes of meteorites and products of their shock-evaporative transformation.

**Experiment:**

We carried out a comparative study of carbonaceous CM2 (Murchison) and CO3 (Kainsaz) chondrites and condensed products of their high-temperature impact-induced evaporation, using pyrolytic gas chromatography coupled with mass spectrometry (Pyr-GC/MS) [1, 2]. Pyr-GC/MS is the main method for *in situ* characterization of volatile and organic compounds in the planetary regolith [3, 4].

We used aNd-glass laser pulse ($\lambda$=1,06μm) to simulate impact-induced vaporization. Pulse duration was$10^{-3}$s, pulse energy ~600 J, power density ~$10^7$ W/cm$^2$. The gas atmosphere in the test chamber during laser ablation of meteorites was inert (helium) or reducing (hydrogen). Temperature in the evaporated cloud was about 4000-5000 K, corresponding to hypervelocity impacts of ~10-15 km/s[5].

We performed stepwisepyrolysis (460°C, 15 min →900°C,10 min) under helium flow of pulverized meteorites (20 mg) and solid condensates (25 mg) from 2-3 laser ablation experiments. We collected the released volatiles at temperature of liquid $N_2$ and desorbed them by pulse heating of cryogenic trap up to ~400°C into the chromatographic system (Chromatec Crystal 5000.2 manufactured by Chromatec) in splitless mode. GC separation was performed by BPX-5 capillary column 60m×0,25mm×0,25μm (non-polar phase) using the following temperature program:35°C (2min)→10°C/min→290°C. Quadrupole mass-spectrometer DSQ II (manufactured by Thermo Scientific) worked in the electron ionization (EI) mode (electron energy: 70eV) with total ion current registration at 34÷450m/z.

**Summary:**

We found significant differences in the composition and ratios of volatile organics between pyrolysates (at 460°C) of the meteorites and their condensates. All condensates gave lesser absolute amounts of OC during pyrolysis then the initial meteorites. The“hydrogen” condensates gave significantly higher amounts of volatiles than the “helium” condensates.

The “helium”condensates gave volatiles which have the higher relative amounts of N-, S-containing compounds and aliphatic hydrocarbons then the initial meteorites and large amounts of $CO_2$ and $SO_2$. The “hydrogen” condensates gave volatiles containing the higher relative amounts of aromatic and alkyl-aromatic hydrocarbons compared to the initial meteorites. At the same time, S-containing OCwere almost absent, but there were huge amounts of $H_2S$.

Residual pyrolysis of all of the condensates at 900°C gave only carbon dioxide, sulfur dioxide, benzene and traces of other aromatics.

Murchison bulk material had higher abundance and diversity of OC in pyrolysates than Kainsaz [1]. Nevertheless, the Kainsaz condensates (both “hydrogen” and “helium”) were much higher in diversity and quantity of volatile organics than the Murchison condensates and gave lesser amounts of $CO_2$ and $SO_2$. This phenomenon can be explained by differences in elemental and mineral composition of both meteorites resulting in different redox conditions in the vapour clouds during evaporation. Kainsaz is more reduced than Murchison. It contains ~5% vol. of nickel iron [6] compared to <0.5% vol. of the same in Murchison[7].Furthermore, nickel iron is well known as a catalyst of a number of chemical reactions (e.g. Fisher-Tropsch). The Fisher-Tropsch reactions can take place during condensation of the vapour cloud. In our case the possible indicator of those reactions is the release of n-alkanes and long-chain alkyl-aromatic hydrocarbons from the condensates during pyrolysis. Especially it is concerned to the Kainsaz condensates.

The large amounts of water involving into the impact-generated vapour cloud may affect to the redox conditions in the cloud and to the results of the organic synthesis. Thus we need to use the composite targets containing both meteoritic matter and water ice to simulate significantly the conditions at the surface of icy satellites.

**Conclusions:**

Exogenous OC delivered to the surface of icy satellites by falling meteorites may consist of a wide diversity of hydrocarbons, O-, S-, and N- containing compounds. An impact-generated cloud has super-high temperature and high oxygen abundance derived from thermal dissociation of colliding silicates [5]. Despite of that new synthesis of OC results in delivery of noticeable quantities of diverse and complex organics to the surface of icy satellites. Mineral phases which are condensed in the vapor cloud can catalyze the synthesis of organic compounds. Moreover the surface organic matter may contain fairly complex molecules directly obtained from the meteorite kerogen-like material.

We need also to elaborate composition- and isotope- based criteria to discriminate between endogenous and exogenous OC.

We must try to find the freshest ices for landing sites in order to avoid exogenous contamination, which is important for efficient searching for endogenous (and possibly biologically produced) organic substances.

**Acknowledgements:**

This work was supported in part by RFBR grant 12-05-01161 and P-28 Program of the RAS.

**References:**

[1] Zaitsev M.A. et al. (2013) *44th LPSC*, abs. 1905.
[2] Ivanova M.A. et al. (2014) *45th LPSC*,abs.1014.
[3] Biemann K. et al. (1976) *Science,* 194, 4260, 72-76.
[4] Leshin L.A. et al. (2013) *Science,*341, 6153, DOI: 10.1126/science.1238937.
[5] Gerasimov M.V. et al. (1998) *Earth, Moon, and Planets,* 80, 205-259.
[6] McSween H.Y. (1977) *Geochim. Cosmochim.Acta,*41, 477-491.
[7] McSween H.Y. (1979) *Geochim. Cosmochim.Acta*, 43, 1761-1770.

# GAS DRAG AND CAPTURE OF PLANETESIMALS IN ACCRETION DISKS OF JUPITER AND SATURN WITH ACCOUNT OF ABLATION AND FRAGMENTATION

**V. A. Kronrod[1], A. B. Makalkin[2],**
*[1]Vernadsky Institute of Geochemistry and Analytical Chemistry, RAS, Kosygin str., 19, 119991 Moscow, Russia;*
*[2]Schmidt Institute of Physics of the Earth, Bolshaya Gruzinskaya str., 10-1 Moscow, Russia.*
*Contact: va_kronrod@mail.ru*

The problem of capture of planetesimals into the protosatellite accretion disks around young Jupiter and Saturn is discussed. The capture is due to gas drag in the disks and is accompanied by ablation and fragmentation of planetesimals, which affect the capture. For estimation of slowdown of planetesimals and their fragmentation the distribution of gas density in the disks is needed. This distribution is obtained in the models of accretion disks around Jupiter and Saturn at the late stage of planet accretion, when regular satellites formed [1-4]. We use the new models [4] which meet currently known cosmochemical and physical restrictions. We take the distributions of midplane density for both disks to approximate them with the power-law functions of radial distance from the planets. We also take into account the mean random velocities of planetesimals entering the Hill spheres of the giant planets and inclination of planetesimal orbits to the central planes of the circum-planetary disks. The distributions of gas density and planetesimal velocity in the disks of Jupiter and Saturn are used in solution the equations of planetesimal motion and ablation to estimate the maximum radius of planetesimals captured by the disks at various distances from the planets. These density and velocity distributions are also used in estimating the threshold aerodynamic pressure, necessary for starting fragmentation at distances of major satellites. Possible variations of bodies' strength are taken into account. Callisto probably formed from smaller bodies ($R$<10–15 m) then Ganymede did. At the Ganymede orbit the bodies of wider size spectrum slowed down and were captured or fragmented and then were captured. This factor as well as higher duration of Callisto accretion due to its higher distance from the planet could contribute to its lower differentiation compared to Ganymede.

**References:**

[1] Makalkin, A.B., Dorofeeva, V.A., and Ruskol, E.L., *Solar Syst. Research,* 1999, vol. 33, no. 6, p. 456–463.
[2] Canup, R.M. and Ward, W.R. *Astron. J.*, 2002, vol. 124, pp. 3404–3423.
[3] Kuskov, O.L., Dorofeeva, V.A., Kronrod, V.A., and Makalkin, A.B., Jupiter and Saturn Systems: Formation, Composition, and Internal Structure of Large Satellites), Moscow: Izd. LKI, 2009.
[4] Makalkin A.B., and Dorofeeva, V.A., *Solar Syst. Res.,* 2014, vol. 48, no. 1, p. 62-78.

# SOME RECENT SPECTROPHOTOMETRIC STUDIES OF JUPITER AND SATURN

**N.N. Bondarenko, A.M. Karimov, P.G. Lyssenko, G.A. Kharitonova, G.A. Kirienko, V.G. Tejfel, V.D. Vdovichenko**
*Fessenkov Astrophysical Institute Alma-Ata, Kazakhstan*
*Contact: tejf@mail.ru*

## Introduction

In the Astrophysical Institute we have been conducting studies of the giant planets for several decades and they are important and traditional scientific direction, along with other observations and studies of the solar system bodies. The main method of observation is spectral measurements of behavior of methane and ammonia molecular absorption bands on the disks of Jupiter and Saturn. Formation of these absorptions occurs during the complex process of radiative transfer in the absorbing and scattering cloud layers and the observed spatial and temporal variations of the absorption are indicators of the state and instability of their structure.

## Jupiter. Vertical heterogeneity of the cloud cover

Carrying out quasi continuous observations, double overlapping all the longitudes of Jupiter (with the step of $1.8^0$), we measured 399 CCD spectrograms of its central meridian and made the maps of longitude-latitude variations of $CH_4$ absorption. We show that these variations are generally preserved at all longitudes, but the locations of extreme (maxima and minima) absorption of different bands are not the same. Zonal differences in absorption do not correlate with the position of light zones and dark belts of Jupiter, except for the 887 nm band, which keeps a well-pronounced minimum in the equatorial belt of Jupiter for many years. Comparison of latitudinal absorption in the 619 and 725 nm bands shows that the ratio of these bands' depths at the low-latitude belt of Jupiter has a loop form. Rough estimates of the effective optical depths of absorption formation and their differences in the terms of a simple two-layer model indicate that there is increasing cloud cover vertical heterogeneity from the equator towards high latitudes [1].

## Jupiter. The Great Red Spot and "barges"

We conducted several cycles of spectral observations of the Great Red Spot (GRS) to investigate changes in its brightness in the strong absorption band of 887 nm $CH_4$ when moving from the central meridian to the disc's edge. We scanned the southern part of the Jovian disk and chose the zonal spectra corresponding to the latitude of the GRS. As a result, we defined basic optical characteristics of the cloud layers and the thickness of the atmosphere above the clouds, as well as the differences between the heights of the aerosol upper boundaries. The GRS is found to be the highest cloudy formation. From our spectral studies, its height is 10 km higher than the surrounding STrZ and 3 km higher than the cloud tops at the equator. Cloud density in GRS is higher than its surroundings' density [2]. We could also record the spectra of extremely rare dark-brown local formations ("barges") on Jupiter. The $CH_4$ absorption in them was slightly higher than in the neighboring regions [3].

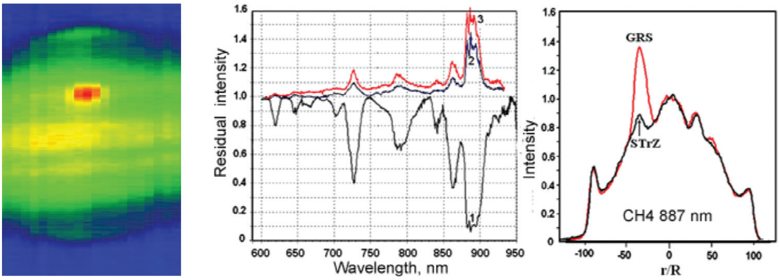


**Fig.1.** (a) The synthetic image of Jupiter in 887 nm, constructed with spectral scans; (b) the Great Red Spot spectrum (1); ratio of the GRS spectrum to the EZ one (2) and to the STrZ one (3); (c) profiles of the central meridian in 887 nm with the GRS on it and half an hour after it has passed off.

## Jupiter. Variations of the ammonia absorption

Study of ammonia absorption in the spectrum of Jupiter is hampered by the fact that the $NH_3$ absorption bands are overlapped with the $CH_4$ absorption bands. To extract them we calculated ratios of Jovian zone spectra to the spectrum of the center of Saturn's disk, where ammonia absorption is almost not observed. Measurements of the 787 nm $NH_3$ absorption band selected in such a way, showed its variations across the disk of Jupiter. Its equivalent width significantly decreases in the equatorial zone towards to the edges of the disk; on the central meridian we observed depression of its absorption that was variable at temperate latitudes in the northern hemisphere [4]. These findings require further observations and analysis.

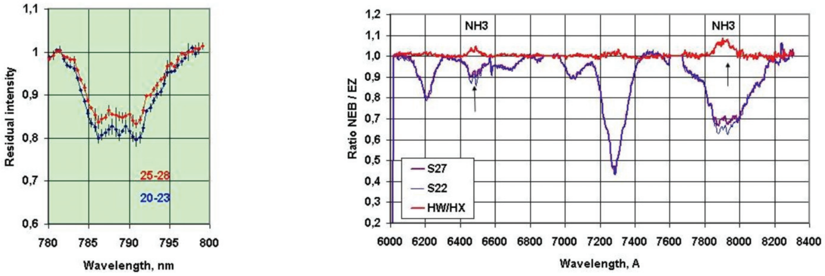


**Fig. 2.** On the left: the selected 787 nm $NH_3$ band profiles in the center of the disk (zones 20-22) and in NEB (25-28); on the right: the ratio of the NEB spectrum to the center of the disc (EZ) spectrum.

## Saturn. Optical asymmetry in the hemispheres

In a totality of our long-term observations of Saturn [5] we note a special period (the end of 2008 - beginning of 2009), when the inclination of the equator and the ring was close to zero. At this time both hemispheres of the planet were in equal conditions of sunlit and visibility. A previous equinox took place in 1995 and that time we observed a considerable asymmetry between southern (S) and northern (N) hemispheres in latitudinal variations of methane absorption: in the S hemisphere, all the $CH_4$ bands were weaker than in the N one [6]. During the last equinox a character of the asymmetry did not change, but it was less pronounced, moreover, it was evident in the weak absorption bands, whereas it was almost absent in the stronger 725 nm band. However we always observed only a remained absorption minimum in the equatorial belt. In the absence of obscuring the equatorial belt with the ring, we could determine a real difference in the $CH_4$ absorption at the equator and at the temperate latitudes and estimate some differences in the density and height of the cloud cover. Estimates of the effective optical depths of absorption band formation indicate some differences in a rate of vertical heterogeneity of the cloud layer: in the S hemisphere it is greater than in the N one. Similar differences were observed in the latitudinal variations of the brightness temperature at 500 mb [7].

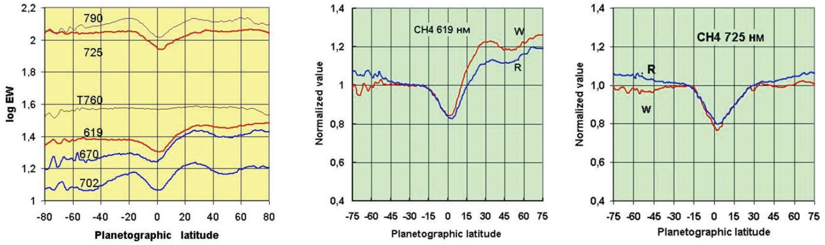


**Fig. 3.** Latitudinal variations of the equivalent widths of the $CH_4$ absorption bands (in logarithmic scale), and a comparison of the latitudinal variations of the normalized values of the 619 and 725 nm $CH_4$ band equivalent widths (W) and depths (R).

**References:**

[1] V.G.Tejfel, G.A.Kharitonova (2013) Astron. Tzirkular No.1600, 1-4; [2] V.D.Vdovichenko et al. (2014) Izv. NAN RK, No4 (in press); [3] V.G.Tejfel, G.A.Kharitonova (2012) EPSC, 7, 2012-80, 2pp; [4] N.N.Bondarenko (2013) Astronomical and Astrophys. Transactions, 28, 81-86; [5] V.G. Tejfel et al. (2013) Astron. and Astrophys. Transactions, 28, 121-134; [6] V.G.Tejfel (1997) Solar System Res., 31, 198-206; [7] L. Fletcher et al. (2010) Icarus, 208, 337–352.

# DYNAMICS OF “JUMPING” TROJANS

**V.V. Sidorenko,**
*Keldysh Institute of Applied Mathematics, Miusskaya Sq.4, 125047 Moscow, Russia.*
*Contact: vvsidorenko@list.ru*

The term ”jumping” Trojan was introduced by Tsiganis et al. (2000) in their studies of long-term dynamics exhibited by the asteroid (1868) Thersites: as it turned out, this asteroid may pass from the librations around L4 to the librations around L5. One more example of a ”jumping” Trojan was found by Connors et al. (2011): librations of the asteroid 2010 TK7 around Earth’s libration point L4 preceded by its librations around L5. We explore the dynamics of ”jumping” Trojans under the scope of the restricted planar elliptical three-body problem. Via double numerical averaging, we construct evolutionary equations which describe the long-term behavior of the orbital elements of these asteroids.

**Acknowledgements:**

This work was supported by the grant of the Russian Academy of Sciences Program: “Fundamental problems of research and exploration of the Solar system”.